NOTE TO USERS

Université d'Ottawa · University of Ottawa

Université d'Ottawa • University of Ottawa

FACULTÉ DE ÉTUDES SUPÉRIEURES ET POSTDOCTORALES

FACULTY OF GRADUATE AND POSTDOCTORAL STUDIES

Warren DUNN

AUTEUR DE LA THÈSE - AUTHOR OF THESIS

Ph.D. (Mechanical Engineering)

GRADE - DEGREE

Department of Mechanical Engineering

FACULTÉ, ÉCOLE, DÉPARTEMENT - FACULTY, SCHOOL, DEPARTMENT

TITRE DE LA THÈSE - TITLE OF THE THESIS

Vortex Shedding from Cylinders with Step-changes in Diameter in Uniform and Shear Flows

S. Tavoularis

DIRECTEUR DE LA THÈSE - THESIS SUPERVISOR

CO-DIRECTEUR DE LA THÈSE - THESIS CO-SUPERVISOR

EXAMINATEURS DE LA THÈSE - THESIS EXAMINERS

M. Johnson

A. Laneville

R. Milane

M. Yaras

J.-M. De Koninck, Ph.D.

LE DOYEN DE LA FACULTÉ DES ÉTUDES SUPÉRIEURES ET POSTDOCTORALES

DEAN OF THE FACULTY OF GRADUATE AND POSTDOCTORAL STUDIES

Vortex Shedding from Cylinders with Step-Changes in Diameter in Uniform and Shear Flows

by

Warren R. Dunn

A thesis presented to the
Faculty of Graduate and Postdoctoral Studies
in partial fulfillment of the
requirement for the degree of

DOCTOR OF PHILOSOPHY
in
MECHANICAL ENGINEERING

Ottawa-Carleton Institute for Mechanical and Aerospace Engineering
Department of Mechanical Engineering
University of Ottawa
Ottawa, Ontario, Canada
August 2004

Your file Votre référence
ISBN: 0-494-01698-1
Our file Notre référence
ISBN: 0-494-01698-1

Abstract

Cylinders with a single step-change in diameter, symmetric double step-changes, and a free end were studied at Reynolds numbers between 40 and 1250, in uniform and shear flows. The diameter ratio of the step-cylinders was 0.51. Streamwise velocity measurements were taken with laser Doppler velocimetry, and observations were made using flow visualization.

Spectral analysis showed that step-changes in diameter caused vortex shedding to occur in cells of constant frequency, with a change in frequency across the cell boundaries. In uniform flow, vortices behind the large cylinder near the step were shed in a cell with a lower frequency compared to the rest of the cylinder, while, in shear flow, cellular shedding was observed behind both the large and small cylinders. Flow visualization showed that the ends of vortices shed in-phase from two adjacent cells in the step region connected across the cell boundary, while those shed out-of-phase looped 180° and joined with vortices shed from the opposite side of the cylinder, in the same cell. Wavelet analysis of velocity signals showed that the two dominant shedding frequencies at the step could be detected in the signal either simultaneously, in which case the signal had a modulated appearance, or alternating, in which case the signal had a quasi-periodic appearance, whose frequency changed with time.

The vortices shed from both cylinders were inclined with respect to the cylinder axes. Spanwise convection of the wakes occurred near the step, in the direction of the large cylinder, caused by flow over the step normal to the cylinder axis. Streamwise vortices were released from the sharp edges of the step, which aided in the formation of vortex loops.

Most of the vortex shedding patterns behind the double-step cylinders and the cylinders with free ends were similar to those observed in the single-step case. In addition, the flow around each of the steps of the double-step cylinder influenced the other, an effect that increased as the step separation decreased. The increased flow over the tip of a finite cylinder, as compared to the step-cylinders, resulted in highly-inclined, cusp-like connections between the streamwise and shed vortices.

Acknowledgements

I would like to thank Professor Stavros Tavoularis for the opportunity to study under his guidance and expertise. I have learned a great deal because of his persistence and advice. He inspired me to become a better teacher, and to delve deeper into the subjects that I used while teaching and researching, in order to fully understand them.

I wish to thank Dr. Tavoularis and NSERC for financial support given as I was engaged in this research, as well as the Faculty of Graduate and Postdoctoral Research, for the tuition scholarships awarded in the early years of this degree.

I am grateful to the staff of the Machine shop in the Department of Mechanical Engineering, for the construction of the models and the very many mechanical accessories that were required in this study, as well as their patience in the various designs that went their way.

I would also like to thank my fellow graduate students, including Matthew Doyle, Sean Bailey, Sadok Guellouz, Mohsen Ferchichi, and many others, for their friendship. The time discussing our work and many other topics were cherished, and helped make my stay at the University of Ottawa more enjoyable. Thanks also go to Guillaume Desjardins for plotting many last-minute figures for me.

I am especially thankful for the support of my family and friends. Mom and dad, your encouragement means a lot to me. Joanne, your patience has finally been rewarded. I could not have done it without you. It has been a long journey, but together with André, we will move into the future proud of our accomplishments.

Contents

List of Tables

List of Figures

Nomenclature

a	Wavelet scale
AR	Aspect ratio
b	Width of the water channel
B	Screen deflection coefficient
d	Diameter of the small cylinder
d_b	Hydrogen bubble diameter
d_w	Diameter of the shear generator wire
D	Diameter of the large cylinder
f	Vortex shedding frequency
g	Gravitational acceleration
h	Water height in the test section
i	Imaginary number unit, $\sqrt{-1}$
l	Mesh size
K	Pressure loss coefficient across a screen
L	Cylinder length
Re	Reynolds number
$s(t)$	Time dependent signal

St	Strouhal number
t	Time
t_o	Reference time
u	Instantaneous speed in the x-direction
U	Mean speed in the x-direction
$\overline{U}$	Time-average of the velocity in the x-direction
U_c	Mean centerline speed
V_s	Speed of hydrogen bubbles
v	Instantaneous speed in the y-direction
W(a, τ)	Wavelet transform
x	Streamwise distance from the cylinder location
y	Vertical distance in the test section
z	Distance from one side wall of the test section
β	Shear parameter
Δt	Time step of an evenly-sampled signal
Δx	LDV control volume dimension in the x-direction
Δy	LDV control volume dimension in the y-direction
Δz	LDV control volume dimension in the z-direction
γ	Wavelet dimensionless frequency
ν	Kinematic viscosity

ψ Wavelet function

σ Screen solidity

τ Dimensionless time variable

Chapter 1

Introduction

This study documents the vortex shedding from cylinders with non-uniformities in their diameters, immersed in uniform and non-uniform flows.

1.1 Motivation

A fluid flowing towards a stationary bluff body must be diverted from its original path in order to move around the obstacle. Fluid far from the body is shifted by only a small amount, but the fluid close to the body surface tends to follow its contour. The curvature of the flow as it is deflected creates a pressure gradient, which, combined with friction from the surface, slows the fluid as it moves around the contour. Depending on the body shape and flow conditions, the flow may separate from the surface, away from its ideal trajectory.

Fluid separating from one side of an elongated body oriented normal to the flow direction will roll into the wake, forming a vortex. If the body is symmetric, fluid that separates from the opposite side will also roll into the wake, forming a vortex that rotates

in the opposite direction. Subsequent vortices will be shed alternately from one side of the body and the other, forming a vortex street (Figure 1).

Vortex shedding may occur from any bluff body under appropriate circumstances, but its regularity depends on the shape and the flow conditions. Air moving around a rectangular bus, for example, is likely to form a more regular wake than air moving around the more complex angles of a tractor. Isolated bodies, like a rural water reservoir tower exposed to the wind, have relatively simpler wakes than multiple-body systems, such as a city centre, in which the flow around one structure is complicated by interactions with flows around other structures.

Many applications for which vortex shedding is important involve long or tall structures exposed to the flow. Most sky-scrapers have square or rectangular cross-sections, while towers, masts and underwater supports for docks and offshore platforms may be circular in cross-section. Many laboratory studies have documented uniform flow around cylinders with square, circular, or other cross-sections (see, for example, Williamson, 1989).

At speeds that are slow compared to the speed of sound, vortex shedding from a circular cylinder depends only on the Reynolds number, Re = UD/ν, where D is the cylinder diameter, U is the cross-flow velocity, and ν is the kinematic viscosity of the fluid. The frequency of vortex shedding, f, is usually presented in dimensionless form as the Strouhal number, St = fD/V. Experimental results showing the relationship between the Reynolds number and the Strouhal number for circular cylinders are presented in Figure 2. If the diameter of the cylinder, and the speed and viscosity of the fluid are known, the frequency at which the vortices are shed can be predicted.

The alternating nature of the vortex street subjects the body to unsteady pressure forces, which might set the body vibrating like a sign in the wind. Flow separation is associated with an increased drag force, due to the low-pressure region in the wake. Although flow separation and the formation of a vortex street may be undesirable in most cases, they are also usually unavoidable.

Various techniques have been devised for the reduction of unsteady loading and drag due to vortex shedding. These include streamlining a bluff object by the addition of an elongated afterbody, or the placement of a splitter plate in the recirculation region, which prevents an alternating vortex street from forming (Roshko, 1961). Devices that force vortices to be shed oblique to the cylinder axis, or the use of cylinders that vary in cross-section over a spanwise distance, can also reduce the average and fluctuating structural loads.

Two-dimensional vortex shedding can be disturbed by flow speed variations along the span of the cylinder, also known as flow shear. Shear occurs, for example, in the atmospheric boundary layer, in which the wind speed decreases towards the ground and increases with altitude. Such natural velocity gradients also exist in oceanic flows. Even if a vortex was initially shed parallel to the cylinder's axis, it would tend to become inclined as it was convected downstream at different speeds along its length.

Laboratory studies of shear flows have employed a simplified configuration, in which the velocity profile is linear, and which is sometimes referred to as uniformly-sheared flow. Vortex shedding from a uniform-diameter cylinder in uniformly-sheared flow occurs in spanwise cells, with a constant frequency in each cell, and an abrupt frequency change across the boundaries of adjacent cells (Mair and Stansby, 1975). As the cell with the higher frequency contains more vortices than the lower-frequency cell, some of these

vortices will have no counterparts in the adjacent cell. Flow visualization shows that some of the vortices in the high-frequency cell appear to be disconnected at the boundary, a phenomenon known as vortex splitting, or vortex dislocation.

Cellular vortex shedding also occurs in uniform flows past cylinders with non-uniform cross-sections. For example, a tapered cylinder, or cone, will shed oblique vortices in constant-frequency cells (Gaster, 1969), while a finite cylinder will generate a cell of lower shedding frequency near its free end due to downwash, the pressure-induced flow over its tip, perpendicular to its axis (Farivar, 1981).

Oblique vortex shedding, cellular vortex shedding, and vortex splitting are common in three-dimensional wake flows. In order to investigate the processes near the boundary of a cell, where vortices split and the frequency changes abruptly, experimental conditions can be designed to generate cellular vortex shedding in a controlled manner at specific locations, such as at the discontinuity of a cylinder with a step-change in diameter placed in a uniform flow. Besides the two obvious cells on either side of the step, it has been found that an additional cell is created behind the large cylinder close to the step (Lewis and Gharib, 1992). By combining flow non-uniformity and cross-sectional variation, investigations can be made into the effect of shear on the cells near cross-sectional discontinuities of cylinders.

Experimental studies of vortices in the laboratory have been conducted in wind tunnels, water tunnels and towing tanks. Wind tunnels have often been employed to study vortex flows of interest at moderate and high Reynolds numbers. Unfortunately, visualizing agents typically used in air, such as smoke or aerosols, diffuse quickly in the turbulent wakes that form at high speeds, which makes it difficult, if not impossible, to identify individual flow features using visual studies. Water tunnel studies have typically

been conducted at lower Reynolds numbers than those in wind tunnels. Visualizing agents used in water flows, such as dyes and hydrogen bubbles, do not diffuse as quickly at low flow speeds, permitting observations of vortex features as they develop and are swept downstream. The use of low Reynolds number results in higher Reynolds number applications, however, must be made with caution.

The recirculating water channel in the Department of Mechanical Engineering at the University of Ottawa was used to study the non-uniform vortex shedding patterns from cylinders in various configurations. The water channel is equipped with shear generators, turbulence grids, carriages for mounting models and equipment, visualization tools, and a high-resolution two-dimensional laser Doppler velocimetry (LDV) system for velocity measurements.

1.2 Objectives and scope of the thesis

The primary objective of the present study is to document and analyze the interactions of vortices shed from cylinders with single and double step-changes in diameter along their span, as well as cylinders with one free end, in both uniform and uniformly sheared flows.

While these cases represent idealized models of realistic geometries, such as buildings and structures in environmental boundary layers and other shear flows, the Reynolds numbers studied here are of a significantly lower order of magnitude than those encountered in many applications. The wake interactions of the examined cases at low Reynolds numbers, however, are interesting and complex fundamental fluid dynamical flows, the understanding of which could be applied to a range of practical problems.

Flow visualization will be used to observe the vortices and their interactions, while the velocity and frequency of vortex shedding will be measured using LDV. Wavelet analysis will help determine the time-varying local frequency in the regions of interest.

1.3 Thesis organization

This thesis began with an introduction to separated flows and vortex shedding, and a statement of the research objectives in Chapter 1. This is followed in Chapter 2 by a review of the most relevant topics among the vast amount of literature available concerning cylinders in cross-flow. Chapter 3 describes the experimental facilities, accessories, models, and methods used in the study, including the data analysis techniques. The results of this study are separated into three chapters, with the LDV data presented in Chapter 4, flow visualization results in Chapter 5, and local frequency analysis in Chapter 6. A general discussion of these results follows in Chapter 7, with conclusions drawn in Chapter 8.

Appendix A compiles the technical drawings of the cylinders and shear generator, while Appendix B contains printouts of the Matlab m-files used to process the data.

Chapter 2

Literature review

2.1 Vortex shedding from cylinders

The wake of a long, thin, circular cylinder has been an area of intense interest for over a hundred years, and has been the subject of hundreds of publications (Williamson, 1996). As fluid flows across a cylinder, the boundary layer separates, and a recirculation region forms causing vortices to be shed into the cylinder wake, alternately from one side to the other. Vortex shedding generates fluctuating pressure forces, which can cause flow induced vibrations and structural failure.

Ideally, vortices are shed parallel to a cylinder axis, at a regular frequency, and are convected downstream at the freestream speed. The vortices are then considered two-dimensional, because the vortex cross section is independent of spanwise location. In reality, even vortices shed from cylinders with large aspect ratios (the ratio of its length to diameter) show signs of three-dimensionality near their ends. However, two-dimensional

vortex shedding can be observed at low to moderate Reynolds numbers in the middle of the cylinder span (Williamson, 1996).

For a large range of Reynolds numbers, the region of vortex development behind a cylinder (Figure 3) is comprised of a boundary layer, a shear layer, and a wake. The flow around the cylinder is completely laminar for $Re < 150$ (Zdravkovich, 1997). For $Re < 5$, the flow remains attached to the cylinder, and no vortices are shed. The flow separates from the cylinder surface in the range of $5 < Re < 40$, forming two symmetric vortices, which remain attached to the cylinder's downstream side, as they are stable to small disturbances. Periodic laminar vortex shedding occurs for $40 < Re < 150$. A quantitative relationship between Strouhal and Reynolds numbers is well-defined in this range.

When the Reynolds number is increased to values between 150 and 300, known as the subcritical regime, laminar vortices are shed just beyond the formation region, the distance required for the shear layer to roll up into a vortex. Transition to turbulence occurs far downstream in the wake in this Reynolds number range, the formation region increases in length, and the first signs of three-dimensionality appear in the form of vortex loops and dislocations. Two discontinuities exist in the Re-St relationship in this regime, around $Re \approx 180$ and $Re \approx 240$, which are caused by two different modes of vortex shedding. At Reynolds numbers between the discontinuities, the vortices are highly three-dimensional, characterized by waviness, and the presence of longitudinal "fingers" along the lengths of the vortices (Williamson, 1989, and Zdravkovich, 1997).

The free shear layer adjacent to the wake becomes turbulent in the range of $300 < Re < 3 \times 10^5$, affecting the development of the near wake. With increasing Reynolds number, the length of the formation region begins to shrink, the transition point

moves upstream, Reynolds stresses increase, and three-dimensional structures comparable to the size of the shear layer vortices begin to develop (Williamson, 1996).

At a critical Reynolds number of 3×10^5, the shear layer has become fully turbulent, and the increased energy allows a partial reattachment of the flow to the cylinder surface. The boundary layer reaches much farther around the cylinder before it separates, creating a narrower wake, which leads to a sudden drop in base suction pressure and drag.

Regular vortex shedding ceases when the boundary layer on the cylinder begins its transition to turbulence in the supercritical regime at $3 \times 10^5 < \mathrm{Re} < 3.5 \times 10^6$ (Zdravkovich, 1997). Symmetric bubbles of reattached flow have been seen in this regime, and velocity fluctuations are so high that they likely suppress the vortex street altogether.

Finally, periodic vortex shedding resumes in a fully turbulent state in the postcritical (or transcritical) regime, after the boundary layer has transitioned, leading to higher drag (Rooney and Peltzer, 1981). The mechanism for this resumption is not well understood, as this range is extremely difficult to reproduce in the laboratory (Zdravkovich, 1997).

2.2 Non-uniform vortex shedding

In general, the frequency of vortex shedding increases monotonically with increasing Reynolds number up to the supercritical regime, as shown by the plot of Strouhal number vs. Reynolds number in Figure 2. Discontinuities are seen in the St-Re curve when the shed vortices become inclined to the cylinder axis, suggesting a three-dimensional effect at low Reynolds numbers (Williamson, 1989). Oblique shedding angles, discrete cells of constant shedding frequency, and vortex splitting are all signs of three-dimensional vortex shedding. Very large aspect ratios are required to prevent the ends from

influencing the behavior of the vortices in the central region, as the high pressure at the ends, or the flow interaction with adjacent surfaces, can affect the vortex evolution. The installation of an endplate at one or both cylinder ends may reduce the influence of these three-dimensionalities (Mair and Stansby, 1975).

Non-uniform cylinders and cylinders subjected to shear flows can be expected to lead to oblique vortex shedding, because either the velocity or the diameter changes from one end of the vortex to the other. In a uniformly-sheared flow, the angle that the vortices make to the cylinder axis should increase with downstream distance (Mair and Stansby, 1975).

2.2.1 Uniform cylinders in uniform flows

Cylinders with uniform diameters in uniform flows have been observed to shed vortices in a three-dimensional manner, even at low Reynolds numbers. Early studies attributed the three-dimensional nature to non-uniformities in the flow, short aspect ratios, or end effects.

At low Reynolds numbers, Williamson (1989) found that vortex shedding could switch from one oblique mode to another along the span, depending on the end conditions. Although its exact cause is unknown, mode switching was determined to be the reason behind the apparent discontinuity in the St-Re curve at Re = 85. Williamson (1989) was able to restore parallel shedding by manipulating the endplates, tilting the leading edges in towards the cylinder, which lowered the elevated base pressure at the ends. With parallel vortex shedding, the discontinuity in the St-Re curve disappeared. It was also found that the discontinuity disappeared when the vortex shedding frequency was calculated based on the streamwise component only, that is, if the frequency was divided by the cosine of the vortex angle.

To investigate the effects of the ends on vortex three-dimensionality, Slaouti and Gerrard (1981) towed a cylinder through a water channel at low Reynolds number. Different end conditions were used, including a reflection condition through the clean free water surface, ends with endplates, and free ends at a variable distance from a fixed wall. They concluded that oblique vortex shedding only occurred when one end effect was stronger than the other. One example of such a configuration is a cylinder with one end free and an endplate on the other. This asymmetry caused inclination of the vortices only near the ends, with parallel shedding in between, while a cylinder with an endplate on one end and at a wall at the other caused oblique shedding along the entire span.

Towing a cylinder from rest, Williamson (1989) found that vortices were initially shed parallel to the cylinder axis. Oblique shedding began quickly near the cylinder ends, and progressed inwards until vortices along the entire span were shed oblique to the axis in a chevron pattern. As the vortices switched from one oblique mode to the next, cells of constant but distinct frequencies formed between the end regions and the central span.

Vortex dislocations were observed at the boundaries of the cells of constant frequency, because adjacent cells shed a different number of vortices over a given time interval. A single vortex from one cell would then join with two vortices from the next cell, at a rate that corresponded to the frequency difference between the two cells, also known as the beat frequency. When the vortices were out of phase, a break in the vortex lines was observed, and a complex reconnection sequence would take place over the next several vortex pairs.

Based on the reconstruction of vortex lines from velocity signals at low Reynolds numbers, Gerrard (1966) was able to deduce the existence of vortex dislocations at certain spanwise locations. He suggested that a fluctuation in the flow speed, or a flow

inclination, might cause breakages in the vortex lines, and that a vortex would loop back 180° to join with the next vortex in the street. Slaouti and Gerrard (1981) used flow visualization to show that a free end very close to a fixed surface always formed a loop close to the end, due to the tip downwash.

According to Williamson (1989), however, vortex loops were really an artifact of the flow visualization process. As shown in Figure 4, the looping vortices C and C' would appear to be joined in the same cell, while the vortices were really connected across the cell boundaries. Disturbances such as connecting vortices that were progressively more out-of-phase could cause sections to be bent in the streamwise direction. The stretching that occurred would reduce the amount of the visualizing agent caught in the vortex, and a loop would appear to form.

At the higher, transitional, Reynolds numbers of Re = 235, Gerrard (1966) found that laminar and turbulent vortices could coexist parallel to each other, and likely formed vortex loops. He postulated that vortex loops would form between the laminar vortices, because the vorticity of laminar vortices is stronger than that of turbulent ones. Interactions between vortices with positive and negative vorticity would weaken the laminar vortices sufficiently to reconnect to adjacent turbulent vortices. The modulation of the velocity signals allowed Gerrard (1966) to observe branching of the vortices at Reynolds numbers greater than 10^4, which occurred at the minimum signal modulation amplitude.

Williamson (1992) forced the formation of vortex dislocations by attaching a thin ring of slightly larger diameter at the mid-span of a cylinder, which introduced a different shedding frequency than that along the rest of the cylinder span. The end conditions were manipulated to give each end cell either the same or a different frequency. Vortex

dislocations formed periodically at the beat frequency between all adjacent cells. When the two side frequencies were different, the vortex lines resembled the one-sided dislocations observed between cells of constant frequency. However, when the two side frequencies were the same and in phase with each other, they resembled the intermittent two-sided dislocations that were observed during the free shear layer transition.

Water channel experiments by Yang *et al.* (1993), using a scanning laser anemometer at a Reynolds number of 200, showed that the amplitude and phase of the shedding frequencies varied continuously along the cylinder span when dislocations were observed. As one frequency peak grew stronger, the other became weaker. At either end of the cylinder, one frequency was dominant, while the peaks at the two frequencies had equal amplitude over a small length of the span. Differences in the phase of the two frequencies caused vortex dislocations, with reconnections occurring over several vortex pairs. Using wave theory, Yang *et al.* (1993) found that the superposition of two waves of slightly different frequency, one oblique and one parallel to the cylinder axis, could reproduce the vortex dislocations observed in the experiments.

Water channel visualizations were compared with numerical simulations at a transitional Reynolds number study by Zhang *et al.* (1995). They attributed the vortex dislocations to the adhesion of the vortices to the cylinder surface at certain spanwise locations. The number of adhesion points increased with Reynolds number. At high Reynolds numbers, the vortices merged across adhesion points that formed too close together, shedding parallel to the cylinder axis once again. Williamson (1996, 1997), however, claims that the vortices only appear to have stopped shedding in the dislocation region, as flow visualization did not show great detail when vortex dislocations occurred. He cites Zhang *et al.* (1995) as the only researchers who see dislocations as adhesions to the cylinder.

2.2.2 Uniform cylinders in shear flows

Maull and Young (1973) were among the first to study the effects of shear on the wake of a circular cylinder, measuring the base pressure and shedding frequency. The frequency of vortex shedding remained constant in each of a number of spanwise cells, with each cell shedding vortices at a different frequency from its neighbors.

Flow visualization showed the existence of longitudinal vortices at each cell boundary as well, which were possibly created by a concentration of distributed vorticity from the shear flow. Tanaka and Murata (1999) suggested, however, that the longitudinal vortices may be the streamwise component of a vortex loop created at that location, as the spanwise vortices are inclined near cell boundaries.

Mair and Stansby (1975) also found cellular vortex shedding, but the cell boundaries in their experiments were not well defined, varying in spanwise location with time, as indicated by a broad peak in the frequency spectrum. The addition of endplates seemed to stabilize the cell boundaries, and, as the size of the endplates was increased, the spectral peaks became better defined.

Cells of constant frequency have been observed through the subcritical regime, but coherent vortex shedding seems to stop in the supercritical regime, similar to this Reynolds number range in a uniform flow (Davies, 1975). In the transcritical regime, vortex shedding began again, at a higher frequency than at lower Reynolds numbers (Rooney and Peltzer, 1981). The cells that were observed behaved in much the same manner as cells in the subcritical regime.

Mair and Stansby (1975) found that the number of cells formed in a shear flow was greatly dependent on the cylinder's aspect ratio. Increased shear at high aspect ratios decreased the length of the cells, increasing the number of cells along the span (Rooney

and Peltzer, 1981; Tavoularis *et al.*, 1987). Cells in the higher velocity section of the shear flow were found to have a more two-dimensional behavior than those in the lower velocity section (Anderson and Szewczyk, 1995).

2.2.3 Tapered cylinders in uniform and shear flows

A tapered cylinder, or conical body, has much in common with a uniform cylinder in shear flow, as in both cases the Reynolds number varies along the cylinder span.

The earliest experiments observing tapered cylinders in uniform flow were performed by Gaster (1969, 1971). As with uniform cylinders in a shear flow, cells of constant frequency were found to be dominant, with discontinuities in frequency between the cells (Hsiao *et al.*, 1998). The frequencies in all of the cells were lower than for a uniform cylinder in a uniform flow at the Reynolds number based on the mid-span diameter. The size and number of cells were found to be highly dependent on Reynolds number and taper ratio (the ratio between the maximum and minimum diameters; Papangelou, 1992). At Reynolds numbers (based on maximum diameter) below 100, no cells existed, and if the Reynolds number was higher than a certain value, the cellular structure also broke down. If the taper ratio was too low, only one frequency could be detected.

The Strouhal number was found to be constant across the cells, when calculated based on the average properties of each cell (Anderson and Szewczyk, 1995). Most researchers, including Gaster (1971), Noack *et al.* (1991), and Papangelou (1992), observed vortices that were shed oblique to the cylinder axis.

At higher Reynolds numbers (around $Re = 10^4$), Hsiao *et al.* (1992) found two constant frequency cells, at the cylinder ends, with a region in between where the frequency changed gradually from one to the other. The middle region was only observed for cylinders with large taper ratios, and became a cell of constant frequency when

endplates were attached within that region, implying that the cells were due to end effects. At lower Reynolds numbers (Re < 150), Papangelou (1992) observed that global changes in the cellular structure, including the formation of additional cells, occurred only when the endplate on the large diameter end was moved, but the cells were not altered by moving the end plate at the small diameter end.

Based on numerical calculations, Noack *et al.* (1991) found that the cell length decreased as the maximum diameter was decreased. As the aspect ratio increased, cells formed with new frequencies, one by one, from the boundaries of existing cells, with very little effect on the existing cells.

Experiments by Gaster (1969, 1971) showed a frequency modulation in the signal measured at the cell boundaries, and that the beat frequency was exactly equal to the difference in frequency between the two cells. Papangelou (1992) showed that, as the tapered cylinder was traversed from the large diameter to the small diameter, frequency modulation peaked at the cell boundary, and a higher modulated frequency was then observed in the next cell. Balasubramanian and Skop (1996) were able to reproduce the signal modulation and cellular structure numerically at low and high Reynolds numbers.

Papangelou (1992) observed several spectral peaks in each cell, but found that only one frequency was dominant, while the others were of much lower power, appearing as sidebands to the main frequency. He speculated that this was the normal frequency associated with the local diameter in that cell. As the cell boundary was approached, a second peak grew stronger, until both peaks were of the same strength. The second peak then became dominant in the next cell, and, farther from the boundary, the previously dominant peak receded. It was concluded that the cell boundaries were not the result of a sudden jump in frequency, but a continuous strengthening of a previously-existing

frequency. The frequency jump would only occur when the local frequency deviated sufficiently from the normal frequency in the cell, due to the constantly changing spanwise diameter. The magnitude of the frequency jump was the same between all adjacent cells.

Flow visualization showed the physical existence of the cells, which shed vortices at oblique angles to the cone (Papangelou, 1992). The angle increased towards the small diameter end of the cone, and the maximum angle increased as the taper ratio (ratio of the largest to smallest diameters) decreased. Vortex splitting appeared to be present at the cell boundaries, due to the different shedding frequencies (Naumann and Quadflieg, 1972; Papangelou, 1992; Anderson and Szewczyk, 1995).

A tapered cylinder could be placed in a shear flow in such a way that the shear reinforced the change in the Strouhal number (an aiding shear flow), or reduced the change in Strouhal number (an adverse shear flow) from one end to the other.

Keeping the ratio *U/D* constant in an adverse shear flow allowed vortices to be shed at a nearly constant frequency, according to Anderson and Szewczyk (1995). The vortices continued to exhibit 3D behavior, however, most notably being inclined to the axis of the cylinder because of the varying convection velocity along the span. It was proposed that a cellular structure may have still been present, but that all of the cells had the same frequency.

Balasubramanian *et al.* (1998) found both experimentally and numerically that cellular vortex shedding existed under an adverse shear with *U/D* constant, but that the jumps in frequency were very small compared to the uniform flow case, and that the overall frequency variation was quite small. In an aiding shear flow, the frequency jumps were very much larger than in the uniform flow case. The two end cells were distinct,

with constant frequencies, but the middle cell showed a more gradual frequency change, with weak, broad peaks. In all cases, the number of cells did not appear to change. All results were reproduced faithfully by a numerical method.

2.3 Vortex shedding from finite cylinders with free ends

A finite cylinder is an idealized geometry that models many applications involving wake flows, as there is a large range of objects of nearly-uniform cross-section that terminate in a fluid. These include such large aspect ratio structures as skyscrapers, down to low aspect ratio fire hydrants, or even human beings.

The aspect ratio of the cylinder is the most important factor in the influence of three-dimensional effects due to a free end. In experiments by Okamoto and Yagita (1973) in the range $1.33 \times 10^4 < \mathrm{Re} < 1.5 \times 10^5$, the vortex shedding frequency decreased with decreasing aspect ratio, and shedding stopped at $L/D < 6$. In a turbulent flow, Farivar (1981) found random fluctuations near the free end, as flow around the tip of the cylinder entrained itself into the vortex formation region. At low aspect ratio, the influence of the tip downwash extended along the entire span (Okamoto and Yagita, 1973; Farivar, 1981; Ayoub and Karamcheti, 1982).

A theoretical study by Holscher and Niemann (1996) found that the shedding frequency should increase sharply but continuously from the tip, to a constant frequency in the middle span, then decrease gradually towards the fixed end. No distinct cells were predicted along the span by the theory. Experiments by Okamoto and Yagita (1973) supported this, as the shedding frequency decreased monotonically approaching the free end in the spanwise direction, at high aspect ratios.

In contrast, a low frequency cell was found near the tip by Farivar (1981), which was attributed to downwash into the wake. In general, tip downwash extended the vortex formation region, which decreased the vortex shedding frequency. A second cell, of higher frequency, was found in the middle range of the span, and a third cell, with an even higher frequency, similar to that in 2D flow around an infinite cylinder, was detected far from the tip. A lower frequency cell near the tip was also observed by Ko and Chan (1984) and Budair *et al.* (1991).

Pressure measurements taken at a cylinder surface by Ayoub and Karamcheti (1982) at Re = 10^5 showed a single vortex shedding frequency along the span. The frequency near the tip at a given location gradually decreased with downstream distance, until cellular shedding began five diameters downstream. This suggests that the cell seen in the flow near the free end formed downstream of the formation region in the wake. In other words, the vortices were shed from the cylinder at a single frequency, and became altered in the wake by the tip downwash.

At Re = 1.8×10^5, Ayoub and Karamcheti (1982) saw the formation of cellular shedding at the cylinder surface, with one long cell far from the tip that was similar to two-dimensional vortex shedding, and a series of unstable cells closer to the tip, with lower, irregular frequencies that occasionally became regular. Increasing the Reynolds number to Re = 7.7×10^5, the unstable cells disappeared, replaced by regular vortex shedding near the tip, at a fluctuating frequency, lower than that from the rest of the cylinder.

At very low Reynolds numbers (around Re = 45), Dauchy *et al.* (1997) found numerically that the lower average frequency observed from velocity spectra near the tip was actually a linear combination of the regular shedding frequency and the beat

frequency, which modulated the velocity signal. This indicates that regular vortex shedding occurred all the way to the cylinder tip, but was coupled with a secondary instability, which was the cause of the three-dimensionality.

Farivar (1981) suggested that three closed vortex loops were shed, to form three cells, independent of aspect ratio when this was higher than a certain value. Etzold and Fiedler (1976) speculated that the cells were caused by a pair of streamwise vortices shed from the base, and another pair that formed as the downwash rotated into the streamwise direction, while the vortices shed far from both ends were periodic. Holscher and Niemann (1996) found that two pairs of streamwise vortices formed, from the tip and base of the cylinder. Flow visualization by Okamoto and Yagita (1973), however, showed a single vortex shed from the cylinder, which was attached to the cylinder base plate and the free end.

Zdravkovich *et al.* (1989) studied cylinders that had two free ends. Periodic vortex shedding was observed even at low aspect ratios, which was interrupted by irregular periods, and followed by periodic vortex shedding at a different frequency. In addition to the flow over both free ends, which quickly turned to enter the near wake, streamwise vortices were formed from separation at the sharp edges. These vortices were strengthened by the tip downwash, and displaced the vortex formation region, lowering the drag and the frequency of vortex shedding. Studies of short aspect ratio cylinders with two free ends by Gerich and Eckelmann (1982) showed that below a certain aspect ratio, the two end cells merged, so that a cell of regular vortex shedding did not form between them, as occurred with larger aspect ratios. They found that the end cells observed from high aspect ratio cylinders with two free ends were similar to the cells created by placing end-plates on a fixed cylinder.

Zdravkovich *et al.* (1989) found that capping the cylinder ends with hemispheres decreased the drag of short aspect ratio cylinders, and showed that the conditions at the free ends, especially the sharp separation point, played a significant role. However, Tanaka and Murata (1999) found that the hemispherical end caps did not significantly alter the velocity or vorticity patterns, at any aspect ratio.

Tanaka and Murata (1999) found no evidence that the streamwise vortices separated from the sharp, free ends had any influence on the wake. Far from the tip, the shed vortices were parallel to the cylinder axis. As the tip was approached from the spanwise direction, the vortices on either side of the cylinder became inclined towards each other until they joined. Around mid-span, the part of the joined vortices closest to the tip was inclined towards the cylinder, in a manner that resembled a hairpin vortex. This deformed region became more inclined as the aspect ratio decreased, even exceeding ninety degrees.

2.4 Vortex shedding from cylinders with a step change in diameter

A cylinder with a step change in its diameter provides a distinct spanwise location where the Strouhal number must change abruptly, and where the sharp edge of the large cylinder causes separation and downwash similar to a free end. This configuration might correspond, for example, to a tall building whose narrow central core extends far above the rest of its wider base. On a small scale, cooling fluid might flow across a piece of machinery where two parts of different diameters were joined.

A parametric study by Yagita *et al.* (1984) indicated that the vortex shedding behind the small cylinder far from the step seemed to be undisturbed from the two-dimensional case with large changes in aspect ratio, diameter ratio (d/D), and Reynolds number

($800 < Re < 10^5$, based on the diameter of the large cylinder). Pressure spectra by Ko *et al.* (1982) for a diameter ratio of 0.5 and $Re = 8 \times 10^4$ indicated a clearly two-dimensional wake behind the small cylinder right up to the discontinuity, which was also confirmed by Ko and Chan (1984). Ko *et al.* (1982) suggested that the large cylinder might be wide enough to act as an endplate to the small one.

The wake of the large cylinder dominated the spectrum only far from the step with a two-dimensional wake (Ko *et al.*, 1982, and Ko and Chan, 1984). Using hot-wire measurements at $Re = 7.5 \times 10^4$, Ko *et al.* (1983) found that the vortex shedding frequency from the large cylinder was absent at the step along the centerline, yet it was found to be present laterally far from the centerline at the same spanwise location.

Approaching the step spanwise from behind the large cylinder, the lateral size of the wake decreased from the width of the large cylinder to that of the small cylinder (Ko *et al.*, 1982). The region of interaction was located almost entirely behind the large cylinder, as the lower pressure there displaced the wakes in that direction. As the small cylinder wake was convected behind the large cylinder in the step region, it expanded to the width of the large cylinder wake (Ko *et al.*, 1983).

When a small tapered section was inserted at the location where the two cylinders were joined, the vortex shedding frequencies from both cylinders were present simultaneously near the large end of the taper (Ko *et al.*, 1983). The shedding frequency of the small cylinder dominated the interaction region with a strong spectral peak (Ko *et al.*, 1982), although the presence of the large cylinder wake was indicated by a frequency peak of much smaller amplitude at the same spanwise location. Vortex shedding from the large cylinder was entirely suppressed behind the plane of discontinuity. Static pressure measurements along the cylinder spans by Ko and Chan (1984) also indicated that

shedding from the small cylinder suppressed shedding from the large cylinder close to the step. At the discontinuity, a leading edge-type vortex was suggested as the cause of a spectral peak distinct from those behind the large and small cylinders close to the step. Chua *et al.* (1998) found two spectral peaks several diameters from the step behind the large cylinder. Sixty eight diameters downstream, the two peaks were visible at a farther spanwise distance from the step, indicating that the convection of the small cylinder wake behind the large cylinder continued far downstream, much as from the downwash over a cylinder with one free end.

Ko *et al.* (1982) found that the dominant local Strouhal number remained constant along the span of each cylinder, even where the two wakes interacted, despite the suppression of the large cylinder wake near the step. They suggested that the vortex shedding mechanism did not change, but that the strength of the shed vortices were reduced by the interaction. Yagita *et al.* (1984), found that at very large aspect ratios, the Strouhal number along the large cylinder span was constant, but decreased as the aspect ratio was lowered. The Strouhal number also decreased as the diameter ratio decreased, until it reached a constant value for $d/D < 0.2$. This dependence was reduced by the addition of a splitter plate at the step between the two cylinders. It was postulated that the plate blocked downwash from the freestream flow over the step. Increasing the size of the splitter plate reduced the Strouhal number dependence on aspect ratio and diameter ratio even more. The Strouhal number was always smaller than in the 2D case. Ko and Chan (1990) also found that, along the entire span of the cylinders, the turbulence intensities and Reynolds stresses were lower than those for uniform cylinders tested under the same conditions.

Lewis and Gharib (1992) studied the interaction zone between the two cylinders for $35 < Re < 200$. In the "direct mode," with diameter ratios greater than 0.8, the vortices

shed from the small cylinder remained parallel to the cylinder axis, but those shed from the large cylinder were oblique. Flow visualization by Norberg (1992) showed oblique vortex shedding inclined away from the step behind the small diameter, and towards the step behind the large cylinder. Ko and Chan (1990) found that none of the vortices were shed parallel to the cylinder axes at $Re = 8 \times 10^4$, though they cautioned that the relatively short aspect ratios used may have had some influence on the flow. The vortices from both large and small cylinders were parallel to each other, and remained parallel as they convected downstream. Yagita *et al.* (1984), reported that the vortex streets from the cylinders each moved spanwise away from the step for $d/D < 0.7$, but connected for $d/D > 0.7$, or for high Reynolds number.

An intermittent joining of the large and small cylinder vortices was observed by Yagita *et al.* (1984), forming a Y-shape as two vortices shed from the small cylinder became attached to a single vortex shed from the large cylinder. The Y-feature was not always visible, but appeared in a nearly periodic manner. Using simultaneous signals from six hot-wire probes, they calculated that a Y-shaped connection appeared behind the small cylinder at a rate approximately equal to the difference in shedding frequencies. Norberg (1992) also observed Y-shaped connections and half-loops at the step. Lewis and Gharib (1992) found that the vortices from both cylinders joined across the interaction zone when they were in phase in the "direct mode"; otherwise, because of the unequal number of vortices shed from each of the cylinders in a given time period, they joined with vortices of opposite sign shed from the same cylinder, forming half-loops at the interface. Valles *et al.* (2002) were able to duplicate numerically the "direct mode" flow patterns, in particular reproducing the half-loop patterns and the inclined vortex shedding.

Eisenlohr and Eckelmann (1989) used large diameter cylinders in place of endplates in order to reduce the three-dimensionality of the shed vortices. They found that at Re = 130, vortices that were normally inclined on a 2D cylinder were straightened with the use of "end-cylinders". It was proposed that the lower-frequency cells caused vortex splitting, which disconnected vortices in the central region from the end conditions.

Naumann and Quadflieg (1972) performed flow visualization and hot-wire measurements in the wake of a step-cylinder in a wind tunnel at $10^5 < Re < 10^6$. They found that there was no vortex shedding for either cylinder at this Reynolds number, similar to the supercritical flow case around a uniform cylinder. They also found that vortex shedding could be forced from both cylinders when a trip-wire was placed at a certain location on the large cylinder. Vortex splitting at the step could be observed with flow visualization.

Norberg (1992) studied the spectra behind stepped-cylinders with diameter ratios greater than 0.5, at $3 \times 10^3 < Re < 13 \times 10^3$. Three main frequencies were found along the span, with the third frequency distinct from those behind the large or small cylinders, lower than both, and found only in the step region. The interaction region between the two wakes was found to extend one diameter behind the large cylinder, shrinking as Reynolds number or diameter ratio increased. Lewis and Gharib (1992) also observed the third, lower, spectral frequency, but only in the "indirect mode", where the diameter ratio was less than 0.65. This "modulated zone" was bordered at the small cylinder by the step, and behind the large cylinder by an inclined interface, which allowed the cell in which this frequency occurred to increase in size with time, until it suddenly disappeared, in a periodic manner. The vortices shed from the different diameter cylinders were not observed to directly interact above this diameter ratio, even far downstream. At higher

Reynolds numbers, multiple interfaces occurred, perhaps caused by an instability due to the shear between the two wakes.

2.5 Wavelet transforms

The wavelet transform, which is a relatively recently-developed signal analysis tool, compares a short-duration wave-form to a signal, yielding time and frequency information. Typical wavelets have sharp local peaks, and tend to zero at the edges, as opposed to the periodic (and infinite) wave-forms used in Fourier analysis. Mathematically, a wavelet must be invertible, and its mean must be zero; for some applications, higher moments must also be zero.

Most commonly, signal analysis is performed in the frequency domain using the Fourier transform, which can identify the occurrence of periodic phenomena. However, by detecting peak frequencies in the signal, Fourier analysis cannot maintain information about the timing of events (Lewalle, 1998). The Fourier spectrum of a signal switching between two distinct frequencies cannot be distinguished from the spectrum of a signal that is made up of the same frequencies superimposed at all times.

The wavelet transform allows the *local* peak frequency to be determined, retaining the timing of each event. Wavelet transforms preserve properties of both the time signal (which does not show frequency information), and Fourier transforms (which shows no time information). As such, the resolutions of both scales are reduced, according to the Heisenberg Uncertainty Principle (i.e.: both time and frequency cannot be known exactly). However, some wavelets have better resolution than others, and different types are more suitable to different applications.

There are three types of wavelet transforms, defined based on the way the transform is applied. The *continuous wavelet transform* dilates and compresses the wavelet continuously with a scaling factor in order to compare it with the local part of the signal. The transform of segments that are well-correlated with the wavelet at a given scale have higher magnitudes, while uncorrelated segments have lower magnitudes. This generates an enormous amount of data, as transform magnitudes are generated for every time instant, at every scale. The *discrete wavelet transform* allows the user to define a subset of scales at which to apply the wavelet, usually based on the power of two, thus reducing the amount of data produced. This is acceptable for many applications which do not require high resolution. *Wavelet packets* are pre-defined functions that are variations of what is known as a "mother wavelet", in which the user can choose to adjust the bandwidth or center of a filtering window to fit the needs of the application. Wavelet packets were initially created for data compression (Farge, 1992).

Continuous wavelet transforms give the most data, and allow greater resolution in the reconstruction of the original signal based on the resulting magnitudes. Many different wavelets are available to choose from. The original wavelet can be traced to Morlet (Lewalle, 1998), and this remains as one of the most popular wavelets for one-dimensional signal analysis. The Morlet wavelet has high spectral resolution, thus it focuses on local periodicity in the signal. It can distinguish, as the Fourier transform can, between random fluctuations and short periodic segments in the signal. The Morlet wavelet is defined by periodic functions inside a Gaussian envelope. It has both real and complex parts, and is thus able to give amplitude and phase information.

Another popular wavelet is the Mexican hat, which is the second derivative of the Gaussian function. This wavelet has better temporal resolution than the Morlet wavelet. It is best used to determine the location of event maxima and minima. A third popular

wavelet is the first derivative of the Gaussian. This wavelet is anti-symmetric, and is best suited to finding gradients. It is therefore most useful for edge-detection, or signals with sharp, sudden changes.

The results of the wavelet transform are given in a wavelet map that has one dimension higher than the signal being analyzed. The time axis is given on the abscissa, while the range of scales applied is displayed on the ordinate of the map. The scales are related to frequency according to a relationship that depends on the wavelet being used, and is normally displayed logarithmically. The magnitude of the wavelet transform (also known as the wavelet coefficients) is normally plotted in contours, color shading, or a combination of both.

Wavelets have been used for a variety of purposes in fluid mechanics. Turbulent coherent structures or flow singularities can be identified, and the different frequencies or wavelengths of turbulent phenomena can be determined (Farge, 1992). Wavelets have been used to determine the concentration of energy in primary and secondary structures in wakes, while indicating the lack of energy present at scales in between (Higuchi *et al.*, 1994). Pattern recognition templates were applied to wavelet maps by Hangan *et al.* (2001) in order to determine the interaction between primary and secondary vortices behind a circular cylinder. The temporal resolution of the wavelet map has also been useful in detecting interruptions of regular vortex shedding, such as vortex dislocations (Higuchi *et al.*, 1994). Lewis and Gharib (1992) used a Mexican hat wavelet to show how the local vortex shedding frequency varied in the modulated zone behind a cylinder with a step change in diameter in uniform flow.

2.6 Conclusion

Non-uniform vortex shedding from cylinders has been extensively studied, in many configurations and under many initial conditions. Cylinders with step-changes in diameter or free ends produce situations where vortices shed at different frequencies interact in some way, whether it is in the form of connections, dislocations, or loops, among others. While a shear flow has been applied to uniform cylinders and, to a lesser extent, tapered cylinders, no research has been identified that considers a sudden change in diameter combined with a non-uniform free stream. Among the tools which can be used to study this flow, the wavelet transform is particularly useful, providing an opportunity to study the wake in both time and frequency.

Chapter 3

Experimental facilities and procedures

Cylinders of various configurations were placed in a water channel with uniform or uniformly-sheared incident flow. Flow visualization was used to observe the resulting vortex patterns, and velocity measurements were made using laser Doppler velocimetry.

3.1 Water channel

The water channel in the Department of Mechanical Engineering at the University of Ottawa (Figure 5) is a closed-circuit, recirculating facility capable of holding up to approximately 16 m^3 of water. Water is pumped into the settling tank and is accelerated through the contraction into the test section, which discharges into the drainage tank. A 0.3 m diameter pipe connects the drainage and settling tanks, completing the circuit.

The flow is produced by a 0.3 m (12 inch) diameter axial flow pump (Cascade), which is driven by a 5.6 kW (7.5 hp) motor (GE), providing a maximum head of 2.13 m (7 ft) at a motor speed of 126 rad/s (1200 rpm). A motor controller (Siemens Relcon Q2000) allows the flow rate to be varied from 0.003 m^3/s to 0.1875 m^3/s.

The settling tank is made of stainless steel, and has a modular design, 1.52 m high by 2.44 m wide, leading to the contraction. It consists of 3 stainless steel sections with a total length of 2.13 m. The open end of the semi-parabolic first section mates with two identical rectangular sections, which lead to the large end of the contraction. All of the joints are kept water-tight using rubber gaskets and silicon caulking. The top of the water tunnel is covered with Fiberglas panels to prevent dirt and debris from contaminating the free water surface. Steel bars brace the tops of the walls to keep them square.

Water is pumped into the first section through a 2 m tall, 0.25 m diameter, vertical cylinder. The cylinder is capped by an adjustable plunger to control the pressure of the inflowing water, and is perforated with 25.4 mm diameter holes and wrapped with a fine nylon screen, to provide a smooth, horizontal discharge that is as uniform as possible.

Several perforated plates, plastic screens and fibreglass sheets have been installed in the settling tank for the purposes of conditioning the flow, as described in Table 1.

A straight length (0.3 m) of the settling tank permits the turbulence produced by the last screen to decay before the flow is accelerated through the contraction. The passage area is changed from 1.5 m × 2.4 m to 0.5 m × 0.75 m over a 1.5 m length. The contraction is symmetric horizontally, 4.5:1. The bottom half is raised 2:1 but the top is open to the free surface at the water height.

The test section is 4 m long, with a cross-section 0.50 m wide by 0.75 m high, and is

Table 1: Settling tank screen information.

Screen	Material	Hole Shape	Hole Size	Screen Thickness	Solidity
1	fiberglass filter	misc.	N/A	75 mm	N/A
2	stainless steel	circular	2.3 mm		0.63
3	fiberglass filter	misc.	N/A	75 mm	N/A
4	aluminum	circular	4.8 mm		0.42
5	nylon	square	1.6 mm		0.40

supported by three steel frames. The two end frames are 1 m long, while the middle frame is 2 m long. Each frame is enclosed on three sides by 9.5 mm thick glass walls, while the top surface may either remain open to the air, or be covered by four clear Plexiglas sections. Fiberglass panels are placed above the test section to reduce dust accumulation on the free surface. All instruments and models are placed in the test section from above. Flow adjusting devices such as the shear generator or flow separator can be held in place by a slot just downstream of the contraction. The test section is raised 1.37 m off the ground to allow for underside viewing, while a walkway and ladder are mounted along one side to allow easy access from above the tunnel.

Boundary layer bleeding slots are mounted flush with the glass along the walls and floor, at the two downstream locations where the test section support frames are joined. Water may be drawn from the boundary layers at these locations by a 124 W (1/6 hp) pump (Grundfos UP 26-99BF) positioned under the recovery tank. The same pump is used to draw water from the tunnel through a filter (Aqua-pure AP801) and a chlorinator (Olympic ACM-94). A 15 micron filter (cartridge AP810) is used on a continuous cycle, with a period of 8 hours on, 4 hours off. Chlorine disks (200 g) are used at a rate of about 1 every two weeks.

After passing through the test section, the water enters the recovery tank, where it is diverted to the sides, in order to reduce upstream disturbances. It drains through two perforated cylinders, equipped with plungers similar to the one in the settling tank, into the pipes under the recovery tank. These pipes are connected to a single 0.3 m diameter pipe, which runs below the midline of the test section and settling tank to the main pump. A window is located at the back of the water recovery tank for viewing from the downstream end.

At very low flow speeds, the water near the free surface was observed to move slower than the deeper water. This is attributed to the fact that water enters and exits the tanks near their bottom. An obstructing PVC plate, approximately 2/3 of the water height, placed vertically at the end of the test section, and far downstream of any instrumentation, forced an increase in the water speed at the free surface. This plate was used in all cases of flow visualization and LDV measurements.

3.1.1 Traverses

Steel rails are mounted on the frame of the water tunnel above, below and to one side of the test section, allowing carriages to move along its length, width and height. The two rails mounted above the test section permit smooth manual positioning of a carriage along its longitudinal (x-) axis (Figure 6). A second carriage runs atop the x-axis carriage, along rails normal to the first set, on the transverse (z-) axis. Instruments can be attached to portable verniers, which can move in two more independent directions. Motorized and hand-cranked traverses are also available. With the use of these carriages and traverses, instruments and models can be placed at any position inside the test section.

Instruments can also be attached to carriages below and to one side of the test section. These two carriages may be motor-driven either separately or together, allowing instruments to capture two views of a moving flow feature. The side carriage holds semi-automated vertical and horizontal traverses, allowing instruments mounted there to be moved in three dimensions.

The side traverses are all controlled by a Labview program which allows manual remote coordination from a single location. The control software can also be linked to the LDV software to provide automated traverse movement during data collection.

3.1.2 Shear generator

Wire mesh screens have been used for shear flow generation for many years. Owen and Zienkiewicz (1957) created a shear flow by using a grid composed of sender rods. Elder (1959) developed equations for curved screens of fine wire diameter, in order to produce a desired velocity profile downstream. These equations were simplified by Maull (1969) for the specific case of a linear velocity profile, with an empirical correction to improve the linearity in the high-speed portion of his tunnel. The theory and equations were collected together and further simplified by Tavoularis (2004).

For a screen of wire diameter d_w, and solidity σ (the ratio of the blocked area to the open area), a coefficient can be defined for the pressure loss across the screen:

$$K = \left(0.52 + \frac{17}{\mathrm{Re}_{d_w}}\right)\frac{\sigma(2-\sigma)}{(1-\sigma)^2}. \tag{1}$$

The curvature of the screen causes a change in the fluid velocity moving tangential to the screen, resulting in the fluid deflecting away from its original trajectory. A deflection coefficient may be estimated by

$$B = 1 - \frac{1}{\sqrt{1+K^{1/2}}}. \tag{2}$$

The shear flow is characterized by the dimensionless shear parameter β, representing the velocity gradient in the y-direction, non-dimensionalized by the water height h and the centerline speed U_c:

$$\beta = \frac{h}{U_c}\frac{dU}{dy}. \tag{3}$$

Given a specified mesh and shear parameter, the shape of a curved screen can be specified for a uniform shear using the method given by Maull (1969). A curve-fit to those equations, including the empirical correction, was given by Tavoularis (2004) as

$$\frac{K}{(2+K-B)\beta}\frac{x}{h} = -0.738\left(\frac{y}{h}\right)^6 + 2.812\left(\frac{y}{h}\right)^5 - 3.839\left(\frac{y}{h}\right)^4 + 2.687\left(\frac{y}{h}\right)^3 - 1.224\left(\frac{y}{h}\right)^2 - 0.0054\left(\frac{y}{h}\right). \quad (4)$$

The variables x and y define the points on the curve to which the screen should be shaped. As the parameter K is inversely proportional to the wire Reynolds number, for a given screen shape, the shear parameter changes with the flow speed at relatively low Reynolds numbers, such as those used in the present study. The shear parameter would be insensitive to the wire Reynolds number in the typical ranges used in wind tunnel studies.

A rigid stainless steel frame was built to support the screen in the water tunnel, holding it in a shape that would provide a linear velocity profile in the downstream flow. The mesh properties and design flow conditions as estimated by equations (1) to (4) are given in Table 2. A sketch of the mounted screen is shown in Figure 7, while the technical drawings are provided in Appendix A.

Table 2: Shear generator mesh and design flow properties.

Wire diameter (d_w)	0.381 mm (0.015 inch)
Mesh size	0.94 squares/mm (24 squares/inch)
Wire centre to centre distance (l)	0.678 mm (0.0267 inch)
Solidity	0.590
Water height (h)	690 mm
Design centerline velocity (U_c)	0.1 m/s
Re_{dw}	38
K	3.8
B	0.57
Design velocity gradient (dU/dy)	0.0565 s^{-1}
Design shear parameter (β)	0.279

3.2 Models

Cylinders were mounted vertically in the test section from above (Figure 8), approximately 700 mm downstream of the contraction. The water height was maintained at 690 mm, the maximum height possible without coming into contact with cross-braces above the settling tank. A thin, transparent, flat plate with a small hole was secured to the bottom of the water channel using silicone. The bottoms of the cylinders were secured in this hole in order to ensure that they were always located at the same position in the test section. The top end of the cylinder was attached to a mini-traverse on a brace that spanned the test section above the water, which allowed small adjustments of the cylinder inclination. A bubble level, accurate to within 10 arcminutes, was used to ensure initial vertical positioning, which was confirmed by taking LDV wake measurements.

3.2.1 Cylinders

All cylinders were composed of stainless steel. Step-cylinders were made by fastening two sections together with a threaded rod, while uniform cylinders were made

Table 3: Cylinder dimensions.

Configuration		Diameter (mm)	Length (mm)	*AR*	*d/D*
Uniform		3.43	634	184.8	-
Step 1	*d*	3.43	318	92.7	0.52
"small"	*D*	6.60	318	48.2	0.52
Step 2	*d*	6.60	318	48.2	0.51
"large"	*D*	13.0	318	24.5	0.51
Free end 1		3.43	392	114.3	-
Free end 2		6.60	392	59.4	-
Double-step 1	*D*	6.60	203	30.8	0.52
"small"	*d*	3.43	12 or 64	3.5 or 18.7	-
	D	6.60	419 or 367	63.5 or 55.6	-
Double-step 2	*D*	13.0	203	15.6	0.51
"large"	*d*	6.60	12 or 64	1.8 or 9.7	-
	D	13.0	419 or 367	32.2 or 28.2	-

from a single piece. Dimensions of all cylinders used in this study are shown in Table 3. The dimensions take into account the additional thickness of the lead foil, 0.13 mm, used for flow visualization purposes. For consistency, the lead foil was also applied during the LDV measurements, even when flow visualization was not taking place.

The configurations tested are shown in Figure 9. The uniform diameter cylinder was tested in the uniform and shear flows, in order to form a basis for comparison with data in the literature. The double-step cylinders were symmetric around the mid-span, and were tested only in the uniform flow. The single-step cylinder was studied in uniform flow, and in two configurations in the shear flow. The "upright" configuration placed the larger cylinder in the high-speed region of the shear, while the "inverted" configuration placed the smaller cylinder in the high-speed region of the shear. Similarly, the finite cylinders were tested in uniform flow, the higher-speed region of the shear, and the lower-speed region of the shear.

3.2.2 Endplates

Endplates were used as a means of reducing end effects. Circular Lexan endplates 100 mm in diameter were used, with a rim that was chamfered 60° to a sharp edge on the side facing the measurement sections. The endplates were placed 25 mm below the water surface and above the bottom of the test section, depending on the configuration being tested (see Figure 8). As endplates that extend far downstream have been found to increase the definition of the cell boundaries in cellular shedding (Mair and Stansby, 1975), the cylinders were placed approximately 25% forward of the center of the endplate (Figure 10 and Appendix A).

3.3 Flow visualization procedures

Hydrogen bubbles and lead foil precipitation were used to visualize the flow around the models, illuminated by spotlights and a laser light sheet, and photographed with a digital video camera.

3.3.1 Hydrogen bubbles

Hydrogen bubbles were produced by the electrolysis of water near a conducting wire. In order to generate the hydrogen bubbles, a power source was connected to the wire cathode and an anode made of graphite (Figure 11), through an electronic pulsing circuit (Figure 12), based on the design by Budwig and Peattie (1989). Voltage to the wire could be pulsed either from the square-wave output of a function generator, or by a trigger switch, to produce a single line of bubbles. Alternatively, a continuous stream of bubbles could be produced by connecting the wire and anode directly into the power source.

The mounting frame used to place the hydrogen bubble wire in the flow could be adjusted from 10 to 300 mm in length (Figure 13), and could be oriented at any angle to the flow. The wire was made of the material Alloy C (Jelliff Corp.), 0.04 mm in diameter, and was supported by two conducting surfaces, attached to thin plastic plates for easy replacement. One of the conducting surfaces was attached to an electrical wire, leading to the pulsing circuit. The plastic plates insulated the mount from the live wire. All electrically conducting surfaces other than the active wire were coated with silicon caulking for safety purposes, and to avoid the production of stray bubbles. The graphite anode was placed in the water nearby, but sufficiently far as not to interfere with the flow being studied.

Hydrogen bubbles rise in water because of their much lower density. When it can be assumed that the Reynolds number based on their rise velocity is small, their motion can be determined from Stokes' Law. Neglecting the density of the bubbles compared to that of water, their terminal rise velocity can be calculated as:

$$V_s = \left(\frac{g d_b^2}{18 \nu_w} \right), \tag{5}$$

where the water kinematic viscosity is ν = 1.0 x 10^{-6} m^2/s, and the gravitational acceleration is g = 9.81 m/s^2. Studies summarized by Merzkirch (1987) have shown that, in general, the size of the bubbles, d_b, is of the order of the wire diameter. Thus, a wire 0.04 mm in diameter would produce bubbles with a terminal rise velocity of about V_s = 0.87 mm/s, corresponding to a Reynolds number of 0.035, which justifies the use of Stokes' theory. Assuming that the flow was horizontal at a high visualization flow speed of 40 mm/s, the bubbles would rise by less than 2.2 mm for every 100 mm it traveled downstream in the test section, which is deemed to be negligible for the purposes of this study. Visual tests confirmed that the bubbles did not rise significantly while entrained in the flow structures close to the models.

3.3.2 Lead foil precipitation

Electrolytic precipitation of metals in water, as documented by Taneda *et al.* (1977), and used to good effect by Anderson and Syzewczyk (1995), produced tracers in the flow using electrolysis. The colloidal suspension was generated by passing an electric current through a thin strip of lead or tin immersed in water, producing white metal oxide particles, roughly spherical in shape, on the order of 1 μm in diameter (Taneda *et al.*, 1979). Hydrogen bubbles were produced from a cathode placed downstream, but were not used for visualization purposes. The strip of lead or tin was thin and malleable so that

it could be molded to a surface, such as a cylinder, making the procedure non-intrusive to the flow. The tracers were generated from the surface of the body being studied, which was particularly suitable for vortex shedding processes, as the visible material originated in the separated boundary layers. When visualized using a laser sheet or a spotlight, the white tracers provided excellent contrast with a black background.

Similar flow tracing could be achieved by coating a surface with dye, which is swept downstream by the flow. In the case of electrolytic precipitation, however, the amount of tracer could be carefully controlled, and it could typically be used for a much longer time. Some of the residual from the chemical process was deposited on the surface of the cylinder after sufficient use. This deposit was removed in order to restore the quality of the flow visualization. Medium grain sandpaper was first applied to the lead, followed by fine grain in order to reduce the surface roughness.

The test cylinders were wrapped entirely with lead foil tape of thickness 0.13 mm (McMaster-Carr). With the lead acting as an anode, a graphite rod cathode was placed in the water downstream. A voltage difference of 100 V was applied between the electrodes, producing a white lead oxide, which precipitated into the flow, allowing visualization of the shed vortices. A lower voltage (40 V) was applied at the lowest Reynolds number to avoid the release of a large amount of precipitate which might have altered the flow characteristics. While both the 750W spotlight and the laser light sheet were used to illuminate the precipitate, the spotlight produced the best images.

The amount of precipitate that was electrolyzed depended on a number of factors. The flow speed determined how fast the precipitate was entrained into the flow, as more precipitate was required for a faster flow. It was found that above a speed of around 50 mm/s, the visibility of the precipitate could not be sufficiently maintained. A pH close

to 7.0 was maintained in order to produce an adequate supply, even at low flow rates. As the water tunnel became naturally more acidic with time, sodium carbonate pH riser was added to maintain the proper level.

3.3.3 Laser light sheet

The laser beam from the 5 Watt Argon-ion laser (Optikon Corp., model 95) located near the water tunnel was passed through a fiber optic cable to a Powell lens (Powell, 1987), which spread the beam into a plane, or sheet. The use of a fiber optic cable ensured that the beam could be pointed anywhere in the test section without having to move the laser. The laser light illuminated a thin slice of hydrogen bubbles or lead oxide precipitate in the region of interest. The power input to the fiber was kept below 1 W in order to avoid burning the fiber.

3.3.4 Illumination and photography

Illumination of the hydrogen bubbles and lead oxide precipitate was produced using a projector lamp (Buhl Optical) with a 750 W bulb (type DDB), which provided uniform light across the entire beam. Additional high power spotlights were also used to reduce shadows.

Most of the visualization observations were made from the side of the test section, so the lead oxide precipitate and hydrogen bubbles were illuminated from below, and a black sheet was placed across the far window of the water channel, in order to increase the contrast. When the observations were made from below, the cylinders were illuminated from the side.

Images were recorded with a digital video camera (Sony DCR-VX1000), at a rate of 30 frames per second. Selected frames were collected as still images without blurring, if

the exposure time was limited to 1/60 of a second or less in adequate lighting. In order to avoid disturbances while filming, a remote control was used to activate the camera, and to adjust the zoom of the telephoto lens. For most of the observations, the camera was attached to the traverses on the side of the water channel, so that it could be moved either vertically, horizontally closer to the tunnel, or horizontally following the flow for a short distance. The downstream travel distance was limited by the width of the light beam in the water, and an obstructing structural beam on the side of the tunnel.

3.4 Laser Doppler velocimetry

A two-component laser Doppler velocimetry (LDV) system (Dantec), operating in backscatter mode, was used to take velocity measurements. The available 5W argon-ion laser (Optikon, model 95) projected a cyan beam directly to the LDV equipment, where the light was separated into its green and blue components, at wavelengths of 514.5 nm and 488 nm, respectively. Each of these beams was further split, and one beam of each wavelength was frequency-shifted by 40 MHz through a Bragg cell. The four beams were transmitted through fiber optic cables to the laser probe.

The laser probe could be fitted with one of four available lenses (see Table 4). A beam expander could be attached to the two larger lenses, giving the beams a larger initial separation, thus a larger angle of entry into the flow, which reduced the longest dimension of the control volume. The LDV software allowed the user to choose one of several discrete velocity ranges based on the lens focal length and beam expander ratio. The speeds used in the water tunnel were within the smallest available velocity range for each lens. Table 4 displays the smallest available velocity range and the resolution (16-bit) achieved by each of the four available lenses using this system. The dimensions of

the control volumes for these lenses, where the two laser beams intersect, is given in Table 5.

The 310 mm lens was selected in order to be able to measure within more than half the width of the test section. Used in conjunction with the beam expander, this lens provided good velocity resolution, and a reasonably small control volume size.

The laser was operated at 1 W, which is the maximum rated power for the fiber optic cables. Particle seeding was necessary in order to maintain a sufficiently high data rate, as required for spectral measurements. About 0.6 ml of silicon carbide spheres (TSI, 1.5 μm diameter), thoroughly mixed into about 2 liters of water, were added to the water tunnel at a time, and the data rate was observed as the water was mixed through the action of the pump and screens. More seeding was required in subsequent tests, as the particles had a tendency to stick to the screens in the settling tank, or were removed by the cleaning filter.

Table 4: Lowest velocity ranges of the available LDV lenses.

Focal length	Beam expander off		Beam expander on	
(mm)	Min. Range (m/s)	Resolution (m/s)	Min. Range (m/s)	Resolution (m/s)
160	0.256	3.9×10^{-6}	N/A	N/A
243	0.387	5.9×10^{-6}	N/A	N/A
310	0.493	7.5×10^{-6}	0.254	3.9×10^{-6}
600	0.952	14.5×10^{-6}	0.489	7.5×10^{-6}

Table 5: Control volume sizes for available LDV lenses.

Lens (mm)	Direction	$\Delta x \times \Delta y \times \Delta z$ (mm)	
		Beam expander off	Beam expander on
160	*u*	0.078 × 0.078 × 0.658	N/A
	v	0.074 × 0.074 × 0.624	N/A
243	*u*	0.118 × 0.118 × 1.513	N/A
	v	0.112 × 0.112 × 1.435	N/A
310	*u*	0.151 × 0.150 × 2.459	0.078 0.077 × 0.650
	v	0.143 × 0.153 × 2.332	0.074 × 0.073 × 0.617
600	*u*	0.291 × 0.291 × 9.199	0.150 × 0.149 × 2.423
	v	0.276 × 0.276 × 8.725	0.142 × 0.142 × 2.298

3.5 Data processing

All data processing was performed using Matlab functions. These functions were stored in Matlab m-files, and are documented in Appendix B.

3.5.1 Resampling: sample and hold

The velocity data obtained from the LDV system were acquired at random intervals, depending on the presence of scattering particles in the laser control volume. In order to perform a frequency analysis of these data, it was necessary to resample the velocity time series at a fixed rate.

For spectral and wavelet analysis, the original velocity data was resampled using the "sample-and-hold" technique (see samplehold.m in Appendix B.1). Alternative techniques are available, such as an exponential fit between data points (Host-Madsen and Caspersen, 1995), or fractal methods (Chao and Leu, 1992), which might give a slightly better accuracy, but which involve more complex implementation. When properly applied, the sample-and-hold technique offers adequate accuracy along with ease of use (Adrian and Yao, 1987).

The sample-and-hold technique assumes that a given value in a series of randomly-spaced data is held constant until the next sample is reached (Figure 14a). The result resembles a series of step functions, which was then resampled at a constant frequency (Figure 14b). As shown in Figure 14c, the resampled signal followed the original one fairly well where the signal changes slowly, while missing the fast changes completely. The resampled signal was an acceptable substitute of the original one for frequencies up to a certain cutoff.

3.5.2 Signal filtering

Early in the study, it was discovered that the water channel flow exhibited a low amplitude, very low frequency wavy motion. Several methods were attempted to remove this wave, but all were unsuccessful. The frequency of the wave was measured at less than 0.1 Hz, which was very much lower than any vortex shedding frequency measured. The energy contained in the wave was much less than the energy from the shed vortices, as evidenced by looking at the spectrum (Figure 15a). The low frequency wave was therefore removed in post-processing by using a high-pass filter. The spectrum (Figure 15b) of the filtered signal shows that filtering did not affect the spectra in the range of interest.

A fourth order Butterworth high-pass filter with cutoff at 0.5 Hz was applied to the signal in order to remove the low frequency wave (see hpfilt.m in Appendix B.2). This consisted of a second order Butterworth filter applied to the signal in the forward-time direction, followed by an identical filter applied in the backward-time direction. This effected a fourth-order amplitude reduction without imposing any phase shift that might have affected the signal waveform shape. The resulting signal was compared to the original and the resampled signals in Figure 16.

The probability density functions (pdf) of a typical signal is plotted in Figure 17. The differences between the original, resampled and filtered signals were relatively small. The skewness, which is a measure of how much the pdf is shifted to one side of the mean value, and the kurtosis, which compares the sharpness of the peak to that of a Gaussian

Table 6: Skewness and kurtosis of resampled signals.

Signal	Skewness	Kurtosis
Original	-0.22	2.76
Resampled	-0.20	2.73
Resampled and filtered	-0.09	2.73

random process (Bendat and Peirsol, 2000) are presented in Table 6. The resampled signal showed nearly the same skewness and kurtosis compared to the original signal. The filtered data, however, showed a small shift towards a positive skewness, with nearly the same kurtosis.

All data analysis was performed using the resampled and filtered data sets.

3.5.3 Spectral calculations

The frequency resolution of the spectrum is inversely proportional to the sample time, thus a longer sample would give better resolution. However, accuracy can be gained if the spectrum can be averaged over a set of samples. This was accomplished by taking a long sample, and breaking it into blocks of equal lengths. A compromise was required between the desired frequency resolution and the length of a given sample. The desired spatial resolution for a cylinder spanning the full height of the water channel required 116 measurements, at 5 mm increments, thus it was not practical to take very long measurements over this distance.

After numerous tests, a frequency resolution of 0.012 Hz was chosen. This allowed small differences in frequency to be differentiated even when the shedding frequency was as low as 1 Hz. The frequency resolution was chosen to be high enough to reduce the appearance of false shedding cells, as the smallest frequency jump between cells was of the order of 0.1 Hz.

The energy spectrum was calculated for 2048 frequencies between 0 and 25 Hz. As only the positive frequency half of the spectrum was used, this range allowed all vortex shedding frequencies from this study to be mapped at the desired resolution. The built-in Matlab command "pwelch" uses an overlapping Hamming window to determine the block that is used to calculate the fast Fourier transform (FFT), and then averages the

results. By using an overlap of 25% on a 205 second measurement resampled at 25 Hz, three blocks could be processed by the FFT (see spect.m in Appendix B.3). While averaging only three blocks did not provide a significant improvement in the statistical analysis, it did allow for a small amount of smoothing in the spectrum due to the averaging process. The peak frequencies in each spectrum could then be extracted for data analysis (see spmax.m in Appendix B.4).

3.5.4 Wavelet analysis

The wavelet transform is applied to a signal in a way similar to the Fourier transform, by the convolution of the signal and the wavelet being used. Unlike the Fourier transform, however, the wavelet transform maintains temporal information contained in the signal in the form of the "local" scale, or period, of events.

One of the most commonly used wavelets is the complex Morlet wavelet (Farge, 1992). The shape of the wavelet is determined by modulating a complex sinusoidal function (of dimensionless frequency $2\pi\gamma$) by a Gaussian envelope (Torrence and Compo, 1998):

$$\psi(\tau) = \pi^{-1/4} e^{i2\pi\gamma\tau} e^{-\tau^2/2}. \tag{6}$$

The wavelet is defined over the dimensionless variable τ, which may be, for example, a normalized time. The Morlet wavelet, shown in its real and imaginary components in Figure 18a, yields magnitude and phase information, which allows it to highlight the local periodicity of the signal, as opposed to isolating the individual peaks and valleys. As mentioned in Section 2.5, the mean of the wavelet should be zero in order to be mathematically admissible for use in time-frequency analysis, which requires a correction term to be added to the Morlet wavelet. However, when $2\pi\gamma \geq 6$, the correction term

becomes negligible (Farge, 1992). It should be noted when using the Matlab functions for this wavelet that the definition in the documentation is incorrect, reversing two of the input parameters (see the notes in the file wlet.m, listed in Appendix B.5), and that there is another Morlet wavelet available in Matlab, which is not a complex function.

Another popular wavelet is the second derivative of a Gaussian, also known as the Mexican Hat. It is a real-valued wavelet, and it picks up the individual peaks within a signal. The wavelet is shown in Figure 18b, and is defined as (Torrence and Compo, 1998):

$$\psi(\tau) = 0.867\left(1-\tau^2\right)e^{-\tau^2/2}. \tag{7}$$

The continuous wavelet transform is the convolution of a one-dimensional signal *s(t)*, and the wavelet function ψ (Daubechies, 1992):

$$W(a,\tau) = \int \frac{1}{\sqrt{a}} s(\tau')\psi^*\left(\frac{\tau'-\tau}{a}\right)d\tau'. \tag{8}$$

The asterisk denotes that the complex conjugate of the wavelet is used to find the magnitudes of the transform. The width of the original wavelet, called the mother wavelet, is scaled by the dimensionless parameter a (a = 1 for the mother wavelet), and shifted along the dimensionless τ axis of the signal. The normalization factor $a^{-1/2}$ is included so that the wavelet always has the same energy, as its overall size is changed at the different scales (Jordan *et al.*, 1997).

The result is a wavelet transform amplitude, called a coefficient, at each time instant and at each scale. The transform amplitudes are expressed as surface plots, or as iso-contours or color maps (called scalograms) in two-dimensions, against the same time axis as the signal, and against the scale a. Often the wavelet transform is normalized by its

largest magnitude within the plot, and a threshold is chosen below which the contours are not displayed in order to increase the clarity of the plots. A threshold of 40% was used in this study, based on the expectation that an amplitude of less than half the maximum would not make significant contribution to the analysis.

By scaling the wavelet width, the parameter a also scales the dimensionless frequency (Abry, 1997). Each scale, therefore, represents an equivalent *local* frequency, similar to the Fourier frequency of a signal, but localized in time. The peak-to-peak dimensionless frequency (γ) of the Morlet and Mexican Hat wavelets can be found by observation in Figure 18a and b, respectively, but can also be calculated more exactly using derived relations (Lewalle, 1998), and are displayed in Table 7.

The equivalent frequency of a given scale, therefore, can be calculated from the following relation (Abry, 1997, and Gordeyev and Thomas, 1999), where Δt is the time step of an evenly-sampled discrete signal such as the one obtained through resampling of the LDV measurements,

$$f = \frac{\gamma}{a\Delta t}. \tag{9}$$

In a signal with rapidly changing periodicity, it is not entirely justifiable to use the term "frequency" to describe f, as this implies some sort of regularity to the cycles. In a particular segment of a signal where there is a slow change in periodicity, the term local frequency may be applicable.

The range of vortex shedding frequencies occurring in this study, as calculated by a

Table 7: Wavelet information.

Wavelet	γ	Scale range	Scale increment
Morlet	1.00	$2 \leq a \leq 50$	0.375
Mexican Hat	0.25	$1 \leq a \leq 62.5$	0.5

Fourier spectrum, covered approximately 1.0 Hz $\leq f \leq$ 12.5 Hz. These were converted into the appropriate scales, with an appropriate resolution at high scales (low frequencies). Trial and error was then used to ensure that none of the contours were cut off by a scale range that was too small (this was particularly true for the Mexican Hat coefficients). For a data rate of 25 Hz, and the appropriate dimensionless frequency of the mother wavelet, the range of scales is shown in Table 7. The equivalent frequencies were converted into Strouhal numbers for consistency with the rest of the data.

Figure 19 displays a signal $s(t) = \sin(2\pi ft)$, where $f = 1$ Hz at $t < t_o$ and $f = 0.5$ Hz at $t \geq t_o$, as well as the Morlet and Mexican Hat wavelet maps for this signal. A Fourier transform for this signal would show two peaks at the relevant frequencies, which would look the same as the spectrum for a signal where two sine waves of different frequencies were added together. The highest amplitudes of the wavelet transform (the darkest shades), however, reflect the temporal variation in the signal frequency. It is clear from the wavelet maps that application of the Morlet wavelet highlights the periodicity of the signal, while the Mexican Hat identifies the individual peaks and valleys.

A sample velocity signal is shown in Figure 20, along with the contour wavelet maps for this signal as calculated using the Morlet and Mexican Hat wavelets. Changes in frequency with time were much easier to read on the Morlet map, which was used in the data analysis in Chapter 6. In this case, two dominant frequencies could be identified, at Strouhal numbers of 0.20 and 0.22. As the signal changed from one frequency to the other, the amplitude of the wavelet transform decreased, as the energy of the signal was spread between the two frequencies. A cross-section through the wavelet map parallel to the frequency axis would show a local frequency-amplitude plot similar to a Fourier spectrum. As with the Fourier spectrum, the peaks could be high with a narrow frequency range, or low, with a wide frequency range (or combinations of these). These two

conditions, properly normalized, could have the same energy, and represent different effects of similar strengths occurring within the signal.

3.6 Measurement uncertainty

The only flow property that was measured directly was the time-dependent streamwise velocity component, from which all other parameters of interest were extracted. The uncertainty in the velocity measurement would propagate to the Reynolds and Strouhal numbers, and could affect the interpretation of the results. As this study was performed at relatively low Reynolds numbers, even a small change in the Reynolds number could potentially cause an appreciable change in the Strouhal number, as shown by the steepness of the curve in Figure 2. Any difference in the freestream velocity from one measurement to the next would contribute to observed differences in the spectral and wavelet plots.

Four sources of uncertainty in flow velocity related to the water channel operation have been identified: low-frequency waves that propagated along the length of the test section, as mentioned in Section 3.5.2, changes in flow speed from one day to another due to evaporation and other undetermined influences, flow non-uniformity across the test section, and positioning of the cylinders and LDV probe.

The largest variation in the velocity came from the low-frequency waves in the test section. All velocity signals were high-pass filtered to remove the wave frequency before spectral and wavelet analyses were performed. Even so, the signals could contain some variability in shedding frequency due to periodic variations in flow velocity due to the waves. This frequency variability cannot be removed and could express itself as a broadening of the spectral peaks. Close to one of the flow speeds used, for example, the

velocity varied about the mean, as U = 101 ±4.4% mm/s. The change in Reynolds number due to this variation leads to a maximum uncertainty in the determination of the frequency of approximately ±2.2% for the large cylinder, and ±3.1% for the small cylinder. It will be seen in Section 4.4 that most of the spectral peaks were quite sharp, and that most of the broadening occurred around the base of the peaks, indicating that the actual uncertainty was much smaller. Most of the cells showed an abrupt change in frequency at their boundaries. The lower bound for the frequency change between adjacent cells at this flow speed was approximately 7% behind the large cylinder, nearly twice the maximum uncertainty in the frequency. The variations due to the waves introduced a random uncertainty, and cannot produce cells of constant frequency along the cylinder span. Because the time interval of each measurement record was 205 s, which was about 20 times longer than the wave period of approximately 10 s, the uncertainty of the Strouhal number was much lower than that of the frequency, as the Strouhal number was normalized by the mean velocity, which mostly averaged out the wave effect, except for a very small residual uncertainty due to the non-linearity of the St-Re curve.

In order to counter losses due to evaporation from the free surface, water was added to the channel daily to the specified height of h = 690 mm. Even very small differences in water height from day to day, however, could cause changes in the free stream flow speed. For this reason, the flow speed was measured before every test run, and adjusted if necessary. Both the Reynolds number and the Strouhal number were calculated based on this velocity. Any differences in the flow speed would therefore show up as systematic differences in the frequency between one test and the next, if they were taken on different days. As measurements along the span of each cylinder were completed within several hours, there was no significant difference in flow speed. The day-to-day variation in flow

speed, therefore, did not affect the uncertainty within a single set of data points. Care must only be taken when comparing two data sets that were assumed to have the same Reynolds number but, due to this effect, did not. Again, the corresponding uncertainty in Strouhal number would be much lower, as its value was based on the actual velocity.

As will be shown in the following chapter, the velocity over the full cross-sectional area of the test section was not entirely uniform, especially at low flow speeds. Typically, however, the differences in velocity between locations were less than 1 mm/s, especially in the central region where the measurements took place. This uncertainty is much smaller than that due to the wave effect.

The initial positioning of the cylinders and the LDV probe was done by eye, which leads to some uncertainty in the relative location of the measurements. A mounting plate was positioned at the bottom of the test section, with an anchor hole that was located by hanging a pendulum weight from another mounting bracket above the test section. The cylinders were secured into these two mounts, and a side-mounted bubble level, accurate to within 10 arcminutes, was used to ensure that they were vertical. Over the maximum length of the cylinder, this corresponds to an error of $\pm 0.12D$, where D is the diameter of the large cylinder. Wake measurements were also taken at several spanwise locations in order to observe any deviations from vertical.

Positioning of the LDV probe along the side of the test section was critical to achieving consistent results. Using the bubble level, the two glass walls to the test section on either side of the cylinder were measured to be vertical and therefore parallel to the cylinder, with an uncertainty of 10 arcminutes, so that reflections could be used to orient the probe. The angle of the probe in two dimensions was determined by removing the lens, and allowing the four beams to be projected parallel into the test section. Points on

the wall nearest the laser due to the originating beam were aligned with points reflected back from the far wall. With the lens attached, the reflected beams were projected onto a wall behind the probe, where both horizontal and vertical beams were compared to cross-hairs that had been drawn using a bubble level with an accuracy of approximately 10 arcminutes.

The traverses that moved the LDV probe ran along rails that were mounted to the side of the test section using precision levels with an accuracy of 1 arcminute. Positioning of the mounting brackets were verified using bubble levels every time a change was made. The lead screws that drove the carriages were accurate to an estimated uncertainty of about 0.01 mm, or $0.002D$.

The LDV probe was positioned relative to the cylinder by eye, using the laser beams as a guide. The vertical zero (y-) was determined by allowing the horizontal beams to intersect the steps or tips of the cylinders, giving an uncertainty of half the height of the control volume created by the intersecting beams, which had a height of 0.073 mm, or $\pm 0.006D$. The downstream zero (x-) contains the largest uncertainty, as the laser beams were projected onto the surface of the cylinder (with the software turned off so as not to overload and burn out the photomultiplier tubes). Positioning the vertical pair of beams along the axis of the cylinder was challenging due to the glare of the reflections, attenuation by the safety glasses, and the curvature of the cylinder surface, but was likely achieved to within $\pm 0.13D$. Zeroing of the cross-axis (z-) to the sides of the cylinder was achieved at first by eye, by placing the laser close to the lower end and centering the laser control volume as much as possible by looking from below the test section, and repeating the procedure near the upper end, to within $\pm 0.13D$. Any offset of the zero was corrected after taking wake measurements of the cylinder.

The distance between adjacent measurement positions using the LDV probe were between $0.3D$ and $0.75D$, so that the uncertainties due to positioning in the vertical direction were not large enough to affect the results. Positioning uncertainties in the other directions were also not significant, as slight changes in downstream or cross-stream locations should not change the observed frequency.

Uncertainties in the Strouhal number, which was used as the variable of interest, were small enough that the location of cell boundaries were not affected. Even a broad peak in the spectrum or wavelet map clearly showed a distinction between dominant frequencies between one cell and the next. At the cell boundaries, the regular variation of the frequency with time made interpretation of the wavelet maps more challenging, but the difference between the dominant frequencies in a single time series were larger than the uncertainty, leading to confidence in the conclusions.

Chapter 4

Experimental results – LDV measurements

Flow velocity measurements were made in the water channel using LDV. The signals were resampled at a fixed rate and filtered as described in Section 3.5.

4.1 Freestream velocity

The mean velocity variation in a cross-section of the unobstructed test section, at the downstream location of the cylinders axes, was measured for three flow speeds. The high and middle speeds, U_1 = 95 mm/s and U_2 = 42 mm/s, respectively, were chosen so that vortex shedding frequencies would be measurable by the available LDV system within the desired spectral resolution. Flow visualization could only be performed at these speeds using hydrogen bubbles. The lowest speed, U_3 = 23 mm/s, was roughly the maximum velocity for which flow visualization using the electrolytic precipitation method showed sufficient detail to be useful. Even lower speeds were used to visualize specific flow features.

The flow velocity was measured at a cross-section 700 mm downstream of the entrance of the test section, in a grid representing 88% of the water height and 68% of the channel width, which was the maximum range obtainable using the selected LDV configuration.

Measurements were first taken in the unobstructed channel, and then with the shear generator inserted into the flow at the entrance to the test section.

4.1.1 Unobstructed flow

In the absence of the shear generator, the centerline speed was defined as the spatially averaged speed in the central 50% of the cross-sectional area. At the high flow rate, the centerline speed was U_1 = 95 mm/s, with less than 1% deviation in the range $0.18 < y/h < 0.78$ (Figure 21a). The largest deviation from the nominal speed was close to the side wall of the test section, where the speed dropped by less than 13% near the bottom surface at y/h = 0.08, and again near the free surface, at y/h = 0.95. The rms fluctuation levels remained relatively constant in the range $0.18 < y/h < 0.78$, at approximately 0.8 to 1.2% U_1 (Figure 21b). As expected, turbulence levels rose significantly in the boundary layer of the bottom surface of the test section. The flow speed near the water free surface was somewhat slower than the mean speed, and the velocity fluctuation level was also higher. As the regions of interest in the present study were located far from the free surface, this was not considered to be a problem.

At the low speed of U_3 = 23 mm/s, the freestream velocity was constant within 5%, away from the side walls (Figure 22a). The rms fluctuation levels away from the side walls ranged from 4 to 7% U_3 (Figure 22b). In the region $0.45 < y/h < 0.65$, where the cylinders steps would be located, the rms velocity fluctuations were typically less than 6% U_3.

At both high and low speeds, the velocity in the vertical direction was within the uncertainty of the LDV system throughout most of the cross-sectional area, with maximum values less than 4% of the mean freestream speed.

4.1.2 Shear flow

The centerline speeds of the shear flows were calculated by spatially averaging the centerline speeds across the width of the test section core. The velocity gradients and shear parameters are listed in Table 8, where they are compared to the design values based on the information given in Table 2 and Section 3.1.2.

At U_1 = 95 mm/s (Figure 23) and U_2 = 46 mm/s (Figure 24), the shear is nearly uniform across at least 80% of the water height, with very little scatter across the width of the test section. The shear parameters were within 6% of the design values, and turbulence levels were only marginally higher than those in the unobstructed flow cases.

At the low flow speed of U_3 = 29 mm/s (Figure 25), the shear parameter was 37% higher than predicted. This is not completely surprising, given that the shear generator was designed for much higher flow speeds. As the shear was higher than expected, this turned out to be advantageous to the study. The turbulence levels corresponding to the higher velocity range were lower than those in the unobstructed case, while at the lower end, the turbulence level was about the same as in the unobstructed case.

Table 8: Shear flow properties.

U_c (mm/s)	$\frac{h}{U_c}\frac{du}{dy}$	$\frac{h}{U_c}\frac{du}{dy}$ (design)	% difference
95	0.265	0.279	-5
46	0.354	0.335	6
29	0.506	0.369	37

4.2 Spanwise variation of shedding frequencies

Velocity measurements were made by LDV in the wakes of the circular cylinders. The data were filtered, and spectra were taken in order to determine the dominant frequencies within the signal, as discussed in Section 3.5. The spectral frequencies with the highest peaks at each location were then plotted against the spanwise length of the cylinders. The largest cylinder occupied less than 2.5% of the cross-sectional area of the test section, and most tests were performed using cylinders with area blockage of less than 1%, so that corrections for tunnel blockage were not considered necessary (Tavoularis, 2004).

Measurements were taken 5 diameters downstream of, and 0.78 diameters off-center from, the cylinder axis (see Figure 26). Early wake tests indicated that this location gave a high data rate which consistently captured the shed vortices by giving high and sharp spectral peaks. Measurements initially overlapped at two downstream locations in the step region of the step-cylinders, at $5D$ and $5d$ from each, in order to ensure that the results were consistent. There was no major difference in the shedding frequencies, so that in all subsequent step-cylinder tests, the measurement location was maintained relative to the cylinder axis using the local diameter.

In most tests, the entire cylinder span was traversed at 116 locations in 5 mm increments, followed by a finer grid of 50 points in 2 mm increments near the step or tip regions. The freestream speed was monitored 20 diameters upstream of the cylinders after each spanwise set was completed, using a coarser grid of roughly 50 mm increments.

The Strouhal number on the ordinate of the graphs (Figure 27 to Figure 35) was calculated using the cylinder diameter and the corresponding centerline flow velocity, U_c.

In order to accentuate the difference in *frequency* at the step, as opposed to the difference in Strouhal number, the vortex shedding frequencies of the step-cylinders were normalized by the large diameter, as were the spans of the step-cylinders on the abscissa. The Reynolds numbers in the shear flow were also calculated using the centerline flow velocity, U_c, and in the case of the step-cylinders, the large diameter, D. Small sketches of the cylinders are provided at the bottom of each figure to help in visualizing their orientations.

4.2.1 Uniform-diameter cylinder in uniform and shear flows

According to numerous sources, a uniform cylinder placed in a uniform flow should shed vortices at a single frequency, except possibly close to the ends. A uniformly-sheared flow should produce multiple cells of constant frequencies. The 3.43 mm diameter cylinder was placed in uniform and shear flows, at Re = 146 and 336. The results are presented in Figure 27, where proposed cell boundaries are indicated along the span, and $y/d = 0$ is located at the cylinder mid-span.

In uniform flows, only one frequency of vortex shedding was detected along the span of the cylinder far from the endplates, for both Re = 146 (cell A in Figure 27a) and Re = 336 (cell B in Figure 27b), clearly reproducing the results from previous observations. At the lower Reynolds number, two additional cells can be seen near the water free surface, where the flow speed was lower than the centerline value. At the higher Re, the frequency dropped close to the endplate (cell A), and by a smaller amount near the water free surface.

In the shear flow, cellular shedding became obvious at Re = 146. Cells A' and F' may be attributed to the endplates, but two distinct cells were observed in the range $-75 < y/d < 39$. The lack of a distinct cell of constant frequency along the upper region of

the cylinder may be attributed to the *local* Reynolds number being in the unstable range of the Re-St curve (see Figure 2), where the frequency might fluctuate even under constant flow conditions. At locations where the local Reynolds number exceeded the unstable range, cell E' appeared to have a nearly constant frequency, especially towards the upper end of the cylinder.

The cellular nature in the shear flow at Re = 336 was less clear, but it appeared that three cellular regions may have formed. Cell A' was wider than cells that formed as a result of end effects, as, for example, can be seen by comparison to cell A in the uniform flow case. The shedding frequency in cell B' appeared to increase continuously with the increase in flow speed, yet there appeared to be frequency jumps at both ends of this cell. For the span $y/d > 40$, the frequency in cell C' also appeared to increase continuously, but at a lower rate.

4.2.2 Step-cylinders in uniform and shear flow – "upright" configuration

The cylinder with a step-change in diameter was placed in both uniform and shear flows in two configurations. In the first case, the large diameter section was placed above the small diameter section, with the step located at $y/D = 0$. This case will be referred to as the "upright" configuration. In order to maintain consistency, all dimensionless numbers were calculated using the diameter D of the large cylinder.

The spanwise variation of the peak frequency is plotted for Re = 275 and 296 in Figure 28, and for Re = 621 and 625 in Figure 29. As was noted by Lewis and Gharib (1992) and Norberg (1992), three cells were detected along the central cylinder span in the uniform flow. Vortices were shed at high frequency behind the small cylinder (cell A), and low frequency behind the large cylinder (cell C), as expected from observations

of the uniform-diameter cylinder. However, the vortices in cell B were shed at a lower frequency than for either cylinder, for several diameters near the step, fully behind the large cylinder. As was the case with the uniform diameter cylinder, there existed regions near the ends that were visibly influenced by end effects.

Ko *et al.* (1983) noticed from pressure measurements that the wake of the small cylinder seemed to drift spanwise towards the large cylinder. This is apparent in Figure 29b by the fact that the vortex shedding frequency associated with the small cylinder (cell A) extended to $y/D = 1$ at the higher Reynolds number. This effect was more pronounced in the shear flow, as cell C' extended well behind the large cylinder even at the low Reynolds number.

The freestream shear caused cells of constant frequency to form behind each of the cylinders. The cells had a shorter length than those in the uniform diameter case, and the cell boundaries were not located at the same spanwise positions. These observations indicate that the cell sizes are likely influenced by the cylinder aspect ratio, as each cylinder was half the total length of the uniform cylinder. The cells were easier to see in the peak frequency plot at Re = 275, as the frequency jump was larger, and the frequency in each cell was nearly constant. At Re = 625, the frequency jump was relatively small, and most of the cells varied in frequency. The number of cells did not appear to change with Reynolds number within the range studied.

The low-frequency cell D' near the step occupied a larger spanwise distance in the shear flow at both Reynolds numbers, compared with the uniform flow cases. Taken alone, it is not clear whether this cell was the result of the same process as the uniform flow cell, or if it was created in a similar manner to the other cells behind that cylinder.

However, comparison with flow visualization, and with the "inverted" cylinder case, shows that the lowest-frequency cell is very likely due to the step.

The frequencies in the cells behind the small cylinder were lower than those in the uniform flow cases, which can be attributed to the lower local Reynolds number in that area. In the region around and above the mid-span, the frequency was nearly identical to the uniform flow case, as the corresponding local Reynolds numbers were nearly the same. For high positive y/D, the local Reynolds number was higher than in the uniform flow case, resulting in higher vortex shedding frequencies.

4.2.3 Step-cylinders in uniform and shear flow – "inverted" configuration

Inverting the step-cylinder from the previous configuration placed the small cylinder above the large one. In the uniform flow, shown by open circles in Figure 30 (Re = 293 and 294) and Figure 31 (Re = 640 and 647), the frequency variations were nearly mirror-images around the step of the previous orientation. Small differences in shedding frequency were likely due to slight differences in the freestream speed. A single cell could be observed behind each cylinder, with an additional lower-frequency cell behind the large cylinder at the step. The frequency dropped in this cell by approximately 7.1% at both Reynolds numbers studied. The boundary of the high-frequency shedding cell behind the small cylinder (cell D in Figure 31b) was deflected by about $0.5D$ behind the large cylinder at Re = 640, which was about 50% less than in the upright orientation.

The shear flow caused cellular shedding behind both cylinders, though the cells behind the large cylinder are more difficult to discern in the figures. Typically, the frequency increased from one cell to the next as the flow speed increased. Four cells might be identified behind the large cylinder at Re = 294 (Figure 30a), based on either

frequency jumps or changes in the rate of the frequency variation. The upper end of cell D' can be seen better in Figure 30b, followed by a very small drop in frequency close to the step, which shows that the step retained an influence in the shear flow. For Re = 647 (Figure 31), only two cells were visible behind the large cylinder before the frequency dropped in cell C'.

The frequency drop of the cell near the step in the inverted orientation in the shear was approximately 3%, which is much smaller than the 9% drop behind the upright cylinder. While there is no doubt that the frequency decreased along the span near the step, the decrease was much more gradual, and it was less obvious where the boundary to the low-frequency cell was located. For that reason, it is difficult to determine whether the spanwise length of the cell was affected by the shear. It appears that the cell might have had the same lengths in shear and uniform flows at lower Reynolds numbers, but that the cell length in the shear flow at the higher Reynolds numbers was smaller than in the uniform flow case.

4.2.4 Finite cylinders in uniform and shear flow

A cylinder with about half the height of the water channel was supported from above the test section. An endplate was affixed to the cylinder about 25 mm below the water free surface, but, at the other end, the tip remained completely free at $y/d = 0$. The Reynolds number was calculated using the diameter of the cylinder.

Results for the 3.43 mm diameter cylinder at Re = 152 and 146 are shown in Figure 32. It is known that the ends can influence the wake of the cylinder for many diameters towards the center of the span (Williamson, 1989). It is not completely surprising, therefore, that even far from the tip ($10 < y/d < 77$), the vortices were shed in five cells, with a 2.3% frequency jump between the cells D and F (cell E is a small spurious dip in

the shedding frequency), and nearly 6.8% difference between cells C and D. However, closer to the tip ($1.5 < y/d < 10$), the frequency dropped by 23.5% between cells B and C. This drop can be attributed to fluid motion around the tip, perpendicular to the vortex direction, which influenced that part of the wake. Measurements were taken beyond the tip of the cylinder to a distance of $y/d = -8.75$, at which point the presence of the vortices was still apparent (cell A), but at a frequency nearly 40% lower than that behind the tip. Investigations were not carried out to determine how far from the tip the vortices could be detected.

As shown in Figure 33, at Re = 331 four cells far from the tip ($10 < y/d < 77$) occupied almost the exact same spanwise positions as the cells at the lower Reynolds number (neglecting cell E at the lower Re), but with frequency jumps about 30% larger. A frequency jump in the middle of cell D, labeled D1, does not appear to be spurious, because it was repeatedly observed over four measurement runs on different days. Two short cells formed in the range $2 < y/d < 10$, both with frequency drops of about 10%. Although measurements were taken beyond the tip to a distance of $y/d = -8.75$, a vortex shedding frequency was not detected in the near wake for $y/d < 2.0$. This is explained by observing the flow visualization, which showed that downwash from the flow moving around the tip deflected the wake spanwise behind the cylinder, a distortion that persisted at the measurement location.

The shear generator spanned the full height of the water channel, so that the cylinders were immersed only in the higher-velocity section, in the range $0.40 < y/h < 0.96$. The effect of the shear was similar at both Reynolds numbers. The cells were of a lower frequency than in the uniform flow cases, though the difference became smaller farther from the tip, and the two frequencies were matched near the endplate, even though the local velocity was higher in the shear flow. The frequencies in cells A and A', beyond the

free end at the lower Reynolds number, were also exactly matched, as the freestream velocity in that range was very close to that in the uniform flow case. The cells close to the free end were shifted spanwise away from the tip, by up to two diameters, and maintained roughly the same lengths as in the uniform flow. Cellular shifting is most pronounced in Figure 32b around $y/d = 12$, and especially in Figure 33b at $y/d = 4$, where vortex shedding was suppressed for an additional two diameters compared to the uniform flow case. Far from the free end, up to two extra cells formed in the range $10 < y/d < 77$, most clearly visible at Re = 331 in Figure 33a (ignoring cell D1). The additional cells seemed to form in the middle of the span, leaving the cells near the tips and endplates nearly unchanged in length.

4.2.5 Double-step cylinders in uniform flow

A less-comprehensive study was made into the vortex shedding patterns in uniform flow past a cylinder with two step-changes in diameter, symmetric around its middle section. Four cases were studied at two different Reynolds numbers each, but the collected data were insufficient for a conclusive assessment.

The first two cases involved two long cylinders 6.6 mm in diameter attached coaxially to a 3.43 mm diameter cylinder around the mid-span. With the middle cylinder spanning $2D$, the expected jump in frequency occurred behind the small cylinder, but no other cellular shedding was observed at Re = 279 (Figure 34a, open symbols). On one end of the middle section ($y/D = 0$), the wake from the large cylinder was deflected by $0.5D$ behind the small cylinder, but on the other side ($y/D = 2$) there was no noticeable shift in the wakes. At Re = 643 (Figure 34a, closed symbols), however, an additional cell formed at both ends of the middle section, about $1D$ long, with boundaries about $0.5D$ into the wake of each of the large cylinders. The frequencies in cells B and D were almost

exactly halfway between the lower frequency in the outer cells A and E, and the higher frequency from the middle section, in cell C. The sudden reduction of the diameter across a short central aspect ratio thus appeared to affect the wake in a manner that depended on Reynolds number. At low Reynolds number, the two wakes had little interaction, but an increase in Reynolds number caused the span over which the small cylinder shed vortices to be reduced in size, likely because it was increasingly affected by end effects.

When the aspect ratio of the small diameter middle section was increased to 10 (based on the large diameter), shown in Figure 34b, a drop in the frequency was evident close to the step behind the large cylinder, at both Re = 295 (cell B') and 643 (cell B). This is similar to the drop that occurred behind the single step cylinder, and was approximately the same length ($6D$). There are insufficient data to tell definitively, but there appeared to be a jump in the frequency at $y/D = 14$ at Re = 295, which might indicate the presence of a cell (E') behind the large cylinder close to that step, as well. This length of middle section seems to be sufficiently large for end effects to be negligible. As with the single-step cylinders, the small-cylinder wake extended slightly behind the large cylinders at Re = 295, and up to nearly $1D$ at Re = 643.

Higher Reynolds numbers were achieved using larger diameter cylinders. At Re = 576 (Figure 35a, open symbols), with a middle section only $1D$ long, the Strouhal number along the span of the middle section was lower than the expected value of approximately 0.4, based on the large diameter. This cell extended up to $0.8D$ behind each of the large cylinders. At Re = 1260 (Figure 35a, closed symbols), the small cylinder wake extended up to $1D$ behind the large cylinders. There appeared to be a small jump in the Strouhal number at the boundary to cell C' at the lower Reynolds number, but it seems likely that this is spurious, caused by a surge in the water speed, or a bubble lodged in the step, for example.

The effect of increasing the length of the middle section between the same cylinders to $5D$ (Figure 35b) was similar to that seen in Figure 34b. The middle section was long enough for vortices to be shed close to the frequency predicted for the local Reynolds number in 2D flow. The wake of the small cylinder extended behind the large cylinder at both steps, for nearly $1D$ at $y/D = 0$, and about $0.5D$ at $y/D = 5$. The data are insufficient to draw conclusions, but it is possible that the apparent jump in Strouhal number between cells A' and B' indicates the presence of a low-frequency cell in the region behind the large cylinder near the step, similar to the single-step case.

It seems likely that, for a fixed Reynolds number, there is a critical aspect ratio for the middle section, below which the end effects become dominant, as in the case of end-effects for uniform diameter cylinders (Zdravkovich, 2003, Gerich and Eckelmann,, 1982). For aspect ratios greater than a certain value, the two steps behaved as nearly-independent single steps (Figure 34a –open symbols, Figure 34b and Figure 35b), even at high Reynolds numbers. For a given aspect ratio below the critical value, increasing the Reynolds number distorted the vortex shedding process, starting from the ends and moving inward, leading to a lower overall shedding frequency in the middle section (Figure 34a –closed symbols, and Figure 35a –open and closed symbols).

4.3 Local Strouhal number variation

With the Strouhal number calculated using the local diameter and the local velocity, the shedding frequency variations for the step-cylinders are as shown in Figure 36. The low-frequency cells near the steps are easy to identify in this figure. In uniform flow, at $Re_D = 294$ ($Re_d = 150$), the Strouhal number was higher behind the large cylinder than behind the small cylinder. Increasing the Reynolds number to $Re_D = 647$ ($Re_d = 330$), increased the Strouhal numbers behind both cylinders, but the increase was higher behind

the small cylinder. According to Figure 2, the Strouhal number increased with Reynolds number in this range, and the lower Re_d lay along a different curve from the other Reynolds numbers. The larger jump in Strouhal number behind the small cylinder, therefore, is in qualitative agreement with predictions based on uniform vortex shedding.

The low-frequency cells near the steps are more difficult to identify in most of the shear flow cases. In the inverted configuration, the Strouhal numbers in general decreased with increasing flow speed (at higher y/D). The average Strouhal numbers in each of the cells were within the same range of each other, and increased with Reynolds number.

In the upright configuration, the average Strouhal number in each cell increased with increasing flow speed (at increasing y/D). This is due to the fact that the local Reynolds number increased much faster in this configuration, because the large diameter was located in the higher-speed fluid, as opposed to the lower-speed flow in the inverted configuration. The local Strouhal number appeared to be nearly constant in the cells behind the large cylinder at $Re_D = 275$, and behind the small cylinder at $Re_D = 625$. The *local* Reynolds numbers of these cylinders were nearly the same, and were very close to the unstable region of the St-Re curve for uniform vortex shedding.

4.4 Spanwise variation of frequency spectra

The spanwise variation of the dominant frequency as described in the previous sections was determined by identifying the peak frequency in the power spectrum of the streamwise velocity at each location. Individual power spectra will be discussed below.

4.4.1 Step cylinders in uniform and shear flows

Analysis of the spectra near the step of a step-cylinder showed that the dominant frequency in a cell was not always the only frequency present. Figure 37 shows a series

of spectra for the inverted step cylinder at Re = 294 in uniform flow, corresponding to some of the data presented in Figure 30b (open symbols). In this configuration, the large diameter cylinder was located at negative values of y/D, and the low-frequency cell was present in the range $-7.5 < y/D < -0.5$.

At y/D = -9.1, the dominant peak was obvious at St = 0.21 (Figure 37a), while the other frequencies present in the spectrum were much weaker. Approaching the cell boundary at y/D = -7.6, however, a second peak increased in strength until it rivaled the dominant peak, and finally became dominant itself. The peak that was originally dominant decreased quickly in strength until it finally disappeared.

As Papangelou (1992) noted in experiments with tapered cylinders, the change in dominant frequency in adjacent cells appears to be simply a continuous changeover from one frequency to another, previously existing, frequency. The cells thus interact with each other near their boundaries. The interaction can be seen in the form of amplitude and frequency modulation of the signal (see Section 4.5), and local frequency analysis shows that the frequency could alternate between one and the other with time (see Chapter 6).

Near the step, a similar changeover occurred, as the dominant frequency peak behind the large cylinder decreased in strength, and the vortex shedding frequency from the small cylinder appeared (Figure 37e). The strength of the spectral peaks decreased significantly at the step, as the vortices were split and formed streamwise loops, so that they were oriented normal to the cylinder axes. This weakened their streamwise velocity component, which was the primary measurement parameter in this study. The change from one dominant frequency to the next occurred over less than $0.5D$, and at y/D = 1.8 from the step, there was no trace of the lower frequency. By contrast, when the frequency dropped at the cell boundary in the range $-7.6 < y/D < -3.3$ (Figure 37b-d), the two

frequency peaks remained at comparable strengths for 1.5D, and both frequencies could be seen for at least two diameters on either side of the boundary.

Figure 38 shows spectra of the velocity signals at different spanwise locations behind the inverted cylinder in a *shear flow* at Re = 647. Peak frequencies were shown in Figure 31a (closed symbols). The main difference in the spectra at higher Reynolds number was the spread of the spectral peak in the region where the dominant frequency changed, that is, at the cell boundary. Two frequency changes are shown, corresponding to an increase at y/D = -16 and a drop in frequency behind the large cylinder at y/D = -4.

As in the previous case, the dominant frequency showed up as a single sharp peak far from the cell boundary (Figure 38a). Close to the boundary at y/D = -15.9, the second, higher, frequency became stronger. As the dominant frequency changed, the peaks in the spectrum were not as sharp, probably indicating a vortex dislocation at y/D = -14.4, as described by Williamson (1992). The peaks became sharper again only when the new frequency dominated at y/D = -13.6. Two diameters farther from the cell boundary, the lower peak had disappeared. The frequency drop near the step behind the large diameter cylinder followed the same pattern, and is shown in Figure 38f-g .

Moving spanwise towards the step under the same conditions (Figure 39a-b), the frequency jump occurred over an even shorter distance than at the lower Reynolds number. No measurement position captured the two frequencies in the same signal, and the spectral peaks were much weaker where the frequency jump occurred. The new, higher, spectral peak appeared directly behind the step, at y/D = 0.0.

Far from the step behind the small diameter cylinder, at y/D = 17.4, the Strouhal number increased continuously, but erratically. The broad spectral peaks shown in Figure 39d indicate that several frequencies of similar strength could have been dominant, and a

fluctuation in the flow speed at that location could cause one to dominate over another for a short period of time. It would likely be more useful to indicate a constant frequency *band* for a cell in this situation, rather than looking for a single constant frequency. Additional wide spectral peaks can be seen in the range $32.6 < y/D < 34.1$, corresponding to the non-constant frequency in cell F' from Figure 31a.

4.4.2 Cylinders with free ends

As mentioned above, vortex shedding was either very weak or suppressed near the tip of the finite cylinder in both uniform and shear flows. Spectra for the finite cylinder at Re = 152 are shown in Figure 40 (corresponding to data in Figure 32b, open symbols). At $y/d = 1.2$, the peaks were more than three orders of magnitude weaker than the peaks far from the tip, but they were pronounced above the background fluctuations nonetheless. The frequency jump at the cell boundary was actually a gradual changeover from the lower to the higher frequency as the cell boundary was approached spanwise at $y/d = 1.8$, and passed at $y/d = 4.1$. The gradual frequency change can be observed again from $10.5 < y/d < 12.3$. All spectral peaks were very sharp behind the finite cylinder at this Reynolds number, even at the cell boundaries.

At Re = 331 (Figure 41, from data in Figure 33b), the spectral peaks were broad up to $11d$ from the tip. Two diameters spanwise from the tip, no spectral peaks were visible. At $y/d = 3.5$, a very weak spectral peak appeared, which became stronger farther from the tip at $y/d = 7.0$, even as a new frequency appeared to grow at the same time. The broad peaks nonetheless showed clearly the gradual change from one frequency to the next, proceeding through three cells from $7.0 < y/d < 11.1$. When cell D was reached at $y/d = 10.5$, the spectral peak narrowed as the frequencies of the end-cells decreased in strength, until a strong sharp peak became dominant for the remainder of the cell.

4.5 Velocity signal traces

As shown by the spectral data in the preceding section, several frequency peaks existed at many spanwise locations in the wake of the step-cylinder, especially near the boundary of a cell with a constant dominant frequency.

Velocity traces at different spanwise locations behind an inverted step-cylinder at Re = 295 in uniform flow are shown in Figure 42. The passage of vortices through the measurement volume (see Figure 26) is represented by velocity signals that are oscillatory and periodic in nature. The velocity increased to a maximum as the vortex passed, followed by a minimum between vortices.

In the three-dimensional flow near a cell boundary, the signal is both amplitude and frequency modulated, as in Figure 42a, exhibiting the influence of the two dominant shedding frequencies influencing the flow by different amounts. According to Papangelou (1992), the modulation frequency is equal to the difference in dominant shedding frequencies between the two cells. This will be discussed further after the local frequency analysis is presented, in Chapter 6.

The signal became more erratic in the low frequency cell near the step behind the large cylinder at y/D = -6.4. The signal modulation was also irregular close to the cell boundaries, as the two competing frequencies became comparable in strength.

The amplitude of the velocity signal decreased as the step was approached spanwise, at y/D = -0.6, and the modulation became more obvious, but with a variable frequency, signifying the increased mixing in this area, including vortex splitting (Williamson, 1992). Closer to the step, at y/D = -0.3, the signal fluctuation amplitude decreased to a minimum, and the modulation appeared to be more regular.

Behind the small cylinder close to the step, at y/D = 1.2, the signal had a higher frequency, and the modulation decreased in amplitude, but it was more regular than behind the large cylinder. Far from the step, only one frequency was present, and it is difficult to discern whether or not the signal was modulated.

4.6 Spanwise variation of average velocity in the wake

4.6.1 Step cylinders in uniform and shear flows

The results for the step cylinder indicate that there was little or no influence of the large cylinder wake on the flow around the small cylinder, at noted by Ko *et al.* (1983). The high frequency associated with the small cylinder dominated up to one diameter behind the large cylinder, although the low frequency peak was visible nearly to the step. However, the low frequency was not present in the spectra taken behind the small cylinder.

The streamwise velocity in the wake of the cylinders at the measurement location (see again Figure 26), as shown in the previous section, was cyclic, and may have contained more than one frequency. Figure 43 shows the mean streamwise velocity along the length of the cylinders. In the inverted configuration, the step cylinder was oriented so that the small cylinder was in the range $0 < y/D < 5$. In uniform flow, the streamwise velocity was essentially constant along the span, except in the step region. At the low Reynolds number, the mean velocity was constant up to two diameters from the step behind the large cylinder, and seven diameters from the step behind the small cylinder. Behind the large cylinder, there was a sharp rise in the mean velocity up to the step, at which point the velocity decreased sharply again behind the small cylinder. The velocity recovered over a distance of one diameter, after which it overshot the nearly constant value behind

the rest of the cylinder. Although the flow around the small cylinder did not appear to be affected in the flow visualization or the spectral analysis, the fact that the average velocity decreased significantly near the step shows that there is some effect. There does not appear to be any connection between the rise or drop in mean velocity near the step, and the size of the low frequency cell behind the large cylinder in that same region.

At higher Reynolds number, Re = 640, the effect of the step extended for nearly three diameters behind the large cylinder, and about $4.5D$ behind the small cylinder. The velocity rise was more gradual towards the step behind the large cylinder, while both the sharp velocity decrease and recovery behind the small cylinder were less pronounced compared to the low Reynolds number case.

The mean streamwise velocity behind the small cylinder was higher than behind the large cylinder, so that differences in the spanwise profiles were evident between the upright and inverted configurations immersed in the shear flow at Re = 640, even far from the step. Figure 43c shows the inverted case where the small cylinder was located at $0 < y/D < 45$. The velocity increased along the span due to the shear, and the slope changed in several locations, most of which corresponded to frequency changes at the cell boundaries, one of which was at the step. The sharp increase in velocity near the step was shifted toward the large cylinder, and was preceded by a small dip at lower y/D. Due to the constantly-increasing velocity along the span in the shear, the sharp velocity drop behind the small cylinder was not as low as in the uniform flow case, there was no noticeable overshoot, and the velocity recovered over a shorter spanwise distance than in the uniform flow.

The streamwise velocity behind the upright step cylinder in the shear flow showed the same general features as in the inverted configuration. Changes in the slope of the curve

often corresponded to cell boundaries, with the largest occurring at the step. In this configuration, the small cylinder was located at $-42 < y/D < 0$. The dip in velocity behind the large cylinder near the step was lower than in the inverted configuration, and the velocity rise towards the step ($4.5 < y/D < 0$) was much more gradual, probably mitigated by the decreasing velocity due to the shear as the step was approached spanwise. The velocity peak was located only about one diameter from the step, behind the small cylinder in this configuration, and the drop was not as sudden.

Ko and Chan (1984) showed that after the flow moved over the flat surface of the step, it was swept into the wake of the large cylinder, similar to the case of the finite end. The decrease in pressure due to the sharp end allowed the small diameter wake to be pulled behind the large cylinder, as shown in the frequency distributions in Figure 28 to Figure 31. Lewis and Gharib (1992) showed that the vortices formed dislocations and streamwise loops at the step, because of the difference in shedding frequency between the two cylinders. The increased velocity near the step in Figure 43 was likely due to the excess fluid flowing over the flat surface of the step and being entrained into the large diameter wake. The increased *spanwise* velocity of the looped vortices behind the small cylinder likely came at the expense of the streamwise component, and so the mean streamwise velocity was decreased.

In the shear flow, the freestream velocity increased along the span. In the inverted configuration, the downwash was aided by the higher freestream speed at the step as compared to the freestream speed at the large cylinder (Figure 44a), resulting in a more sudden rise in the velocity. In the upright configuration, the freestream shear imposed a higher velocity at the large cylinder than at the step location, leading to a region where the velocity dropped behind the large cylinder, before accelerating over the flat surface of the step (Figure 44b). The decreased streamwise velocity behind the small cylinder, likely

due to vortex inclination near the step, was partly balanced by the increase in velocity due to the shear, thus only a small decrease was observed.

4.6.2 Cylinders with free ends

The finite cylinder was oriented so that it could be considered similar to a step cylinder in the upright configuration, with a small cylinder diameter of zero. The downwash around the tip at Re = 152 caused a decrease in the mean streamwise velocity behind the cylinder in uniform and shear flow (Figure 45), which recovered over a short spanwise distance, with oscillations over a longer distance. In the uniform flow case, the oscillations decreased to a nearly constant level around $y/d = 35$, which corresponded to the boundary between cells C and D (from Figure 32), with another small jump around $y/d = 55$, at the boundary to cell F. At Re = 331 (Figure 45b), recovery of the velocity after the dip in the curve occurred over a slightly larger spanwise distance, and the oscillations stopped around $y/d = 40$, which is close to the boundary between cells D and E (from Figure 33). The dip in the velocity was not as great as at the lower Reynolds number, and it occurred slightly closer to the tip of the cylinder. As with the step cylinders, the spanwise location where the average velocity was minimum did not correspond with any of the proposed cell boundaries.

The spanwise variation of the average wake velocity in the shear flow at the Re = 159 (Figure 45c) was similar to the uniform flow case. However, the streamwise velocity constantly increased due to the uniform freestream shear, and the minimum velocity around the tip was lower. The velocity continued to recover beyond $y/d = 20$, even as oscillations in the mean velocity began around $y/d = 10$. Although the amplitude of the oscillations decreased, the mean never stabilized to the extent of the uniform cases, due to the increasing velocity in the shear.

Chapter 5

Experimental results –flow visualization

Flow visualization was performed in the water channel using electrolytic precipitation and hydrogen bubbles. The precipitation method was used at lower speeds than the LDV measurements, so that sufficient precipitate could be entrained in the flow, whereas the hydrogen bubbles could also be used at higher speeds. As in Chapter 4, the Reynolds numbers for the step-cylinders were calculated using the large diameter, unless specifically stated otherwise.

Images were transferred from the digital video recorder to a computer, where still images were selected using video editing software (Ulead VideoStudio 5.0).

5.1 Types of vortex connections

Vortices were shed from both the large and the small diameter sections of step-cylinders with Re > 100. Vortex streets were formed as in Figure 1, with the shed vortices alternating from one side of the cylinder to the other, and the individual vortices in a vortex pair rotating in opposite senses. The vortices remained visible downstream until they were broken down by flow instabilities and dissipated by friction. At the discontinuity in the cylinder diameter, the different frequencies of vortex shedding caused

more vortices to form in one cell than in the other over a given time interval. If the vortices in both cells were shed from the same side of the cylinder, and were therefore rotating in the same sense, some of these vortices could connect across the cell boundary, as sketched in Figure 46a. However, some of the vortices from the high-frequency cell would not have counterparts in the low-frequency cell, and would be left with unattached ends at the cell boundary. The unattached end of a vortex that was shed earlier was observed to rotate by up to 180°, joining in a loop with the next vortex, as in Figure 46b. By turning 180°, vortices shed from opposite sides of the cylinder, and initially rotating in opposite senses, could be joined in together.

Leading-edge style streamwise vortices, as described by Ko and Chan (1984), were observed to form from the junction between the large and small cylinders, and from the sharp edges of the step region. The junction vortices were not observed downstream because of a lack of visualizing particles, so only the edge vortices will be described here, and will be called streamwise vortices. These vortices were oriented nearly parallel to the streamwise direction, with a rotation from the flat surface toward the large cylinder. The streamwise vortices would be caught up in the induced flow from vortices shed on the same side of the small cylinder, and would become looped and twisted until they became favorably inclined to each other and formed a connection (Figure 46c).

At very low Reynolds number, when the small cylinder stopped shedding vortices, the streamwise vortices became connected with the low-frequency vortices shed from the same side of the large cylinder. The unattached ends of the vortices could not join together seamlessly, as their rotations were in opposite senses. Instead, the vortices became inclined parallel to each other, so that they had the same rotation sense, and one would wrap around the other, forming a cusp at the connection location (Figure 46d).

5.2 Step-cylinder in uniform and shear flow

Two sets of step-cylinders were used in the flow visualization studies (see Table 3). The smaller diameter set was the same as used in the LDV measurements, while the larger diameter set provided a higher Reynolds number at a lower flow rate, and a larger surface area from which the lead foil could precipitate, which often allowed for better flow visualization.

5.2.1 Away from the step region

Step cylinders with a diameter ratio d/D = 0.51 are shown in uniform flow in Figure 47, at Re = 168 and Re = 152. The same shedding patterns were observed for both upright and inverted configurations. Different images do not in general show exactly the same features, even under the same flow and lighting conditions, because of the non-stationary nature of the observed shedding patterns. These include differences in the location of gaps in the vortices, vortex curvature, and the apparent thickness of the vortices themselves.

The vortices shed from the large and small cylinders were inclined in the same direction with respect to the cylinder axes. The inclination of the vortices behind the inverted configuration was also inverted compared to the upright configuration. The vortices shed from the small cylinder were inclined such that the sections closest to the step were always farther downstream than the sections away from the step. Vortex sections behind the large cylinder near the step were always upstream of the sections away from the step. This implies that vortex shedding from the small cylinder began in the step region, and moved spanwise away from the step, while vortex shedding from the large cylinder moved spanwise toward the step. Vortex inclination varied slowly and

irregularly with time between about 0° and 30°. The inclination of vortices shed from the small cylinder were more often observed in the higher portion of this range, while those from the large cylinder were more often in the lower portion.

In the shear flow, the higher local speed at larger *y/D* forced the vortices to be convected downstream at different rates along their lengths. The inclination of the vortices shed from both cylinders in the upright configuration (Figure 48a) was increased in the shear flow compared to the uniform flow, often reaching values as large as 45°.

The vortices shed in the inverted configuration in shear flow (Figure 48b) changed from negative to positive inclination compared to the uniform flow case. The angles varied with time between 0° and 30°, which implies that the shear added a nearly constant inclination to the vortices.

A comparison of typical maximum apparent angles that the vortices made to the cylinder axes for the uniform and shear flows is presented in Table 9, for both the upright and the inverted configurations.

The vortex cores tended to have more kinks and distortions along their lengths in the shear flow as compared to the uniform flow case. This was especially true for the vortices in the higher local speed compared to the uniform flow (compare the upper parts of Figure 47b and Figure 48b).

The cylinders were tested at Reynolds numbers (based on the large diameter) that ranged from 80 to 1230. At the lowest Reynolds numbers, the small cylinder (at

Table 9: Typical maximum vortex inclination in uniform and shear flows.

Cylinder configuration		Upright		Inverted	
Flow type		Uniform	Shear	Uniform	Shear
Figure number		Figure 47a	Figure 48a	Figure 47b	Figure 48b
Vortex angle	Large cylinder	5°	20°	-5°	30°
	Small cylinder	15°	32°	-25°	-5°

Re_d = 39) stopped shedding vortices, forming instead a nearly symmetric wake (Figure 49). The vortices shed from the large cylinder, however, were laminar, and they remained laminar up to about Re = 122 (Figure 50a). Increasing the Reynolds number caused the vortices to eventually become turbulent, leading to the diffusion of their cores, and the formation of streamwise "fingers" which appeared to link subsequent vortices (Figure 50b). The streamwise fingers formed soon after the vortices detached from the cylinder surface, and grew as they moved downstream, until they were dissipated. The shed vortices remained visible and nearly parallel to the cylinder for a much farther downstream distance than the fingers. The streamwise "fingers" have often been observed in the wakes of uniform cylinders in uniform flows (Bailey *et al.*, 2002, Wu *et al.*, 1994).

As discussed with regard to the frequency data presented in Sections 4.2.2 and 4.2.3, the addition of uniform shear caused cellular shedding behind both cylinders, even far from the step. Examples of cellular shedding can be seen behind the large cylinders in Figure 48, where gaps were visible in the shedding pattern. The frequency difference between the cells meant that some vortices from one cell would not be connected with a vortex from the next cell, but instead of terminating in the fluid, they would connect with another vortex in the same cell, as described above.

The cell boundaries were visible when the vortices, shed at different mean frequencies, were out of phase (Figure 51). The formation of a cell boundary was identified by a sudden change in the inclination of the vortices, where no such change existed before (from Figure 51a to b). The location of the inclination change drifted spanwise with each subsequent vortex (Figure 51c), indicating that the spanwise location of the cell boundary may not be fixed. Once the vortices were sufficiently out of phase, they would split, forming streamwise filaments (Figure 51d). A filament from a vortex

shed earlier would typically turn by 180° so that two consecutive vortices could be joined in a half-loop. Others would simply deflect around the looped pair to be connected with the next vortex in the adjacent cell. Once the vortices were in phase again, the disturbance would disappear for some time (Figure 51e). The vortices that were shed after the disturbance were once again parallel to each other, such that the cell boundary could not be discerned. A sudden inclination of the vortices has also been found to indicate the formation of cell boundaries in the case of a cylinder with uniform square cross-section (Bailey *et al.*, 2002).

5.2.2 Step region

As indicated by the LDV measurements (Figure 28 to Figure 31), the vortices shed by the small cylinder were drawn into the wake of the large cylinder downstream of the step, for both upright and inverted configurations. This could be observed in the flow visualization images as the vortices shed by the small cylinder were convected into the wake of the large cylinder, drifting farther from the step with downstream distance.

Many of the vortices in this region were connected across the cell boundary at the step. As with the cell boundaries far from the step, the higher shedding frequency behind the small cylinder meant that not all of these vortices had counterparts behind the large cylinder. The larger difference in frequency across these cells caused disconnected vortices to form more often than at other cell boundaries. Many of the extra vortices twisted into the streamwise direction, and appeared to connect with the next vortex in the sequence, forming half-loops, as shown in Figure 52. The vortices were never completely isolated from the rest of the vortex street, as streamwise filaments lingered between the looped pair and the next vortex, sometimes extending back to the cylinder surface and often connecting with other vortices (Figure 52c).

Williamson (1992) observed that the appearance of loops at the boundary to cells with a small frequency difference were simply an artifact of the flow visualization. He indicated that, instead, several consecutive vortices overlapped to form the apparent loop, as shown in Figure 4. He claimed that each of the vortices were weakly connected across the cell boundary, but that the visualizing agent was too tenuous to see within the weak linkage.

With the large frequency jump between the cells at the step, video of the loop formation showed that thin linkages did remain across the cell boundary, but that the streamwise vortices attached to some of the shed vortices could become disconnected, twisting fully around as they moved downstream, and becoming connected to the next vortex in the same cell. In this way, two subsequent vortices appeared to wrap around each other, and eventually merged, as in Figure 53. The loop at the end of the high-frequency vortex b, which is all that remained of the streamwise vortex, grew into a more complex knot downstream, as each vortex twisted the other. By the last frame, vortices b and c had combined in a three-dimensional half-loop that was completely disconnected from the streamwise filaments that had connected them to other vortices. The influence of the half-loop on the rest of the wake could be seen as the various nearby filaments, like the one connected to vortex d, were twisted in the vicinity of the knot.

In a uniform flow, the large diameter cylinder shed vortices with a larger strength than the small cylinder (Zdravkovich, 1997). In order for the strength of each vortex behind the large cylinder to be preserved at the step boundary, each low-frequency vortex was connected to both one or more vortex shed from the small cylinder and one or more counter-rotating vortex from the same low-frequency cell, as shown in Figure 54. Vortices e and e' were shed in-phase, and connected across the cell boundary along an uninterrupted, nearly straight line. Vortex e', having a larger strength than vortex e,

appeared to have looped its excess circulation around to connect with vortex f', which was shed from the opposite side of the large cylinder. Vortex f' was also connected across the cell boundary to vortex h. Each of the low-frequency vortices appeared to be connected by thin streamwise filaments that could form into loops, preserving the circulation of each.

The vortices in the cell behind the small cylinder were more numerous than those behind the large cylinder, and as a result the connections across the cell boundary became increasingly inclined with each new vortex, reaching as much as 90°. The most usual cross-boundary vortex connections were thus not straight. Vortices c-c' and d-d', for example, were connected across the cell boundary, but the connecting sections were inclined to the axes of the main vortex sections, because each high-frequency vortex was always downstream of its low-frequency counterpart.

The spacing between the vortices eventually became large enough that the two counter-rotating vortices f and g in the high-frequency cell had no counterparts to connect with in the low frequency cell. As a result, the ends of vortices f and g looped around to connect with each other, forming a continuous horseshoe vortex with constant strength and sense of rotation. At Re = 152, between three and four high-frequency vortices could be observed to connect across the cell boundary at the step, followed by two that formed a half-loop. For example, the half-loop formed by vortices f and g in Figure 54 was followed by connecting vortices e-e', d-d', and c-c'. Vortices a and b formed the next half-loop within the high-frequency cell.

The formation of the half-loops between vortices is best documented by observing the flow closer to the cylinder surface, where the streamwise rotation was added to the wake by the streamwise vortices. As the upstream flow approached the step region, it was

deflected over the step, creating a recirculation zone with clockwise rotation at the base of the junction between the large and small cylinders (Figure 55a and b, visualized using hydrogen bubbles, generated from a wire parallel to the cylinder axis on the symmetry plane and slightly upstream, at Re = 1230), which resulted in a horseshoe vortex anchored on the small cylinder. Both legs of this junction vortex turned roughly into the streamwise direction, forming counter-rotating vortices on either side of the small cylinder. The rotation sense of these vortices was such that, when viewed from downstream with the small cylinder located above the large cylinder (the inverted configuration), the vortex on the left was rotating clockwise and the one on the right was rotating counterclockwise. The rotation sense relative to the cylinder was maintained in the upright configuration. These vortices interacted with the shed vortices, but they could not be visualized by electrolytic precipitation, because they were generated in a low-shear region. They have, however, been clearly observed to form by the hydrogen-bubble method, with the wire positioned on the step upstream of the small cylinder.

The flow displaced by the small cylinder spilled over the side edges of the step, forming a pair of vortices that were counter-rotating to the adjacent junction vortices, so that, when viewed from downstream, with the cylinder in the inverted configuration, the one on the left was rotating counterclockwise and the one on the right was rotating clockwise. As with the junction vortex, the rotation sense relative to the cylinders was maintained in the upright configuration. The streamwise edge vortices stretched downstream several diameters, where they interacted with the shed vortices. In this way, streamwise vorticity was added to the wake in the step region.

The interaction of the streamwise edge vortices with the higher-frequency shed vortices was visualized using electrolytic precipitation at Re = 118 in Figure 55c-h. Figure 55c shows three vortices behind the small cylinder, two of which (b and d) were

shed from the same side of the cylinder, and were connected by a streamwise vortex, which was stretched into a large arc. Vortex c, shed from the opposite side of the cylinder, twisted a streamwise vortex into a tight loop; the streamwise vortex would later become an arc connecting vortices c and a. In Figure 55d, the arc connecting vortices b and d was much larger, and a small arc linked vortices a and c. The two arcs became entangled (Figure 55e) as their rotations twisted each other, allowing vortices b and c to become intertwined (Figure 55f) and the arcs to become disconnected from the upstream vortices. The knot at the end of vortex b, however, was pulled in the direction of the large cylinder, reaching past the arc that originally connected it to vortex d, and caused a deflection in that arc (Figure 55g). The tip of vortex c can also be seen wrapping around the extended knot from vortex b (Figure 55h), and might have become completely disconnected from the arc originally connecting it with vortex a. It is clear from this sequence that half-loops between vortices shed from opposite sides of the cylinder did not form immediately, but required time to do so.

The paths of the streamwise vortices from opposite sides of the step approached each other closely as they arced between the ends of the vortices behind the small cylinder. The presence of the step also caused the vortices shed from the small cylinder to lag behind in that region, so that they became oriented more towards the streamwise direction than in regions farther from the step. All of the vortices near the step were therefore twisted and stretched helically by each other, forming complex knots and streamwise arcs which often traveled spanwise behind the large cylinder.

The effect of the vortices shed from the small cylinder on the streamwise edge vortices, based on the previous figure, has been sketched in Figure 56, which only shows vortices from one side of the cylinder, with one exception (vortex S6 in Figure 56b, which was shaded a different color). The streamwise vortex developed a kink in the

vicinity of the high-frequency vortices (vortex S1). Downstream, the shed vortices twisted the kink so that it formed a small loop around itself (between B and D), which could evolve into a knot. If the vortices on either side of the step were in-phase with each other and connected across the cell boundary, the streamwise vortex could split and also form a connection with the vortex behind the large cylinder, as they were rotating in the same sense (at point C). The streamwise vortex was drawn toward the large cylinder in the space between subsequent high-frequency vortices, so that it formed a long arc that appeared to connect them (point D or points E-F-G in Figure 56a). The downstream branch of the streamwise vortex (point E) turned counter-clockwise on the plane of the figure, so that it became oriented more and more in-line with the upstream branch (point D). The two branches of the streamwise vortex were counter-rotating, in a way that their induced fields would nearly cancel each other (points F and G). However, the high-frequency vortices induced a twisting action of one branch around the other, so that they began rotating together. The streamwise vortices could then either form part of a connection between vortices across the cell boundary (points H and I in Figure 56a), or assist in the half-loop formation between two high-frequency vortices shed from opposite sides (point J in Figure 56b). When two vortices in different cells were close enough to form a connection, a section of the streamwise vortex would become detached from its upstream and downstream ends and it would become nearly completely integrated into the connection. As shown in Figure 54, some connections were nearly parallel to the cylinder axis, and others were largely inclined. These are represented in Figure 56a by the connections between vortices S9 and L5, and S7 and L3, respectively. Alternatively, the twisted branches of the streamwise edge vortex at D and E in would continue their counter-clockwise rotation, detach from the upstream shed vortex, and become attached to a high-frequency vortex shed from the opposite side of the cylinder, completing a half-

loop between counter-rotating vortices, as shown by point J between vortices S6 and S7 in Figure 56b.

The streamwise vortices were not observed to interact directly with the vortices behind the large cylinder above Re_D = 80. They formed connections only when the rotation induced by the higher-frequency vortices pulled them in-line with the vortices on both sides of the cell boundary.

Below a certain Reynolds number, a laminar vortex street formed behind the large cylinder, while a non-shedding symmetric wake formed behind the small cylinder. If the downstream end of a streamwise vortex was turned toward the large cylinder, it would have a different rotation sense than the ends of shed vortices from the same side of the cylinder. Instead, the low-frequency vortices bent back toward the cylinder, and became nearly inclined into the streamwise direction near the step, parallel to the streamwise vortices. The ends of the two vortices were then rotating in the same sense, and one would wrap around the other, forming a cusp at the connection location (as sketched in Figure 46d).

At Re_D = 80 and 63 (Figure 57), the small cylinder did not shed vortices, and vortices in the low-frequency cell near the step did not appear to fully form, perhaps because of interactions with the flow around the small cylinder. Downstream of the cylinder, therefore, vortices were only shed in the main cell behind the large cylinder, and the vortex interactions appeared at the boundary to that cell.

At Re_D = 80 (Re_d = 41), the vortices in the cell near the step curved back toward the cylinder (Figure 57a), and were convected downstream at a slower speed, as their ends become oriented nearly parallel to the streamwise vortices. The cusped connections between the streamwise vortices and the low-frequency vortices generally drifted into the wake of the large cylinder as they traveled downstream. Near the cell boundary farther

from the step, the vortices were bent toward the cylinder, in order to accommodate the large curvature within the cell. They often appeared to merge together as they trailed back towards the cylinder. The vigorous motion of the streamwise vortices also induced some weak shedding from the small cylinder in the region close to the step, which also became inclined nearly parallel to the streamwise direction.

A smaller amount of the visualizing precipitate was used in Figure 57b-d, at $Re_D = 63$ and $Re_d = 32$, and as a result, the cusped connections were more difficult to see, and they likely dissipated within a few diameters downstream of the cylinder. At least two cusped connections are visible in the area close to the step in Figure 57b, where the vortex sections closest to the step were highly-curved. The remaining vortex patterns were not likely directly related to the streamwise vortices. The vortex sections at the cell boundaries were largely inclined to the streamwise direction, and extended nearly all the way back to the cylinder surface. Streamwise filaments from the earlier vortices twisted subsequent vortices helically, creating knots and sharp kinks, which show up as bright patches in Figure 57b. The streamwise filaments themselves were twisted by the vortices shed from the large cylinder, becoming wavy close to the knots (Figure 57c). Sufficient twisting of the streamwise filaments could cause them to become attached to the shed vortices, as in Figure 57d, which shows how a streamwise filament associated with the vortex on the right looped around and became entangled with the knot formed in the vortex on the left. In general, the streamwise filaments from each of the shed vortices stretched back in a wavy pattern to the cylinder surface, with the wave "minimum" occurring close to each of the shed vortices. The streamwise connections and loops appear remarkably similar to vortices shed from a cylinder with a free end.

The streamwise vortices may be a major element in the formation of the low-frequency cell near the step, as they changed the overall orientation of the vortices in the

step region. The rotation of the streamwise vortices caused the vortices near the step to bend back towards the cylinder, even reversing direction in the segments close to the step (Figure 57b). As the arcs that connected high-frequency vortices moved into the wake of the large cylinder, they disrupted the vortices more, and they may have altered the flow so that the shedding frequency was periodically reduced.

5.2.3 Low-frequency cell near the step

The streamwise vortices at the step periodically twisted the shed vortices into a helical pattern, which traveled spanwise along the surface of the large cylinder, away from the step, for several diameters (Figure 58). This caused the vortices to deform, and, as mentioned above, may be the cause of the low-frequency cell observed in the LDV measurements.

The low-frequency cell behind the large cylinder near the step, called the "modulated zone" by Lewis and Gharib (1992), was visible as a series of horseshoe-shaped vortices that occurred periodically between apparent gaps. One of these gaps was formed by the step region, while the gap at the boundary between the cells behind the large cylinder was the "inclined interface" observed by Lewis and Gharib (1992), and was not always visible in the flow.

The low-frequency cell near the step can be seen in Figure 47 between the disconnected vortices. The gaps near the step, and several diameters spanwise behind the large cylinder, were caused by the difference in frequency between those cells, as the vortices could not maintain the connection because they moved out of phase with each other.

Figure 59 shows one cycle in the development of the low-frequency cell near the step. When the vortices in this cell were in phase with those behind the rest of the large

cylinder, the inclined cell boundary could not be seen. The cycle began as a knot-like disturbance appeared near the step (Figure 59a, arrow). At the same time, the vortices in the cell farther from the step became wavy and inclined further to the cylinder axis. Subsequent vortices within the low-frequency cell became more curved, with streamwise filaments trailing back towards the cylinder near both of the cell boundaries (Figure 59b). As mentioned previously, the loops are assumed to be a method of preserving the vortex strengths where the frequency abruptly changes. Eventually, when the vortices in the two cells behind the large cylinder were completely out of phase, they would become disconnected (Figure 59c). As the dislocation moved downstream, each of the lower-frequency vortices remained connected to a vortex in the higher-frequency cell, though some of the connections appeared rather tenuous. The ends of both unconnected vortices in the higher-frequency cell arced back towards the cylinder. These arcs may be related to the streamwise "leading-edge" vortices observed by Mair and Stansby (1975) at the boundaries to cells behind a uniform-diameter cylinder in a shear flow. As the unconnected pair moved downstream, the downstream arc was caught by the upstream vortex, as highlighted by the arrow in Figure 59d and the pair joined together with a constant strength, while the upstream arc dissipated. As in the step region, most of the vortices in the adjacent cells remained somewhat connected through the dislocation event, although many of the linkages were barely visible as they underwent serious deformations. Continuous vortex connections resumed after several shedding cycles, so that the cell boundary was no longer visible. This was followed soon after by another knot-like structure near the step, which signaled the beginning of a new cycle in the formation of the low-frequency cell (Figure 59e). The inclined boundary between the two cells behind the large cylinder did not occur regularly in time. One boundary could begin

to form as the previous one was ending, as in Figure 59e, or many continuous vortices could separate two consecutive boundaries in the same flow conditions.

The vortices within the low-frequency cell near the step were highly curved (as in Figure 59b), leading with the middle of the cell, while the two outer sections, turned by nearly 90° to the streamwise direction, trailed back towards the cylinder close to the cell boundaries. The outer sections of the vortices in this cell, which were turned in the streamwise direction, did not have the same structure as the streamwise "fingers" that can be observed linking vortices in higher Reynolds number flows, as in Figure 50b. In that case, the fingers existed alongside the shed vortices, where in the low-frequency cell, the entire shed vortex, split from both adjacent cells, was highly inclined at both ends.

The spanwise length of the low-frequency cell near the step was enlarged by the flow shear in the upright configuration, and decreased in the inverted configuration. This is likely due to the deflection of the flow towards the higher velocity in the uniform shear, as described in the previous chapter.

5.3 Finite cylinder with one free end

The finite cylinders were either suspended from above the water channel or anchored to the floor of the test section, so that in either case their free ends were at about half the water height. An endplate was attached to the opposite end of each cylinder, about 25 mm from either the free surface or the test section floor. At the large aspect ratios of the cylinders used in this study, the endplates did not disturb the flow along most of the span. Two different diameter cylinders were studied (see Table 3) in uniform and shear flows. In the shear flow, the cylinders were located either in the higher velocity region (suspended from above), with the flow speed decreasing spanwise toward the tip, or in

the lower velocity region (anchored to the bottom of the test section), with a velocity increase toward the tip.

5.3.1 The tip region

The span of the cylinder close to the tip showed similar vortex patterns and interactions as the step region behind the step-cylinder. However, the flow was completely unimpeded around the flat end, as opposed to the step-cylinder case, in which the small-cylinder blocked some of the end-flow, causing fluid to spill over the edges of the step. The fluid separated from the sharp edges of the tip, therefore, in the opposite sense from the step-cylinders, rotating instead from the cylinder toward the tip. The separated flow around the tip was then deflected spanwise into the wake of the cylinder, a phenomenon called "downwash", also seen by other authors (Ayoub and Karamcheti, 1982; Tanaka and Murata, 1999). The wake was displaced spanwise by several diameters, so that the vortices shed from the cylinder were forced away from the tip, even far downstream (Figure 60). The displacement was larger for higher Reynolds numbers (compare Figure 60a and b), which is in agreement with the frequency data presented in Figure 32 and Figure 33. However, there was no sign of any vortices that would have been shed at lowest frequency, measured beyond the tip at low Reynolds number, as shown in Figure 32.

Streamwise vortices that originated from flow over the sharp edges of the tip could be seen interacting with the shed vortices, which were oriented in the spanwise direction. In the case of the step-cylinder, if the streamwise vortices were oriented parallel to the large cylinder vortices, they were rotating in opposite senses. The streamwise vortices from the edges of the finite cylinder tip, however, were rotating in the same sense as the shed vortices, and could therefore join end-to-end, instead of in a cusp.

Both the streamwise and the shed vortices were twisted by each other to form complex patterns. The streamwise vortices became inclined nearly parallel to the cylinder axis, and were deflected far from the tip near the cylinder surface (Figure 61a). The streamwise vortices could cause helical kinks in the spanwise vortices many diameters from the tip (Figure 61b), which would lead to vortex splitting farther downstream.

The rotation of one vortex by the other caused a helical pattern which ended up with a rotation normal to both vortices. When the length between cell boundaries was short, as in Figure 62, shed vortices that originally formed a half-loop could be rotated counter-clockwise at the other cell boundary, looping a full 360° (Figure 62d). This contributed to the gaps in the vortex patterns closest to the tip, where vortex dislocations were expected to appear.

At the tip of the cylinder, the end of almost every vortex was linked to the subsequent vortex by a streamwise loop, all the way back to the cylinder (Figure 63). These vortices became twisted into knots as they acted upon each other (see the arrow in Figure 63), and behaved in a similar manner to the downstream patterns in very low-Reynolds number step-cylinder cases.

As with the step-cylinders, breaks in the vortex pattern caused by dislocations and looping indicated the locations of cell boundaries. Figure 64 shows one boundary close to the tip, which was only a few vortices wide, while another one farther from the tip extended much farther downstream, indicating that the upper cells were out of phase for a longer period of time.

The shear had the effect of increasing the size of the downwash region near the tip, and disturbing the shed vortices further (Figure 65). In the upper configuration (Figure 65a and b), the size of the downwash was increased, while in the lower configuration

(Figure 65c), the size of the downwash was decreased, similar to the observed pattern behind the step-cylinders. In all cases, the streamwise vortices moved along the cylinder surface away from the tip, and either rolled into a connection with a spanwise vortex, or caused a disturbance that would lead to vortex splitting. The vortices formed loops at the tip, as they did in the uniform flow, and their development appeared to follow the same evolution.

5.3.2 Away from the tip

In uniform flow, the vortices shed far from the tip of the cylinder were generally unbroken, and showed very few disturbances (Figure 66a), although they were always inclined toward the tip. At higher Reynolds number, disturbances became visible, leading to vortex splitting (Figure 66b). The cell boundaries drifted spanwise with every subsequent vortex, and their downstream development was the same as in the step-cylinder cases, that is, with a sudden change in vortex inclination, followed by a spanwise disturbance and the formation of a gap. The gap was generally wider than in the step-cylinder cases.

The shear increased the general disorganization of the vortices (Figure 65), in addition to changing their inclination. In the upper configuration, the vortices were inclined more than they were in the uniform flow case. In the lower configuration, the vortices changed from being inclined towards the step (see Figure 61) to being inclined slightly away from the step (see Figure 65c).

5.4 Cylinders with double step-changes in diameter

As with the LDV measurements (see Section 4.2.5), a less-comprehensive study was undertaken to observe the vortices that were shed from a small diameter cylinder attached

coaxially between two large diameter cylinders, giving two symmetric step changes in diameter. Of the two sets of models (see Table 3), only the larger diameter cylinder sets were observed (corresponding to the frequency data in Figure 35), in order to have a sufficiently large surface area from which the lead foil could precipitate. The small diameter middle cylinder was studied at two different aspect ratios, with lengths of $5D$ and $1D$.

5.4.1 Large aspect ratio middle cylinder

With the middle section spanning $5D$, vortices could be observed from all three cylinders, and many of the features observed at each step had also been seen behind the single step-change in diameter (Figure 67). The large aspect ratio in the middle allowed the flow at each step to evolve nearly independently. For example, the curved vortices of low-frequency cells were observed close to the steps behind both of the large cylinders, and streamwise vortices could be seen from both steps.

Each of the large cylinders, however, influenced the other by dominating the wake of the small cylinder alternately in time. The frequency data in Figure 35 showed that the high-frequency cell behind the small middle cylinder could be seen up to $1D$ behind each of the large cylinders at higher Reynolds numbers. Flow visualization showed that the wake shifted first towards one large cylinder, then towards the other, in an irregular cycle. In Figure 68a, the wakes were all deflected towards the lower cylinder, while Figure 68b shows a deflection towards the upper cylinder. Each of the wake deflections was usually accompanied by vortex splitting on one or both sides.

The vortices shed from the middle section changed inclination continuously in an irregular manner that did not appear to be related to the cycle of wake deflections. Far

from the steps, the vortices shed from the large cylinders were consistently inclined towards the steps.

As with the other configurations, streamwise vortices were observed flowing into the wake from the sharp-edged step. The streamwise vortices were generally rolled up by the induced velocity of the vortices shed from the small cylinder, becoming attached farther downstream, which is consistent with the single-step cases. They forced an inclination in the shed vortices until half-loops formed, which connected some of the consecutive vortices at the step (Figure 69).

When the vortices from the middle cylinder were shed in phase with vortices from one or both of the large cylinders, they were connected across the cell boundaries at the steps with only a little deformation, where streamwise filaments were observed (Figure 70a). In general, the large cylinders shed vortices slightly out of phase with each other, a situation that, according to Williamson (1992), could be altered by inclining the endplate configurations. The phase shift thus occurred at different rates between the two steps, so that the vortices from the small cylinder would move out of phase with those shed from the upper cylinder (Figure 70b) at a different time from the lower cylinder (Figure 70c), forming half-loops as they did so. Occasionally, all three cells were out of phase at the same time, and a deformed full loop would develop (Figure 70d).

5.4.2 Small aspect ratio middle cylinder

Williamson (1992) studied a ring of small aspect ratio attached concentrically to a cylinder of slightly smaller diameter, which is the geometrically opposite configuration to the small aspect ratio case in the present study, although the diameters of the ring and the outer cylinders were nearly the same. The effect of a short section of small diameter set between two large-diameter cylinders was similar, in that disturbances and dislocations

were observed between the vortices shed from the large cylinders, while the vortices shed by the small cylinder could not be seen.

Although a distinct frequency of vortex shedding from behind the small cylinder was measured by the LDV (Figure 35a), no shed vortices were observed at the lower Reynolds number used for the flow visualization. The steps did not influence the flow independently, as with the longer aspect ratio.

When the vortices shed from the large cylinders were in phase with each other, they could connect across the small distance of the middle section with only a mild disturbance (Figure 71a), while when they were completely out of phase, vortex splitting occurred, and they formed double half-loops (Figure 71b).

The disturbances to the large vortex patterns were mainly visible in the form of streamwise filaments that extended back toward the cylinder (Figure 72). As with the other configurations, the streamwise filaments originated with streamwise vortices shed from the sharp edges of the step, which moved away from the step along the surfaces of the large cylinders.

The effect of the streamwise vortices can be seen in Figure 72. Vortex "b" joined with a streamwise vortex in a cusp that pointed downward (Figure 72a), which resulted in a helical twisting as the vortices rotated around each other (Figure 72b). The helical twisting caused a section of the vortex to bend back toward the cylinder (Figure 72c), moving against the free stream. A thin vortex filament could be observed crossing the disturbance spanwise, but this also had a kink at its center. By the time the vortex had traveled several diameters downstream (Figure 72d), only very thin filaments could be seen to connect the shed vortices across the cells. The actual disconnection occurred where the streamwise vortex had diffused so much that vortex "b" began to turn by

nearly 180 degrees (Figure 72e), after which it started to join with vortex "a" (Figure 72f). The actual merging of the vortices occurred outside the camera view, downstream.

Most of the vortex patterns were not symmetric around the steps. The vortices shed from the upper cylinder dominated the flow, most often convecting behind the middle cylinder, and sometimes far into the wake of the lower cylinder (see Figure 72). The disturbance created by the middle cylinder was then also displaced into the wake of the lower cylinder. It seems likely that this is due to end effects, and that properly aligned endplates might be able to create a symmetric vortex shedding pattern.

5.5 Summary

The various cylinder configurations observed using flow visualization all had much in common. In general, the vortices were shed at an angle to the cylinder axes, the wake was deflected away from the step or tip towards the large diameter cylinders, and cellular shedding developed close to the step or tip, with the boundaries between the cells easily identified by the splitting of out-of-phase vortices. The gaps in the vortex patterns due to splitting were accompanied by a complex interaction, some of which formed vortex loops. All of these loops were connected, however tenuously, by streamwise vortices shed from the step or tip. The streamwise vortices traveled spanwise along the cylinder surfaces away from the steps or tips for several diameters, interacting with the shed vortices by twisting them in a helical manner. This is likely the cause of the low frequency region behind the large cylinders close to the steps of the step-cylinders and the tips of the finite cylinders.

Chapter 6

Experimental results –local frequency analysis

It was clear from the data presented in Chapter 4 that two or more spectral peaks, representing different frequencies, could be present in the velocity signal measured near cell boundaries. One peak was dominant up to a certain spanwise location, after which the other would dominate. The velocity signals presented in Section 4.5 indicate that at times the frequencies could be modulated, while at other times, the frequency of the signal appeared to remain constant. The wavelet transform, using the Morlet wavelet, was applied to signals in the regions of interest in order to obtain an understanding of how the dominant frequency varied with time.

As mentioned in Section 3.5.4, the amplitudes of the wavelet transform results were normalized by the corresponding maximum value in a given signal. The wavelet map thus shows the relative significance of phenomena recurring at different frequencies. Larger amplitudes of the wavelet transform are indicated by darker shading, while the lowest contour level represents a cutoff of 40% of the maximum amplitude, in order to

increase the clarity of the wavelet map. While this removed some information from the signal, it was felt that any periodic components with such a low relative strength would not contribute much to the phenomena being studied.

Each of the wavelet figures are presented in the same format. The signal, normalized by its mean, is displayed on top ("a" in each figure). The wavelet contour plot is shown in the middle ("b"), with the largest amplitudes shown by the darkest shades. The associated frequencies are given in the form of the Strouhal number. The term "amplitude peak" will be used to describe the largest amplitudes, similar to the use of the term "spectral peak" in a power spectrum. Cross-sections of the wavelet map parallel to the Strouhal number axis at a given instant in time can be considered as "local" frequency spectra, showing peaks at dominant local frequencies. As with the Fourier spectrum, the amplitude peaks may be narrow-band or wide-band. The strength of a quasi-periodic phenomenon is better indicated by the area under the peak rather than the peak maximum. The frequency at which the local amplitude peaks occurred is plotted against time on the bottom of each figure ("c"). This plot should be used in conjunction with the wavelet map, because the relative amplitude of each peak is not taken into consideration. For example, a peak with an amplitude of 45% at one instant cannot be distinguished from a peak with an amplitude of 95% at another instant.

As in the previous chapters, unless stated explicitly, the Reynolds and Strouhal numbers were calculated for the step-cylinders using the large diameter, and using the centerline speed in the case of shear flow.

6.1 Step-cylinders – inverted configuration

6.1.1 Uniform flow at Re = 294

Spectral results shown in Figure 37 showed that, in the step region at Re = 294 in uniform flow, peaks at Strouhal numbers of 0.198 and 0.390, corresponding to vortex shedding frequencies from both the large and small cylinders, respectively, were detected in the measured signals.

The wavelet map for y/D = -0.3 is given in Figure 73. The velocity signal at the step was much weaker compared to signals at other spanwise locations (see again Figure 42), likely due to the large inclination of vortices in that region. It was shown in Chapter 5 that the vortices shed at the step location were bent more and more in the streamwise direction, until they formed loops that were oriented perpendicular to the cylinder axes. In those cases, the streamwise velocity component was not affected significantly by the vortex motion, and at times its fluctuation became so weak that it could not be distinguished as a deviation from the average speed of convection.

The velocity signal was clearly modulated in the time-frame shown. During time intervals when the signal exhibited the largest modulation amplitude, the wavelet map showed two simultaneous peaks of comparable amplitude at the two dominant Strouhal numbers. The minimum modulation amplitude of the signal occurred in the same time intervals during which the wavelet transform amplitude was lower than the cutoff value, for example in the ranges 12 s < t < 15 s, and 35 s < t < 37 s. Williamson (1989) showed that vortex splitting occurred at times when the signal modulation amplitude was minimum. This may be due to the large streamwise inclination of the vortices, as mentioned above. Flow visualization showed that vortex splitting occurred when the vortices from different cells were shed completely out-of-phase (see Figure 54). It could

be speculated that, when the modulation amplitude of the signal was maximum, which corresponded to wavelet amplitude peaks at two frequencies simultaneously, vortices in the two cells were shed in-phase, and joined across the cell boundary. Examples of this can be seen in the ranges 27 s $< t <$ 30 s and 41 s $< t <$ 45 s. When the vortices from different cells were only slightly out-of-phase, peaks would occur at one local frequency or the other, as in the ranges 6 s $< t <$ 9 s (peak at the low frequency) and 15 s $< t <$ 25 s (peak at the high frequency).

The amplitude of the peaks at each dominant frequency increased and decreased non-periodically with time, independently of each other. This is consistent with the idea that the vortices shed from each cylinder were not directly influenced by the other vortex street. Long durations when the amplitude peaked at only one frequency might indicate that the cell boundary fluctuated in spanwise position with time, as has been noted in Chapter 5.

The time variation of the local frequency at which the amplitude peaks occurred is plotted in Figure 73c. At instants when two peaks were discernable, both corresponding frequencies were shown for the same instant. The local frequencies varied in a gradual, non-periodic, manner about their means. The lower frequency varied at a slower rate than the higher frequency. Williamson (1996) indicated that the wide frequency band in a Fourier spectrum of non-uniform vortex shedding was likely due to the continuous change in vortex inclination with time, which would change the frequency observed in the measurement direction. It was noted in the flow visualization that the vortex inclination varied slowly with time, which would account for the fluctuations seen in this figure.

In the low-frequency cell near the step, behind the large cylinder, spectral analysis showed that the dominant frequency in this region was lower than the shedding frequency of the other cells. The wavelet map for y/D = -6.4 is shown in Figure 74. This location is at the boundary between cells A and B, so that the Fourier spectra showed peaks at the dominant frequency from both cells, at Strouhal numbers of 0.209 and 0.198, respectively.

The modulation of the signal in Figure 74a was not as obvious at this location as it was closer to the step, but the signal had a much larger oscillation amplitude. The wavelet map (Figure 74b) showed that, in general, amplitude peaks did not occur at the dominant frequencies simultaneously, as in the previous figure. Instead, the amplitude peak at one of the dominant frequencies gradually increased with time to a maximum, diminished, and was followed later by a peak at the other dominant frequency.

The highest amplitudes in the wavelet map also had the widest frequency band, indicating that there was some interaction between vortices with different frequencies. In the ranges centered around 3 s, 35 s, 47 s, 50 s, and 58 s, for example, the amplitude peaked at one of the dominant frequencies, yet the peak had not diminished significantly at the other, slightly weaker, frequency. The presence of multiple frequencies led to the modulation observed in the velocity signal.

The continuous variation in the amplitude of the peaks is likely related to vortex splitting, which is due to different numbers of vortices shed in cells of different frequency over a given time interval. The flow visualization performed at this location showed that parallel shedding at the cell boundary was followed by vortex tilting and eventually vortex splitting (see Figure 59). The cycle was recurring, but, in general, not periodically. There are short durations in the wavelet map for which both the amplitude peak and the

frequency were relatively constant, such as in the range 20 s < t < 27 s, which may correspond to the time between dislocation events, when the cells were in phase and the vortices were shed parallel to each other.

The cyclic nature of the low-frequency cell near the step seems likely to be the cause of the continuous variation in the wavelet peak amplitude and local frequency. The two cells behind the large cylinder became indistinguishable from each other in flow visualization images such as Figure 59a when the vortices were in-phase, and it is possible that the low-frequency cell ceased to exist for short durations. If that was the case, the measurement volume would have been located in the cell farther from the step at some times, and in the low-frequency cell near the step at others. It was shown in Figure 59 that the boundary between these two cells changed spanwise location with time. The higher frequency measured in one cell would be followed by a short duration of vortex dislocations, after which the probe would have measured the lower frequency in the cell closer to the step. If the low-frequency cell ceased to exist for several shedding cycles, the probe would have suddenly measured inside the higher frequency cell once again.

The local frequency at which the amplitude peaks occurred (Figure 74c) varied gradually with time, as in the step region. The amplitude of the frequency fluctuation was about the same as at y/D = -0.3, but the average period between maxima and minima was longer. Lewis and Gharib (1992) found that the time between local frequency minima was equal to $1/(f_A - f_B)$, where $f_A - f_B$ is the beat frequency, and f_A and f_B are the dominant frequencies in the adjacent cells. On average, the period of the local frequency at this location was equal to the beat period of 13.5 s, however, the local period, between *individual* minima, varied considerably.

The wavelet map of a signal at y/D = 1.8, located in cell C, far from the cell boundary, is shown in Figure 75. The signal appeared to be of nearly constant amplitude, with only weak modulation. The wavelet transform amplitude peak was nearly uniform in time over a large frequency band, tapering off over a much wider frequency than in other cases. This indicates that the total energy contained in the vortices shed from the small cylinder was quite large. The local frequency of the amplitude peaks was nearly constant, with semi-regular, short duration jumps, which may be artifacts of the transform due to the low signal data rate.

6.1.2 Uniform flow at Re = 647

At a Reynolds number of 647 in uniform flow, the features of the wavelet map were not significantly affected, except that the amplitude peaks were generally of a shorter duration, which would be expected due to the increased number of vortex dislocations. Figure 76 shows the wavelet map for y/D = -4.85, at the boundary between cells B and C in Figure 31. The amplitude of the signal oscillations was relatively large, and strong modulation could be seen. As in the lower Reynolds number case, the amplitude peaks of the wavelet map (Figure 76b) occurred at the same time interval during which the signal modulation amplitude was at maximum. Each of the amplitude peaks, although narrow along the time axis, was broad in the frequency direction. Lower amplitude peaks generally had a narrower frequency range. The amplitude peaks occurred on average at the beat period of 4.5 s, while the frequencies of individual peaks deviated from the beat period less than at the lower Reynolds number. The local frequency variation of the amplitude peaks (Figure 76c) was similar to the lower Reynolds number case, except that the local period was shorter, as would be expected for a higher speed flow.

The amplitude of the velocity oscillations at the step was very small, and did not show much regularity. The wavelet map at that location did not show any detail, other than some very narrow sharp peaks of very short duration. Most of the amplitudes were below the cutoff of the contour plot. Lowering the cutoff did not increase the visibility of the peaks, and increased the background noise, yielding no additional information. The fast mixing of the flow due to vortex splitting in that region at high Reynolds number likely made the vortices difficult to distinguish from the background flow, at least in the available streamwise velocity signal.

6.1.3 Shear flow at Re = 289

Velocity signals in the low-frequency cell near the step were strongly modulated in the shear flow at a Reynolds number of 289 (Figure 77a). At y/D = -3.9, located at the boundary between cells D' and E' of Figure 30, the Fourier spectrum showed peaks at Strouhal numbers of 0.202 and 0.196, respectively. The wavelet map showed fewer fluctuations in amplitude in the shear flow (Figure 77b), compared to the uniform flow case. The highest amplitude peaks were more uniform in magnitude over longer durations, and appeared with a nearly regular frequency. Immediately following many of the highest peaks, the amplitude dropped quickly with time. The frequency band of the amplitude peaks was approximately the same size as in the uniform flow case.

The local frequency of the peaks showed a fluctuation amplitude of nearly half that in the uniform flow case at this location, although the fluctuation period was about the same (Figure 77c). This indicates that the vortices were likely changing inclination, but by a smaller amount than in the uniform flow. The beat period in this case was 25 s, which was much longer than the observed period.

At the step (y/D = 0.0), signal modulation was stronger, and the signal had a smaller oscillation amplitude than at other spanwise locations (Figure 78a). The wavelet map contained amplitude peaks at the frequency associated with vortex shedding from both the large and small cylinders, at Strouhal numbers of 0.196 and 0.405, respectively (Figure 78b). At this location, the peaks at the lower frequency were higher, and occurred more often, showing that the vortices shed from the large cylinder were not deflected away from the step in this configuration, which had been the case in the uniform flow. The amplitude of the modulation in the velocity signal was maximum at the same time as when the wavelet transform peaked at the two dominant frequencies simultaneously, as at t = 18 s, even though they did not have comparable magnitudes. There were many more time intervals during which no frequency was dominant; at these times, the velocity signal was usually at its lowest amplitude. As in the uniform flow case, the local frequency of the amplitude peaks varied irregularly with time (Figure 78c), which is consistent with the continuous change in vortex inclination at the step.

Behind the small cylinder, far from the step, the shedding frequency did not appear to be affected by the vortices shed from the large cylinder. This was also seen in the spectral analysis and the flow visualization. The wavelet map was similar to the uniform flow case, with little variation in amplitude, and at a frequency that was nearly constant.

6.1.4 Maximum frequency deviations

Comparing the plots of the local frequency of the amplitude peaks in the preceding figures, it can be noted that some showed a larger deviation from the mean than others. Lewis and Gharib (1992) noted that the maximum deviation from the mean frequency increased as the boundary between the two cells behind the large cylinder was approached. The maximum deviation of the local Strouhal number from its time average

was plotted against spanwise distance in Figure 79. The large cylinder was located at $y/D < 0$ in all cases, and the cell boundaries proposed in Section 4.2.3 are depicted on the figure. The largest deviations would be expected to occur at cell boundaries, where amplitude peaks occurred at the two dominant frequencies, or where there were large irregular fluctuations in the velocity signal. The maximum deviation was expected to occur at the step, as the largest difference in frequency was at that location.

At Re = 294 in uniform flow (Figure 79a), the largest deviations occurred in general very close to the cell boundaries, although relatively large deviations also occurred at other spanwise locations. In general, the maximum deviation from the mean frequency decreased between the cell boundaries. At Re = 647 in uniform flow (Figure 79b) the results were more ambiguous, as the maximum frequency deviation occurred not only near the proposed cell boundary at y/D = -5.3, but peaks of similar magnitude also occurred at y/D = -4 and y/D = -6, where there were large fluctuations in the velocity signal. In the shear flow at Re = 289 (Figure 79c), the maximum deviations did not correspond to the cell boundaries, even at the step. According to the spectral analysis, one cell boundary was located at y/D = -4, but it was not well-defined, so the peak is within an adequate error. A large-amplitude deviation also occurred for a larger spanwise distance at y/D = -2, where there was no obvious cell boundary.

6.2 Finite cylinders at Re = 152

Spectral analysis of the finite cylinders at low Reynolds numbers indicated that cellular shedding occurred along the span, with lower frequency cells closer to the tip. A cell of even lower frequency was measured beyond the tip of the cylinder (cell A in Figure 32). Observations using flow visualization, however, could not detect any vortices beyond the tip at the measurement location. A wavelet map (Figure 80) was produced for

the location at the edge of the cell boundary (y/d = 1.2), in order to compare the local frequency f_A to the frequency f_B in the next cell. The velocity signal was very weak, but the wavelet map shows amplitude peaks at Strouhal numbers of 0.078 and 0.130, corresponding to the frequencies in the two cells. Peaks in the wavelet map alternated between one frequency and the other in time, with similar amplitudes, indicating that some low frequency event was occurring around the tip, although it is unclear whether that was a vortex street or an oscillation of the downwash stream over the free end.

Figure 81 shows the velocity signal and wavelet map at y/d = 4.1, within cell B of Figure 32. This signal and wavelet map are typical for locations measured within cells B and C, but far from the cell boundary BC. Compared to the step-cylinders, the amplitude of the peaks was relatively constant, as was the local frequency of the amplitude peaks. The velocity signal had a slightly modulated appearance, although the amplitude of the modulation did not appear to correspond to instants of maximum or minimum amplitude in the wavelet transform.

Approaching cell boundary BC at y/d = 11.1, the velocity signal was highly modulated (Figure 82). Fourier spectra showed peaks at Strouhal numbers of 0.124 and 0.160 at this location. The amplitude peaks occurred at the average Strouhal number of 0.142, and alternated regularly between its highest and lowest magnitudes. The shape of the amplitude peaks, however, was different from those seen behind the other cylinders, as the peaks can almost be traced between one frequency and the other as they varied with time. This is easier to see in Figure 82c, where the variation between the two dominant frequencies was almost regular. As in the case of the step-cylinder, the period of the local frequency variation was on average equal to the beat period of 2.2 s, while the period between individual maxima and minima varied. The amplitude of every

second peak was reduced significantly compared to the preceding peak, which may be an artifact of the low data rate of the velocity signal.

Measurements in the middle of the cells B' and C' in the shear flow showed little difference from the uniform flow cases. The amplitudes of the wavelet maps were nearly uniform, with only slight fluctuations. The local frequencies were also nearly constant.

In the shear flow, the cell boundary B'C' was shifted to $y/d = 12.8$, closer to the tip than in the uniform flow. The signal, wavelet map, and the local frequency of the amplitude peaks (Figure 83) showed similar features to the uniform flow case. The dominant frequencies calculated using the Fourier spectrum occurred at Strouhal numbers of 0.113 and 0.148. Contrary to the uniform flow case, however, the largest amplitudes usually occurred at the dominant frequencies, and not at the average value. The local frequency of the amplitude peaks (Figure 83c) varied regularly between the dominant frequencies, with a period of approximately 16 s. A high-frequency oscillation was imposed on top of this, likely due to a continuous and periodic change in the vortex inclination at this cell boundary.

The local frequency of the wavelet map amplitude peaks at five locations close to the cell boundary, in the range $11.7 < y/d < 14.0$, are plotted together in Figure 84. The regular high frequency variation was present in all signals, but the amplitude increased slightly as the cell boundary was approached from both directions. At $y/d = 11.7$, the local frequency oscillated around the dominant frequency of the lower cell. Closer to the boundary, oscillations around the dominant frequency of the higher cell appeared at regular intervals, but only for short durations. At the boundary, both frequencies were present for nearly equal durations. Beyond the boundary, the higher frequency became dominant, with the lower frequency appearing at regular intervals of shorter duration.

Finally, at $y/d = 14.0$, only oscillations around the higher frequency were visible, and the amplitude of the oscillations began to decrease slightly.

The maximum deviation of the local frequency from its time average is plotted in Figure 85 for the uniform and shear flow cases. Aside from the tip region, where there is a great deal of mixing, the largest deviations occurred at the cell boundaries BC and B'C'. However, large deviations also occurred around $y/d = 3.5$ in both conditions, where no cell boundary can be deduced from spectral analysis.

6.3 Double-step cylinders

6.3.1 Large aspect ratio middle section

Spectral analysis of a small diameter double-step cylinder, with a middle section spanning 10 diameters between the steps, suggested that the frequency dropped slightly in the step regions (cell B' in Figure 34b), as in the single-step cylinder cases. Cells with lower vortex shedding frequencies were also observed behind the large cylinders near the steps during flow visualization (see Figure 68). The signal and wavelet map at the location of lower cell boundary A'B' are presented in Figure 86. Amplitude peaks occurred at each of the two dominant frequencies (St = 0.199 at $t = 8$ s, and St = 0.188 at $t = 17.5$ s, for example), although the small difference in frequency magnitude made it difficult to distinguish between them. The amplitude of the peaks varied gradually and nearly periodically with the beat period of 11.7 s. As in the previous configurations, maxima and minima of the velocity signal modulation amplitude occurred at the same times at which the amplitude peaks of the wavelet maps were also at maxima and minima. Maxima occurred, for example, in the ranges 26 s $< t <$ 30 s, 37 s $< t <$ 42 s, and 48 s $< t <$ 55 s. The amplitude of the wavelet map dropped below the cutoff several times,

but usually reached a minimum value above the cutoff. The local frequency of the amplitude peaks was nearly constant over long durations, followed by sudden variations, which often coincided with sudden drops in the amplitude of the wavelet map.

The wavelet map constructed from the velocity signal at the lower step, cell boundary BC, (y/D = -0.30), is presented in Figure 87. As was the case close to the steps of other cylinders, the velocity signals were weak compared to other spanwise locations, and showed strong modulation. The amplitude peaks in the wavelet map had comparable magnitudes, and occurred at both dominant frequencies, alternately in time. This is in contrast to what was observed in the single-step cylinder case, in which the peaks at the dominant frequencies were usually observed simultaneously. In the flow visualization, the vortices shed from the small cylinder in the middle section were rarely aligned in-phase with those shed from the large cylinders on either side, which is consistent with what is displayed on the wavelet map. The long gaps in the wavelet map, as in the single-step case, are likely the result of the large amounts of mixing and vortex splitting, which weakened the vortices significantly, and rotated them into the streamwise direction.

The velocity signals measured in the middle of the high-frequency cell behind the small cylinder (y/D = 5.2) were weakly modulated (Figure 88). Consistent with the data presented for other cylinders far from the steps, the amplitude of the peak at the dominant frequency fluctuated much less than at other spanwise locations, rarely falling below the cutoff. The local frequency of the amplitude peaks varied with time, indicating a changing vortex inclination.

6.3.2 Short aspect ratio middle section

The small-diameter double-step cylinders with a middle section spanning 2 diameters showed a smaller jump in frequency at the steps (see Figure 34a) than in other cases. The

wavelet maps for the middle of the small cylinder section (Figure 89) generally showed short-duration amplitude peaks, even though a distinct shedding frequency was not observed with the flow visualization. Lower amplitude peaks also occurred at the lower frequency associated with the outer cells (A' and C'), at t = 19 s, 35 s, and 59 s, which is consistent with the flow visualization observations, in which the lower frequency was often identifiable behind the small cylinder.

At the upper cell boundary (y/D = 2.1) amplitude peaks occurred at the frequency from cell C' (Figure 90), along with smaller amplitudes at the higher frequency associated with cell B'. The wavelet map showed that peaks often occurred at the two frequencies simultaneously, though the peak at the higher frequency was almost always of a much smaller amplitude. The local frequency of the amplitude peaks varied continuously and erratically between the two dominant frequencies.

Chapter 7

Discussion

7.1 Effect of a sudden diameter change

The three configurations of cylinders with diameter discontinuities showed similar vortex shedding patterns and frequency variations along their spans. The case with the single step-change in diameter can be used as a reference for the other two cylinder configurations. The flow around the double step-change in diameter, symmetric about the mid-span of the cylinder, showed similar features to the single step-change, at both steps. When the distance between the steps was relatively large, the wakes behind the steps evolved nearly independently of each other, while the interaction between the step flows increased for smaller step-to-step distances. The finite cylinder can be considered similar to a special case of a single-step cylinder, in which the small cylinder has zero diameter, and thus does not cause the flow to spill over the edges toward the large cylinder. The results in this case were remarkably similar to those in the case with two finite diameters, the main difference being an increase of flow over the unobstructed cylinder tip, and streamwise vortices that were rotating in opposite senses to the step-cylinder cases.

7.1.1 Vortex inclination

Even in uniform flow, the vortices shed from all cylinder configurations were observed to be inclined to the cylinder axes. Flow visualization showed that the vortices were not inclined at a fixed angle, but that the inclination varied slowly with time. The inclination may be due to the shear layer between the flows around the different diameter cylinders, combined with the downwash effect over the step or free end. As the flow moved over the sharp trailing edge of the step, it separated and rolled up into the wake of the large cylinder. This "downwash" likely triggered the shedding of a small-cylinder vortex earlier close to the step than away from the step. The same effect likely caused vortices shed from the large cylinder to "stick" to the surface close to the step longer than away from the step.

Williamson (1996) has noted that power spectra at locations where the vortices continuously changed inclination contained peaks that were broader than those at other locations. Spectra behind the single-step cylinders contained both broad and narrow peaks, as shown in Figure 37. The spectral peaks behind the cylinder with a free end (Figure 40) were much more narrow, which is consistent with the lower velocity fluctuation amplitude observed along much of the span in that configuration.

The wavelet maps of many signals showed high-frequency oscillations in both the amplitude of the peaks, and in the local frequency at which the peaks occurred. These oscillations may be due to the continuously varying inclination of the vortices. The oscillations were more regular farther from the steps or tips of the cylinders, and, in most cases, reached maximum amplitude near a cell boundary, as in Figure 84, which may be related to the sudden increase in vortex inclination observed at cell boundaries.

7.1.2 Spanwise deflection of the wake

In every configuration, the flow was deflected over the flat, horizontal part of the step (or tip) and into the wake of the large cylinder (as in Figure 47 and Figure 60). The cylinder wakes were deflected in the direction of the large cylinder, and moved farther away from the steps with downstream distance. At the LDV measurement location, which was five diameters downstream, the wake of the single-step cylinder was deflected by less than one diameter at Re = 304, and by a full diameter at Re = 627 (Figure 30 and Figure 31). The results for the double-step cylinder were consistent with this, as the wake deflection increased with an increase in both flow speed and diameter (Figure 34 and Figure 35). The deflection of the wake at the tip of a finite cylinder was reported by Etzold and Fiedler (1976) using flow visualization, and sketched by Zdravkovich *et al.* (1989) and Tanaka and Murata (1999) based on observations of surface visualization and pressure measurements. Ko *et al.* (1983) also showed that the higher-frequency vortices shed from the small diameter of a single-step cylinder was deflected into the wake of the large cylinder. The flow visualization images by Eisenlohr and Eckelmann (1989), however, show vortices shed from the small cylinder that were deflected toward the large cylinders for only a few diameters downstream, after which the wakes were deflected toward the small diameter middle section farther downstream. This is likely due to the combination of the endplate locations and the short aspect ratio of the large cylinders. It was seen in Figure 68 that the wakes oscillated spanwise behind the double-step cylinder, in which the wake deflection would be away from the large cylinder at one step, but towards the other large cylinder at the opposite step. It may be noted that, in the study by Eisenlohr and Eckelmann (1989), the endplates were located very close to the steps, limiting the amount of deflection that could take place, and probably forced the flow to rebound and become redirected towards the central span.

7.1.3 Constant-frequency cells

As with other configurations in which the Reynolds number varied along the span, such as a uniform cylinder in shear flow, or a tapered cylinder in uniform flow, the discontinuity in diameter induced cellular vortex shedding. Specifically, a cell of lower frequency was observed behind the large cylinder near the step, and near the tip of the cylinder with a free end. Lewis and Gharib (1992) called this the "modulated zone", because the vortex shedding frequency at every location within that region was modulated by the average frequencies in the adjacent cell behind the large cylinder (cell A in Figure 30, for example). The amplitude of the modulation increased as the cell boundary was approached, and they showed that the local frequency varied regularly from one of the dominant frequencies to the other. In the present study, irregular signal modulation was observed near all cell boundaries (see Figure 42), with a decreasing amplitude towards the centers of the cells. Close to the cell boundaries, local frequency analysis within the low-frequency cell near the step showed peak amplitudes at the two dominant frequencies. Near the cell boundary at the step, the two peaks often occurred simultaneously (Figure 73), while at other cell boundaries, the peaks usually alternated between one dominant frequency and the other (Figure 74).

Previous authors have observed modulation in the velocity signals obtained within constant-frequency cells in various cylinder configurations, such as end cells behind a uniform diameter cylinder equipped with endplates (Williamson, 1989), cones in uniform flow (Gaster, 1969), and near the tip of a finite cylinder (Ayoub and Karamcheti, 1982). According to Williamson (1996), vortex dislocations, or splitting, should occur at the minimum amplitude of the modulated signal. This offers an interpretation of the wavelet maps for these signals, in which the lowest amplitudes may coincide with the minimum modulation amplitude in the signal. Conversely, the highest amplitude peaks often

coincided with the maximum modulation amplitude in the signal, which may indicate vortex connections across the cell boundaries.

Papangelou (1992) showed that the spectra at the boundaries between cells contained two or more frequency peaks, constituting a dominant peak with lower sidebands. As the boundary to a cell with higher frequency was approached, the higher sideband would grow stronger and eventually dominate in the next cell. Norberg (1992) found a similar shifting of the spectral peaks into the low frequency region near the step of a single-step cylinder. Velocity spectra at the boundaries to all cells (see Figure 37 to Figure 41) showed a peak representing the dominant frequency in one cell, which decreased in amplitude as another became dominant. The local frequency variation behind the finite cylinder, in Figure 84, shows the switch from one frequency to the next, both in space and in time. Approaching the cell boundary, the amplitude peak occurred more frequently at the lower frequency, but was interrupted regularly by a shorter duration during which the peak occurred at the higher frequency. The durations over which the peaks occurred at either frequency became nearly equal at the boundary, while, in the next cell, the signal had longer durations at the higher frequency.

From wavelet analysis, it was found that many of the largest deviations of the local frequency from the mean value occurred at the cell boundaries, as shown in Figure 79 and Figure 85. However, this cannot be used as a tool for detecting cell boundaries, as large frequency variations could also be observed in velocity signals in areas of strong mixing, for example within cells next to the endplates.

When the difference in shedding frequencies was large, as at the steps, the different cells could be discerned by eye in flow visualization, as in Figure 47. At other locations, the boundaries could only be observed when the vortices were largely out-of-phase, and

gaps formed when vortex splitting occurred. The ends of the vortices were often inclined oblique to the axes of the cylinders at the cell boundaries, and formed complex connections before and after splitting.

Cell boundaries were observed to drift spanwise by several diameters immediately before vortex splitting occurred (see Figure 51). This leads to an uncertainty in the exact location of the boundary. The wavelet maps near the cell boundaries reflect this uncertainty. Figure 73c, for example, shows the variation of the local frequency with time. Peaks occurred at the higher frequency for long durations, while the peaks at the lower frequency appeared for short durations almost regularly. This implies that the high-frequency cell was dominant at this location, but that vortices from the low-frequency cell occasionally appeared at the same location. Flow visualization has shown that this was a likely occurrence immediately before vortex splitting occurred.

The spectra at the cell boundary near the step looked similar to those at any other cell boundary, the only difference being the wider separation of the peaks, at the two dominant frequencies. As at the other cell boundaries, the peak at one frequency would recede as the measurement location was moved along the span, while the peak at the next frequency would become dominant. The local frequency at the step location, as computed by the wavelet transform, alternated irregularly with time from one value to the other. The amplitude of the peaks in the wavelet map also varied with time, but the peaks often occurred at the dominant frequencies with comparable amplitudes at the same instant. When studying a single-step cylinder, Ko and Chan (1984) noted a relatively wide spectral peak near the step behind the large cylinder, which they attributed to the "leading-edge-type" vortex shed from the step. It is likely that their spectra did not have the resolution to identify the double-peak signifying the difference between the frequencies in the two cells at this location.

7.1.4 Vortex splitting and looping

Near the boundaries of cells in which the average shedding frequencies were different, vortex splitting and looping appeared to connect vortices across the cell boundaries such that they would not terminate in the fluid. However, as Williamson (1989, 1992) pointed out, this phenomenon is not as simple at it seems at first glance. Several authors (Yagita *et al.*, 1984, among others) have reported seeing a Y-shaped connection across the step using flow visualization. The images typically show large amounts of dye in the flow, however, which can mask the true vortex dislocations. Many vortices from the two cells at the step were connected in-phase across the boundary, forming a single vortex. As a result of the large difference between the frequencies in the two cells, however, most of the vortices in the two cells were shed out-of-phase, with the phase difference changing as time progressed.

As described by Williamson (1992), a local disturbance, such as a larger-diameter ring, can cause part of the vortex to lag behind the rest of it, leading to high vortex curvature (see Figure 4). Some sections of the vortices in his study were bent into the streamwise direction, and often stretched nearly back to the cylinder surface. The vortices were most likely to split at these locations. Flow visualization of a double-step cylinder, which was a small diameter cylinder of length $1D$, flanked by two cylinders of larger diameter, showed very similar vortex shedding features (Figure 72). In both configurations, the sudden discontinuities caused vortex splitting, and streamwise disturbances in the vortices shed from the outer cylinders. Yet the middle sections were sufficiently short that, although the frequency jumps at the discontinuities were fairly large, vortices that were obviously shed from the middle cylinders could not be observed.

The single-step cylinders were not influenced by changes in the aspect ratio in the region of interest. For a vortex shedding frequency ratio of nearly 2, it could be expected that one vortex from the low-frequency cell would connect with two vortices from the high-frequency cell, thus forming the Y-shaped pattern. Although vortex splitting of this sort occurs at the boundaries between cells with a small difference in frequency behind uniform diameter cylinders (Williamson, 1989), the streamwise vortices formed at the sharp edges of the step complicated the flow by twisting the shed vortices in a helical manner, slowing them down and causing them to lag behind. The streamwise sections became thinner as they were stretched downstream, and eventually grew too thin to see. When vortices in the two cells were out-of-phase, those shed in the high-frequency cell behind the small cylinder twisted the streamwise vortices into the same sense (see Figure 46c), which then turned by 180°, to eventually connect with the next consecutive vortex, shed from the opposite side of the cylinder. The low-frequency vortices simply curved around the looping pair on either side, and connected across the step, though not always perfectly in-phase. Based on the appearance of Figure 54, one may incorrectly conclude that a Y-shaped connection could be traced between vortices e, f and e'. Such interpretations are particularly likely when only vortices shed from one side of the cylinder are visible in the images. When loops connect vortices on opposite sides of the cylinder, visualization from only one side would miss half of the looped pair.

In the case of the finite cylinder, in which no vortices were shed beyond the tip, all connections of the spanwise vortices were made with the streamwise vortices shed from the sharp edges of the flat surface. When inclined in the same direction, the streamwise vortices had a rotation in the same sense as the shed vortices on the same side of the cylinder, and could connect end-to-end. This case was similar to the single-step cylinder at very low Reynolds number, where only the large cylinder was shedding vortices,

except that those vortices were rotating in the opposite sense to the streamwise vortices, and formed cusp-like connections. In both cases, however, the result was a low-frequency region similar to the "modulated zone" behind the single-step cylinder at higher Reynolds numbers. The actual observed pattern of vortex interactions is more complicated than that implied by the sketch of the inclined horseshoe-shaped vortices by Tanaka and Murata (1999), who concluded that the streamwise vortices had little effect on the rest of the flow.

7.2 Effect of Reynolds number

In the relatively low Reynolds number range studied, the Strouhal number varies with the Reynolds number. As with uniform vortex shedding results (see Figure 2), the Strouhal number increased in all cells as the Reynolds number was increased (compare Figure 28 and Figure 29, for example), for all of the cylinder configurations in this study.

The amplitude of the wavelet map peaks fluctuated more quickly at the higher Reynolds number compared to the lower Reynolds number case tested. In the low-frequency cells near the step, the peaks in the wavelet map at higher Reynolds number were generally of very short duration, rising to a maximum, then falling suddenly below the cutoff threshold (Figure 76). At the step, vortex dislocations and general mixing of the flow was significantly greater than at the lower Reynolds number. The amplitude of the streamwise velocity fluctuations was very small compared to other spanwise locations, and the associated peaks in the power spectra and wavelet maps had very low amplitudes.

At higher Reynolds numbers, the region affected by the downwash from the flat surface of the step (or tip, in the case of the finite cylinder) became larger. This is most obvious in Figure 60, but the effect of the downwash can also be seen in the deflection of

wakes in plots of the spanwise peak frequency variation. At Re = 304, as mentioned in Section 7.1.2, the wake of the step-cylinder was deflected very little in uniform flow conditions, but at Re = 627, the wake at the measurement location was deflected towards the large cylinder by almost a full diameter. Behind the finite cylinder, shed vortices were detected much closer to the tip at Re = 74 (Figure 32) than at Re = 152 (Figure 33).

The relative lengths of the cells observed behind the cylinders changed with Reynolds number, although the number of cells did not. In general, the cells farther from the steps (or tips) increased in length, while the lengths of cells near the steps (or tips) decreased. Norberg (1992) reported that the low-frequency cell near the discontinuity of a single-step cylinder decreased in spanwise length with increasing Reynolds number. That cell was observed to decrease in length in both the upright configuration (Figure 28 and Figure 29), and in the inverted configuration (Figure 30 and Figure 31).

7.3 Effect of freestream shear

The free stream shear flow created disturbances in the vortices shed by all of the cylinders, forming many more longitudinal "fingers", as shown in Figure 48, especially behind the large cylinder, which was at a larger local Reynolds number.

Similar to observations in the case of a uniform cylinder in shear flow (e.g., Rooney and Peltzer, 1981), additional cells of constant frequency were observed to form behind each of the cylinders. Qualitatively, the result of the shear flow on the step-cylinders appears to be a superposition of the effect of shear flow on uniform cylinders and the effect of diameter change in uniform flow. Far from the step, the wake of each cylinder resembled a uniform cylinder in shear flow, as the vortices were shed in cells of constant frequency, with a sudden jump in the shedding frequency across the cell boundaries. As in the case of a step-cylinder in uniform flow, a low-frequency cell could be observed

behind the large cylinder near the step. The frequency *drop* was apparent compared to the sudden *increase* in frequency between the other cells in the shear flow.

The length of the low-frequency cell near the step was changed with the application of the shear. This may be the result of a shifting of the cell boundaries due to the shear, or it could be due to the change in the local Reynolds number. Figure 32 shows that the cell boundaries near the tip of the finite cylinder were shifted spanwise away from the tip in the shear flow compared to the uniform flow. Near the discontinuity of the step-cylinders, the cell boundaries farthest from the step, behind the large cylinder, were shifted by a larger amount than those closest to the steps, which were likely limited by the much higher frequency jump at the discontinuities. In the upright configuration, therefore, the length of this cell was increased, while, in the inverted configuration, the length was reduced. However, in the upright configuration, the low-frequency cell was located in slower moving fluid compared to the uniform flow case, resulting in a lower local Reynolds number, while the opposite was true of the inverted configuration. As noted in the previous section, the cell lengths close to the steps decreased at higher Reynolds number. Although no LDV measurements were taken in the wake of a finite cylinder in the lower-speed section of the shear flow, flow visualization (Figure 65c) showed that the downwash effect was reduced in that configuration compared to the higher-speed section (Figure 65a). It was therefore concluded that the orientation of the non-uniform cylinders relative to the shear flow was a significant factor in the length of the cells near the discontinuity.

Chapter 8

Conclusions and recommendations for future studies

The objective of this study was to observe and document the effects of step-changes in diameter on the vortex shedding from circular cylinders. Although the present study reproduced some of the trends and phenomena observed by other researchers, it also generated some unique and original results, and documented in more detail phenomena that were previously only studied in passing or were the subject of controversy. Its main strength lies in the combination of high-quality flow visualizations with high-resolution spectral and wavelet analyses.

Velocity spectra showed that a step-change in diameter caused the vortices to be shed in cells of constant frequency, with different frequencies in each cell (also seen by Lewis and Gharib, 1992, and Norberg, 1992). Specifically, a cell with a shedding frequency lower than those away from the step on either side was detected in the near-step region behind the large cylinder. Flow visualization showed that this cell changed size cyclically

time and downstream distance. Wavelet analysis showed that the local frequency varied with time within this cell, confirming that the cell size varied.

Streamwise vortices were observed in the step region, generated by flow around the junction between the large and small cylinders, and by flow spilling over the sharp edges of the step. Both sets of these vortices interacted with the vortices shed from the small cylinder, though the junction vortex was not observed downstream due to the lack of precipitate in that region. The streamwise edge vortices were turned and twisted so that they formed connections between shed vortices either in adjacent cells or in the same cell.

At the cell boundary close to the discontinuity, the vortices were highly curved, and interacted with the streamwise edge vortices, which led to splitting and looping involving vortices on either side of the step. The shed vortices were disturbed near the step, appearing to slow down, and were bent sharply into the streamwise direction. The curving and slowing of the vortices behind the large cylinder near the step can explain the formation of the low-frequency cell that was observed in that region.

This is the first study to describe the effect of shear flow on the vortex shedding patterns in the wake of a step-cylinder. Free stream shear increased the numbers of cells located behind each of the cylinders, and shifted the locations of the cell boundaries. The size of the low-frequency cell near the step decreased in the inverted orientation, while it increased in the upright orientation.

Although Williamson (1996) was the first to study a double-step cylinder, the diameters of his cylinders were only slightly different from each other. In this study, with a diameter ratio $d/D = 0.52$, the aspect ratio of the central section of double-step cylinder affected considerably the properties of the shed vortices. At an aspect ratio of 10, the

vortices near each step appeared to evolve independently of the other, displaying features similar to the single-step case. With a smaller separation of $1D$ between the steps, disturbances from the central section triggered vortex splitting in the wake, although vortex shedding from the central section could not be detected at Re = 118 in the flow visualization. At Re = 294, vortex shedding from the middle section was detected using LDV. Vortices shed in-phase within the cells behind the large outer cylinders connected across the step region, while vortices shed out-of-phase looped around and joined with vortices in the same cell.

In addition to the above contributions, the following conclusions build on, and confirm, previously-reported results.

1. Cellular vortex shedding was observed behind all non-uniform cylinders. Cells with lower frequencies were detected close to the tips of cylinders with free ends.
2. Streamwise vortices were generated through flow separation and roll-up from the edges of the flat steps or tips, leading to vortex loops in those regions.
3. Spectral peaks occurred at multiple frequencies within the low-frequency cell near the steps of the step-cylinders. The signal was modulated by the dominant frequencies in the adjacent cells. Wavelet analysis showed that peaks at multiple frequencies could occur simultaneously or alternate in time.
4. The formation of cell boundaries was characterized by a sudden vortex inclination, which travelled spanwise with each subsequent vortex, until a disturbance formed, and the vortices were split between one cell and the next. The vortex ends rotated in the streamwise direction, weakly forming loops with the next vortex in the same cell, but shed from the opposite side of the cylinder. A small gap was visible at the cell

boundary where the vortices split. The cell boundaries could be detected using power spectra of the velocity signals, in which peaks occurred at the dominant frequencies of both cells. The amplitude of one peak was reduced approaching the cell boundary, as the next peak increased. On the other side of the cell boundary, the peak at the new frequency became dominant, while the previous peak disappeared.

5. Vortex splitting and looping was observed more often at the step than elsewhere, because of the larger difference between frequencies in the two cells. The disturbance caused by the step, and helical twisting by the streamwise vortices, aided in the formation of loops between subsequent vortices within the same cell.

6. Fourier spectra showed that the high-frequency vortices shed from the small cylinder were detected behind the large cylinder, at a distance that depended on Reynolds number. The wakes were observed to deflect towards the large cylinder, with a larger deflection farther downstream. Behind two symmetric steps, the wake of the central section was alternately deflected towards one large cylinder or the other.

7. Free stream shear increased the numbers of cells and shifted cell boundaries behind cylinders with free ends, as well as those behind the step-cylinders. The size of cells close to the tips decreased, while the size of those farther from the tips increased.

8. The wake deflection behind a cylinder with a free end was larger than in the case of the step-cylinder, due to the larger amount of downwash over the free end, and the streamwise vortices were inclined further compared to the step-cylinder cases. Freestream shear caused the size of the region affected by the downwash to decrease in the lower-velocity range, and increase in the higher-velocity range.

9. Vortices shed from both the large and small cylinders were inclined away from the step, at an angle that changed gradually with time. The addition of free-stream shear increased the vortex inclination.

10. At Reynolds numbers sufficiently low that the small cylinder formed a symmetric wake, vortices shed from the large cylinder were attached to the streamwise vortices by cusp-like connections, which persisted from the cylinder surface far downstream.

In light of the above conclusions, some recommendations for further work on the wakes of circular cylinders with step-changes in diameter can be made.

1. Velocity measurements should be taken behind the step-cylinders at additional Reynolds numbers to document in more detail the effect of Reynolds number on the flow around the step. Specifically, studies should be made at the higher Reynolds numbers achievable in a wind tunnel.

2. The understanding of vortex shedding from the step-cylinder would be enhanced by replacing the abrupt step by a tapered or contoured section. This change is expected to reduce the effect of the streamwise vortices.

3. LDV measurements should be taken with the finite cylinders placed in the lower-velocity region of the shear flow, to observe the change in the cellular regions, and compare them to the flow visualization results in that orientation.

4. LDV measurements should be taken along longer spanwise distances for the double-step cylinders. This would clarify whether low-frequency cells occurred at both steps and whether they were symmetric.

5. The double-step cylinders should be placed in the shear flow to explore the expected asymmetry in vortex shedding patterns near the two steps.
6. Phase maps of wavelet transforms should be studied in order to determine the phase change between the different frequencies at cell boundaries, especially near the step.
7. LDV measurements should be synchronized with the flow visualization, in order to correlate vortex appearance with the properties of the velocity signals.

References

Abry, P., 1997, Ondelettes et Turbulences: Multirésolutions, algorithmes de décomposition, invarience d'échelle et signaux de pression, Diderot Multimedia, Paris

Adrian, R.J., and Yao, C.S., 1987, "Power spectra of fluid velocities measured by laser Doppler velocimetry", Exps. Fluids, 5: 17-28

Anderson, E.A., and Szewczyk, A.A., 1995, "Vortex shedding from a straight and tapered circular cylinder in uniform and shear flow", Proc. Sixth Intl Conf. On Flow Induced Vibration (P.W. Bearman, ed.), London, U.K.: 61-71

Ayoub, A., and Karamcheti, K., 1982, "An experiment on the flow past a finite circular cylinder at high subcritical and supercritical Reynolds numbers", J. Fluid Mech., 118: 1-26

Bailey, S.C.C., Martinuzzi, R.J., and Kopp, G.A., 2002, "The effects of wall proximity on vortex shedding from a square cylinder: 3D effects", Phys. Fluids, 14: 4160-4177

Balasubramanian, S., Skop, R.A., 1996, "A nonlinear oscillator model for vortex shedding from cylinders and cones in uniform and shear flows", J. Fluids and Struct., 10: 197-214

Balasubramanian, S., Haan, F.L., Szewczyk, A.A., and Skop, R.A., 1998, "On the existence of a critical shear parameter for cellular vortex shedding from cylinders in non-uniform flow", J. Fluids and Struct., 12: 3-15

Bendat, J.S., and Peirsol, A.G., 2000, Random Data Analysis and Measurement Procedures, Third Edition, John Wiley & Sons, New York

Budair, M., Ayoub, A., and Karamcheti, K., 1991, "Frequency measurements in a finite cylinder wake at a subcritical Reynolds number", AIAA J., 29: 2163-2168

Budwig, R., and Peattie, R., 1989, "Two new circuits for hydrogen bubble flow visualization", J. Phys. E: Sci. Instrum., 22: 250-254

Chao, Y.C., and Leu, J.H., 1992, "A fractal reconstruction method for LDV analysis", Exps. Fluids, 13: 91-97

Chua, L.P., Liu, C.Y., and Chan, W.K., 1998, "Measurements of a step cylinder", Int. Comm. Heat Mass Transfer, 25: 205-215

Daubechies, I., 1992, Ten Lectures on Wavelets, CBMS-NSF Regional Conference Series in Applied Mathematics, SIAM, Philadelphia, PN

Dauchy, C., Dusek, J., and Fraunié, P., 1997, "Primary and secondary instabilities in the wake of a cylinder with free ends", J. Fluid Mech., 332: 295-339

Davies, M.E., 1975, "The effects of turbulent shear flow on the critical Reynolds number of a circular cylinder", Nat. Phys. Lab. (U.K.), Mar. Sci. Tech. Memo, TM-108

Eisenlohr, H., and Eckelmann, H., 1989, "Vortex splitting and its consequences in the vortex street wake of cylinders at low Reynolds number", Phys. Fluids A, 1: 189-192

Elder, J.W., 1959, "Steady flow through non-uniform gauzes of arbitrary shape", J. Fluid Mech., 5: 355-368

Etzold, F., and Fiedler, H., 1976, "The near-wake structure of a cantilevered cylinder in a cross-flow", Z. Flugwiss, 24: 77-82

Farge, M., 1992, "Wavelet transforms and their applications to turbulence", Ann. Rev. Fluid Mech., 24: 395-457

Farivar, D., 1981, "Turbulent uniform flow around cylinders of finite length", AIAA J., 19: 275-281

Fey, U., Konig, M., and Eckelmann, H. 1998, "A new Strouhal-Reynolds-number relationship for the circular cylinder in the range $47 < Re < 2 \times 10^5$", Phys. Fluids, 10: 1547-1549

Gaster, M., 1969, "Vortex shedding from slender cones at low Reynolds numbers", J. Fluid Mech., 38: 565-576

Gaster, M., 1971, "Vortex shedding from circular cylinders at low Reynolds numbers", J. Fluid Mech., 46:749-756

Gerich, D., and Eckelmann, H., 1982, "Influence of end plates and free ends on the shedding frequency of circular cylinders", J. Fluid Mech., 122: 109-121

Gerrard, J.H., 1966, "The three-dimensional structure of the wake of a circular cylinder", J. Fluid Mech., 25:143

Gordeyev, S.V., and Thomas, F.O., 1999, "Temporal subharmonic amplitude and phase behaviour in a jet shear layer: wavelet analysis and Hamiltonian formulation", J. Fluid Mech., 394: 205-240

Hangan, H., Kopp, G.A., Vernet, A., and Martiuzzi, R., 2001, "A wavelet pattern recognition technique for identifying flow structures in cylinder generated wakes", J. Wind Eng. and Ind. Aerod., 89: 1001-1015

Higuchi, H., Lewalle, J., and Crane, P., 1994, "On the structure of a two-dimensional wake behind a pair of flat plates", Phys. Fluids, 6: 297-305

Holscher, N., and Niemann, H.-J., 1996, "Turbulence and separation induced pressure fluctuations on a finite circular cylinder -application of a linear unsteady strip theory", J. Wind Eng. and Ind. Aerod., 65: 335-346

Host-Madsen, A., and Caspersen, C., 1995, "Spectral estimation for random sampling using interpolation", Signal Processing, 46: 297-313

Hsiao, F.-B., Pan, J.Y., and Chiang, C.H., 1992, "Study of vortex shedding frequencies behind tapered circular cylinders", Bluff Body/ Fluid and Hyd. Machine Interact., ASME, FED Div., 138: 103-112

Hsiao, F.-B., and Chiang, C.-H., 1998, "Experimental study of cellular shedding vortices behind a tapered circular cylinder", Exp. Thermal and Fluid Sci., 17: 179-188

Jordan, D., Miksad, R.W., and Powers, E.J., 1997, "Implementation of the continuous wavelet transform for digital time series analysis", Rev. Sci. Instrum., 68: 1484-1494

Ko, N.W.M., and Chan, A.S.K., 1984, "Pressure distributions on circular cylinders with stepwise change of the diameter", ASME, 84-WA/FE-13

Ko, N.W.M., and Chan, A.S.K., 1990, "In the intermixing region behind circular cylinders with stepwise change of the diameter", Exps. Fluids, 9: 213-221

Ko, N.W.M., Chan, A.S.K., and Kan, S.M., 1983, "Flow behind stepped and tapered coaxial cylinders", Proc. 2nd Asian Cong. Fluid Mech., Beijing, China, 755-760

Ko, N.W.M., Leung, W.L., and Au, H., 1982, "Flow behind two coaxial circular cylinders", J. Fluids Eng., 104: 223-227

Lewalle, J., 1998, "Wavelets without lemmas", VKI Lecture Series, Syracuse, New York

Lewis, C.G., and Gharib, M., 1992, "An exploration of the wake three dimensionalities caused by a local discontinuity in cylinder diameter", Phys. Fluids A, 4: 104-117

Mair, W.A., and Stansby, P.K., 1975, "Vortex wakes of bluff cylinders in shear flow", J. Appl. Math., 28:519-540

Maull, D.J., 1969, "The wake characteristics of a bluff body in a shear flow", AGARD, CP-48, Paper 16, Munich, Germany

Maull, D.J., and Young, R.A., 1973, "Vortex shedding from bluff bodies in a shear flow", J. Fluid Mech., 60:401-409

Merzkirch, W., 1987, Flow Visualization, Second Edition, Academic Press, Inc., Orlando, Florida

Naumann, A., and Quadflieg, H., 1972, "Vortex generation on cylindrical buildings and its simulation in wind tunnels", Flow-Induced Structural Vibrations, Proc. IUTAM / IAHR Symp., Karlsruhe, W. Germany: 730-747

Noack, B.R., Ohle, F., and Eckelmann, H., 1991, "On cell formation in vortex streets", J. Fluid Mech., 227:293-308

Norberg, C., 1992, "An experimental study of the flow around cylinders joined with a step in diameter", 11th Australasian Fluid Mech. Conf., 507-510

Okamoto, T., and Yagita, M., 1973, "The experimental investigation on the flow past a circular cylinder of finite length placed normal to the plane surface in a uniform stream", Bull. JSME, 16: 805-814

Owen, P.R., and Zienkiewicz, H.K., 1957, "The production of uniform shear flow in a wind tunnel", J. Fluid Mech., 2: 521-531

Panton, R.L., 1984, Incompressible Flow, John Wiley & Sons, New York, New York

Papangelou, A., 1992, "Vortex shedding from slender cones at low Reynolds numbers", J. Fluid Mech., 242: 299-321

Powell, J., 1987, "Design of a laser beam line expander", Appl. Optics, 26: 3705-3709

Rooney, D.M., and Peltzer, R.D., 1981, "Pressure and vortex shedding patterns around a low aspect ratio cylinder in a sheared flow at transitional Reynolds numbers", J. Fluids Eng., 103: 88-96

Roshko, A., 1961, "Experiments on the flow past a circular cylinder at very high Reynolds number", J. Fluid Mech., 10: 345-356

Slaouti, A., and Gerrard, J.H., 1981, "An experimental investigation of the end effects on the wake of a circular cylinder towed through water at low Reynolds number", J. Fluid Mech., 112: 297-314

Tanaka, S., and Murata, S., 1999, "An investigation of the wake structure and aerodynamic characteristics of a finite circular cylinder", JSME Intl. J., Ser. B, 42: 178-187

Taneda, S., Honji, H., and Tatsuno, M., 1979, "The electrolytic precipitation method of flow visualization", Flow Visualization: Proceedings of the International Symposium on Flow Visualization, (Tsuyoshi Asanuma, ed.), 1977, Tokyo, Japan, 209-214

Tavoularis, S., 2004, Measurement in Fluid Mechanics, Cambridge University Press, New York, in preparation.

Tavoularis, S., Stapountzis, H., and Karnik, U., 1987, "Vortex shedding from bluff cylinders in strongly sheared turbulent streams", J. Wind Eng. and Ind. Aerod., 26: 165-178

Torrence, C., and Compo, G.P., 1998, "A practical guide to wavelet analysis", Bull. Amer. Meteorological Soc., 79: 61-78

Valles, B., Andersson, H.I., and Jenssen, C.B., 2002, "Direct-mode interactions in the wake behind a stepped cylinder", Phys. Fluids, 14:1548-1551

Williamson, C.H.K., 1989, "Oblique and parallel modes of vortex shedding in the wake of a circular cylinder at low Reynolds numbers", J. Fluid Mech., 206: 579-627

Williamson, C.H.K., 1992, "The natural and forced formation of spot-like 'vortex dislocations' in the transition of a wake", J. Fluid Mech., 243: 393-441

Williamson, C.H.K., 1996, "Vortex dynamics in the cylinder wake", Ann. Rev. Fluid Mech., 28: 477-539

Williamson, C.H.K., 1997, "Advances in our understanding of vortex dynamics in bluff body wakes", J. Wind Eng. and Ind. Aerod., 69-71: 3-32

Wu, J., Sheridan, J., Soria, J., and Welsh, M.C., 1994, "An experimental investigation of streamwise vortices in the wake of a bluff body", J. Fluid Struct., 8: 621

Yagita, M., Kojima, Y., and Matsuzaki, K., 1984, "On vortex shedding from circular cylinder with step", Bull. JSME, 27: 426-431

Yang, P.-M., Mansy, H., and Williams, D.R., 1993, "Oblique and parallel wave interaction in the near wake of a circular cylinder", Phys. Fluids, 7: 1657-1660

Zdravkovich, M.M., 1997, Flow Around Circular Cylinders, Vol 1: Fundamentals, Oxford University Press, New York

Zdravkovich, M.M., 2003, Flow Around Circular Cylinders, Vol 2: Applications, Oxford University Press, New York

Zdravkovich, M.M., Brand, V.P., Mathew, G., and Weston, A., 1989, "Flow past short circular cylinders with two free ends", J. Fluid Mech., 203: 557-575

Zhang, H.-Q., Fey, U., Noack, B.R., Konig, M., and Eckelmann, H., 1995, "On the transition of the cylinder wake", Phys. Fluids, 7: 779-794

Figures

Figure 1: A vortex street behind a circular cylinder at Re = 80. Flow visualization was performed using the electrolytic precipitation method illuminated with a laser light sheet.

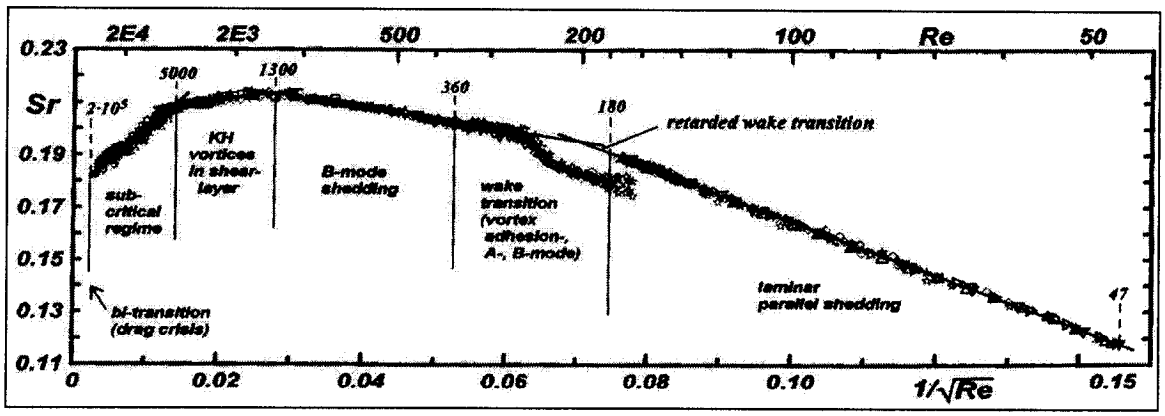

Figure 2: Relationship between Reynolds and Strouhal numbers, reproduced with permission from Fey *et al.* (1998).

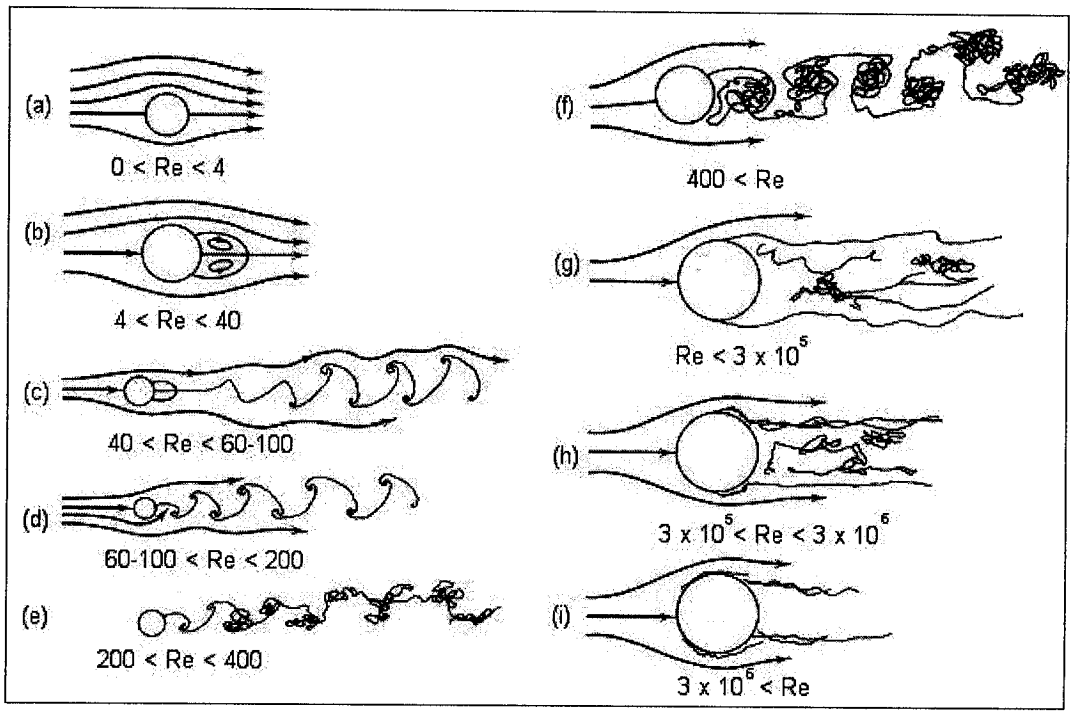

Figure 3: Vortex shedding regimes behind circular cylinders in crossflow, at low to high Reynolds numbers. Reproduced with permission from Panton (1984).

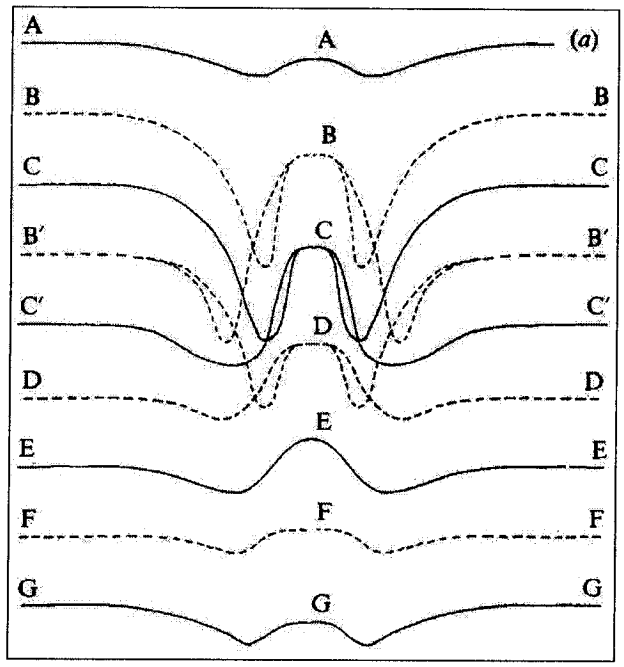

Figure 4: Sketch of vortex loop formation. Loops appear to form between vortices C and C' on the left and right. Reproduced with permission from Williamson (1992).

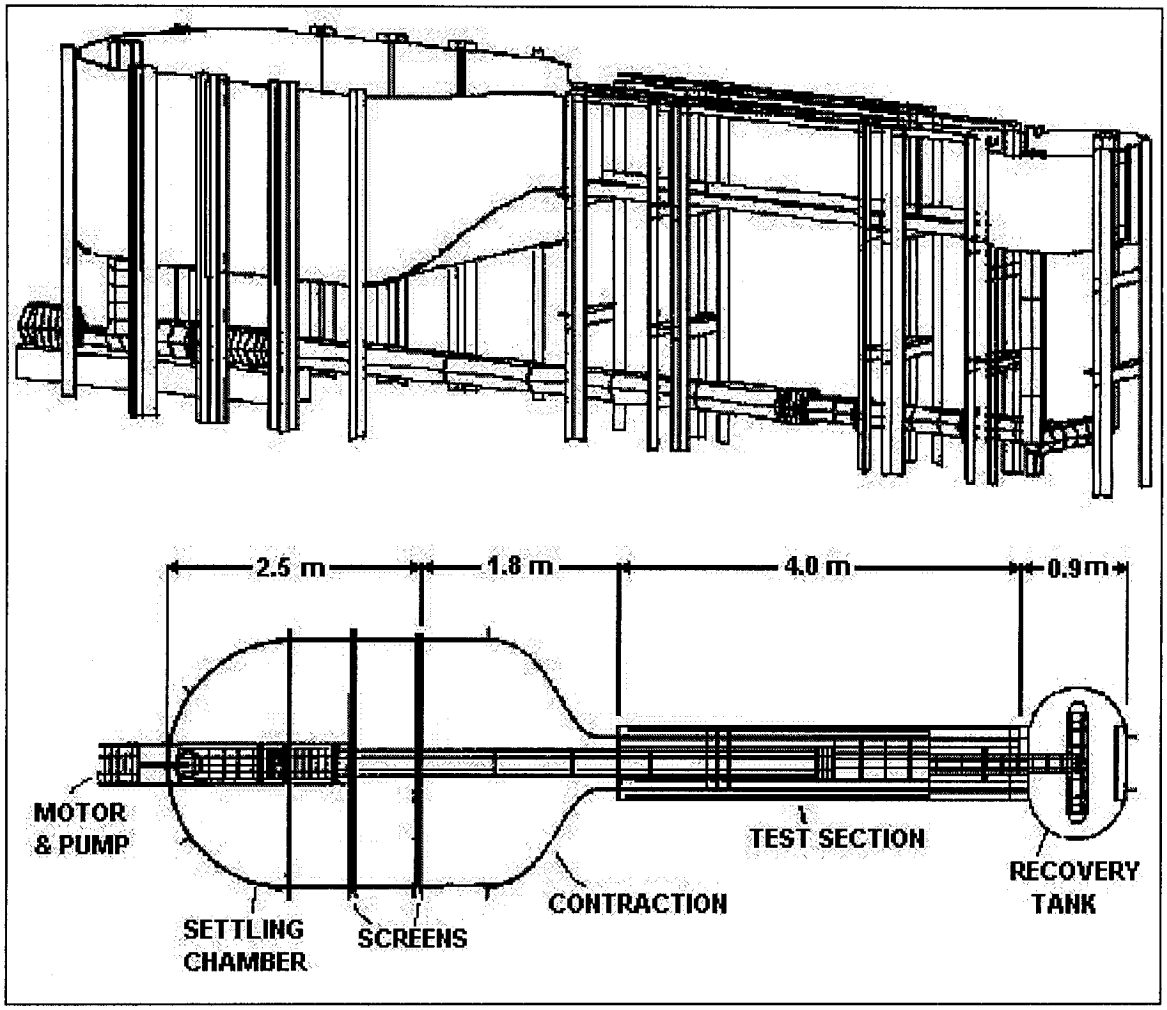

Figure 5: The water channel in the Department of Mechanical Engineering at the University of Ottawa.

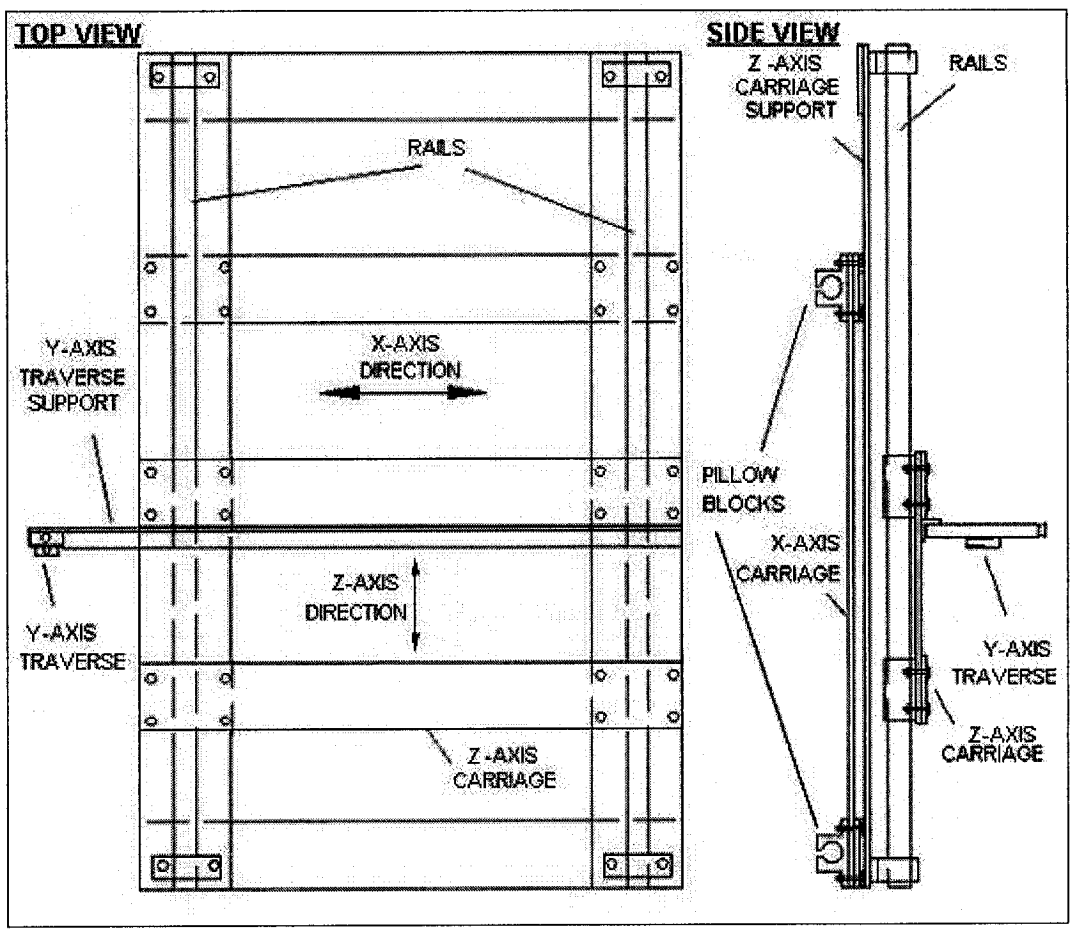

Figure 6: Traverses located above the test section.

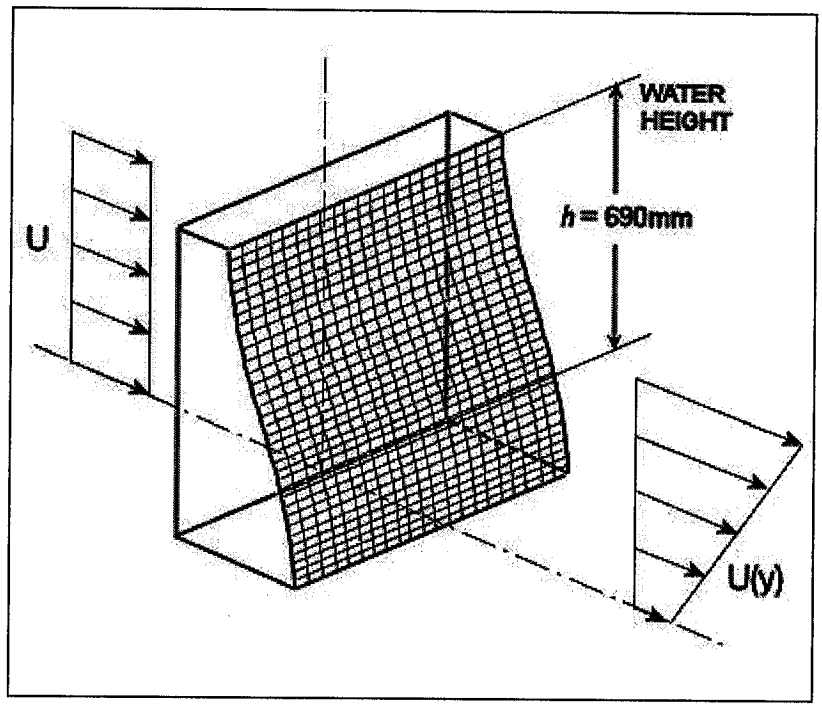

Figure 7: Sketch of the shear generator.

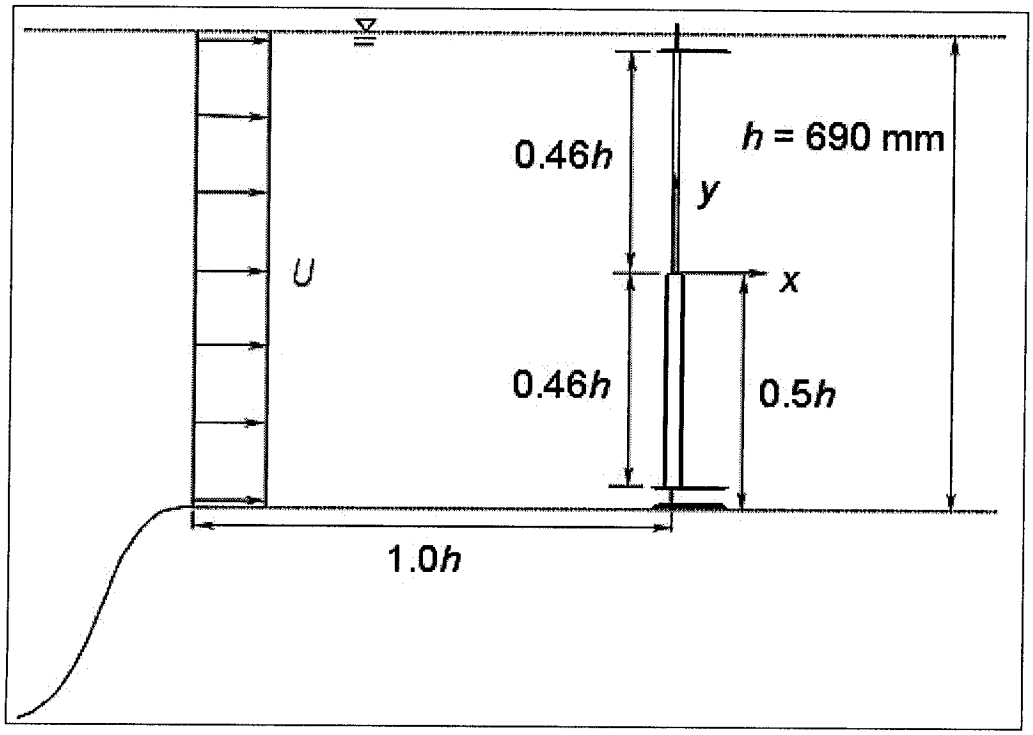

Figure 8:Cylinder layout within the water channel.

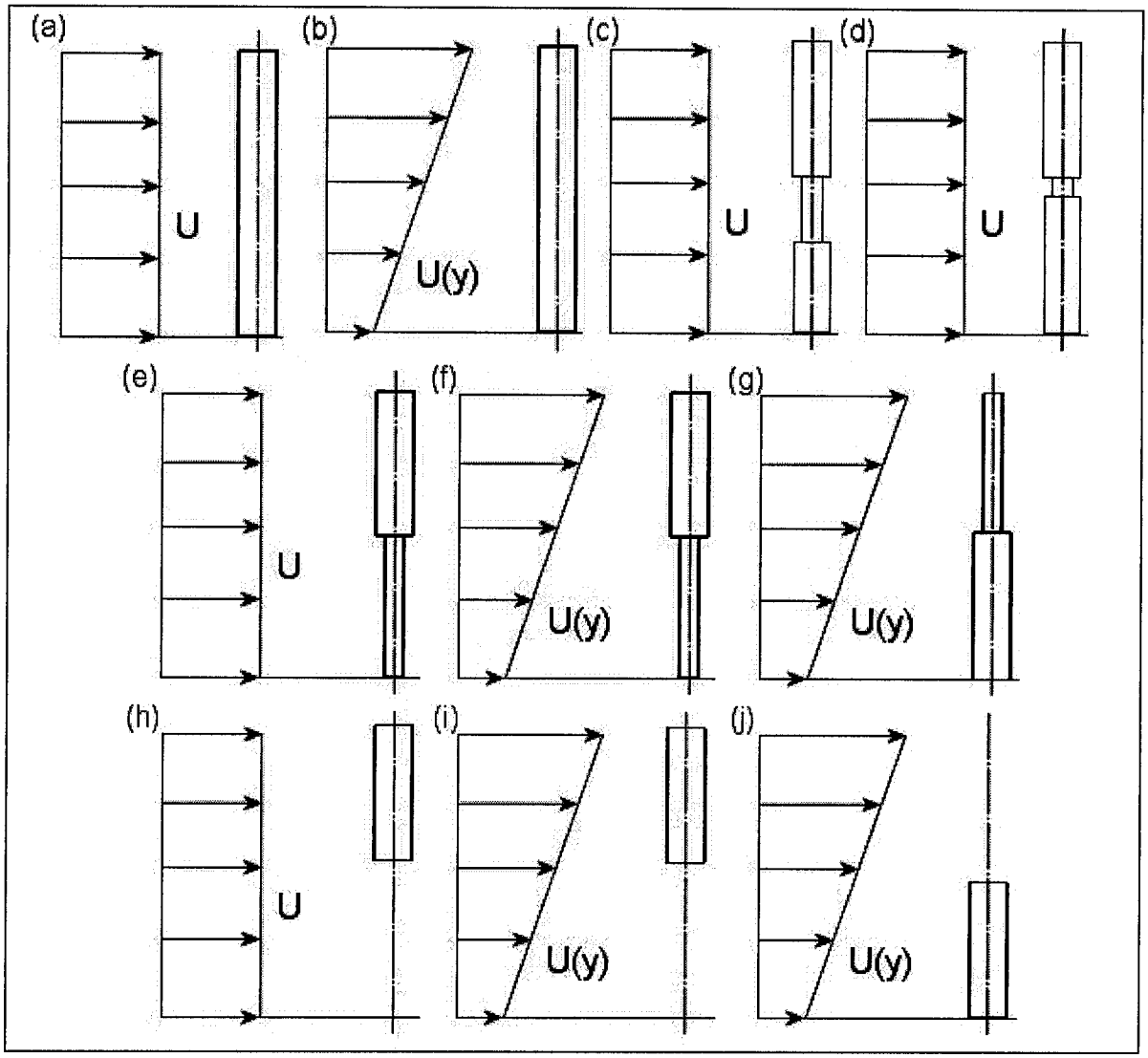

Figure 9: Cylinder configurations. Top row: Uniform cylinder in (a) uniform flow and (b) shear flow. Double-step cylinders with (c) long, and (d) short aspect ratio middle sections. Middle row: Single step-cylinder in (e) uniform flow, (f) upright in shear flow, and(g) inverted in shear flow. Bottom row: finite cylinder in (h) uniform flow, (i) upper portion of the shear flow and (j) lower portion of the shear flow.

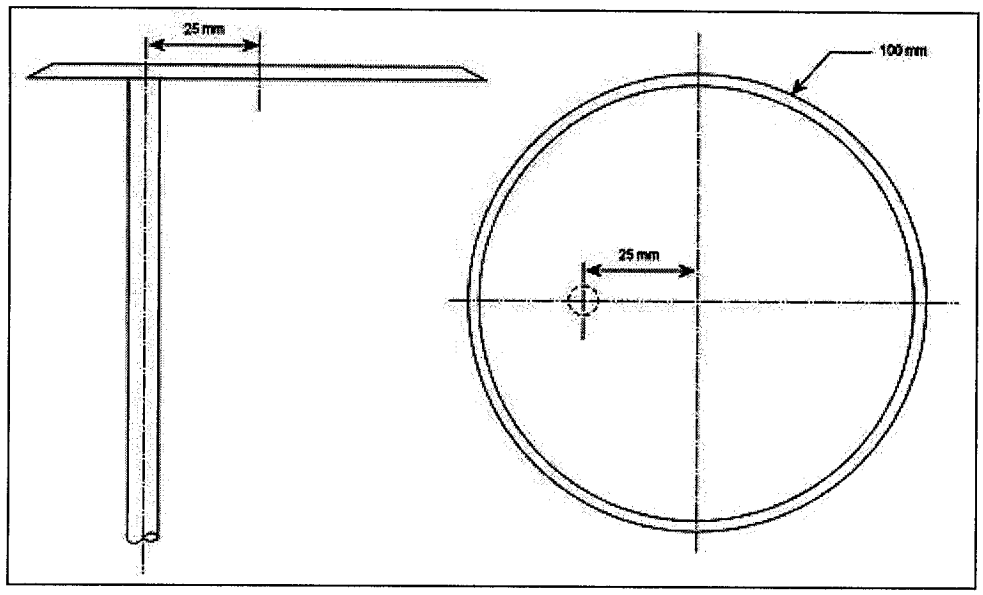

Figure 10: Endplate orientation and dimensions. See Appendix A.1 for details.

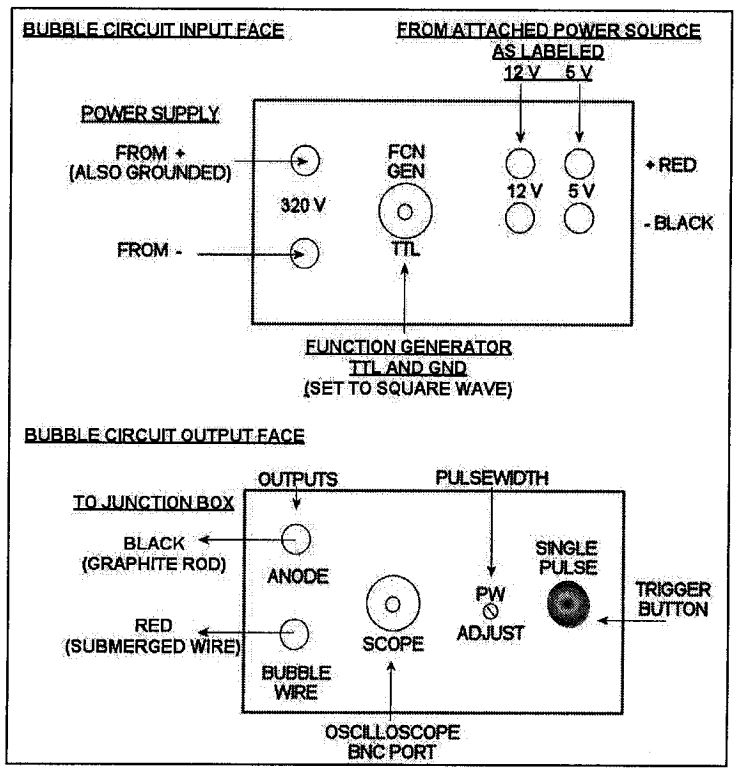

Figure 11: Hydrogen bubble circuit connections.

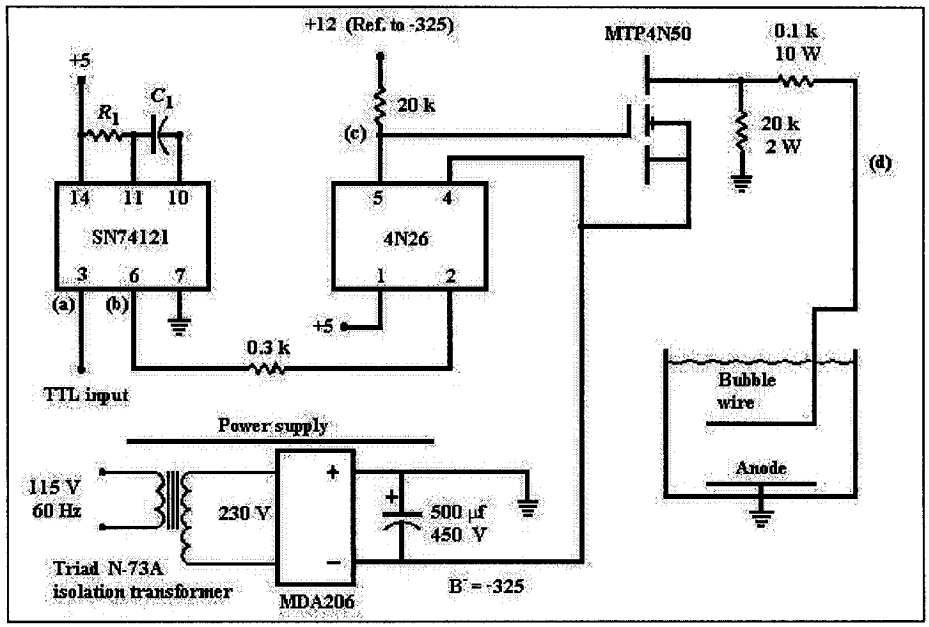

Figure 12: Hydrogen bubble pulsing circuit. Reproduced with permission from Budwig and Peattie (1989).

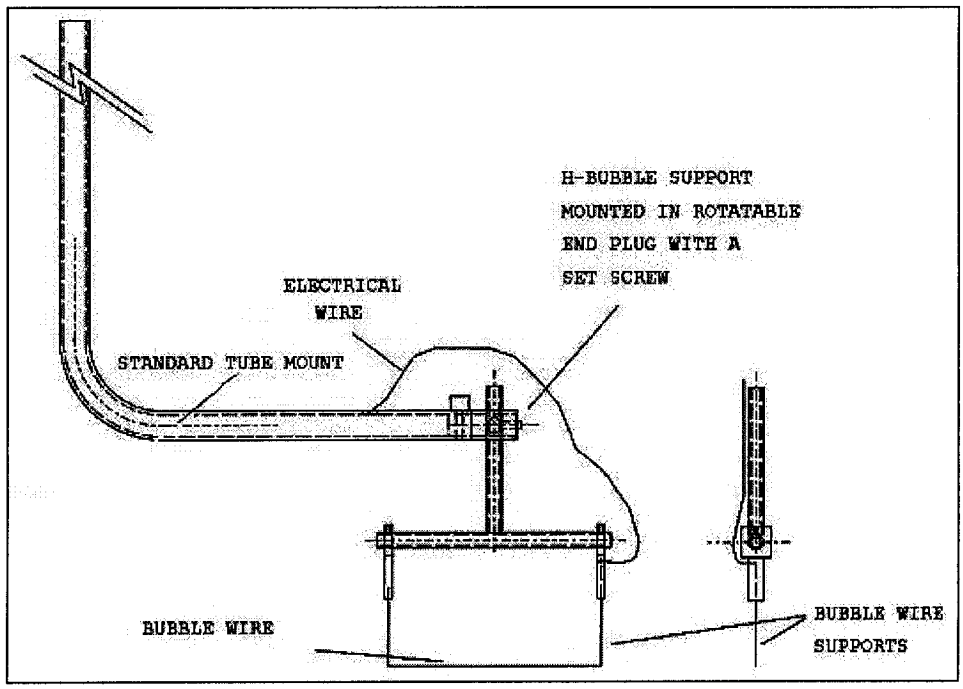

Figure 13: Hydrogen bubble wire and support rods.

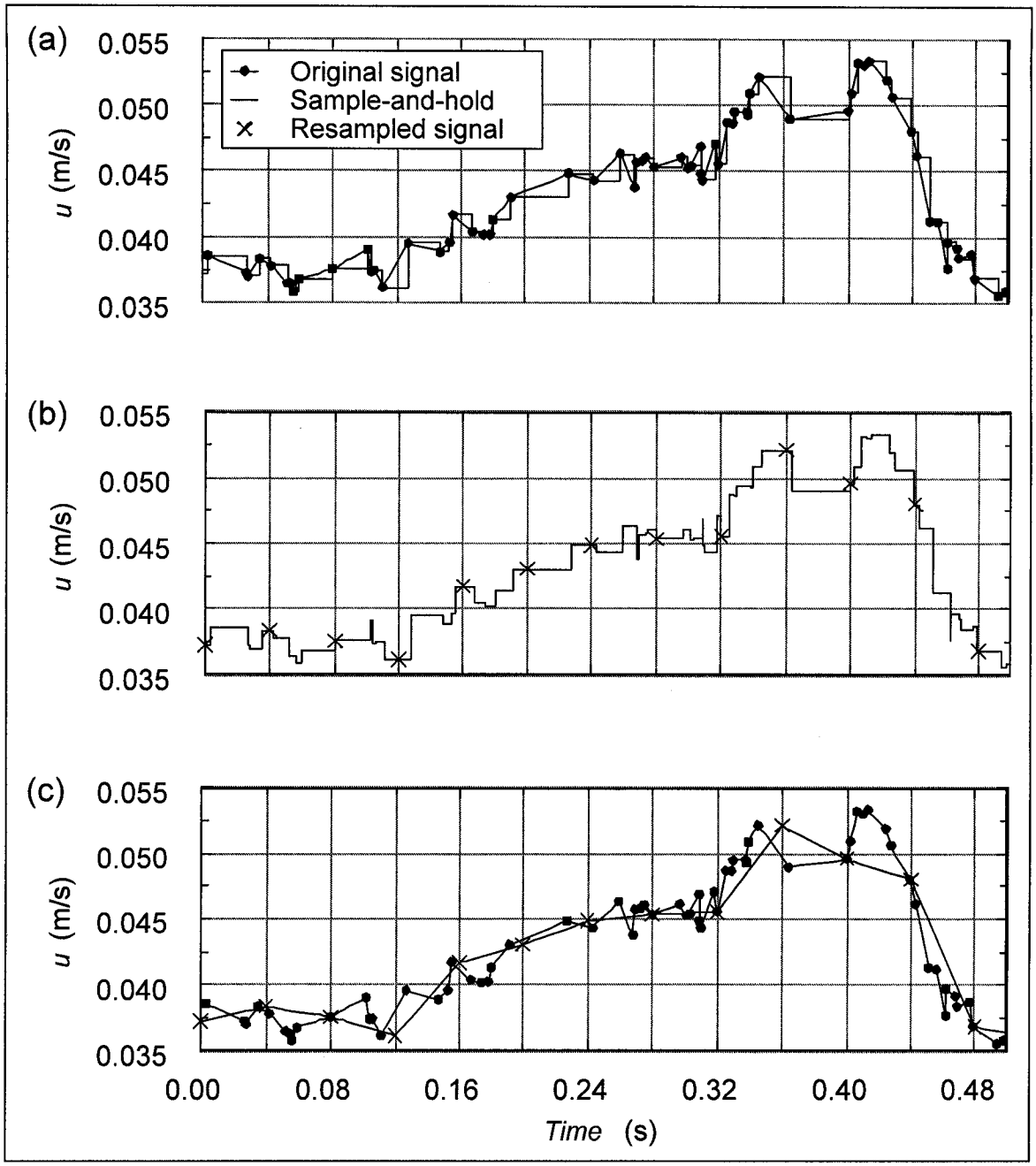

Figure 14: Example of sample-and-hold signal resampling. (a) Each point on the original signal is held constant until the next point is reached. (b) The new signal is resampled at a constant rate. (c) The resampled signal approximates the original signal.

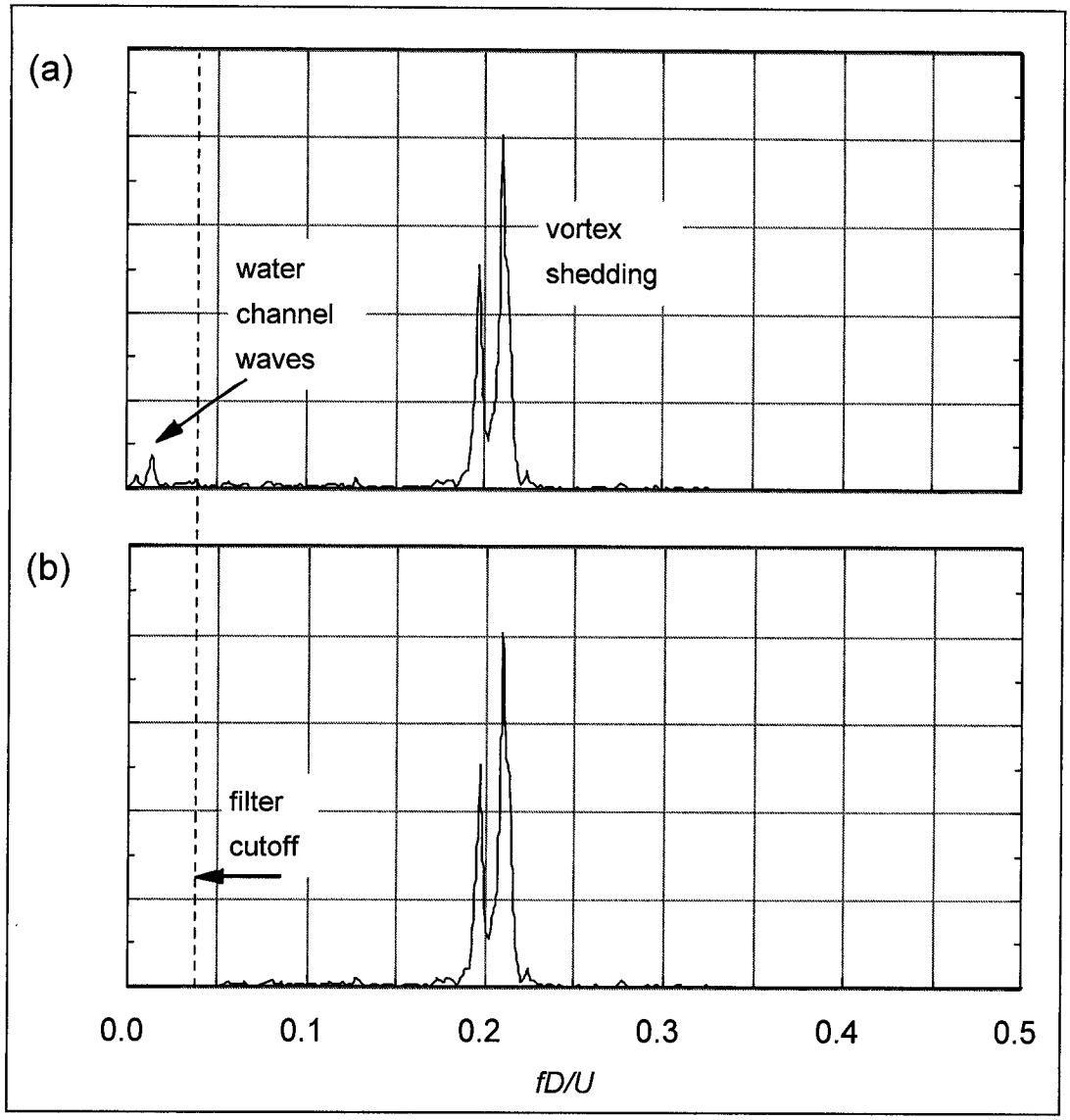

Figure 15: Velocity spectra for the signal presented in Figure 14. The resampling rate was *fD/U* = 3.72 (25 Hz), and the high-pass filter cut-off was *fD/U* = 0.0373 (0.25 Hz).

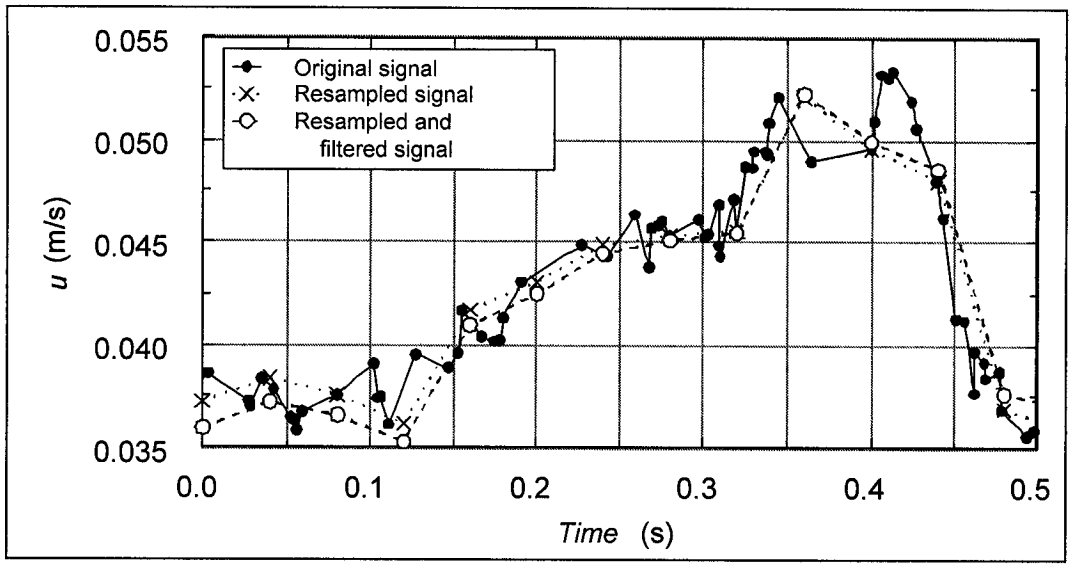

Figure 16: Comparison of the original signal with the resampled and filtered signals presented in Figure 14 .

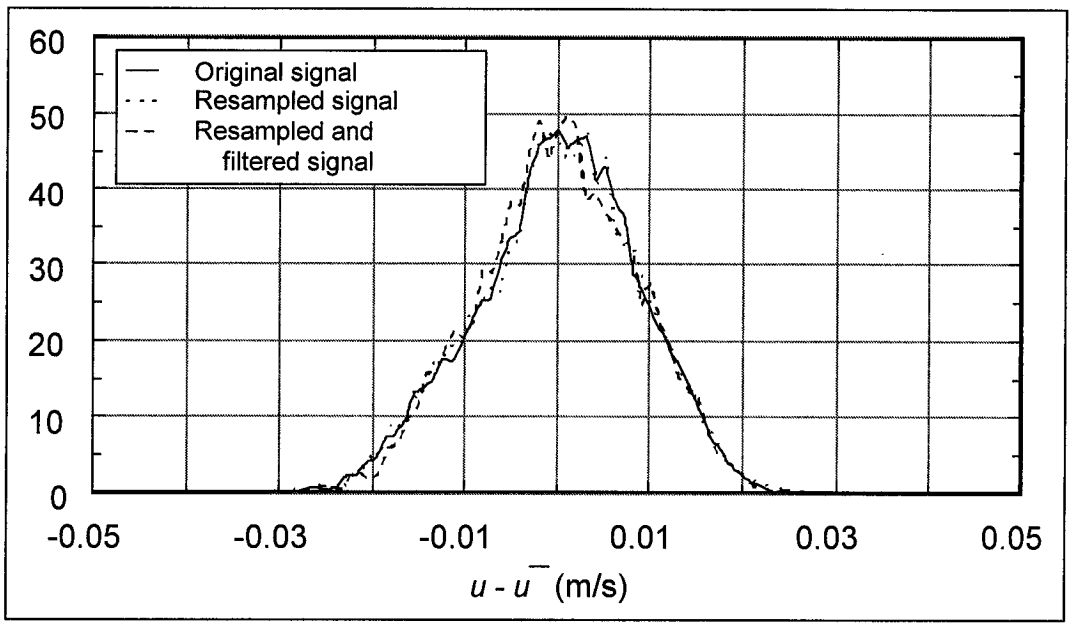

Figure 17: Comparison of the probability density functions for the original, resampled and filtered signals presented in Figure 14.

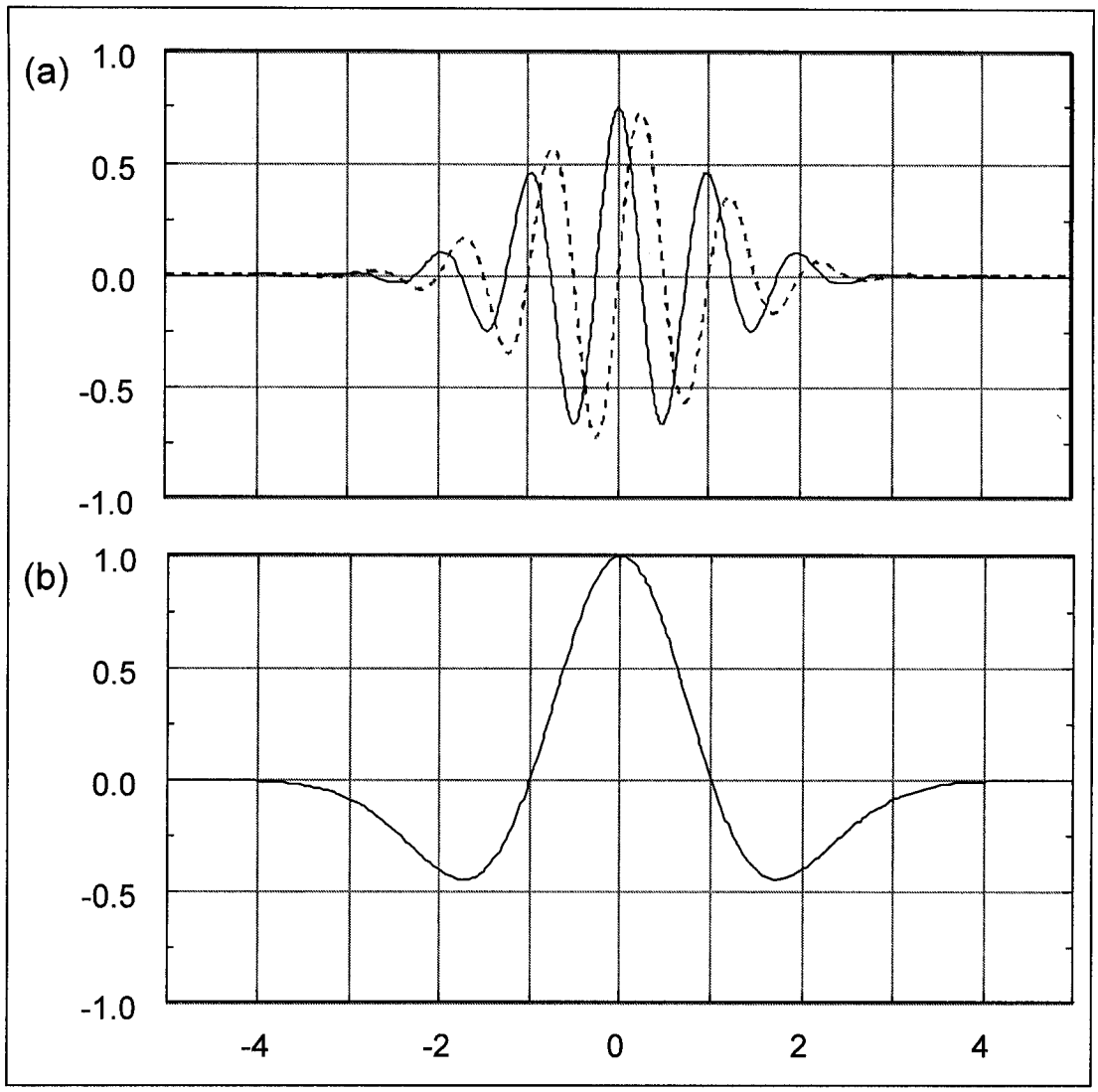

Figure 18: Wavelet shapes. (a) The Morlet wavelet (— real part, --- imaginary part), (b) Mexican Hat wavelet.

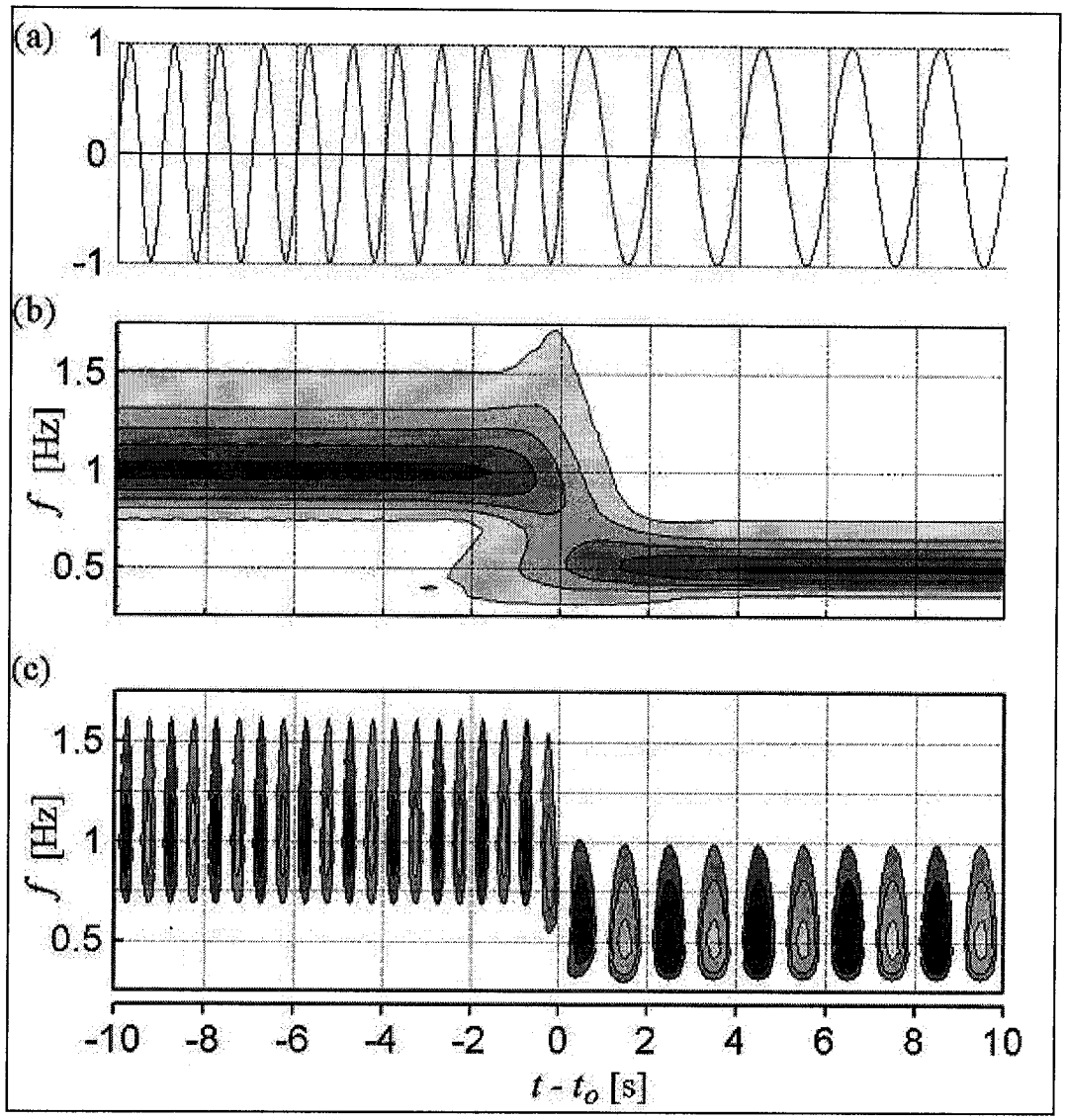

Figure 19: Wavelet transforms of $s(t) = \sin(2\pi f)$, where $f = 1$ for $t < t_o$, $f = 0.5$ for $t > t_o$. (a) Original signal, (b) Morlet wavelet map, (c) Mexican Hat wavelet map.

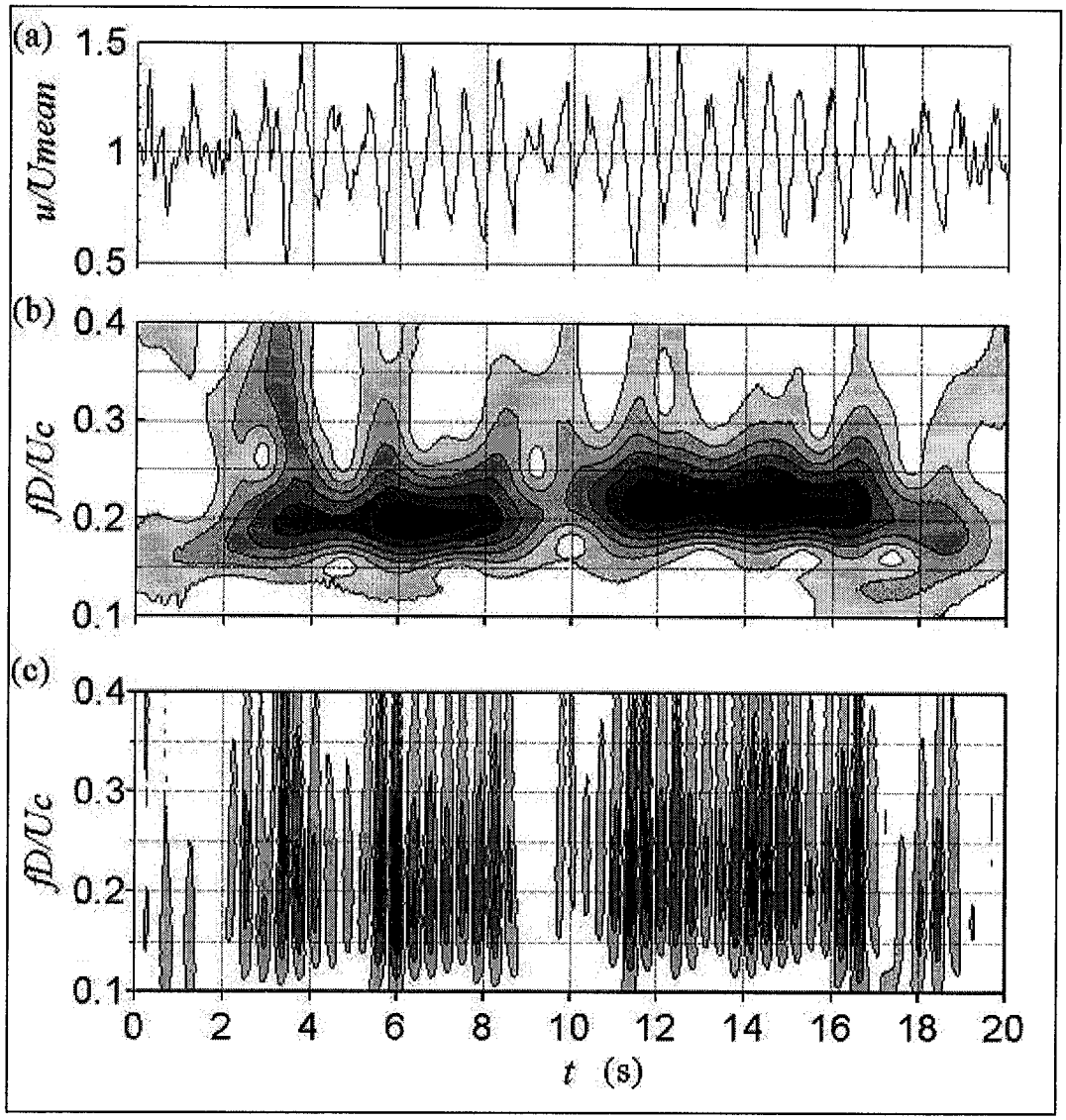

Figure 20: Wavelet transforms of a sample velocity signal from a step-cylinder. (a) Original signal, (b) Morlet wavelet map, (c) Mexican Hat wavelet map.

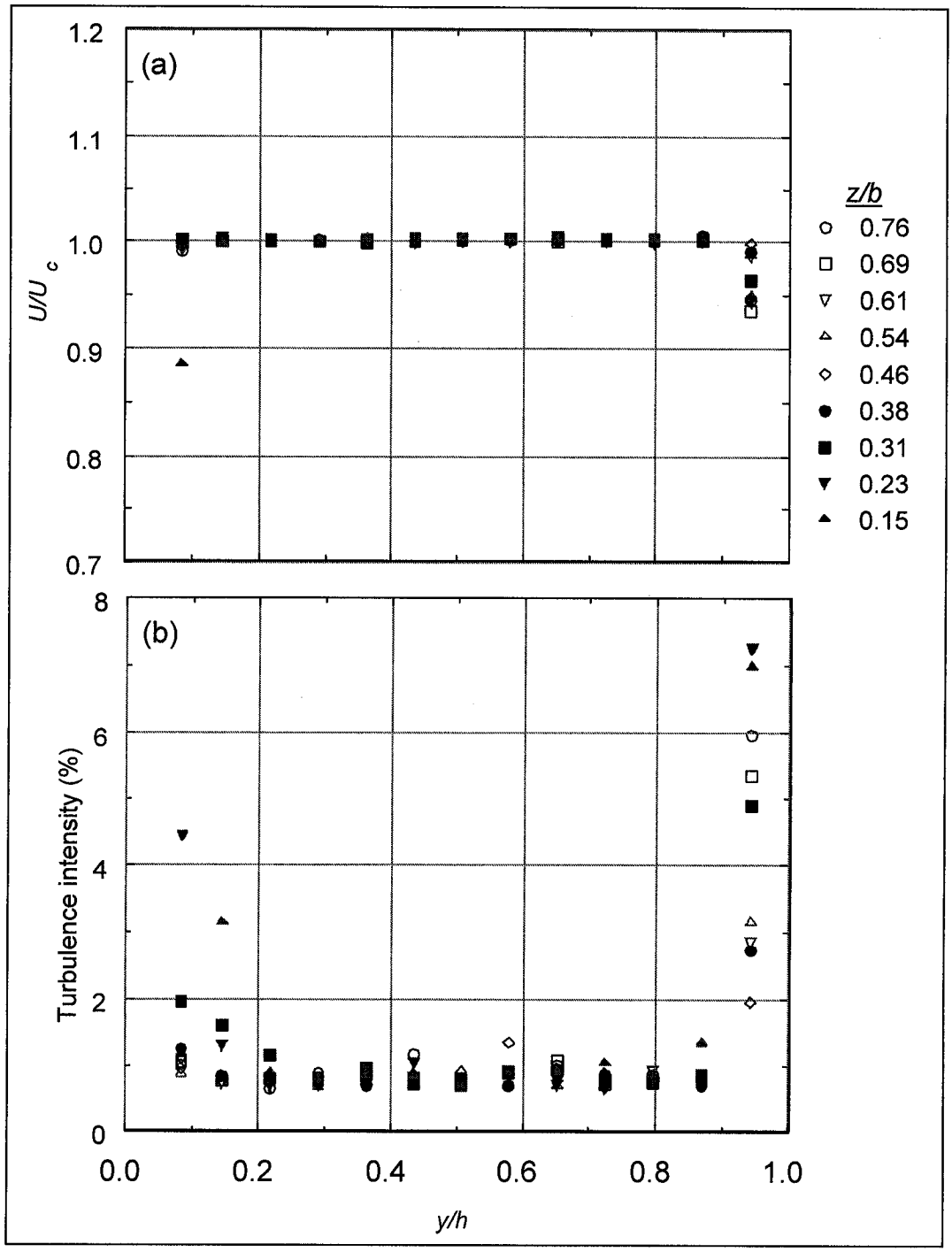

Figure 21: (a) Freestream velocity profile at U_c =95 mm/s and (b) turbulence intensity.

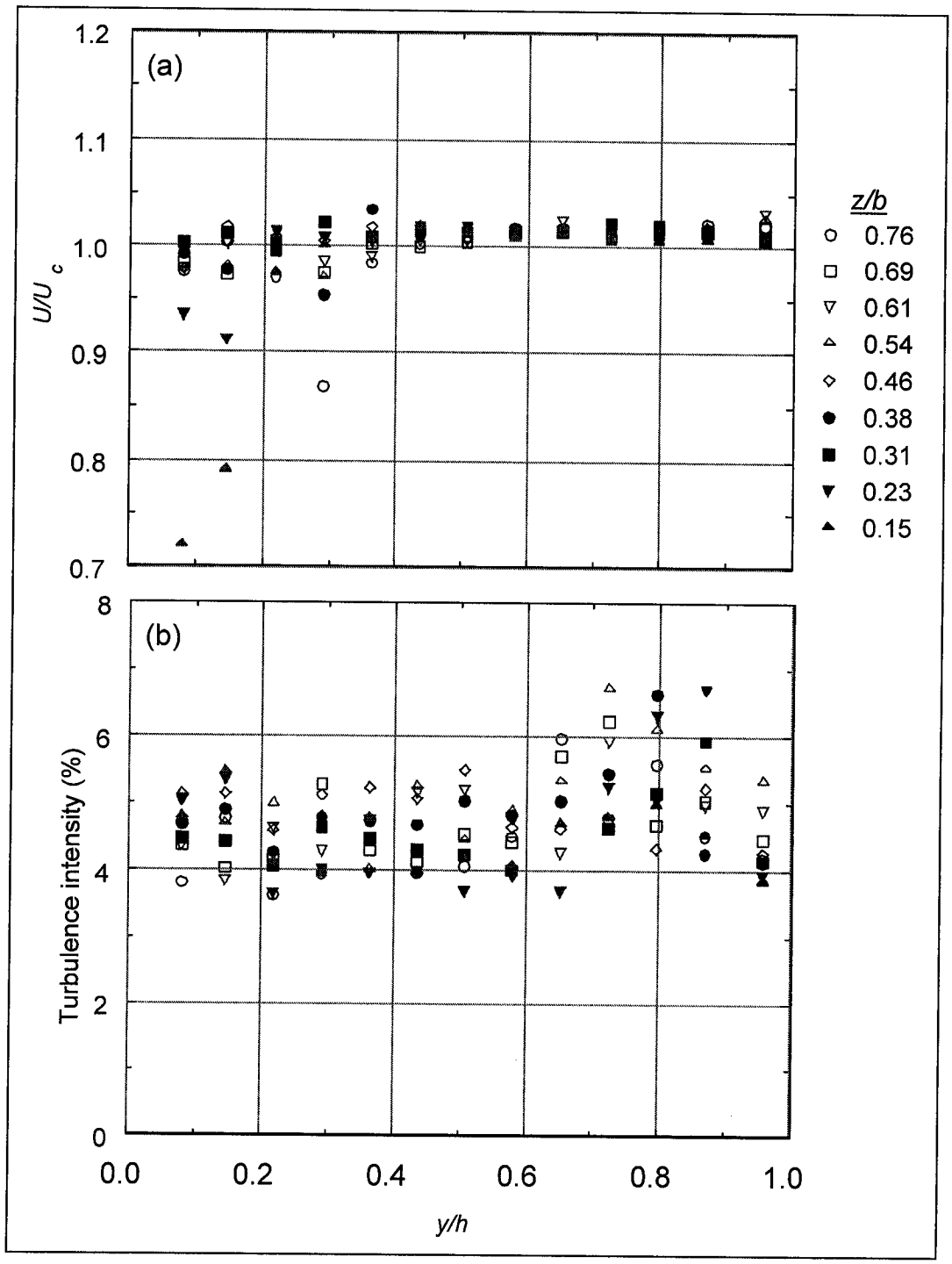

Figure 22: (a) Freestream velocity profile at U_c = 29 mm/s and (b) turbulence intensity.

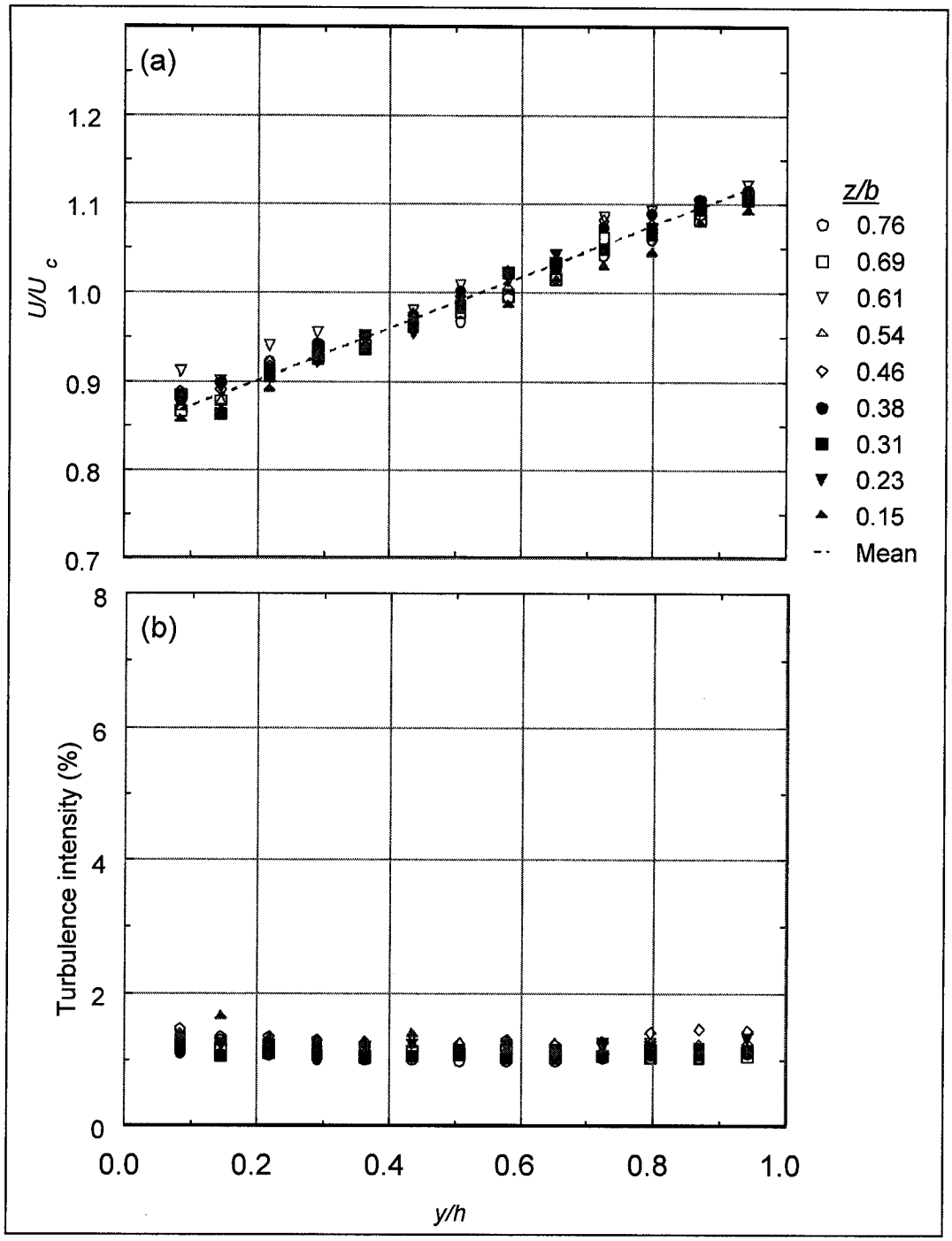

Figure 23: (a) Shear velocity profile at U_c = 95 mm/s and (b) turbulence intensity.

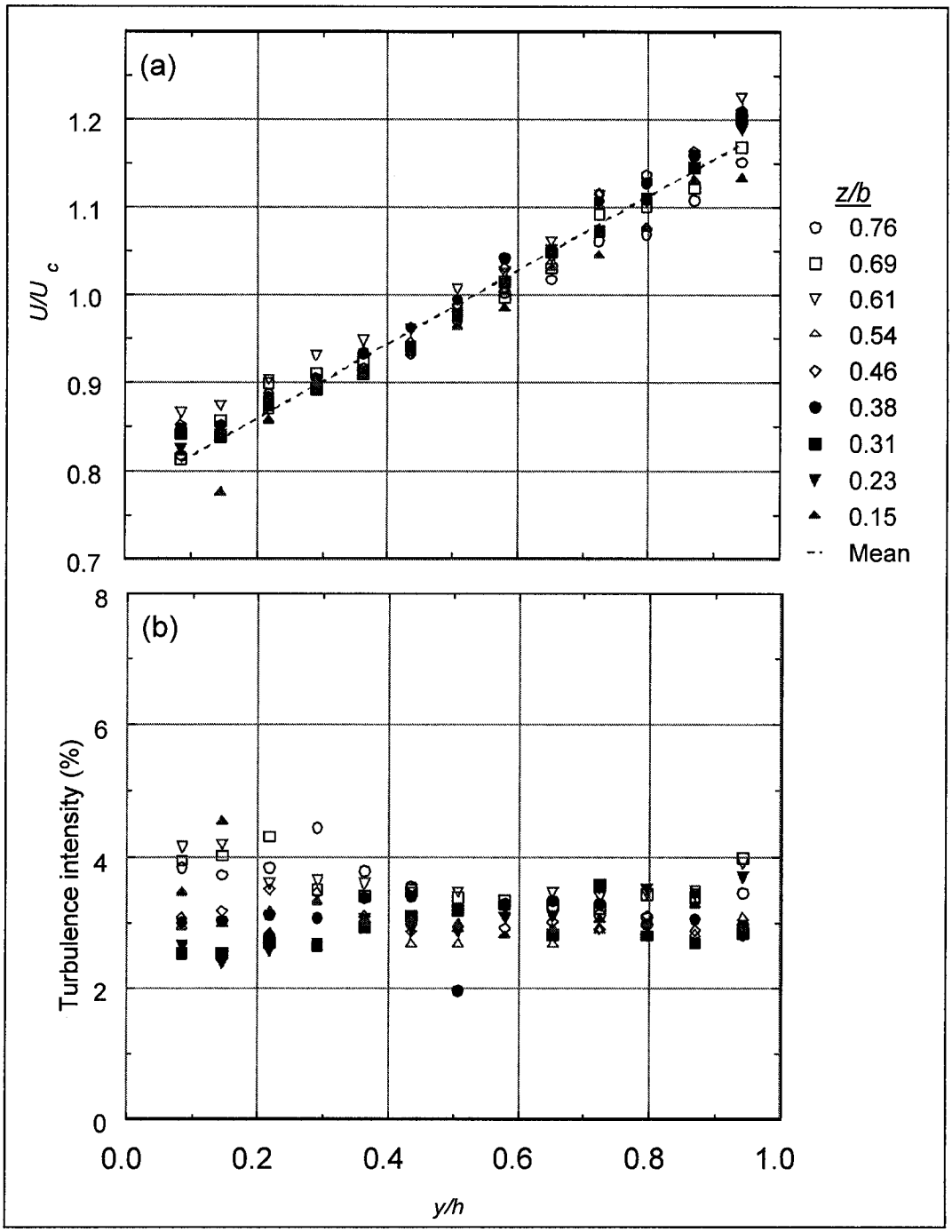

Figure 24: (a) Shear velocity profile at U_c = 46 mm/s and (b) turbulence intensity.

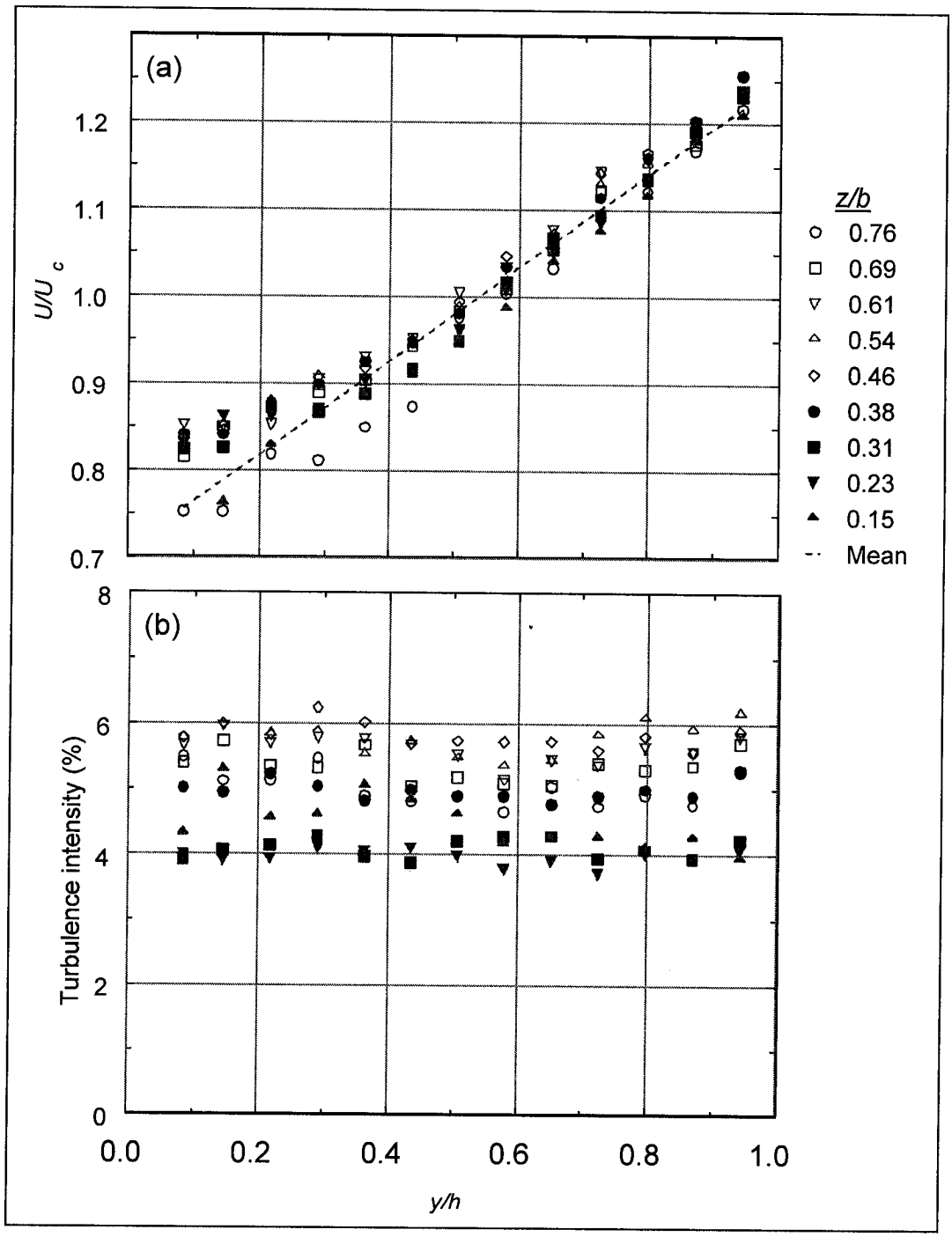

Figure 25: (a) Shear velocity profile at U_c = 29 mm/s and (b) turbulence intensity.

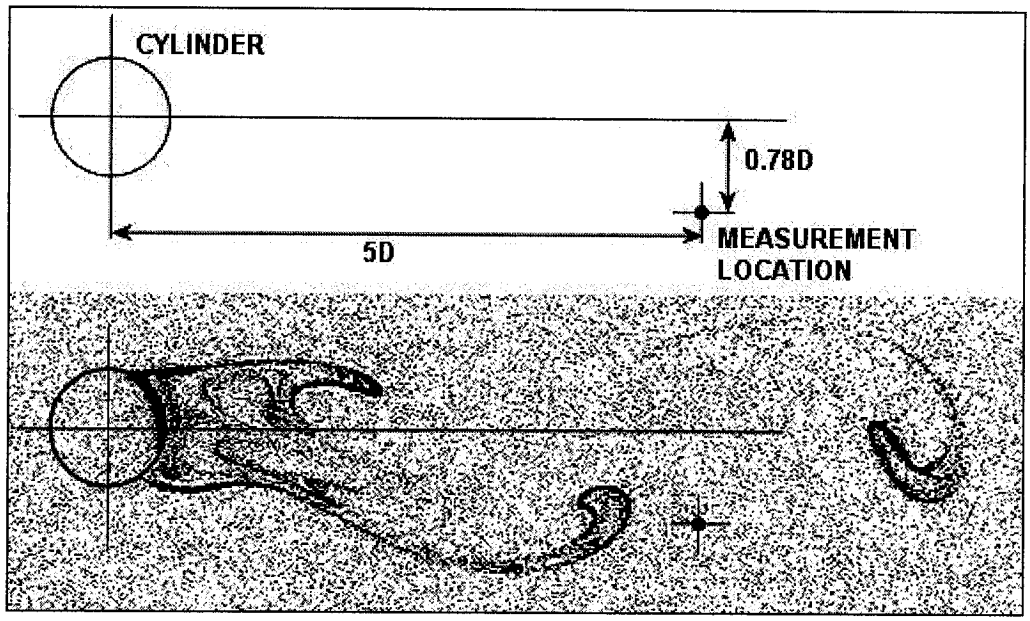

Figure 26: Location of LDV measuring volume in relation to the cylinders.

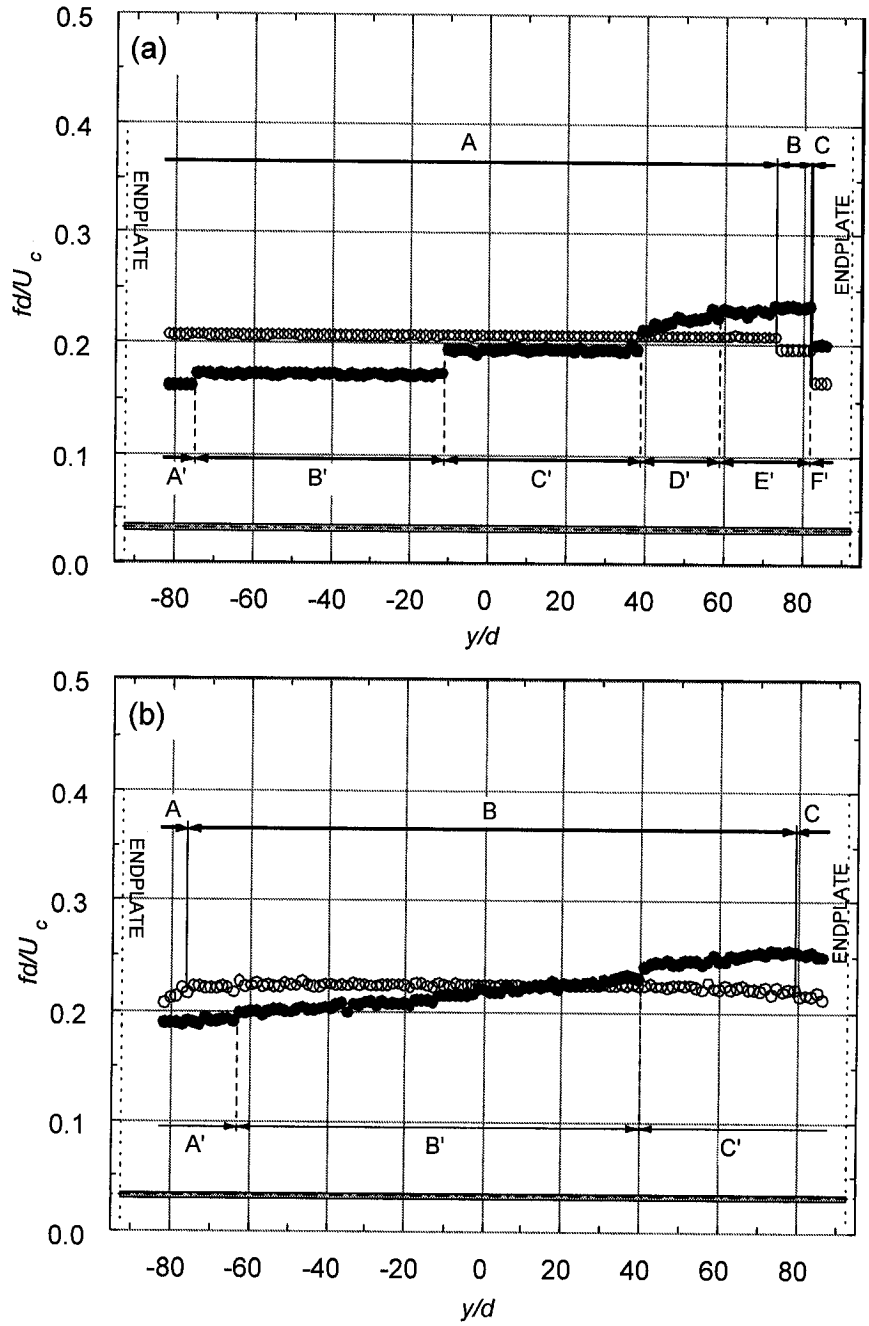

Figure 27: Dimensionless vortex shedding frequency from a uniform cylinder in uniform (○) and shear (●) flow, at (a) Re= 146 and (b) 336.

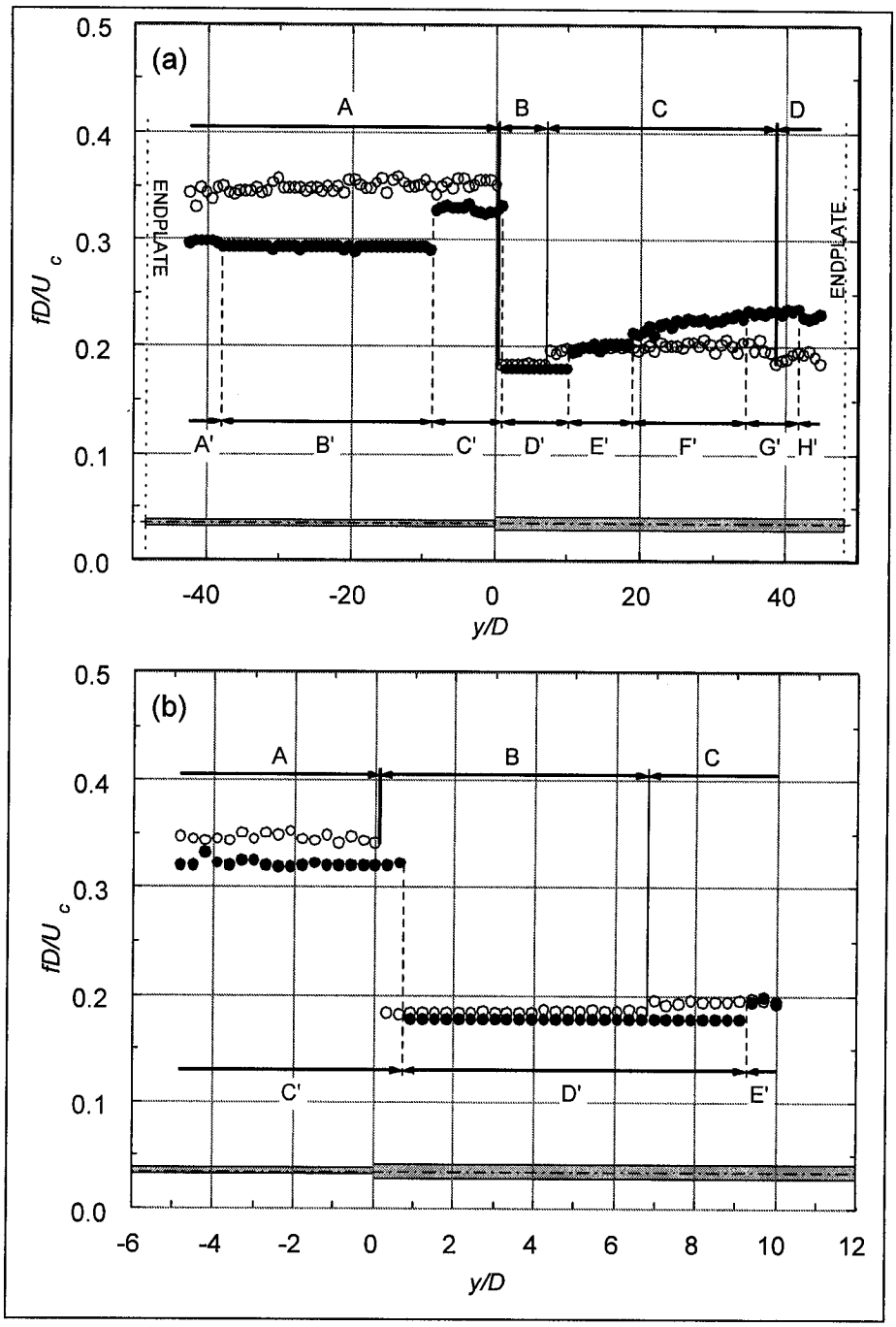

Figure 28: Dimensionless vortex shedding frequency from an upright step-cylinder in uniform (○) and shear (●) flow. (a) Full span at Re = 275, (b) step region at Re = 296. The velocity in the shear flow increased with increasing *y/D*.

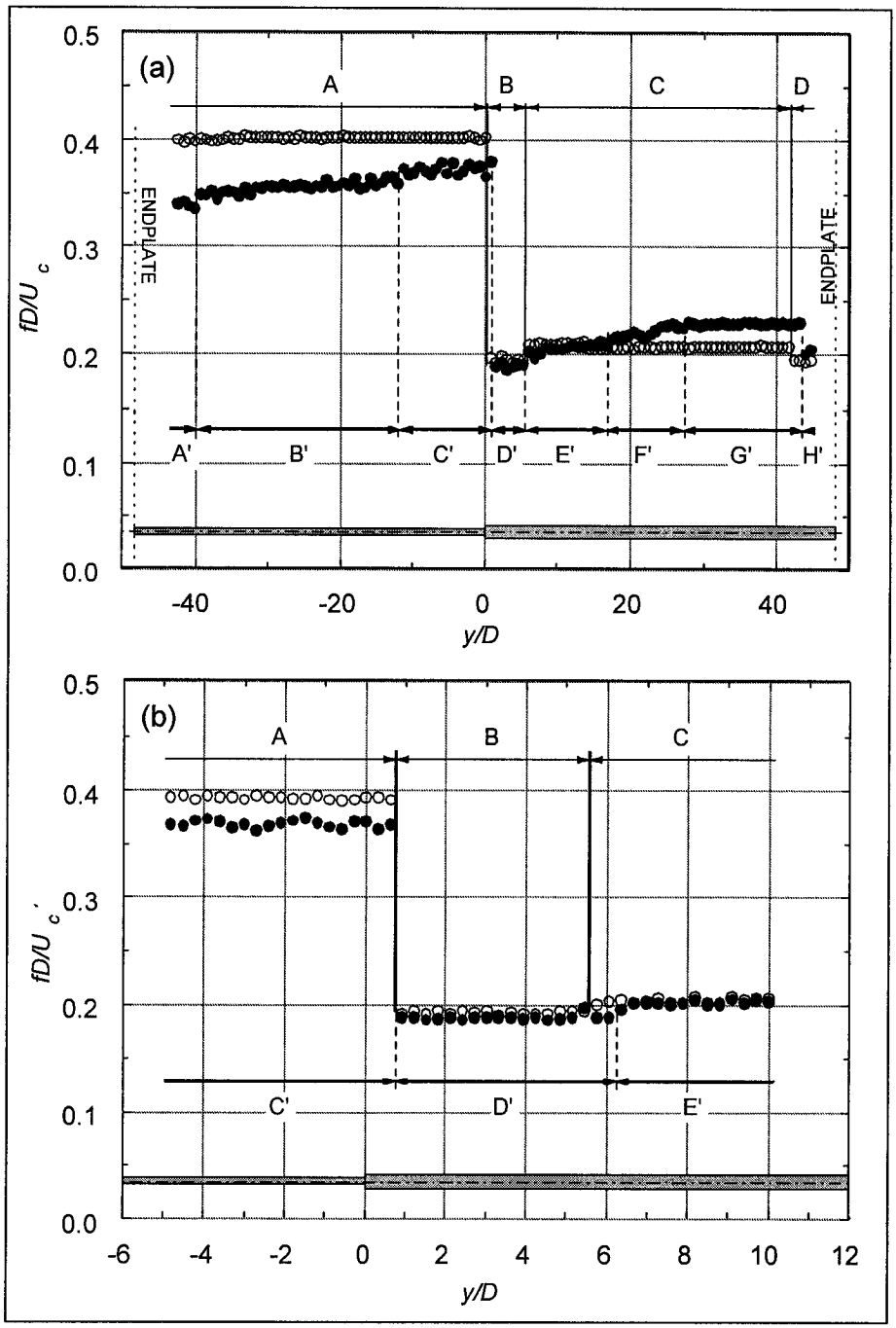

Figure 29: Dimensionless vortex shedding frequency from an upright step-cylinder in uniform (○) and shear (●) flow. (a) Full span at Re = 625, (b) step region at Re = 621. The velocity in the shear flow increased with increasing *y/D*.

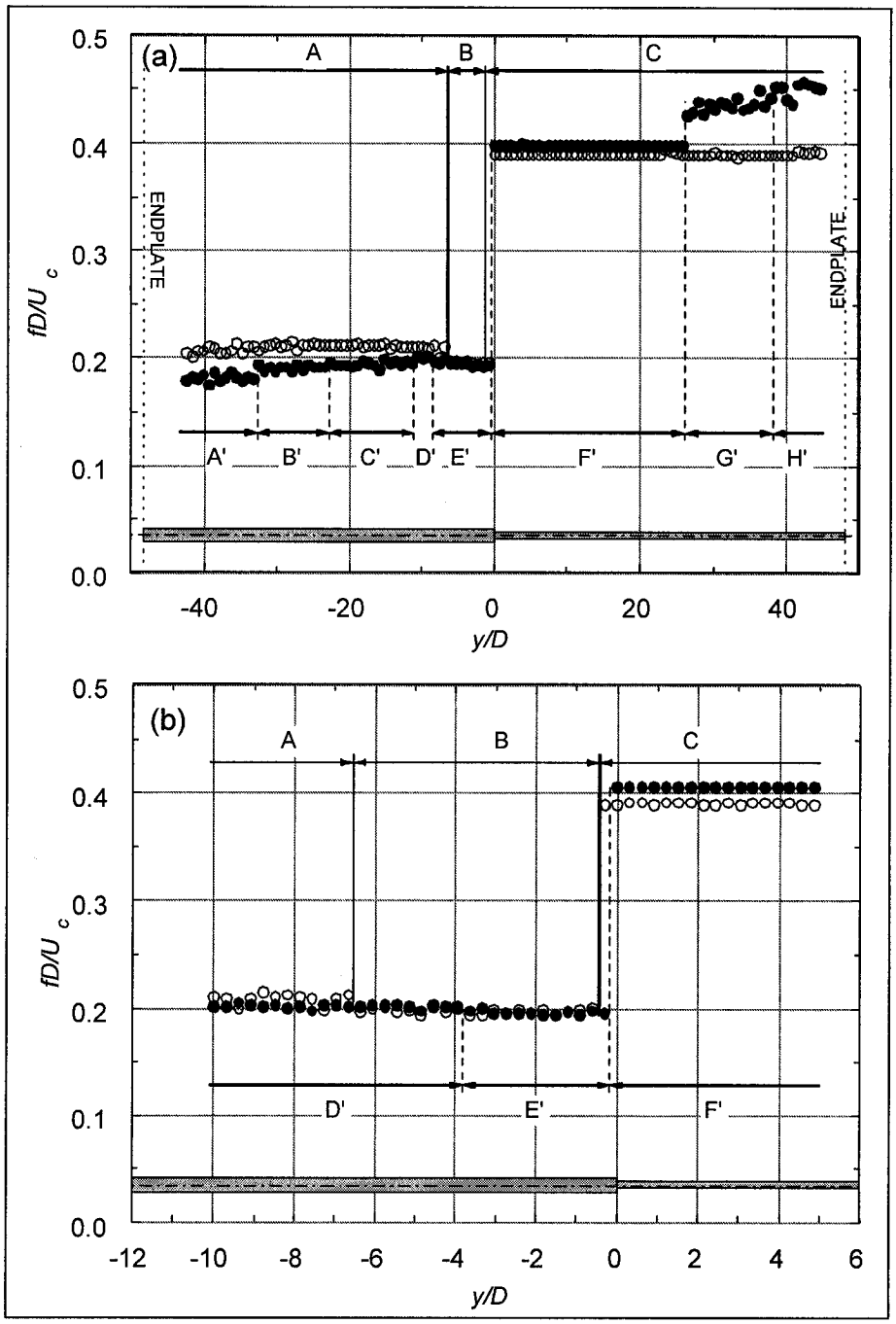

Figure 30: Dimensionless vortex shedding frequency from an inverted step-cylinder in uniform (○) and shear (●) flow. (a) Full span at Re = 294, (b) step region at Re = 293. The velocity in the shear flow increased with increasing *y/D*.

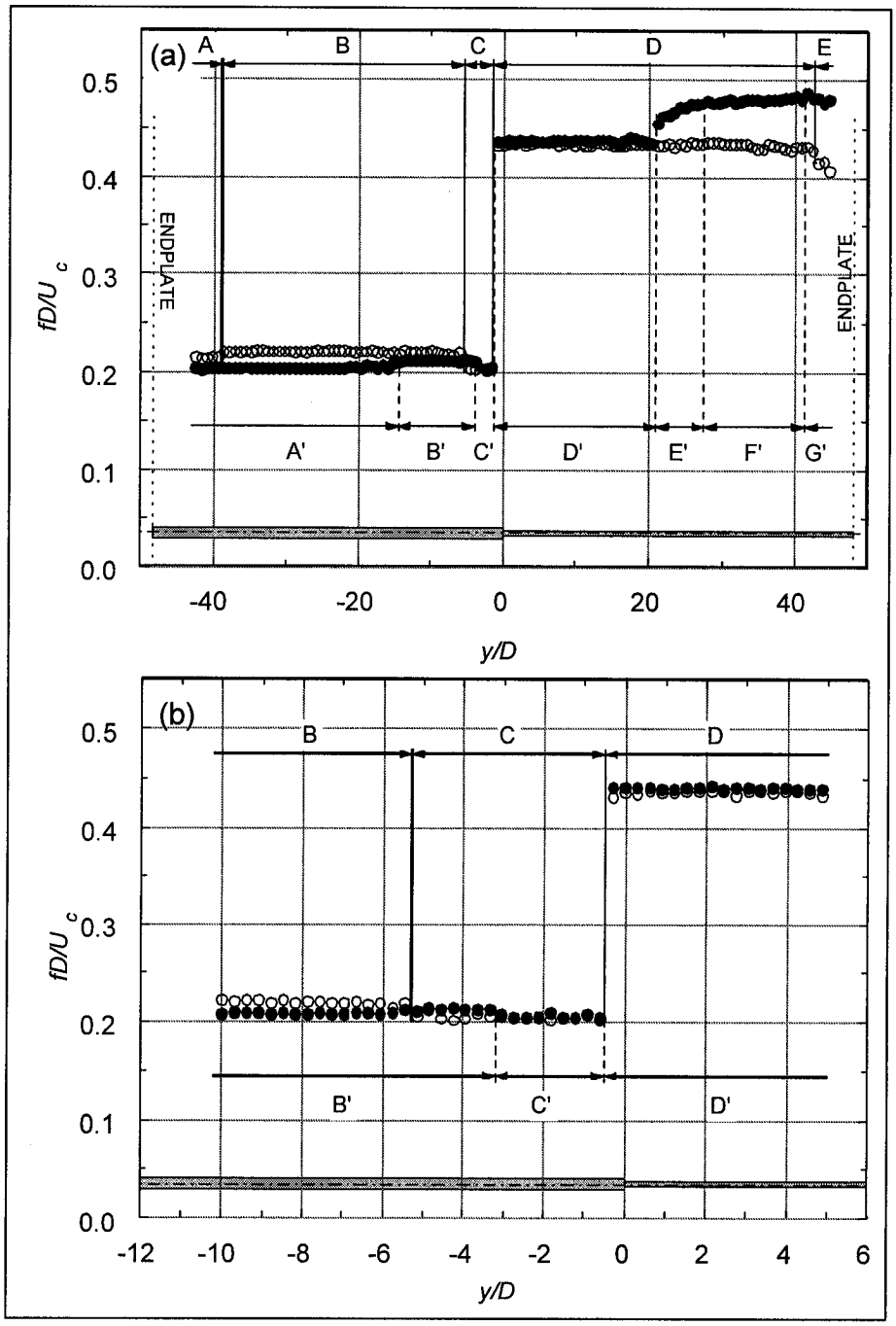

Figure 31: Dimensionless vortex shedding frequency from an inverted step-cylinder in uniform (○) and shear (●) flow. (a) Full span at Re = 647, (b) step region at Re = 640. The velocity in the shear flow increased with increasing *y/D*.

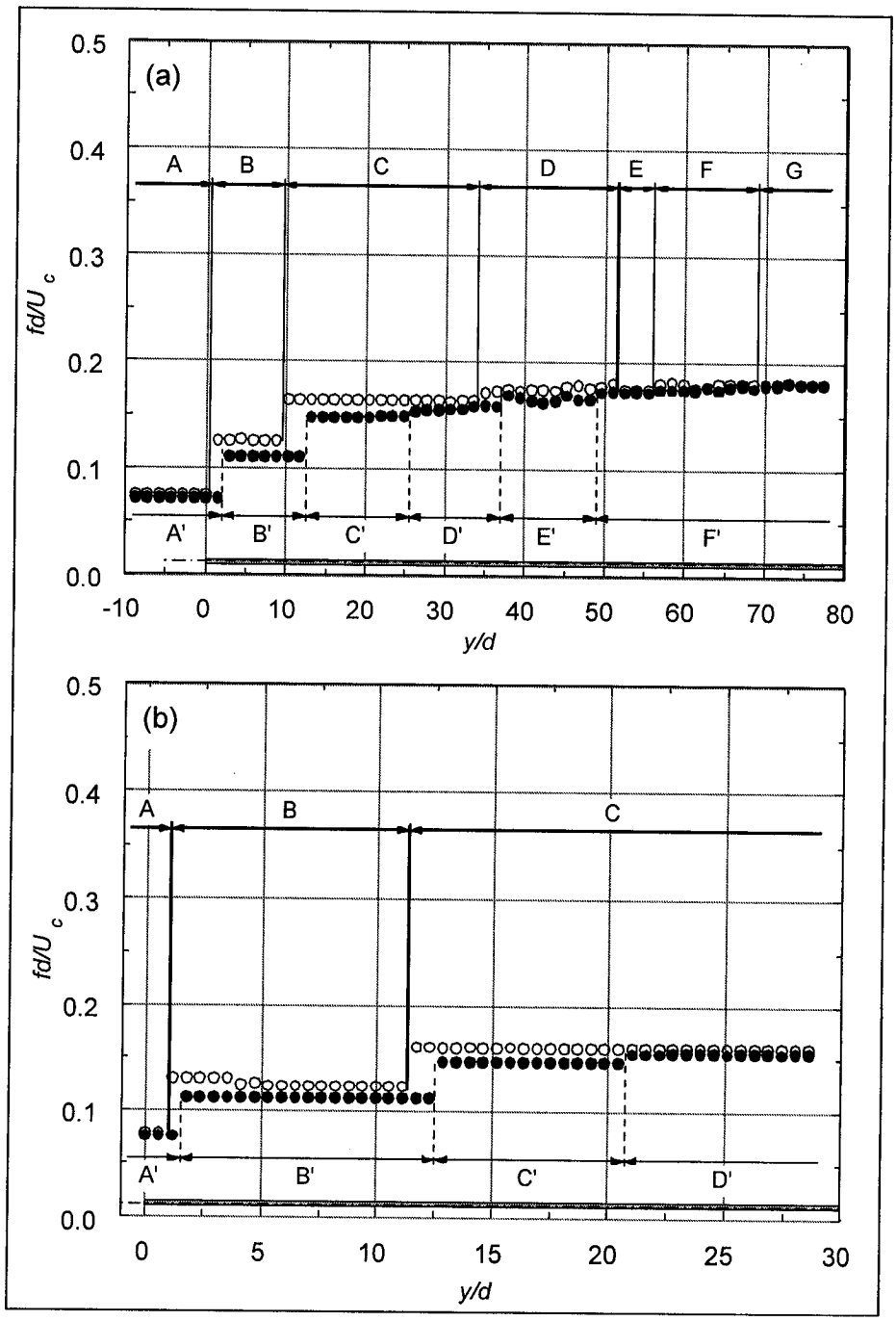

Figure 32: Dimensionless vortex shedding frequency from a finite cylinder in uniform (○) and shear (●) flow. (a) Full span at Re = 152, (b) tip region at Re = 146. The velocity in the shear flow increased with increasing *y/d*.

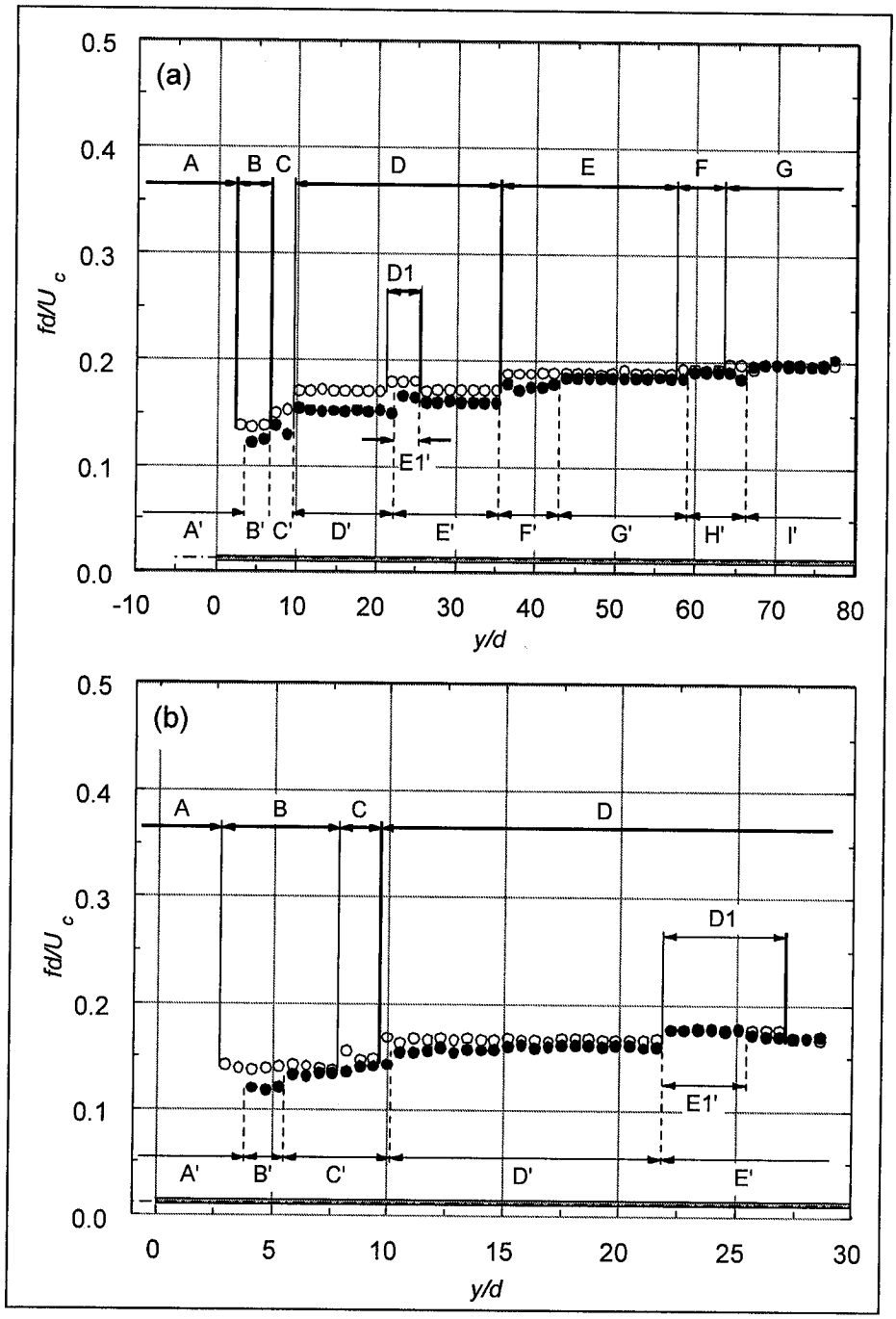

Figure 33: Dimensionless vortex shedding frequency from a finite cylinder in uniform (○) and shear (●) flow. (a) Full span at Re = 331, (b) tip region at Re = 329. The velocity in the shear flow increased with increasing *y/d*.

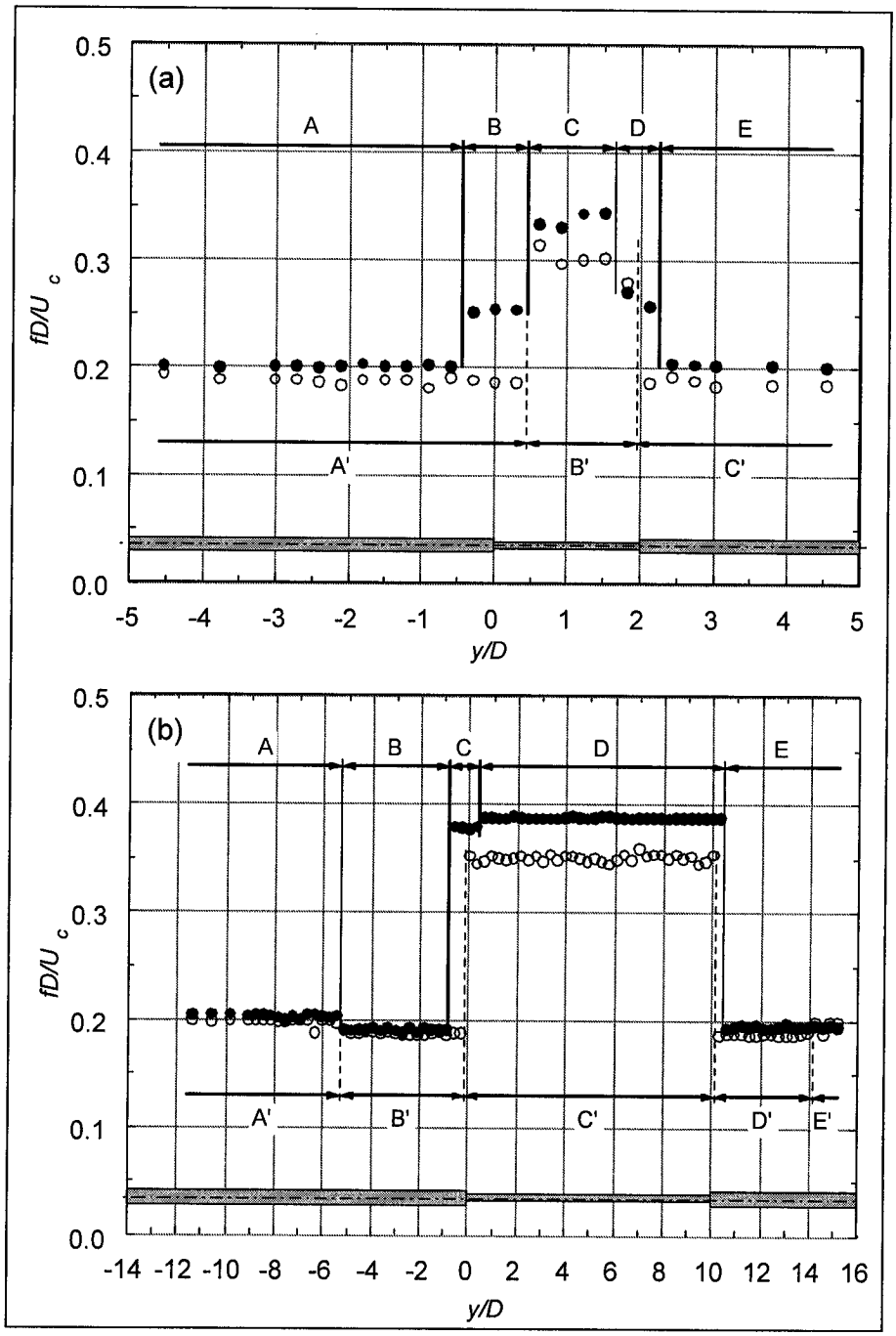

Figure 34: Dimensionless vortex shedding frequency from the small double-step cylinders in uniform flow, at Re = 279 (○) and 643 (●). Middle section length (a) 2*D*, (b) 10*D*.

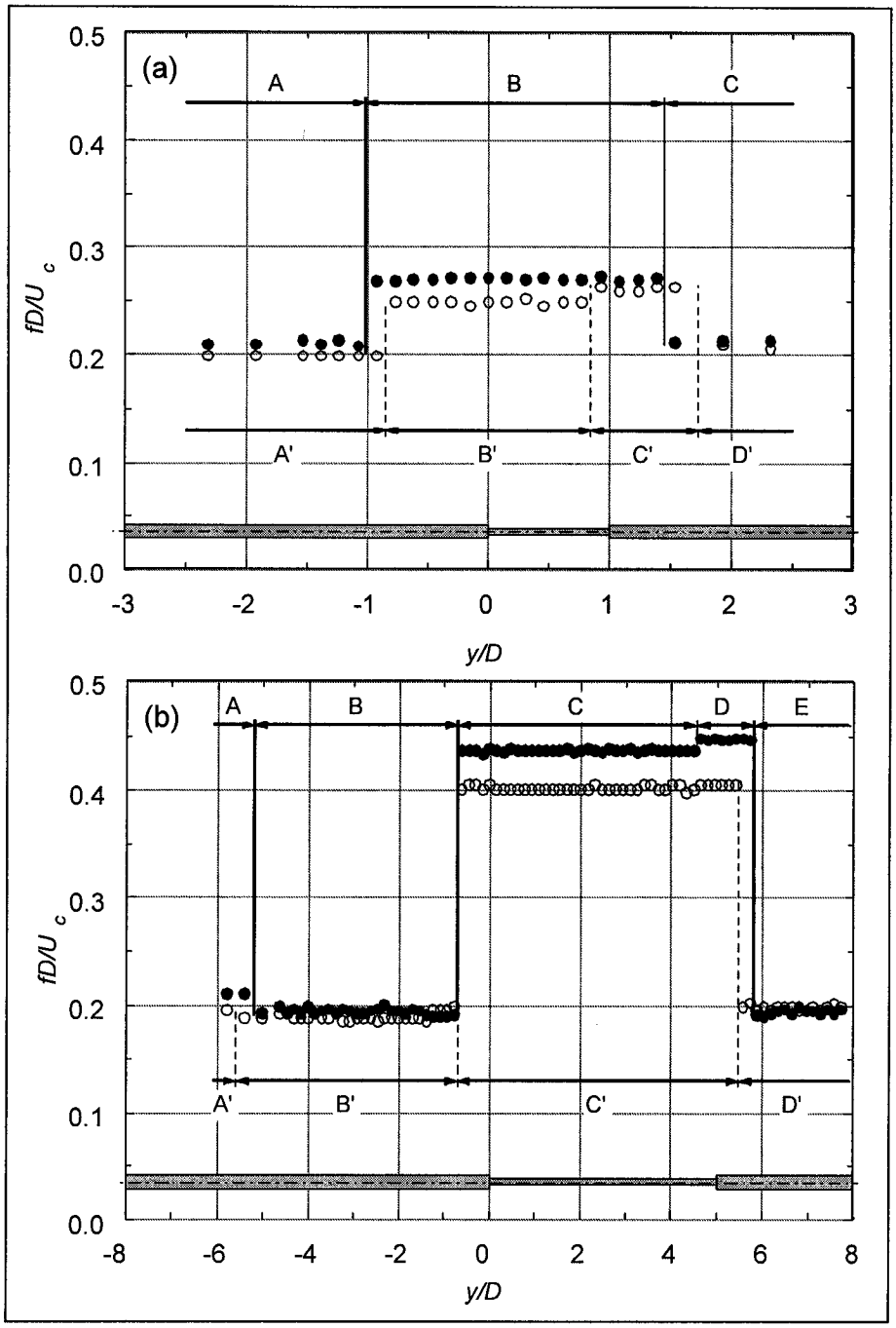

Figure 35: Dimensionless vortex shedding frequency from the large double-step cylinders in uniform flow, at Re = 576 (○) and 1260 (●). Middle section length (a) 1*D*, (b) 5*D*.

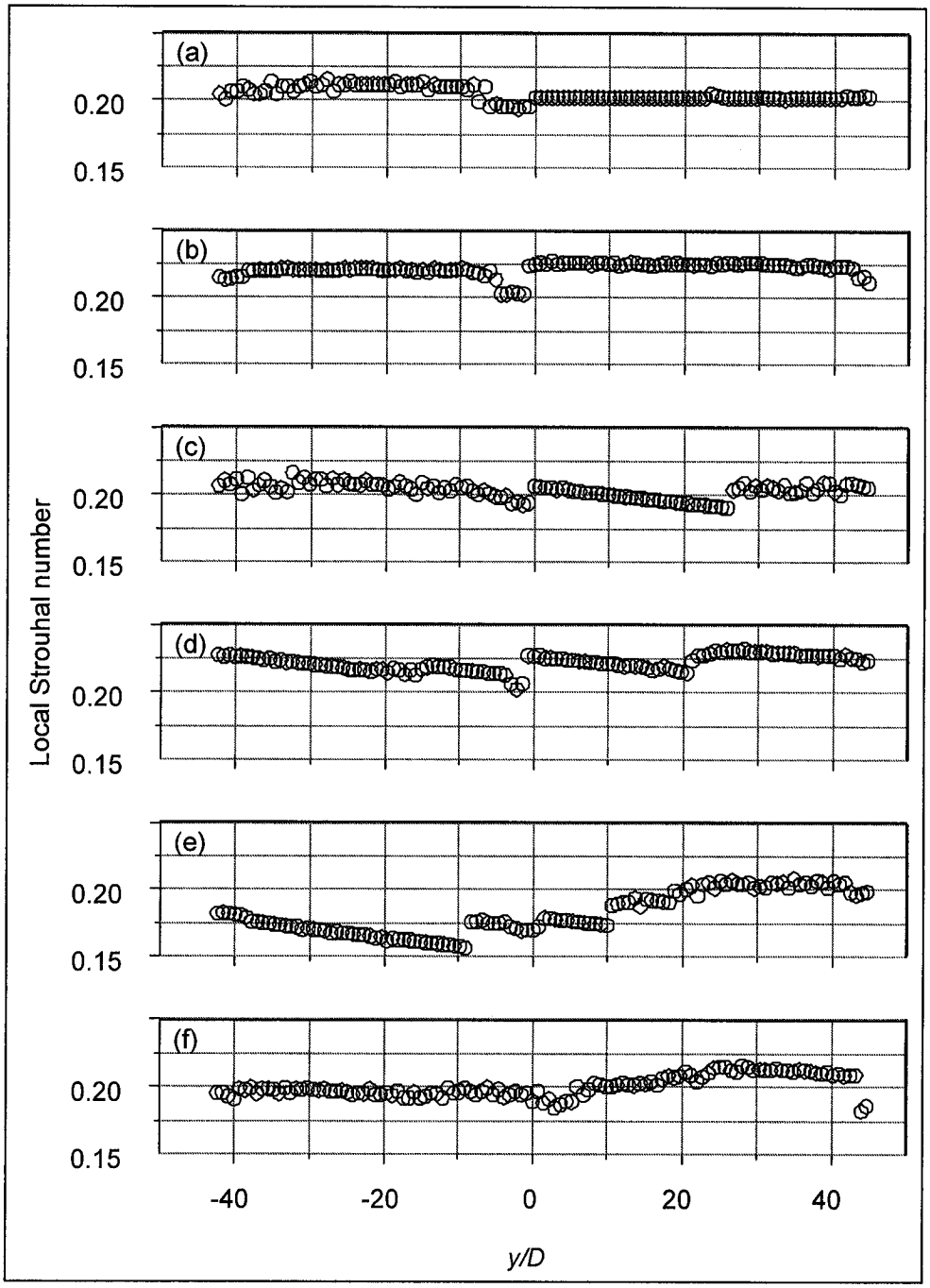

Figure 36: Local Strouhal numbers for the step-cylinder. Inverted (large cylinder at $y/D < 0$) in uniform flow at (a) $Re_D = 294$, (b) 647, shear flow at (c) $Re_D = 289$, (d) 640. Upright (large cylinder at $y/D > 0$) in shear flow at (e) $Re_D = 275$, (f) 625.

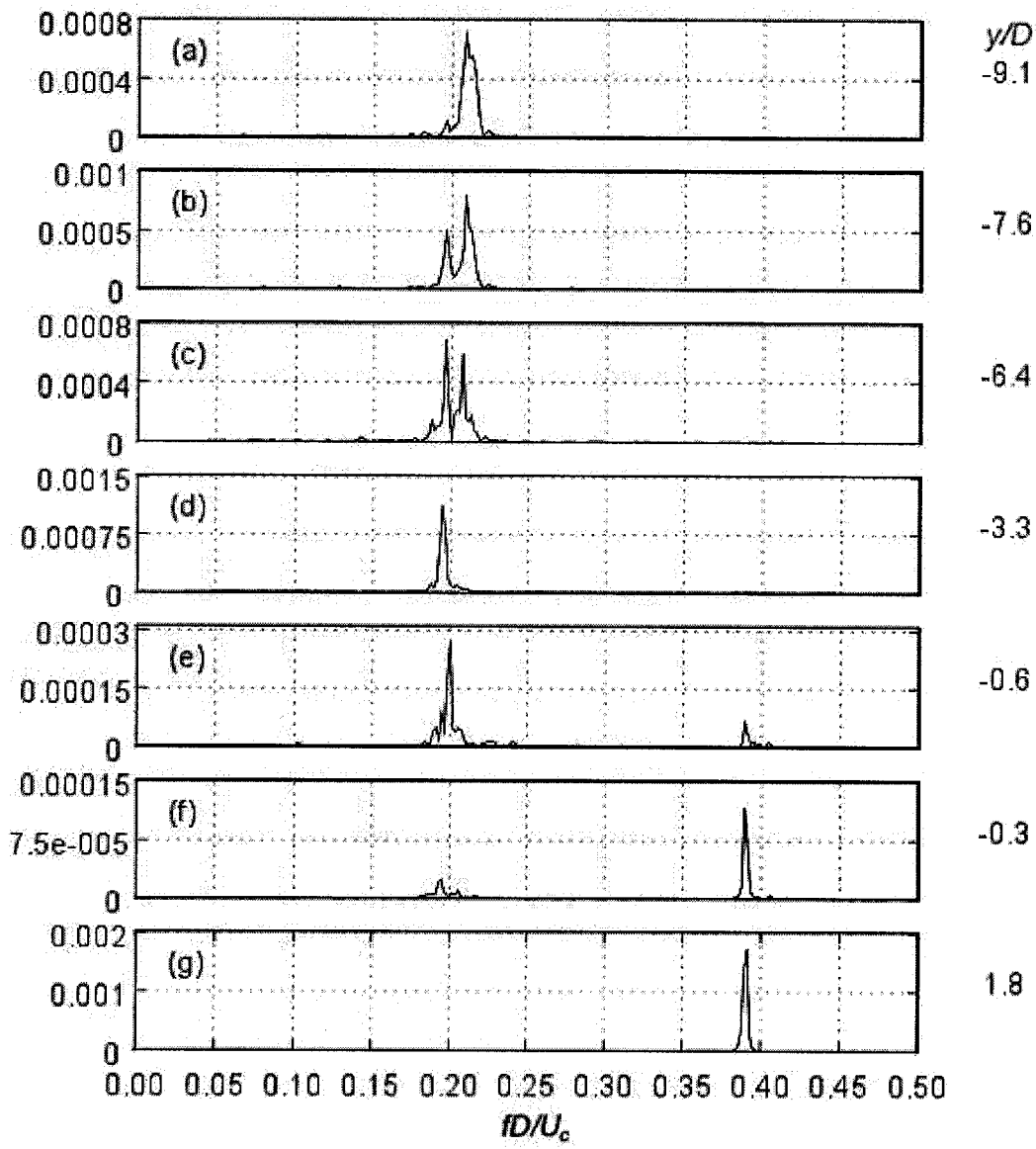

Figure 37: Velocity spectra for the inverted step-cylinder at Re = 294 in uniform flow. The large cylinder was located at $y/D < 0$.

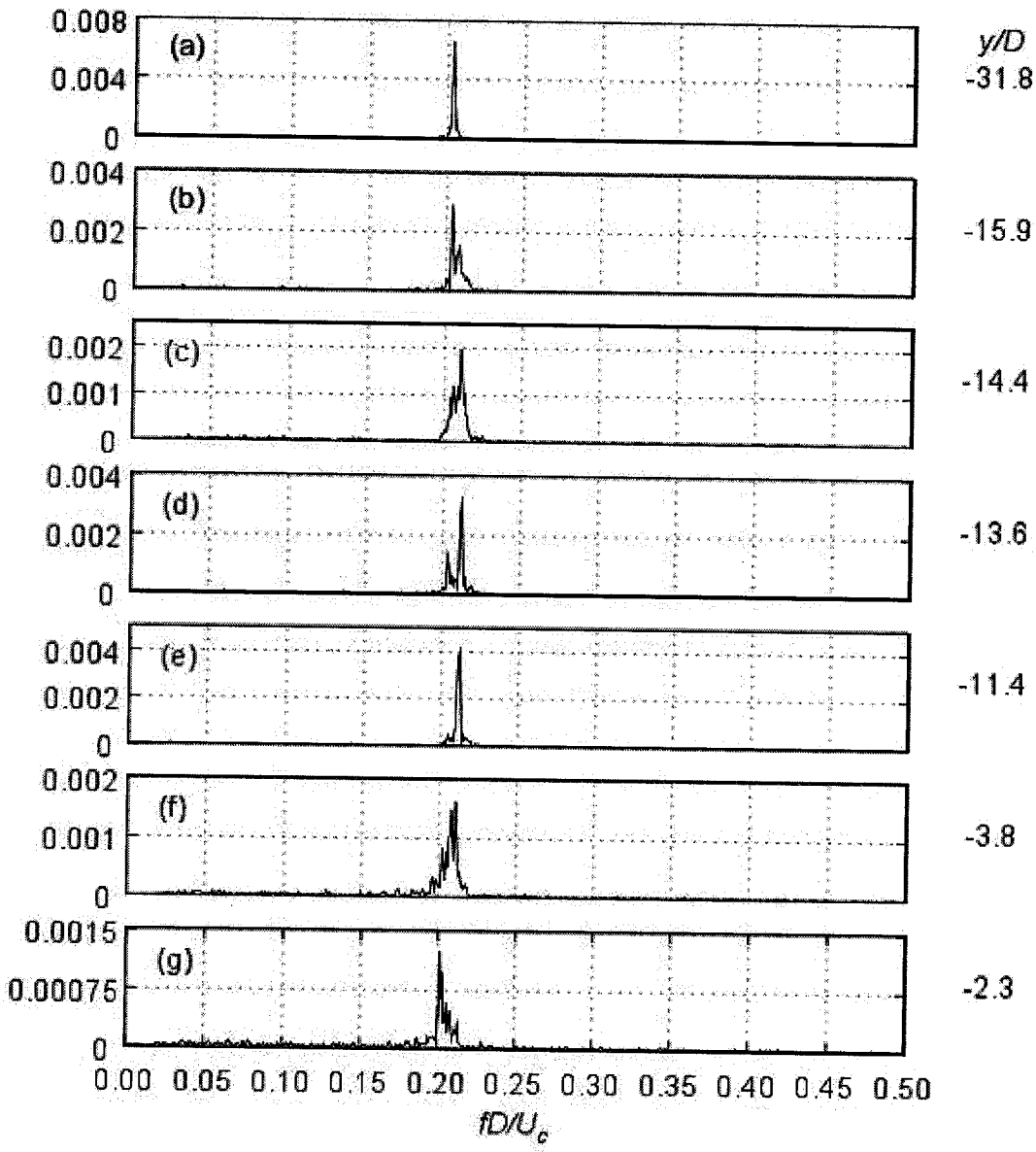

Figure 38: Velocity spectra for the inverted step cylinder at Re = 647 in shear flow. The large cylinder was located at $y/D < 0$, and was in the lower-velocity fluid.

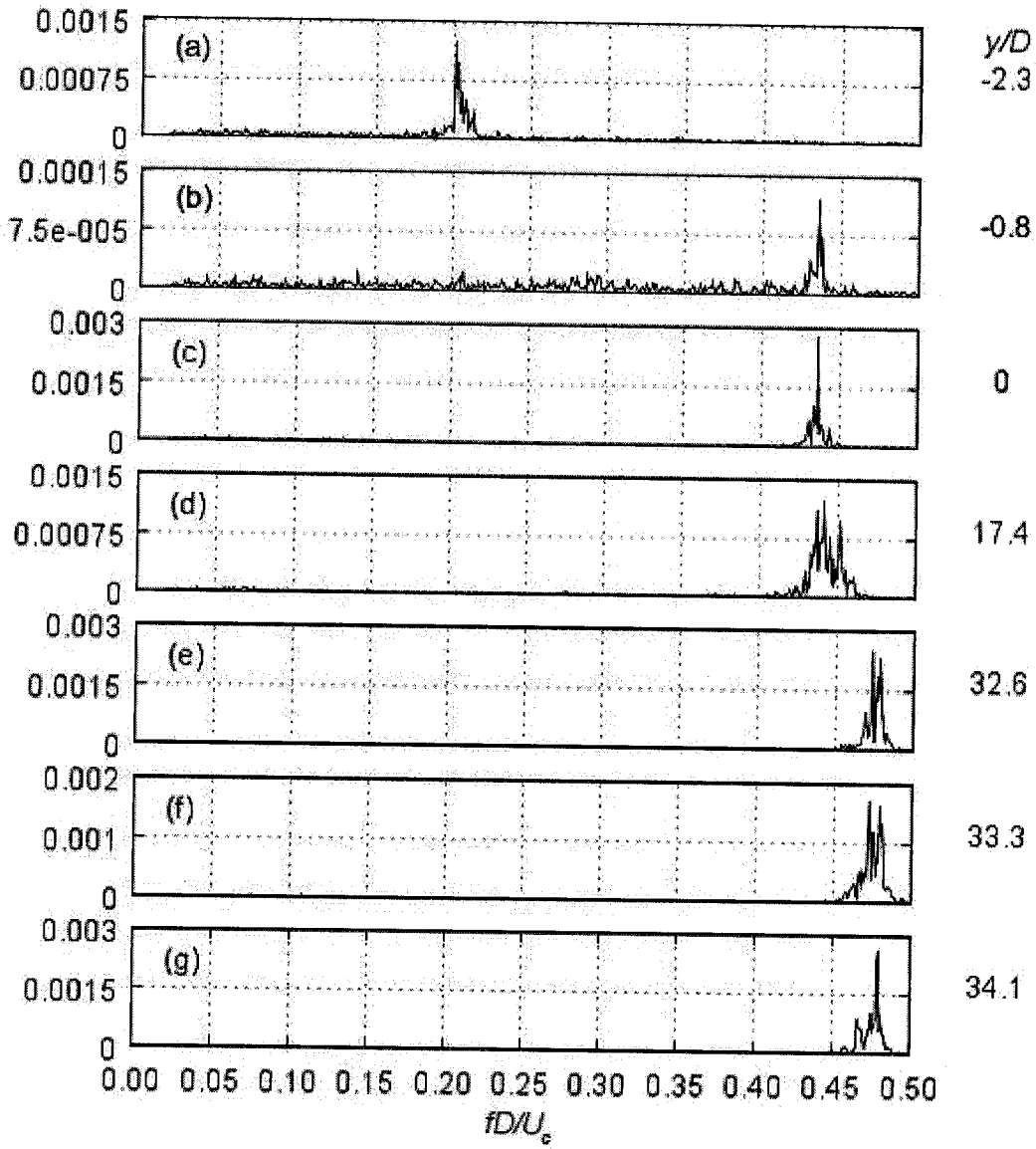

Figure 39: Velocity spectra for the inverted step cylinder at Re = 647 in shear flow. The large cylinder was located at $y/D < 0$, and was in the lower-velocity fluid.

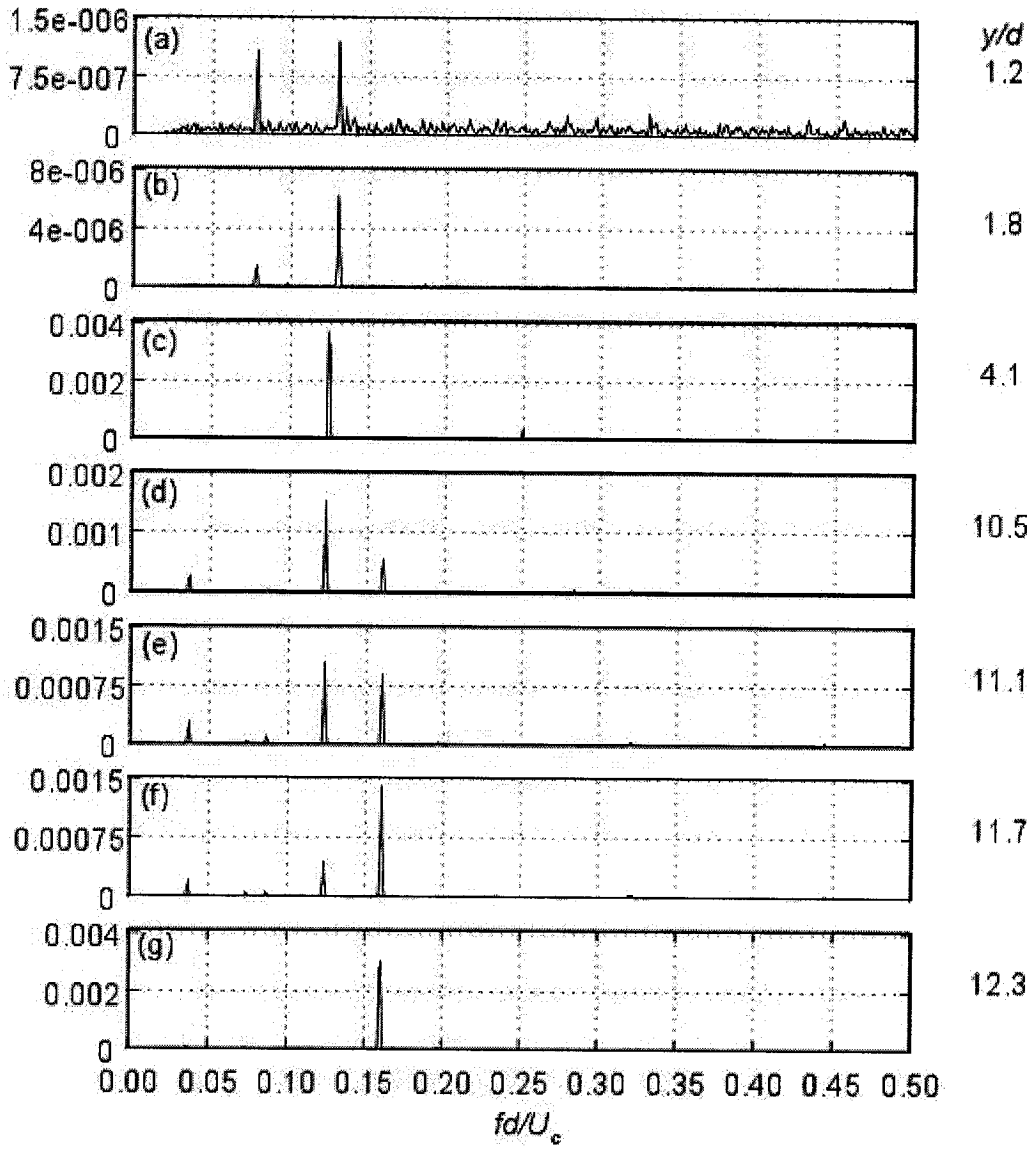

Figure 40: Velocity spectra for the finite cylinder at Re = 152 in uniform flow.

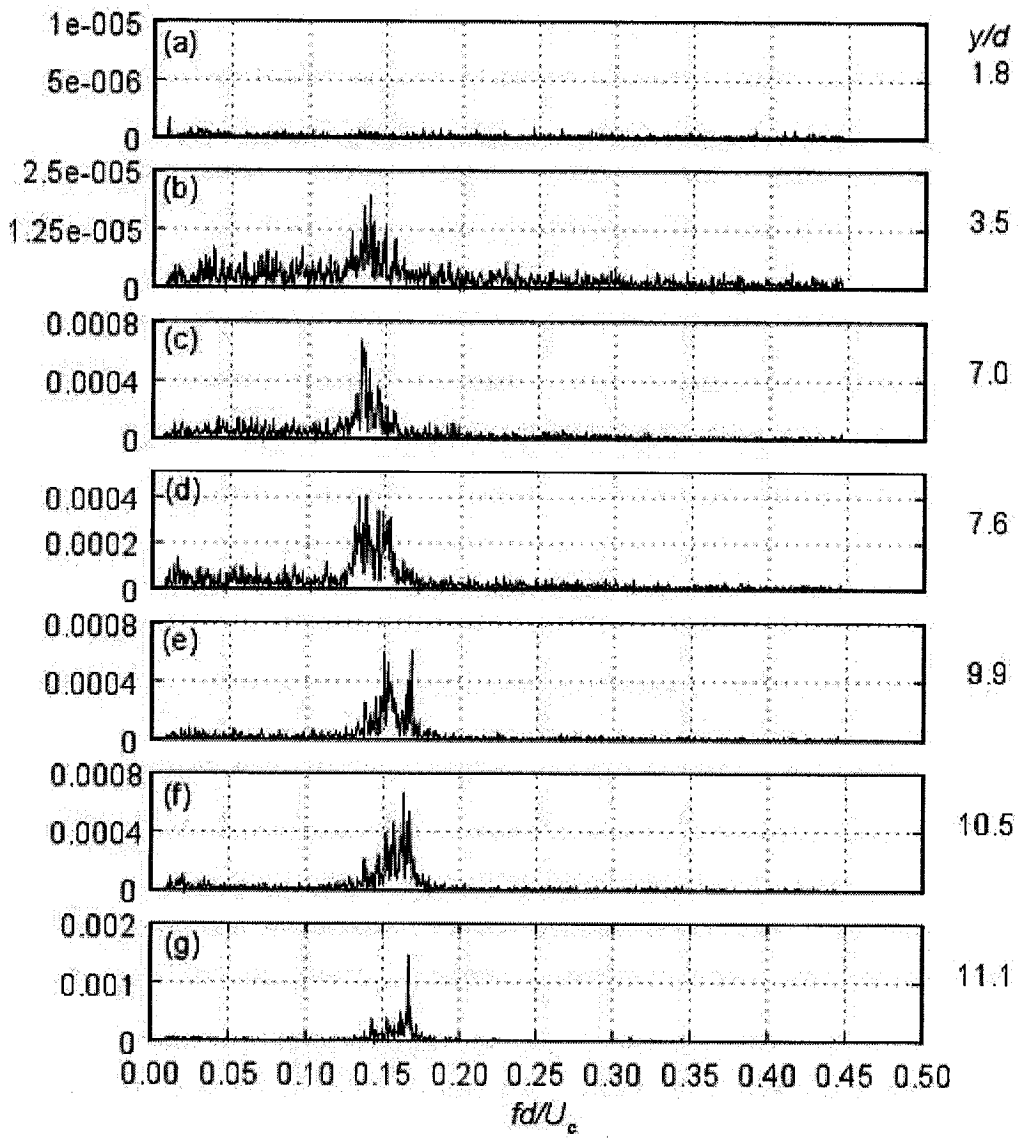

Figure 41: Velocity spectra for the finite cylinder at Re = 331 in uniform flow.

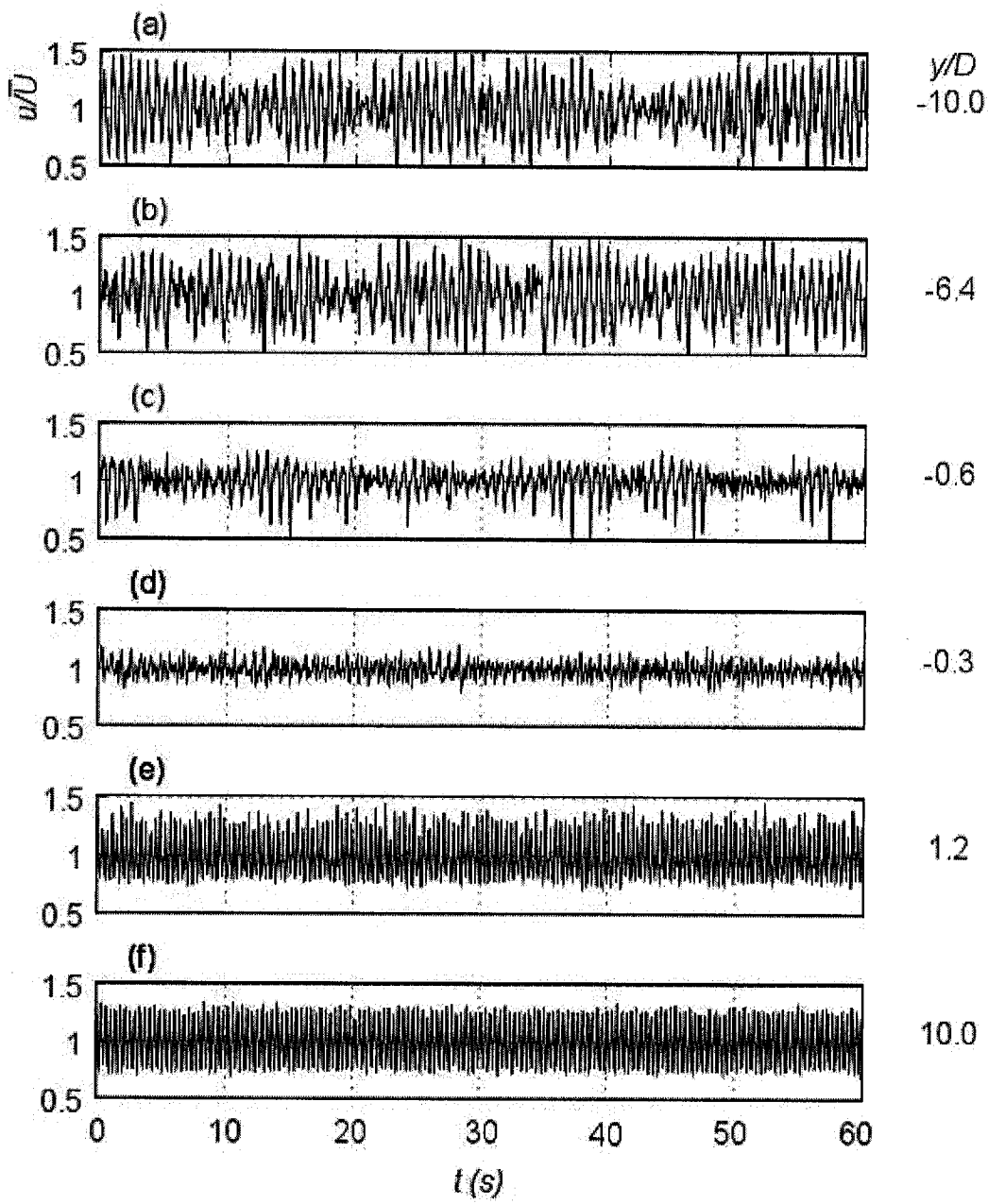

Figure 42: Streamwise velocity signals for the inverted step cylinder at Re = 351 in uniform flow. The large cylinder was located at $y/D < 0$.

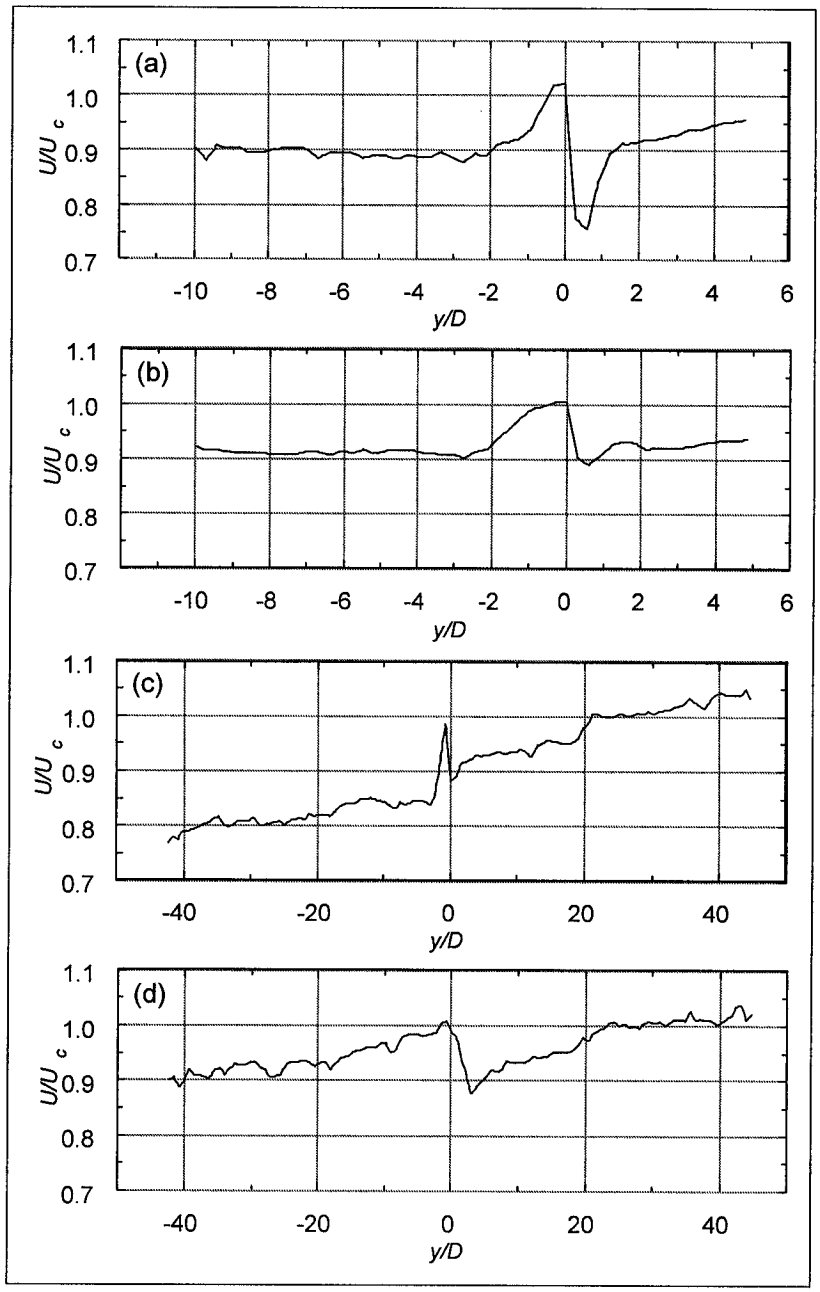

Figure 43: Mean streamwise velocity behind the step-cylinder. Inverted (large cylinder located at $y/D > 0$) in uniform flow at (a) Re = 293, (b) 640, (c) in shear flow at Re = 640, (d) upright (large cylinder located at $y/D < 0$) in shear flow at Re = 626. The velocity in the shear increased with increasing y/D.

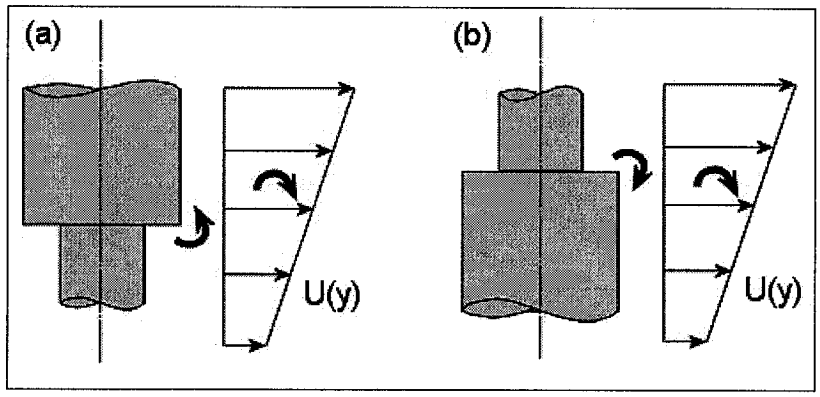

Figure 44: Relative rotation of the downwash over the step, compared to the shear flow.

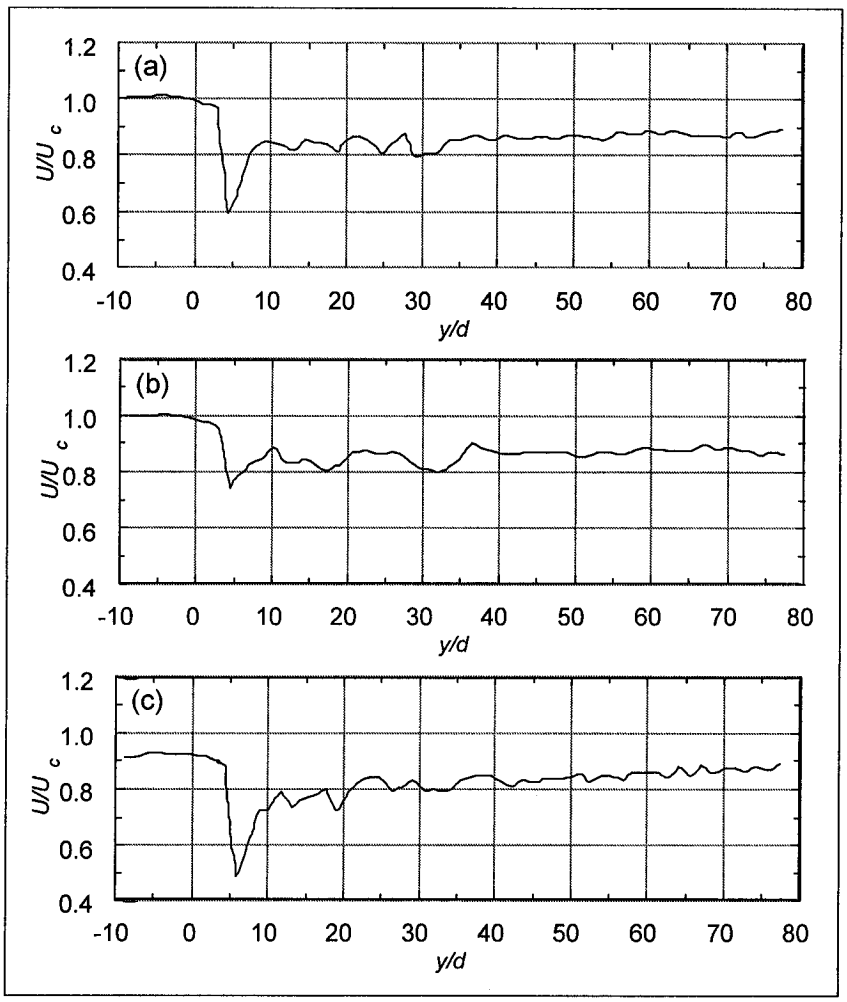

Figure 45: Mean streamwise velocity for the finite cylinder. (a) Uniform flow at Re = 152, (b) 331, (c) shear flow at Re = 159, where the velocity increased with *y/d*.

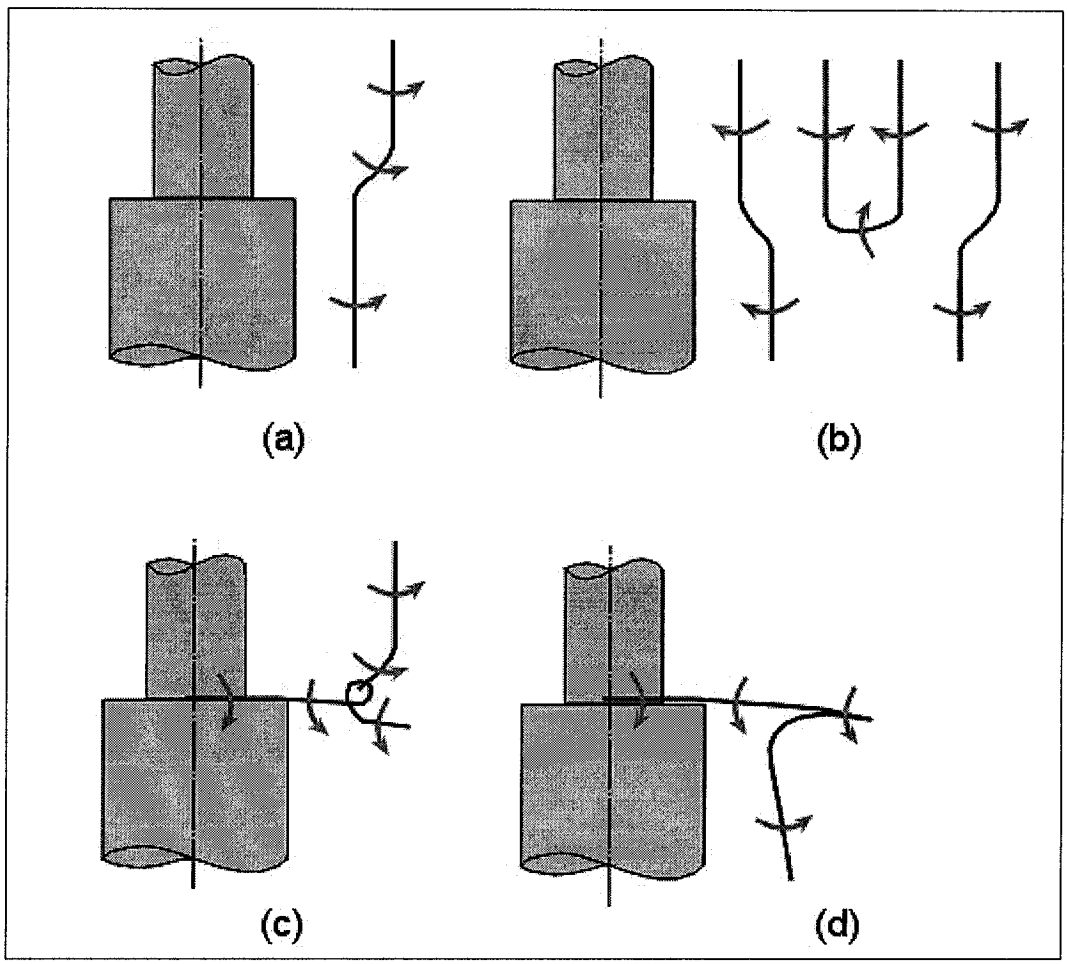

Figure 46: Connections and loops between vortices shed from the same and adjacent cells, and the streamwise vortices shed from the step. Note that the arrows always pass in front of the vortices from this point of view.

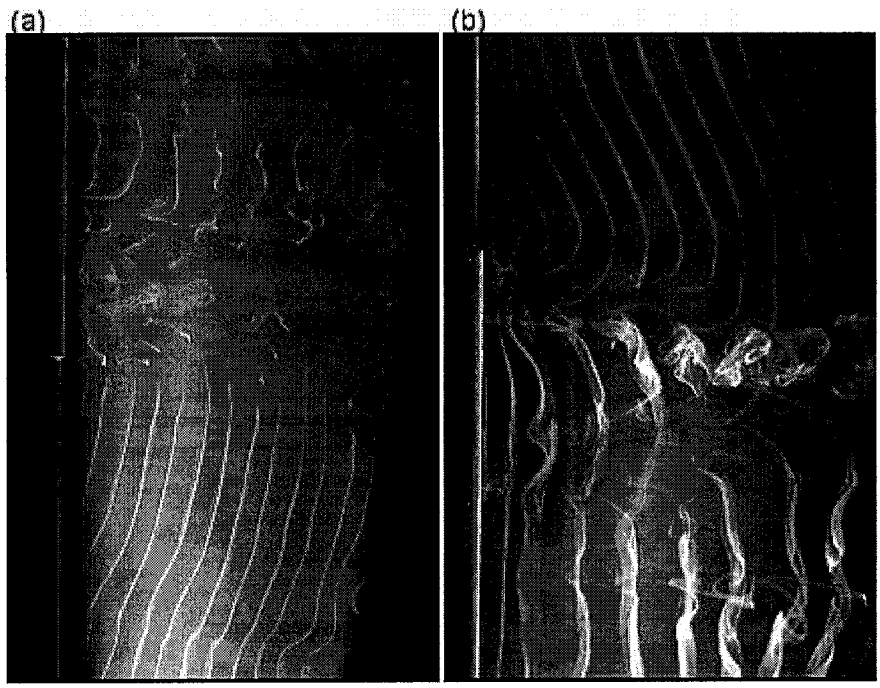

Figure 47: Step cylinders in uniform flow. (a) Upright at Re = 168, and (b) inverted at Re = 152.

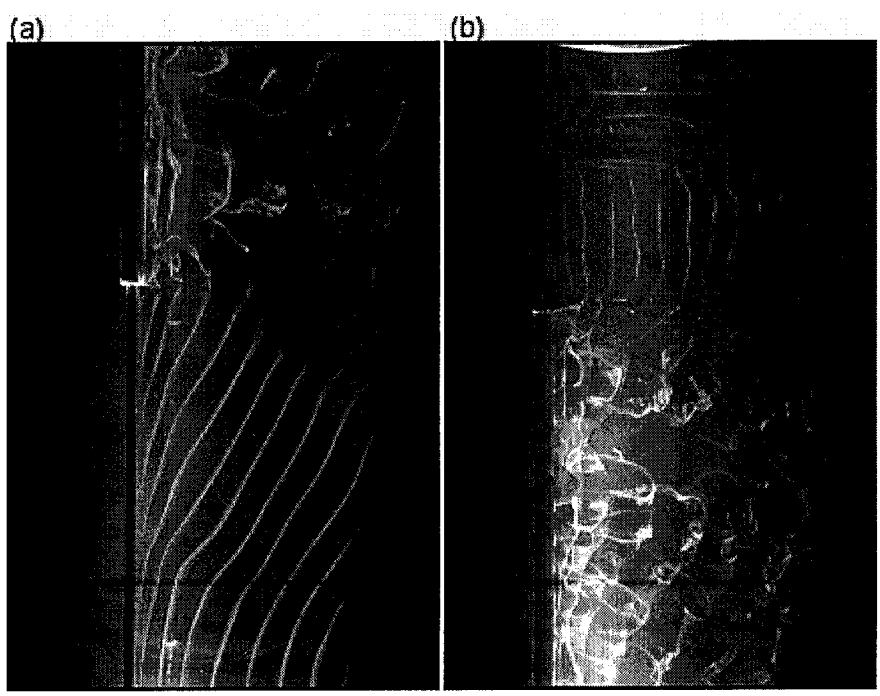

Figure 48: Step cylinders in shear flow. (a) Upright at Re = 159, and (b) inverted at Re = 168.

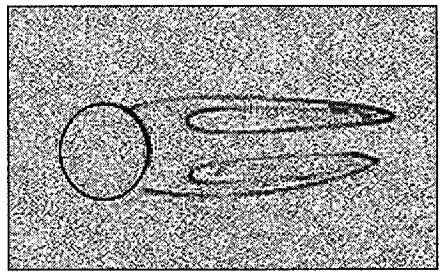

Figure 49: Non-shedding flow regime, at $Re_d = 40$.

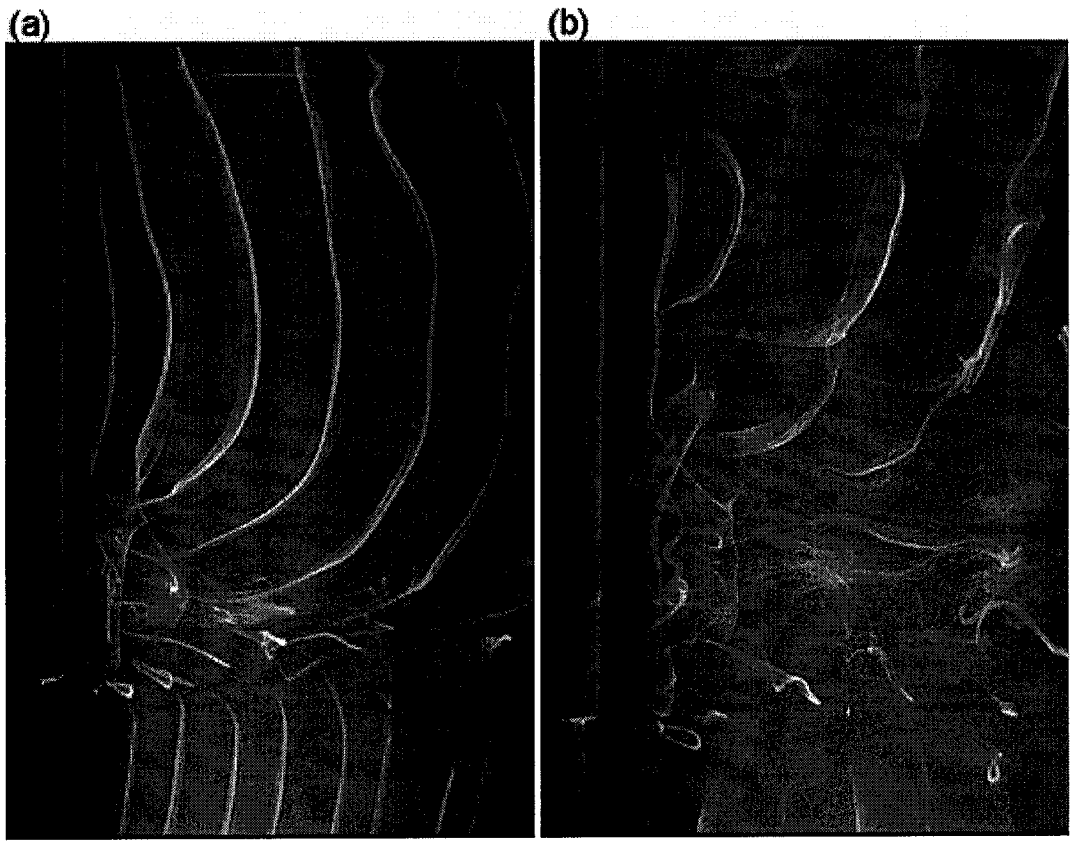

Figure 50: (a) Laminar shedding at Re = 122, (b) turbulent "fingers" at Re = 180.

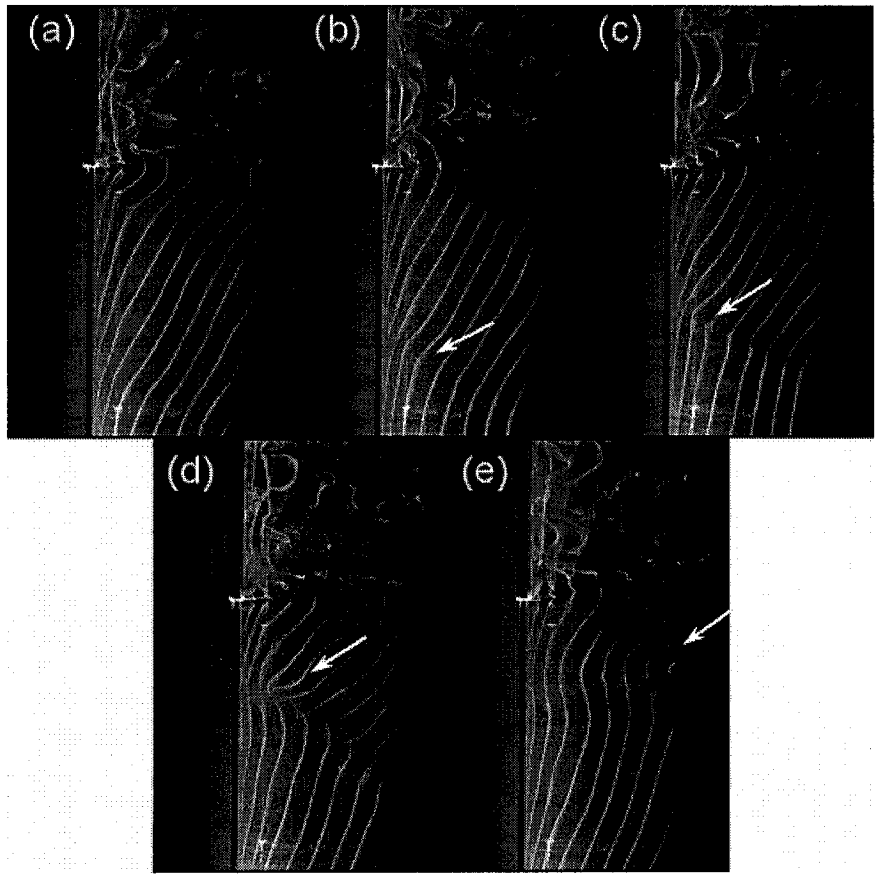

Figure 51: Cell boundary development, at Re = 159 in shear flow. (a) nearly parallel shedding, (b) a sudden change in vortex inclination, (c) spanwise drift, (d) vortex splitting, (e) streamwise loop formation.

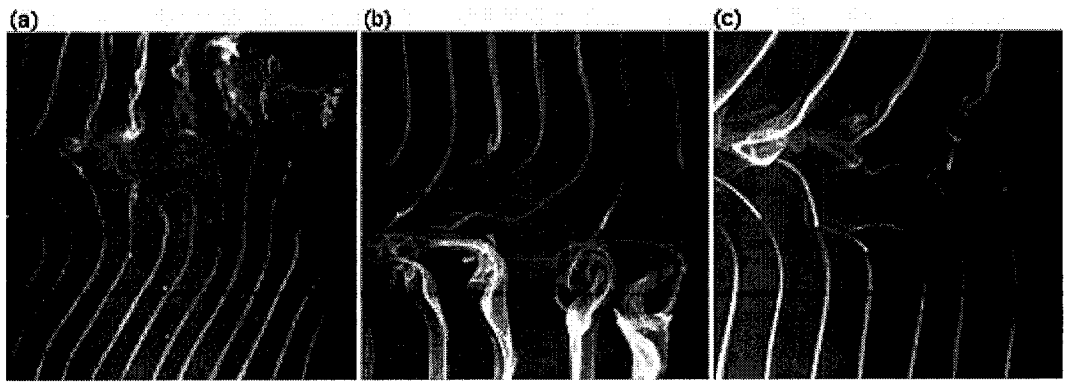

Figure 52: Vortex half-loops in the step region. (a) Upright in shear flow at Re = 152, (b) inverted in uniform flow at Re = 152, (c) upright in uniform flow at Re = 122.

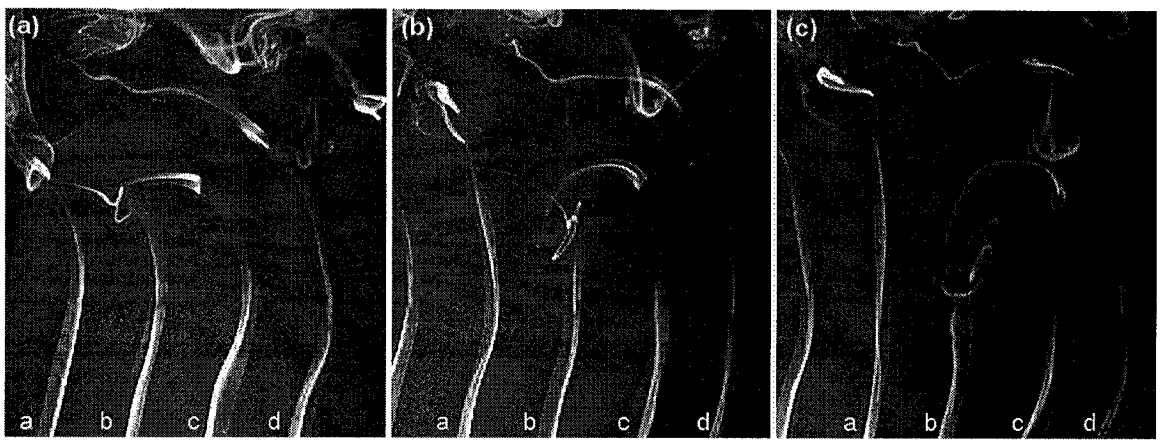

Figure 53: Vortex half-loop formation; upright in uniform flow at Re = 168.

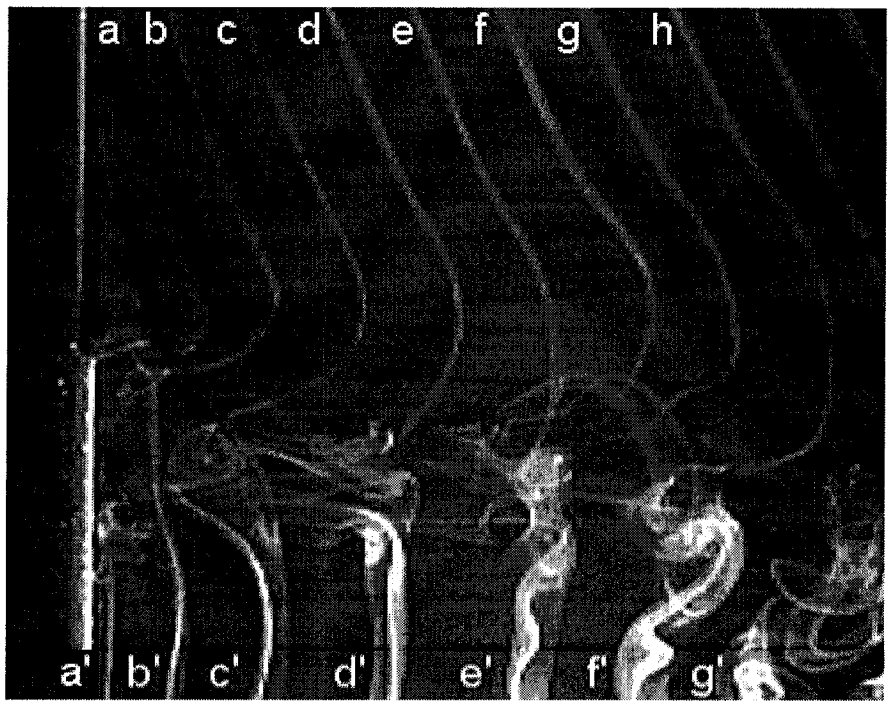

Figure 54: Vortex shedding at Re = 152 in uniform flow. Vortices e and e' are in-phase, while c and c' form a more commonly observed connection.

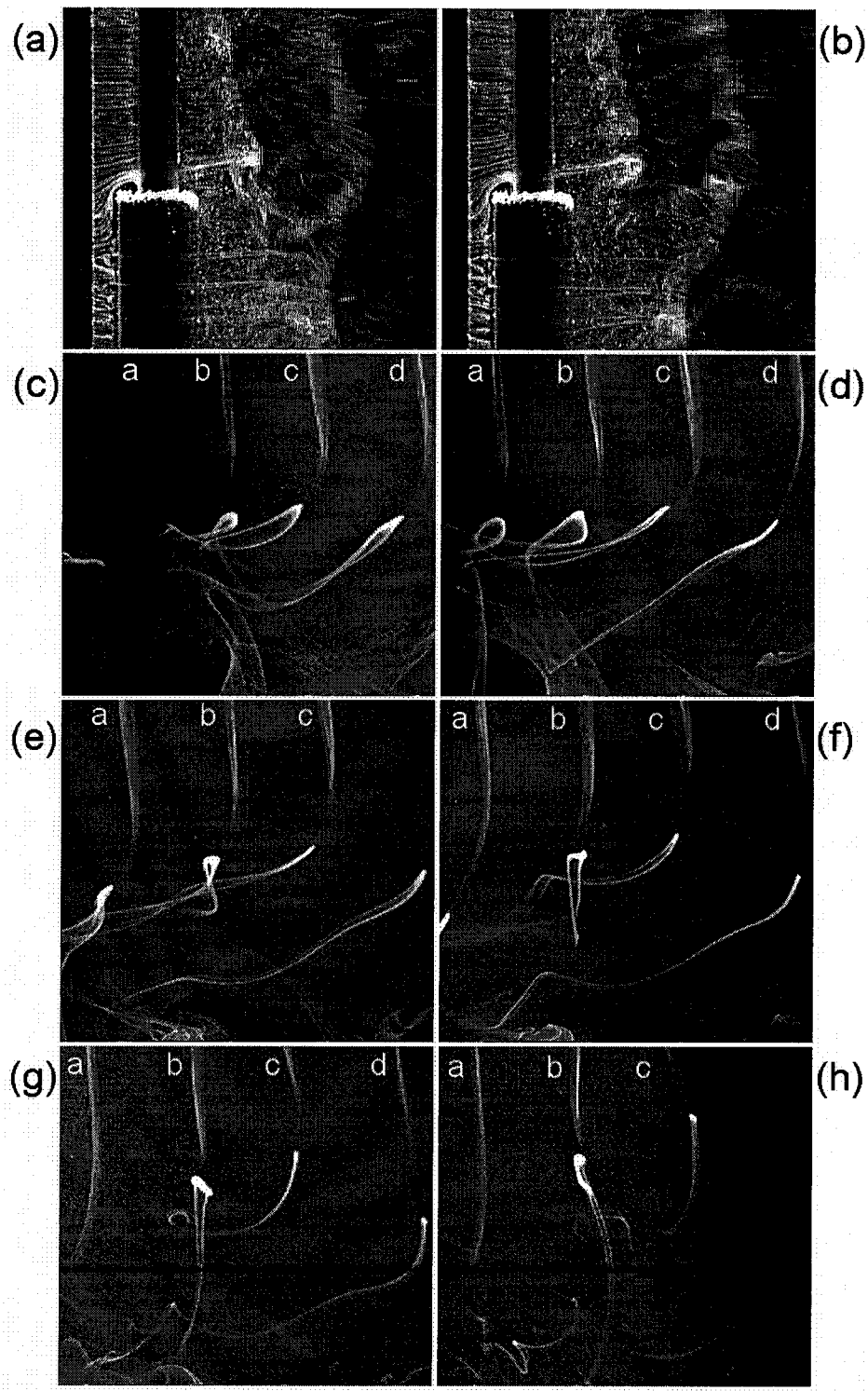

Figure 55: Vortex half-loop downstream progression. (a) and (b): Hydrogen bubbles at Re = 1230. (c) to (h): Lead foil visualization at Re = 118.

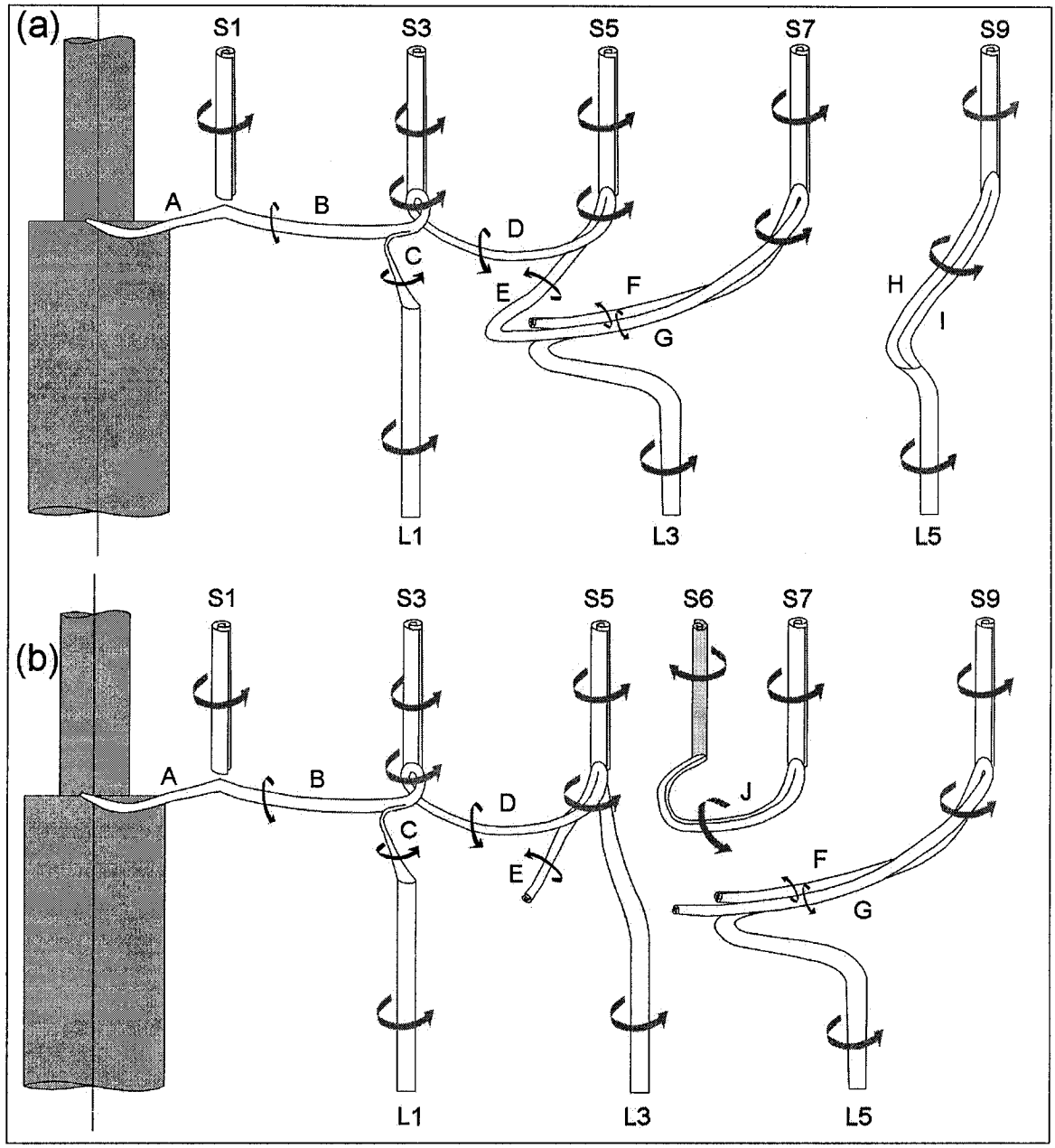

Figure 56: Connections between streamwise vortices and those shed from the small cylinder. (a) Formation of a link between vortices in adjacent cells, (b) a half-loop between vortices in the same high-frequency cell.

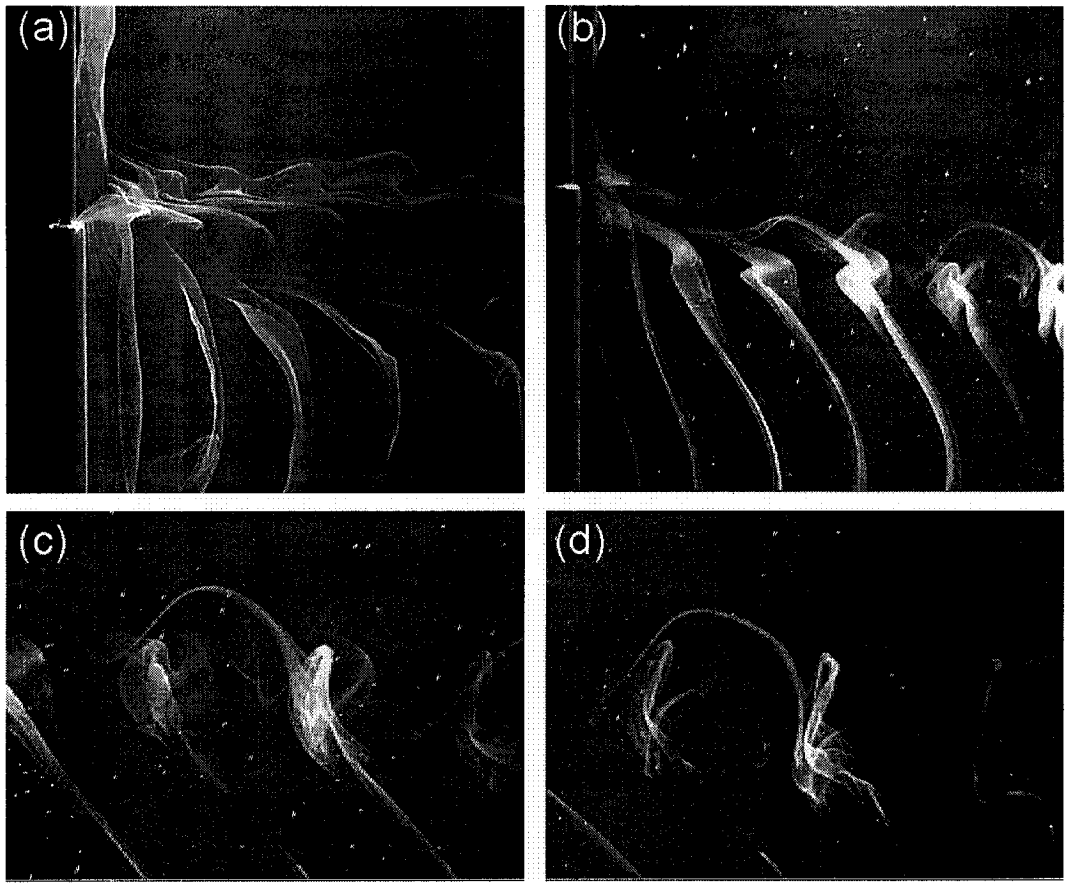

Figure 57: Vortex shedding from only the large cylinder, in uniform flow. Cusps formed near the step and the vortices curved backwards at (a) Re = 80, (b) Re = 63. Half-loops formed downstream at Re = 63 (c) and (d).

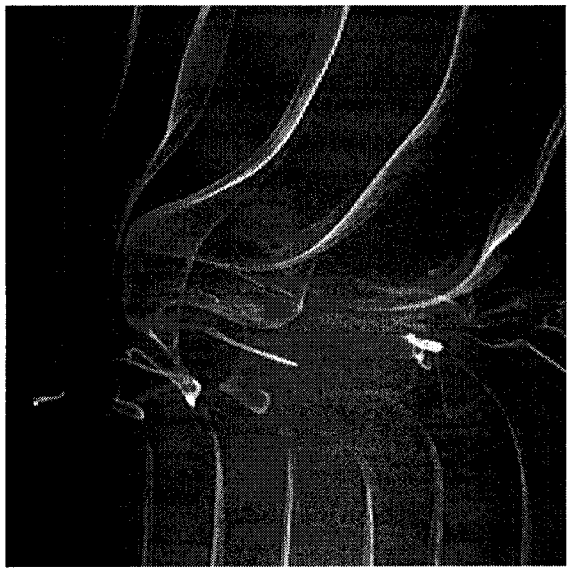

Figure 58: Low-frequency region near the step in uniform flow at Re = 118.

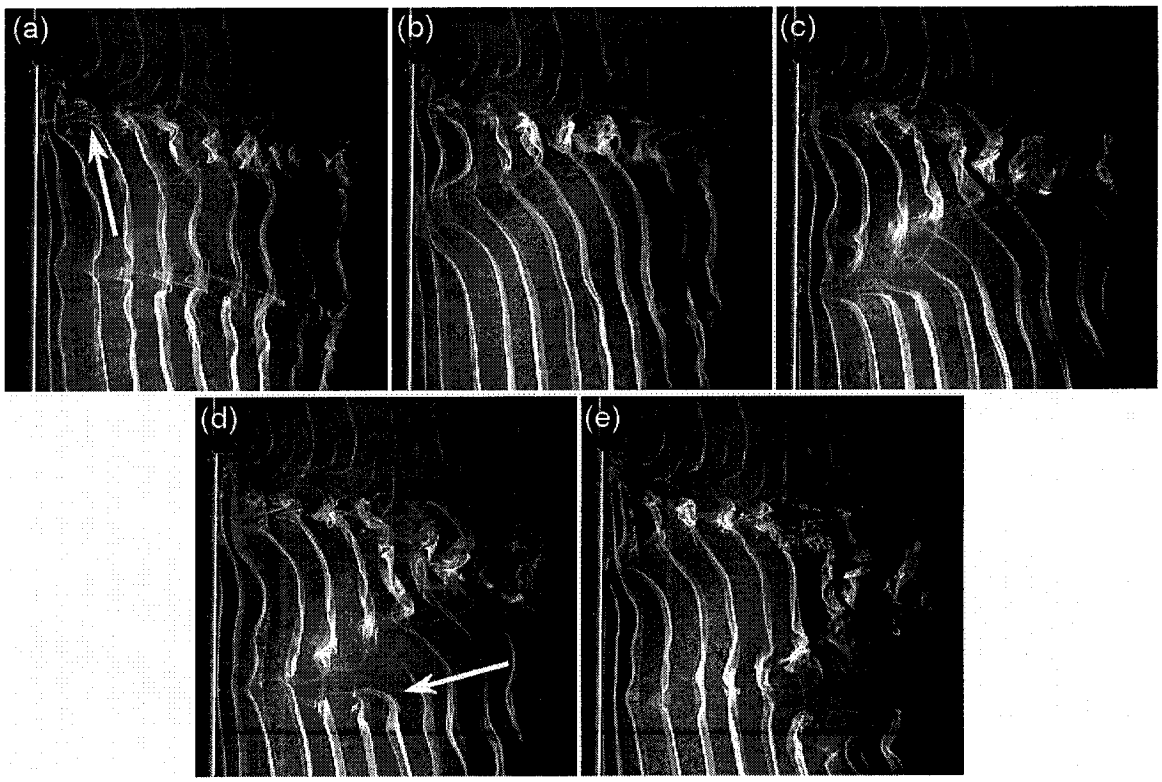

Figure 59: The low-frequency cell near the step of an upright cylinder in uniform flow at Re = 152. (a) Sudden change in vortex inclination, (b) spanwise growth, (c) vortex splitting, (d) boundary and half-loop formation, (e) restart of the cycle.

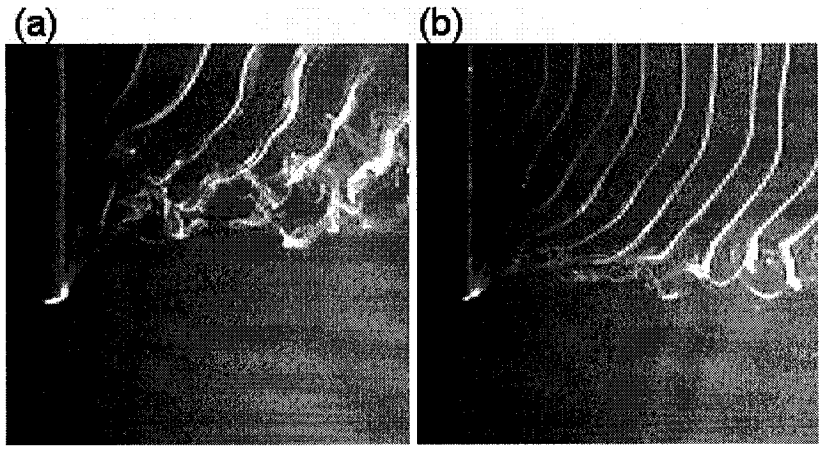

Figure 60: Finite cylinder in uniform flow at (a) Re = 152, (b) Re = 74.

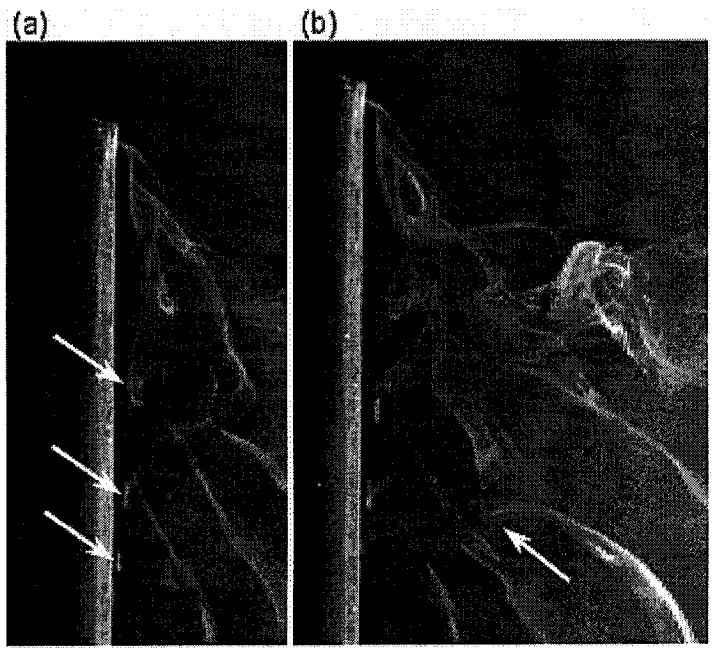

Figure 61: (a) Tip vortices moved spanwise, (b) forming helical connections with the shed vortices. Finite cylinder in uniform flow at Re = 152.

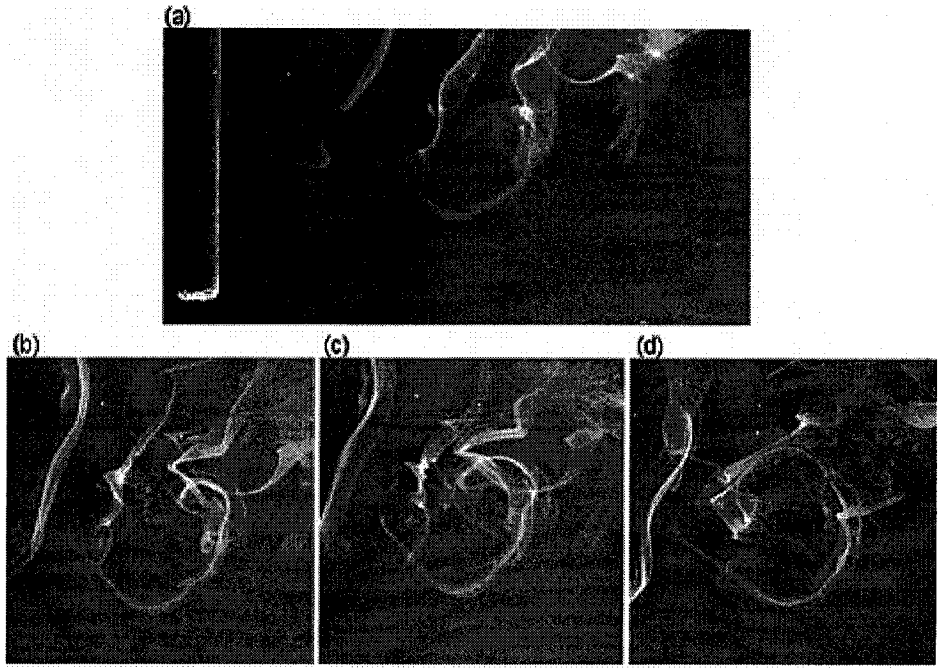

Figure 62: Vortex ends near the cell boundaries were rotated (a) until a full circular loop formed (b-d). Finite cylinder in uniform flow at Re = 152.

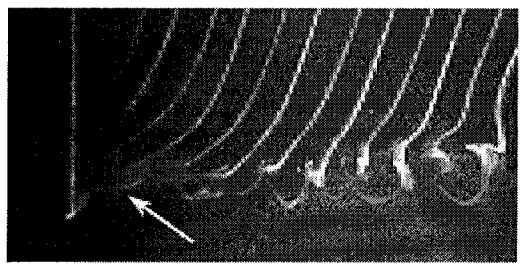

Figure 63: The tip and shed vortices formed cusps and half-loops connected back to the cylinder surface. Finite cylinder in uniform flow at Re = 74.

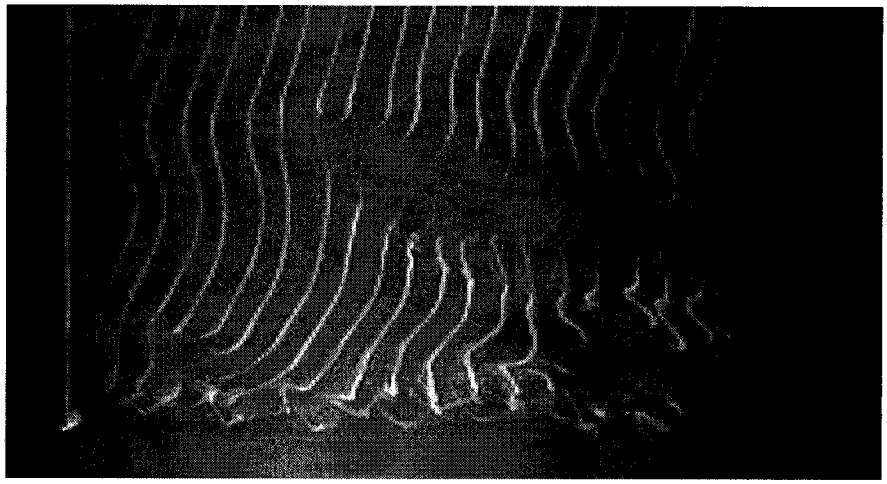

Figure 64: Gaps formed between the cells, where the vortex linkages were weak. Finite cylinder in uniform flow at Re = 74.

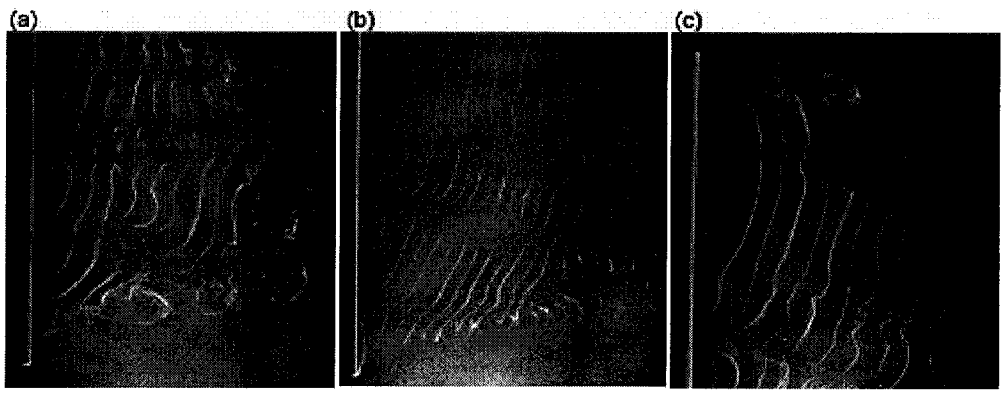

Figure 65: Finite cylinder in shear flow. (a) Re = 152 in the higher-speed section, (b) Re = 74 in the upper portion, (c) Re = 152 in the lower-speed section. See Figure 9h-j for orientation.

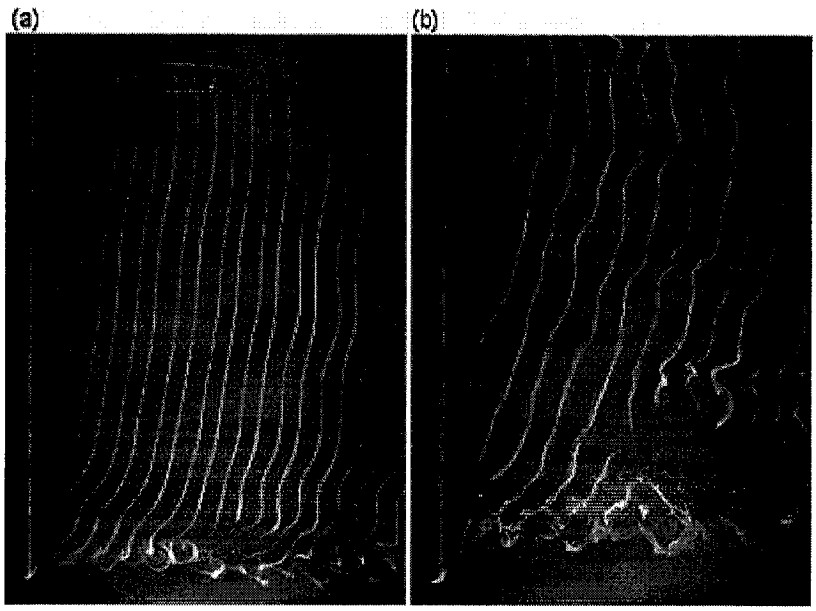

Figure 66: (a) Continuous vortices at Re = 74, (b) while disturbances were visible at Re = 152. Finite cylinder in uniform flow.

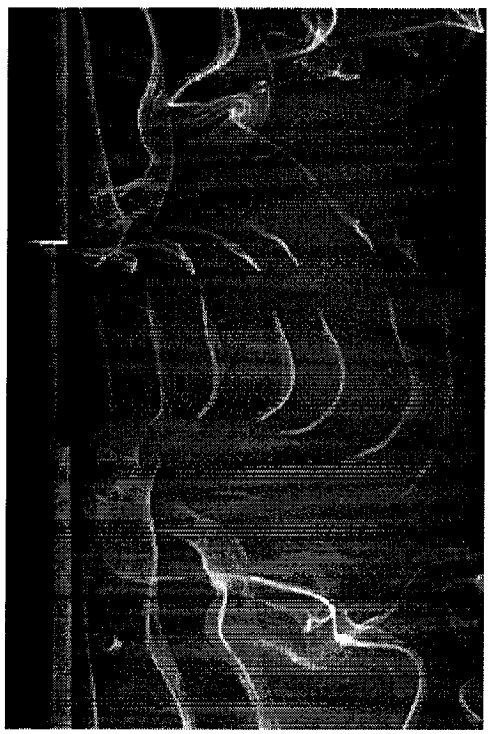

Figure 67: Double-step cylinder with large *AR* middle section, in uniform flow at Re = 118.

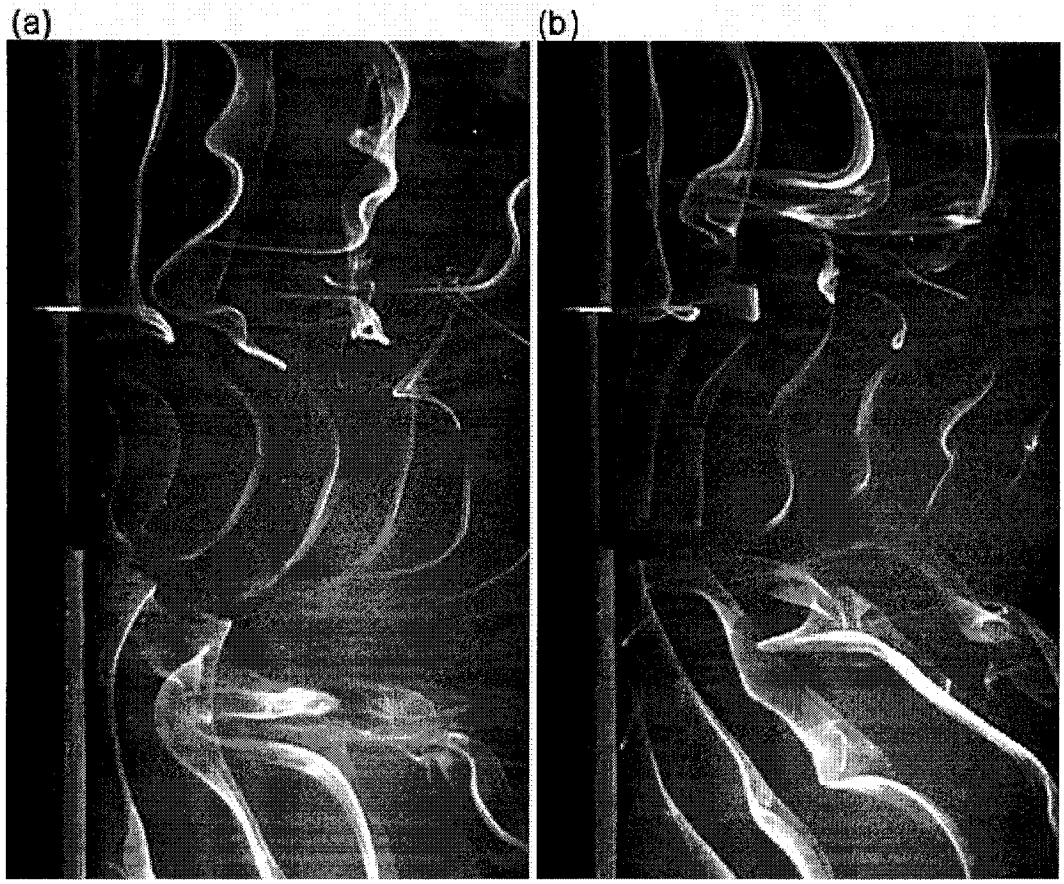

Figure 68: Wake deflection towards (a) the lower cylinder, (b) the upper cylinder. Double-step cylinder with large *AR* middle section in uniform flow at Re = 118.

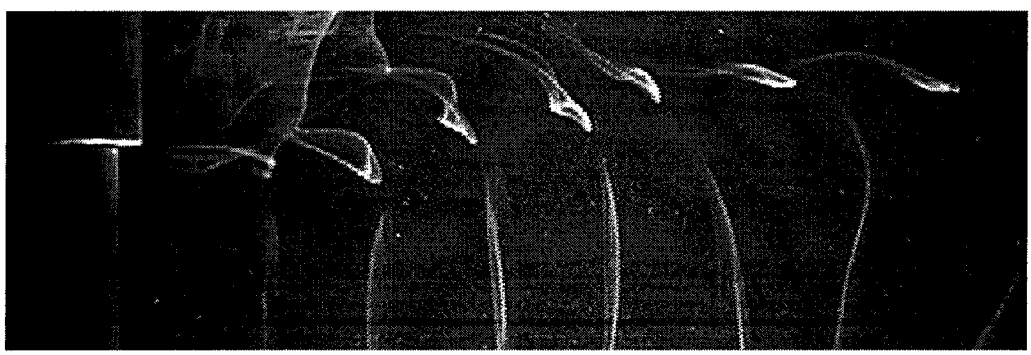

Figure 69: Shed vortices were bent in the streamwise direction until they formed half-loops. Double-step cylinder in uniform flow at Re = 118.

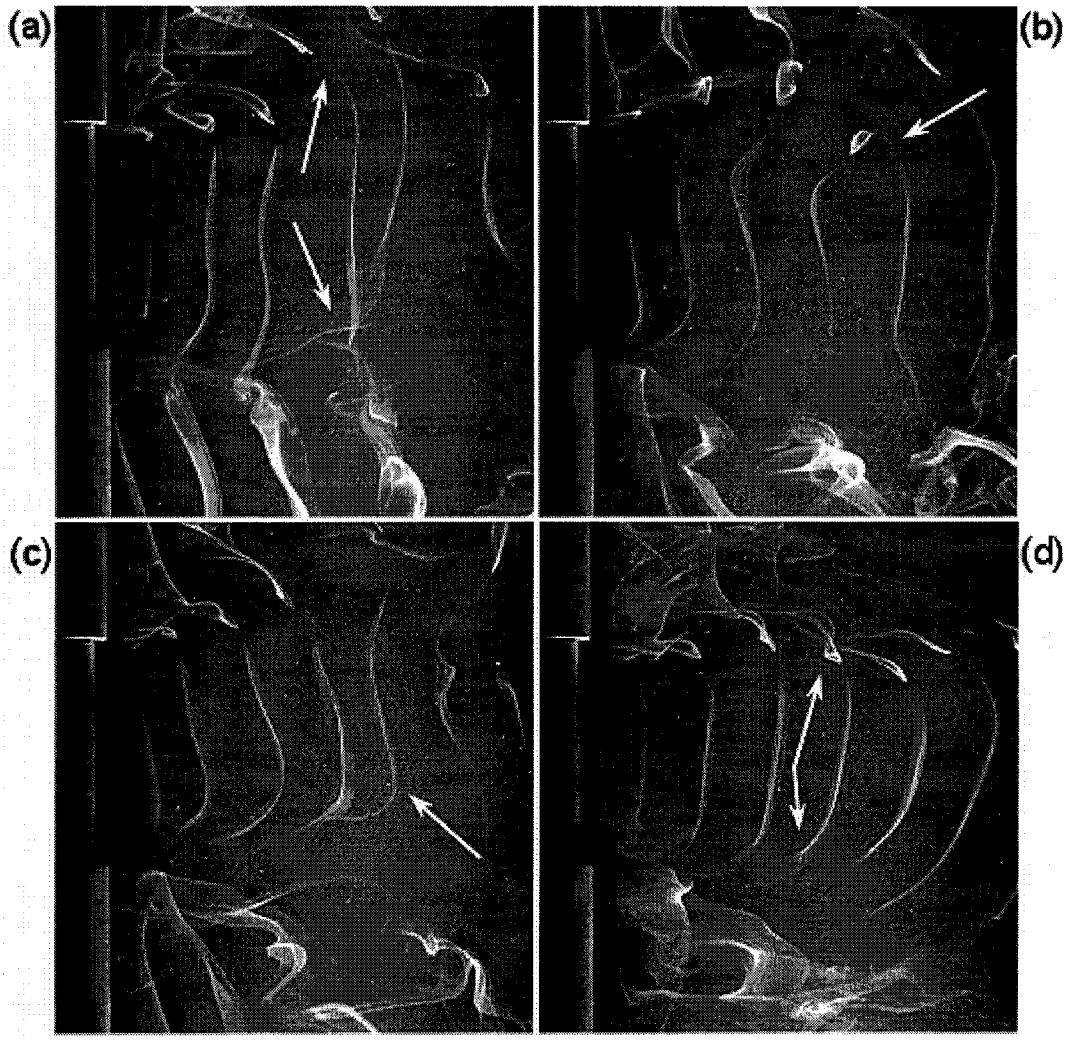

Figure 70: Double-step cylinder in uniform flow at Re = 118. (a) Vortices shed in-phase at both steps, (b) only at the upper step, (c) only at the lower step, (d) out-of-phase at both steps.

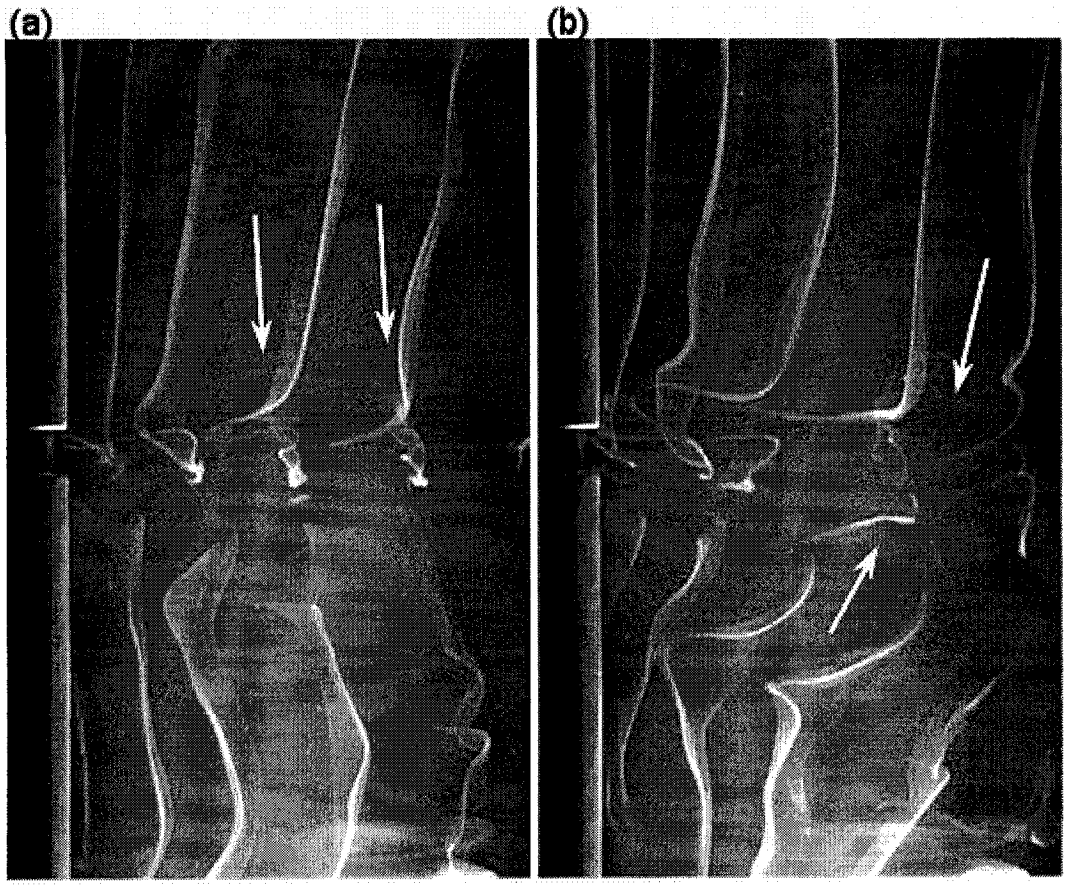

Figure 71: (a) In-phase vortices connected across the steps with only a mild disturbance, (b) out-of-phase vortices formed double half-loops. Double-step cylinder with short aspect ratio middle section in uniform flow at Re = 118.

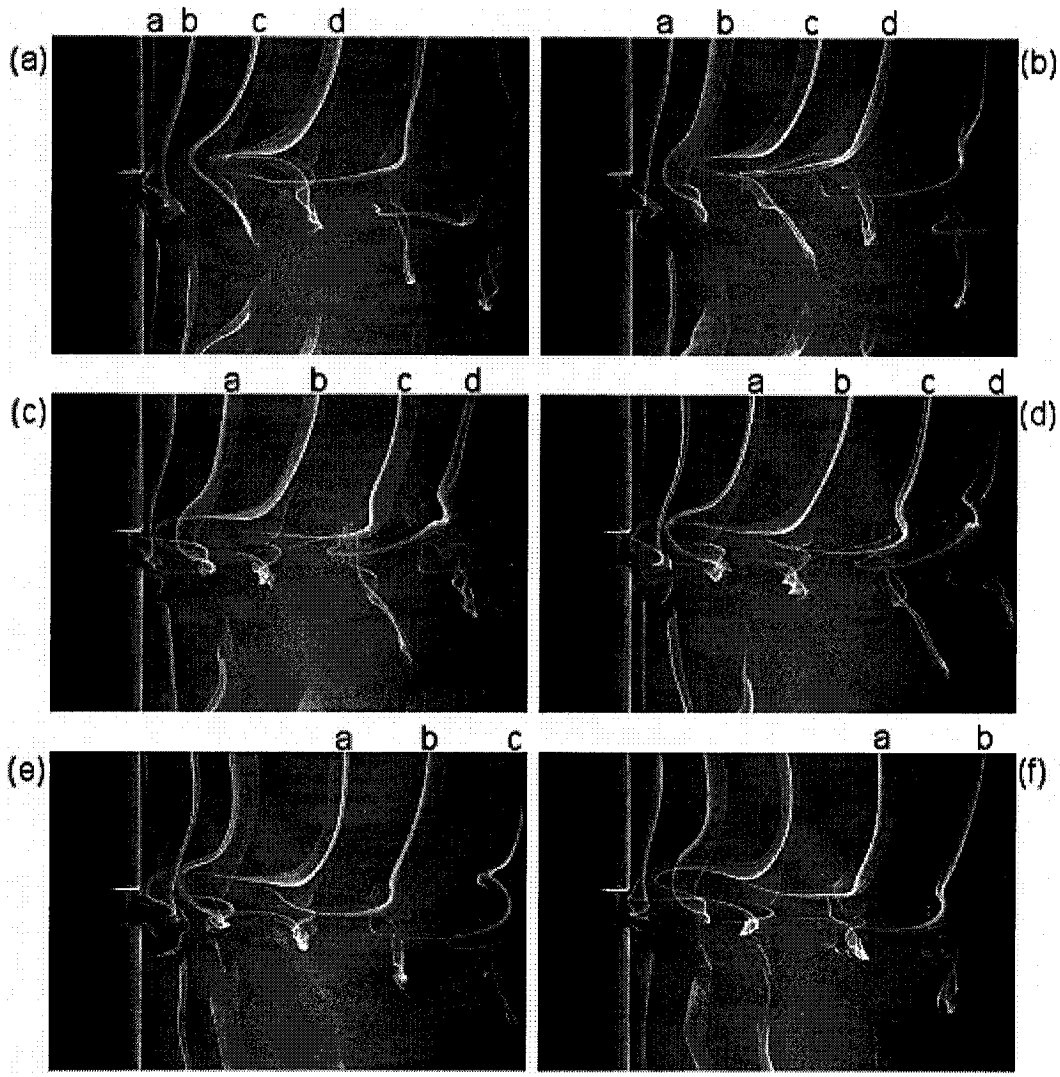

Figure 72: Vortex "b" (a) formed a cusp at the step, (b) began helical twisting, (c) bent back towards the cylinder, (d) disconnected from the vortex in the lower cell, (e) began to loop, and (f) began to connect with vortex "a". Double-step cylinder with short aspect ratio middle section in uniform flow at Re = 118.

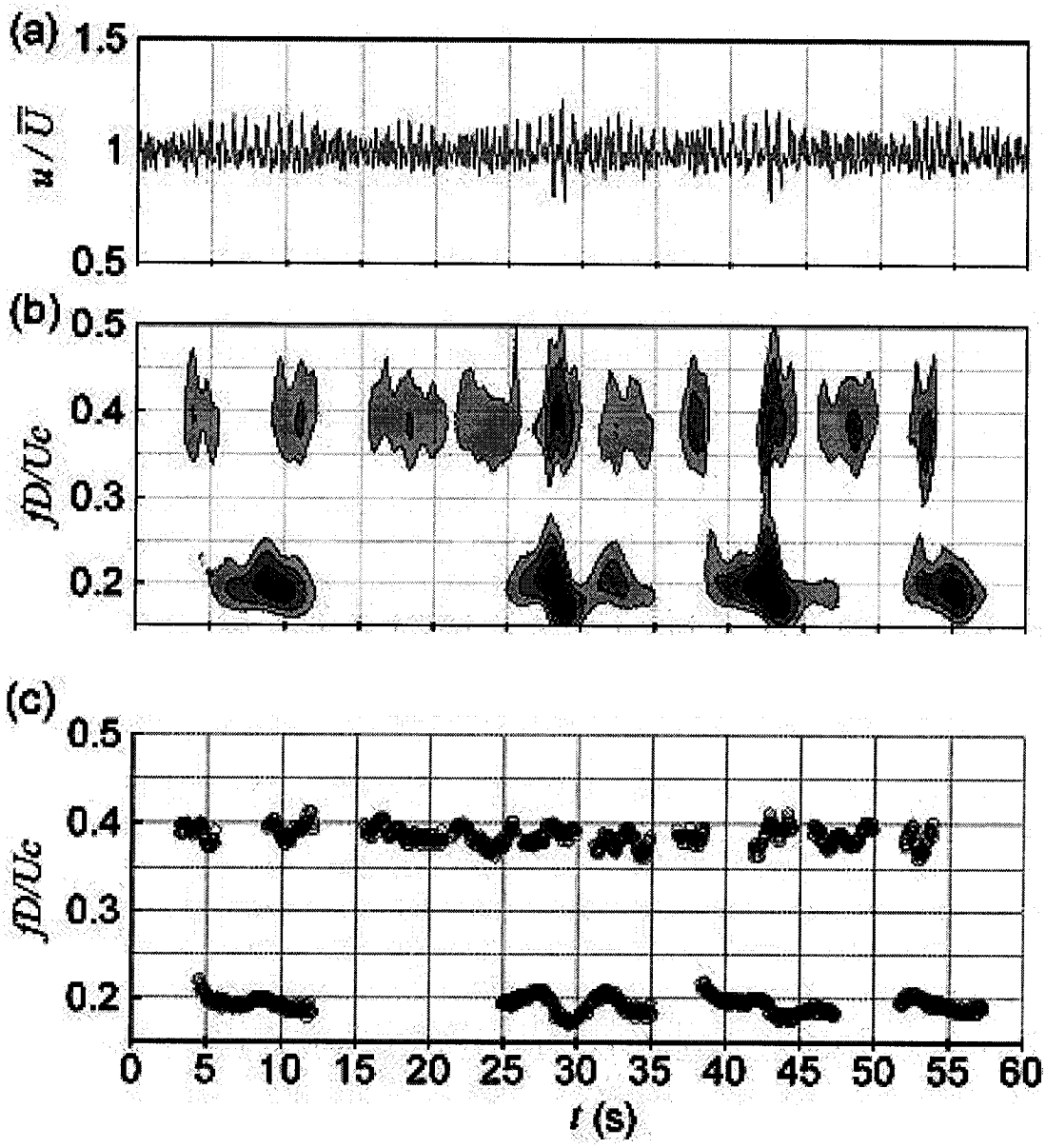

Figure 73: Inverted step cylinder at *y/D* = -0.3 (behind the large cylinder, near the step), Re = 294 in uniform flow. (a) Velocity signal, (b) wavelet map, and (c) peak local frequencies.

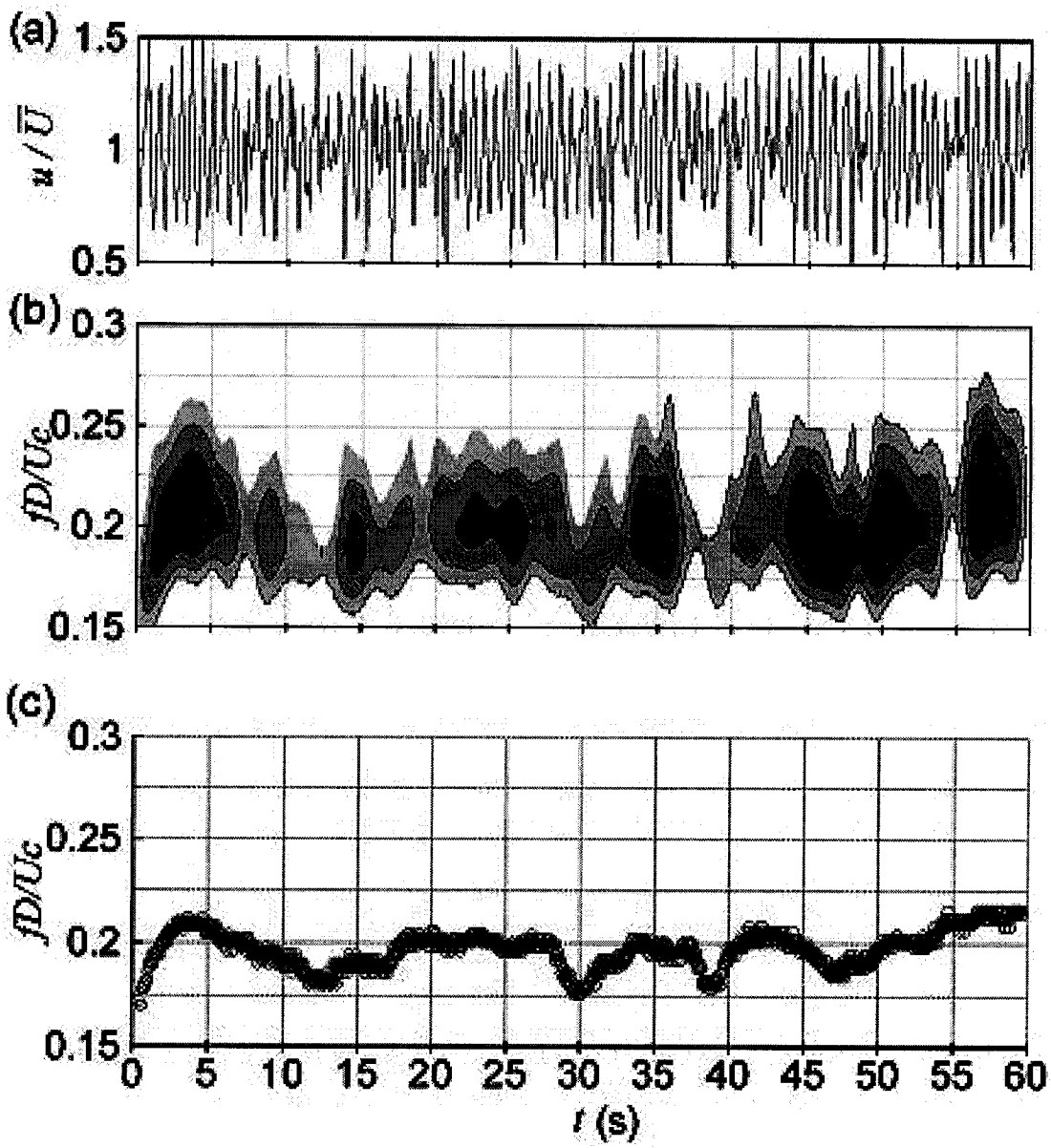

Figure 74: Inverted step cylinder at *y/D* = -6.4 (near the cell boundary behind the large cylinder), Re = 294 in uniform flow. (a) Velocity signal, (b) wavelet map, and (c) peak local frequencies.

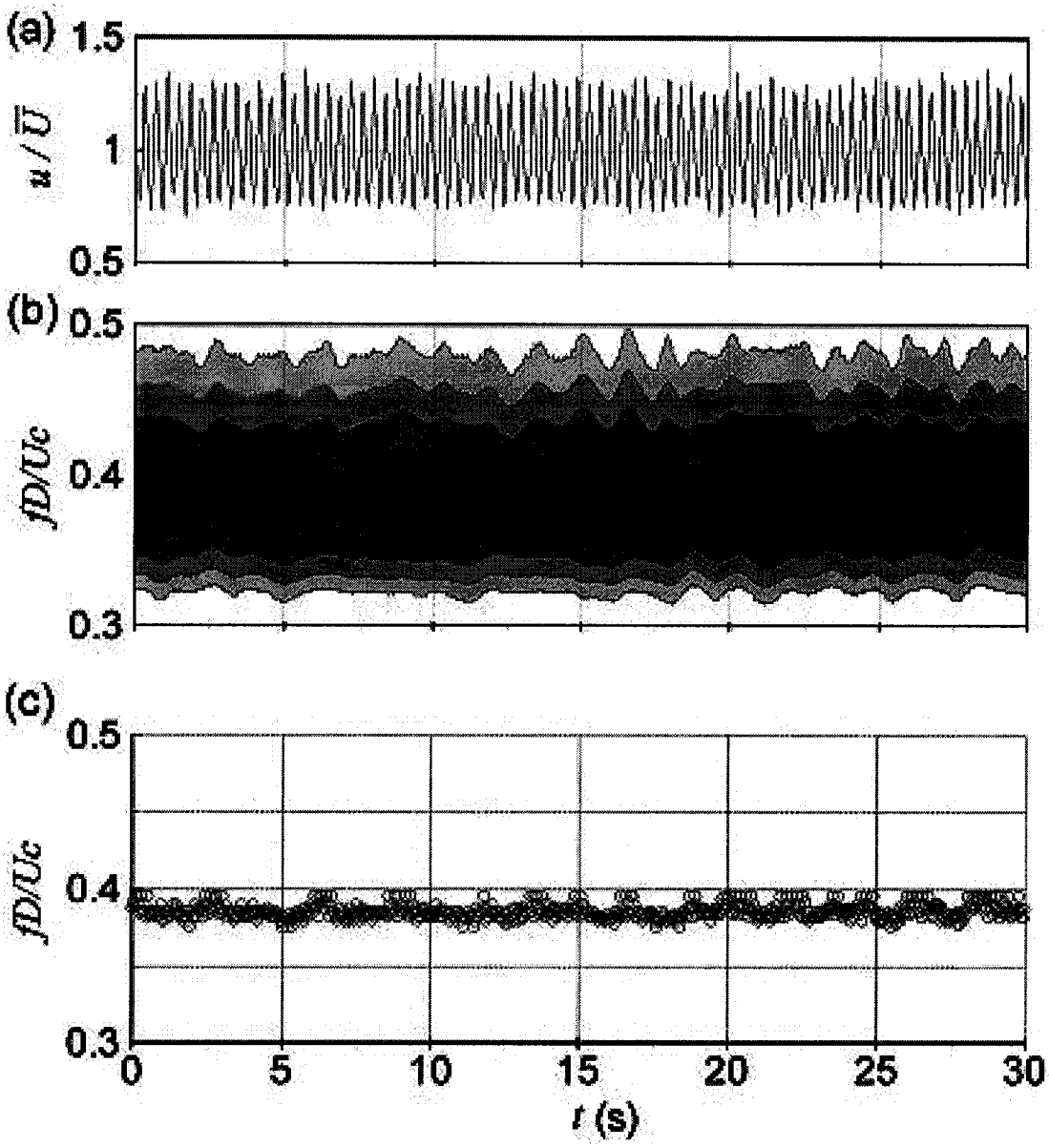

Figure 75: Inverted step cylinder at *y/D* = 1.8 (behind the small cylinder), Re = 294 in uniform flow. (a) Velocity signal, (b) wavelet map, and (c) peak local frequencies.

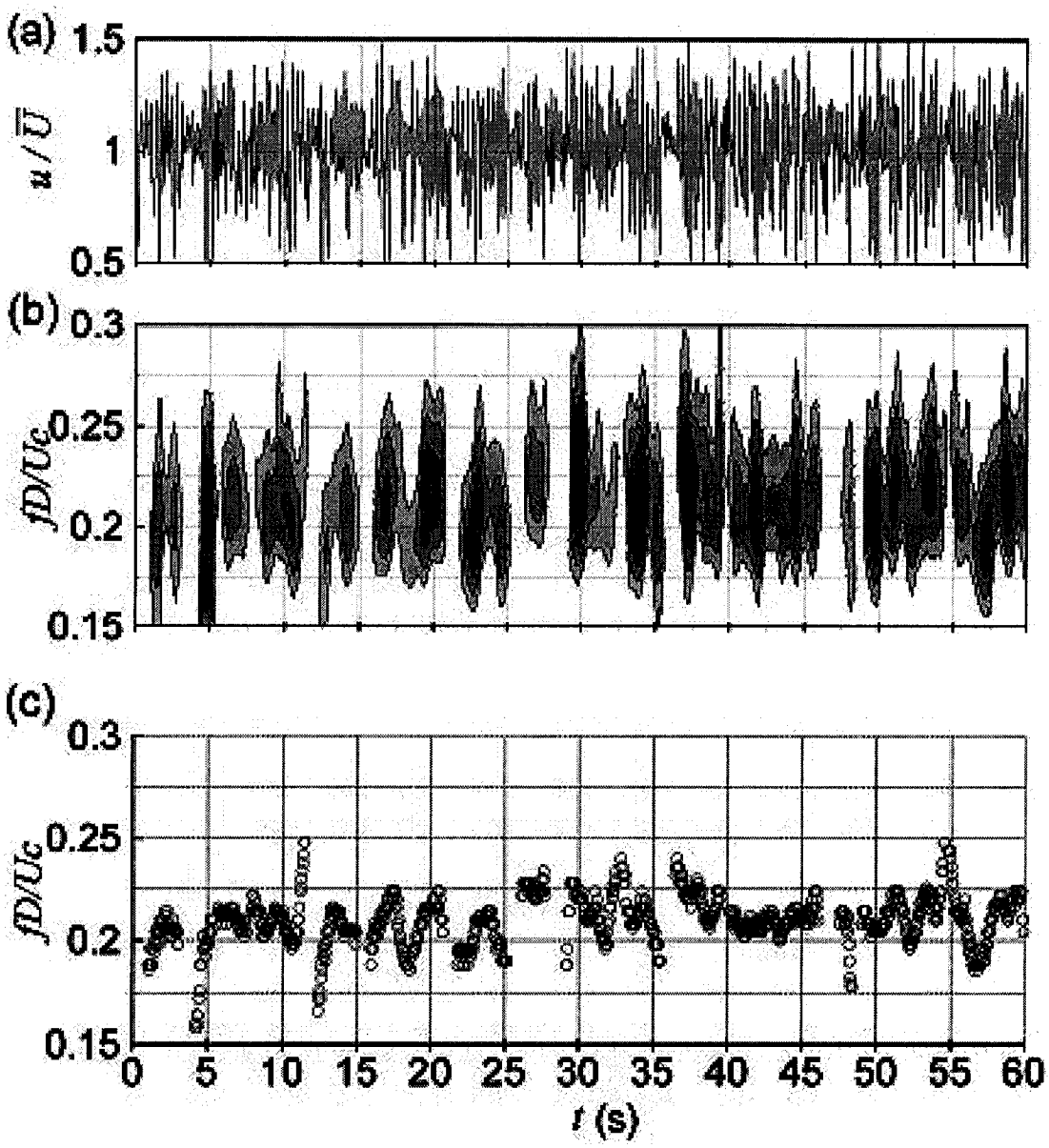

Figure 76: Inverted step cylinder at *y/D* = -4.9 (behind the large cylinder, near the step), Re = 647 in uniform flow. (a) Velocity signal, (b) wavelet map, and (c) peak local frequencies.

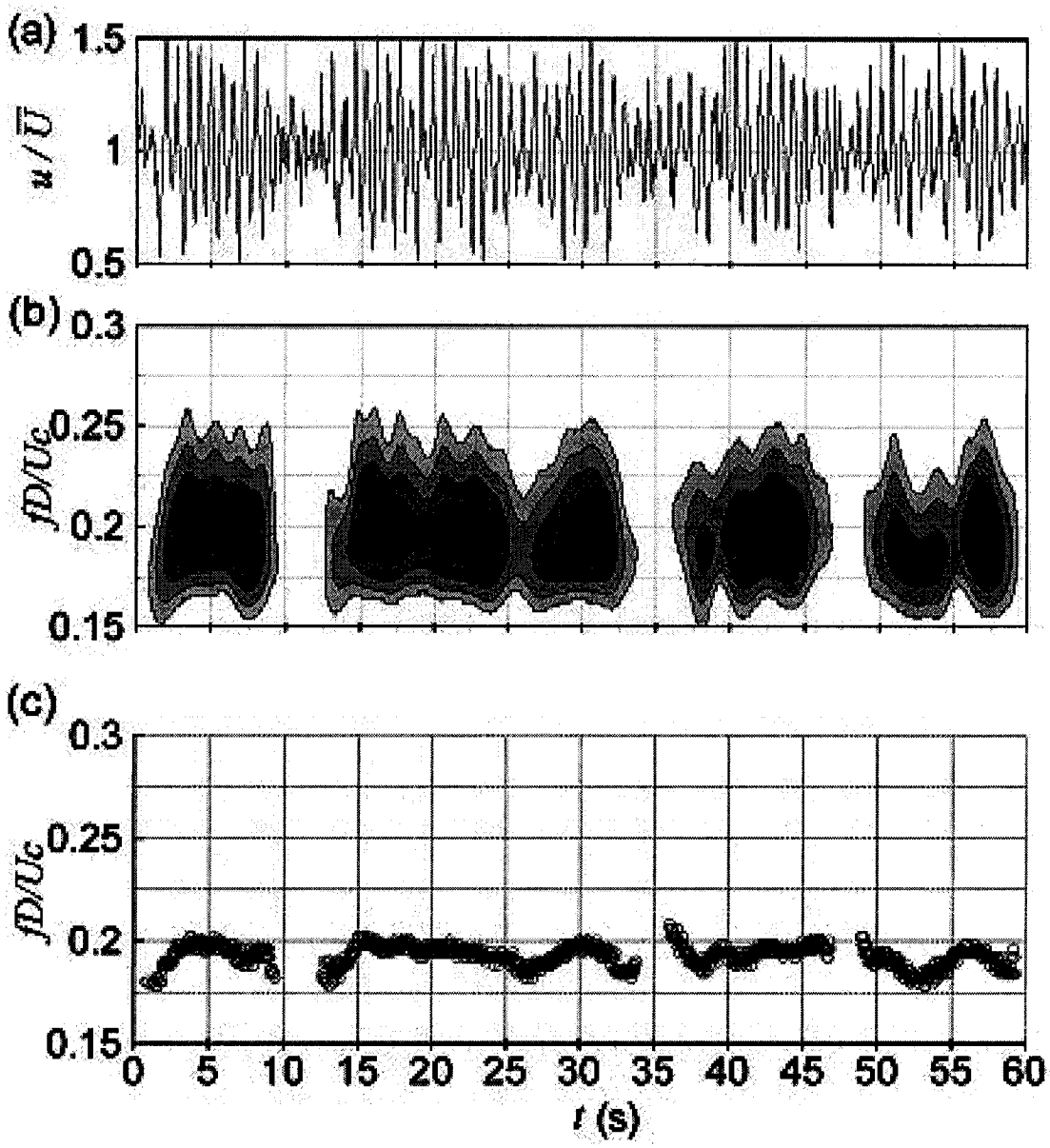

Figure 77: Inverted step cylinder at *y/D* = -3.9 (near the cell boundary behind the large cylinder), Re = 289 in shear flow. (a) Velocity signal, (b) wavelet map, and (c) peak local frequencies.

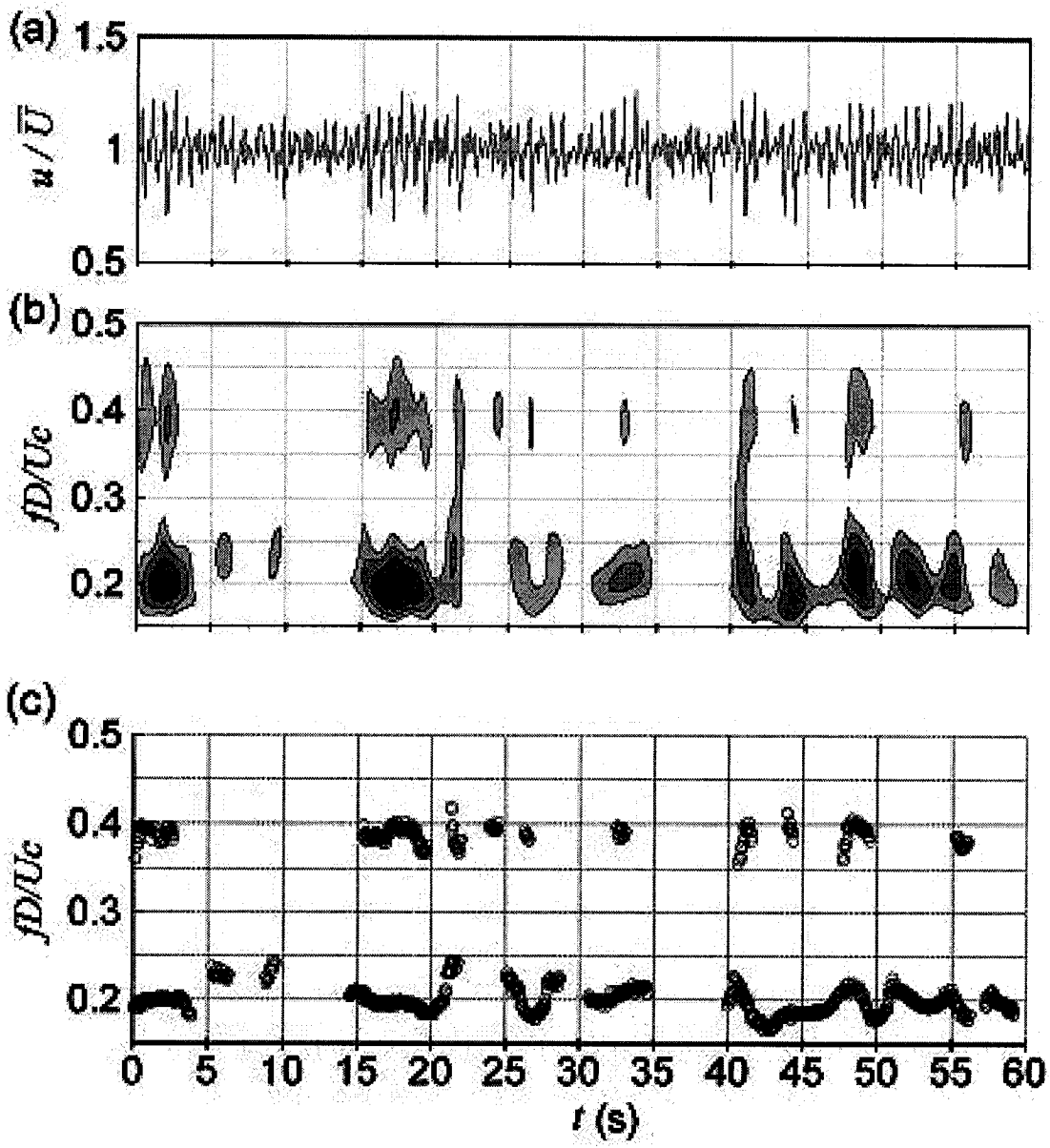

Figure 78: Inverted step cylinder at *y/D* = 0.0 (at the step), Re = 289 in shear flow. (a) Velocity signal, (b) wavelet map, and (c) peak local frequencies.

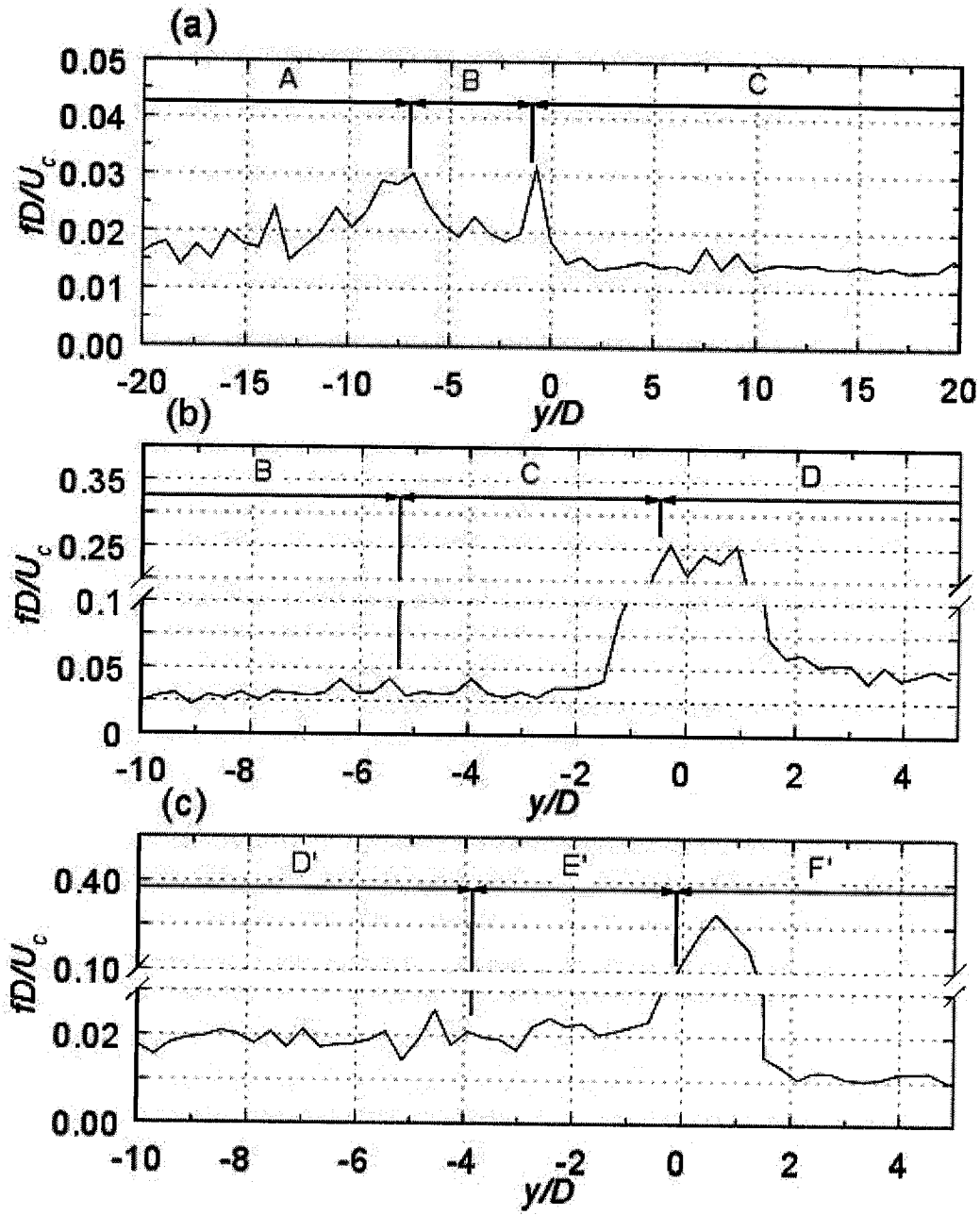

Figure 79: Maximum local frequency deviation from the mean, for an inverted step cylinder. (a) Re = 294 in uniform flow, (b) Re = 647 in uniform flow, (c) Re = 289 in shear flow. The large cylinder was located at y/D <0.

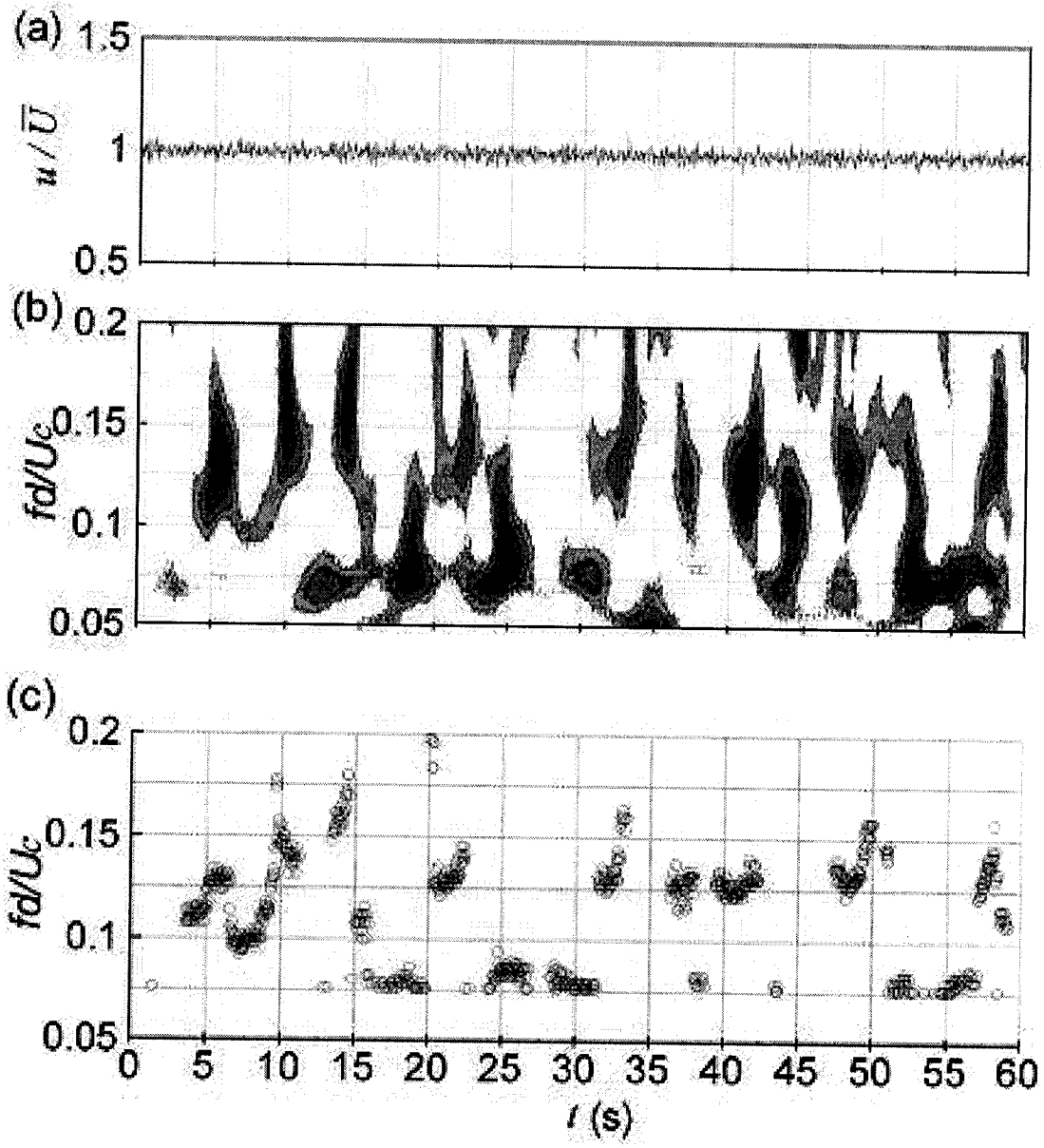

Figure 80: Finite cylinder at y/d = 1.2, Re = 152 in uniform flow. (a) Velocity signal, (b) wavelet map, and (c) peak local frequencies.

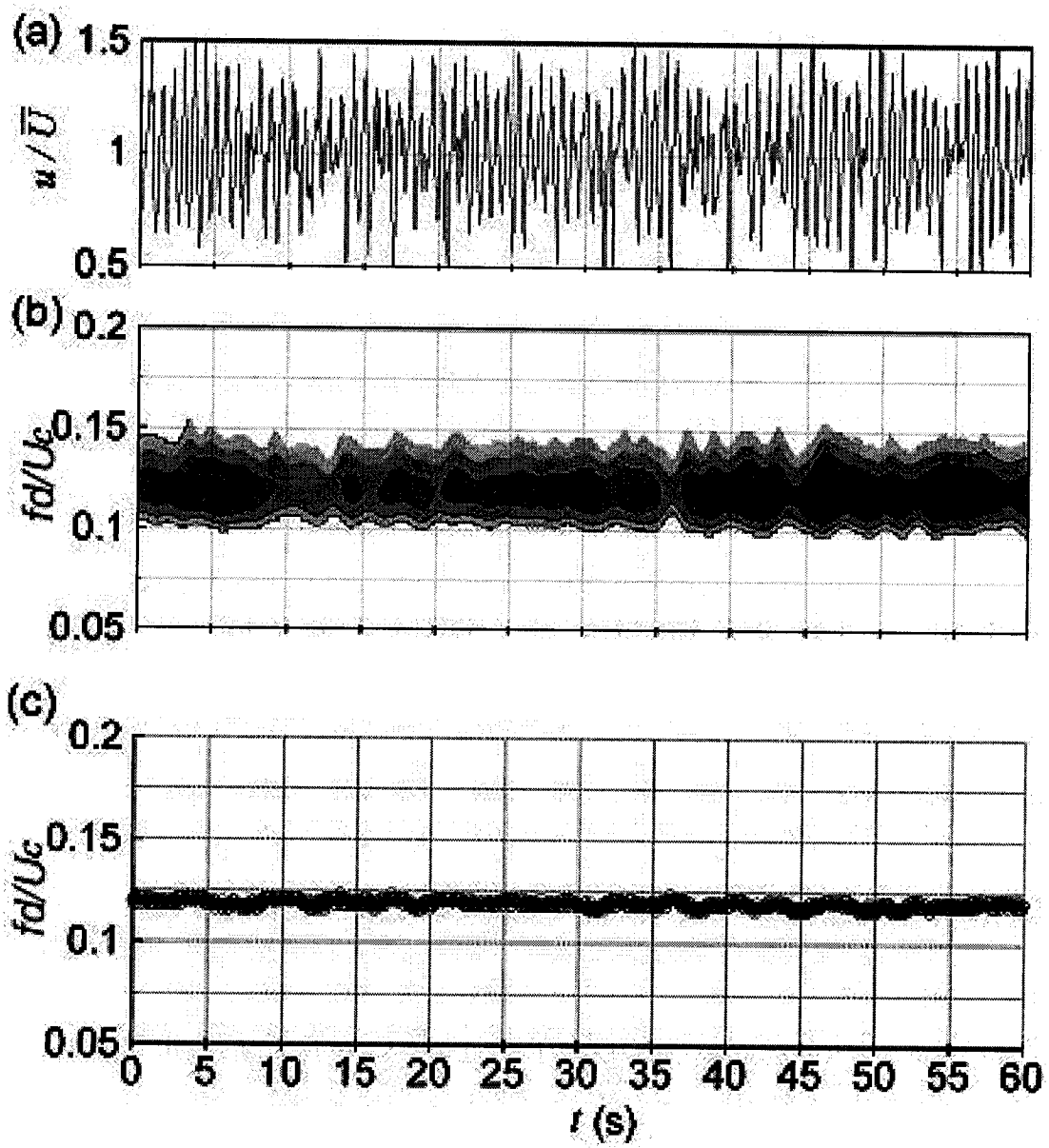

Figure 81: Finite cylinder at y/d = 4.1, Re = 152 in uniform flow. (a) Velocity signal, (b) wavelet map, and (c) peak local frequencies.

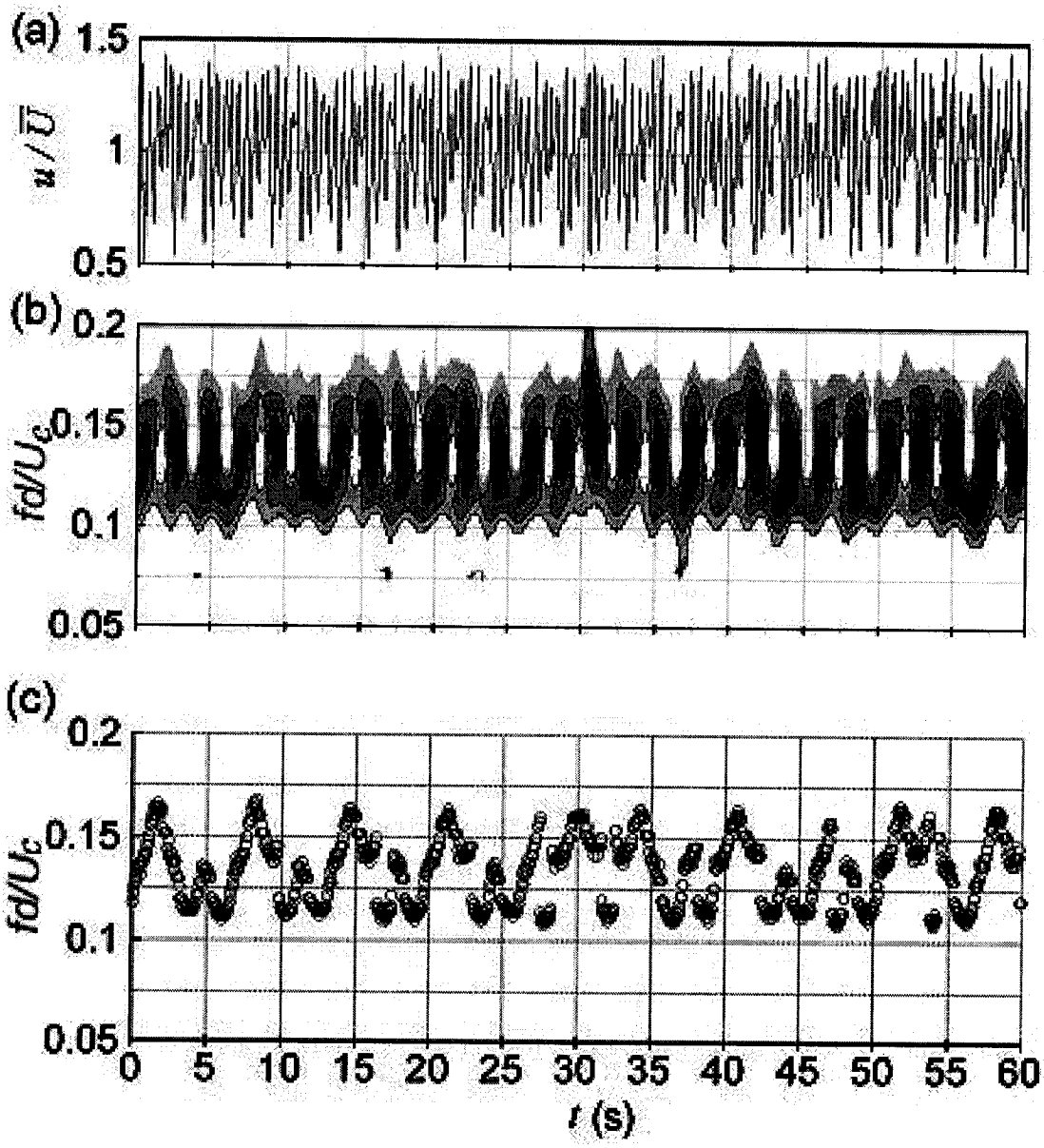

Figure 82: Finite cylinder at y/d = 11.1, Re = 152 in uniform flow. (a) Velocity signal, (b) wavelet map, and (c) peak local frequencies.

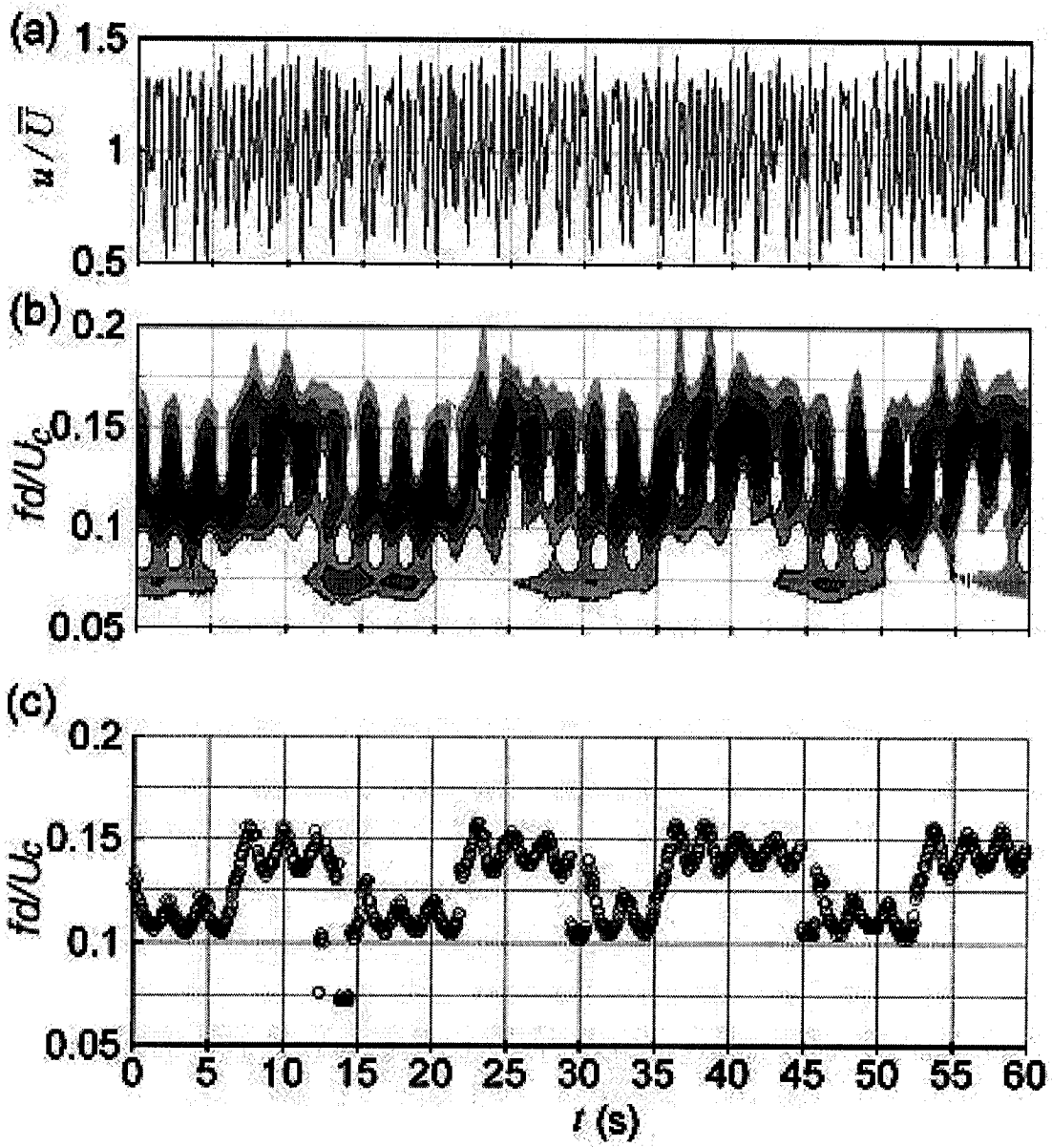

Figure 83: Finite cylinder at *y/d* = 12.8, Re = 159 in shear flow. (a) Velocity signal, (b) wavelet map, and (c) peak local frequencies.

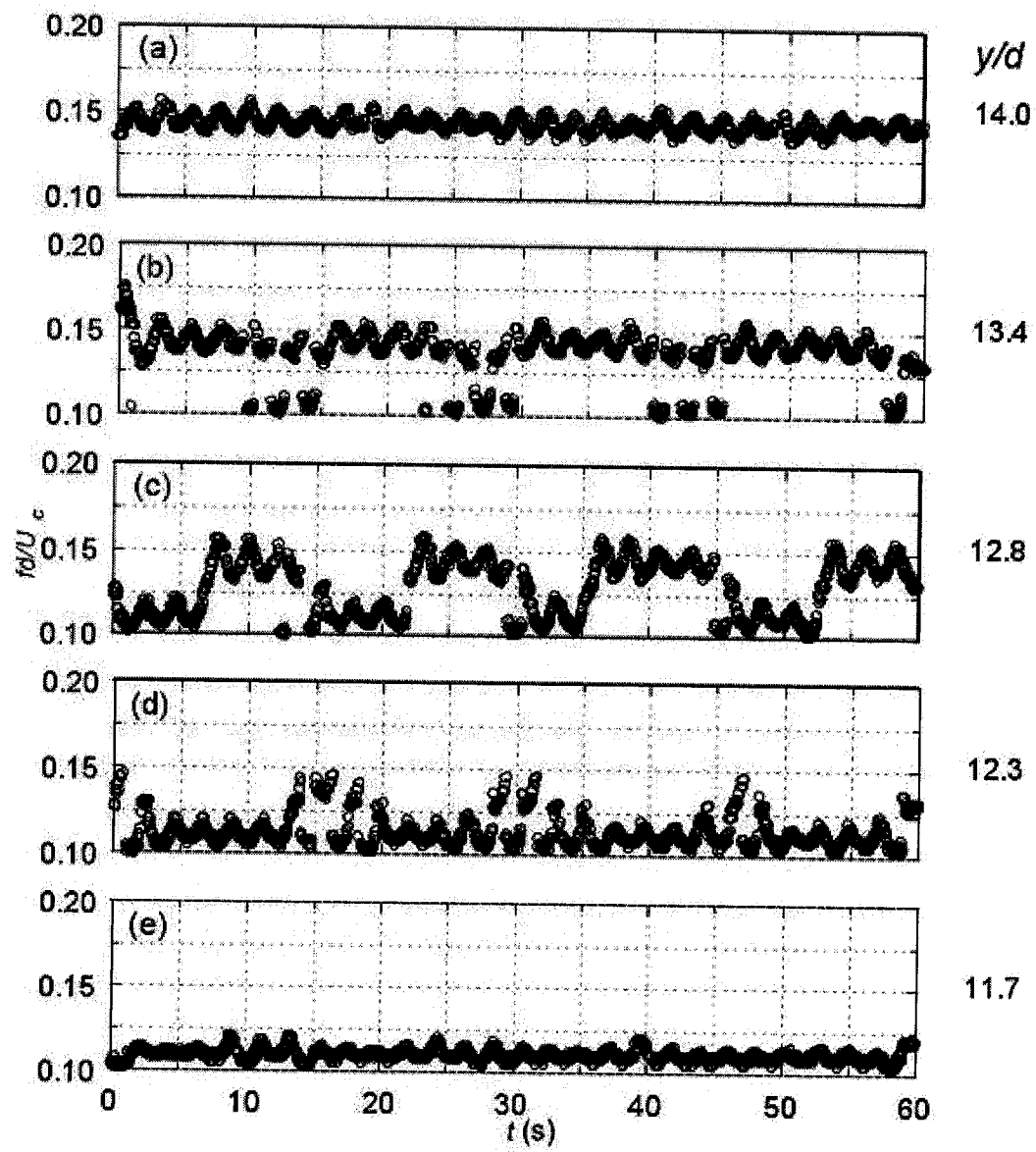

Figure 84: Peak local frequencies behind a finite cylinder Re = 159 in shear flow, where the velocity increased with increasing y/d.

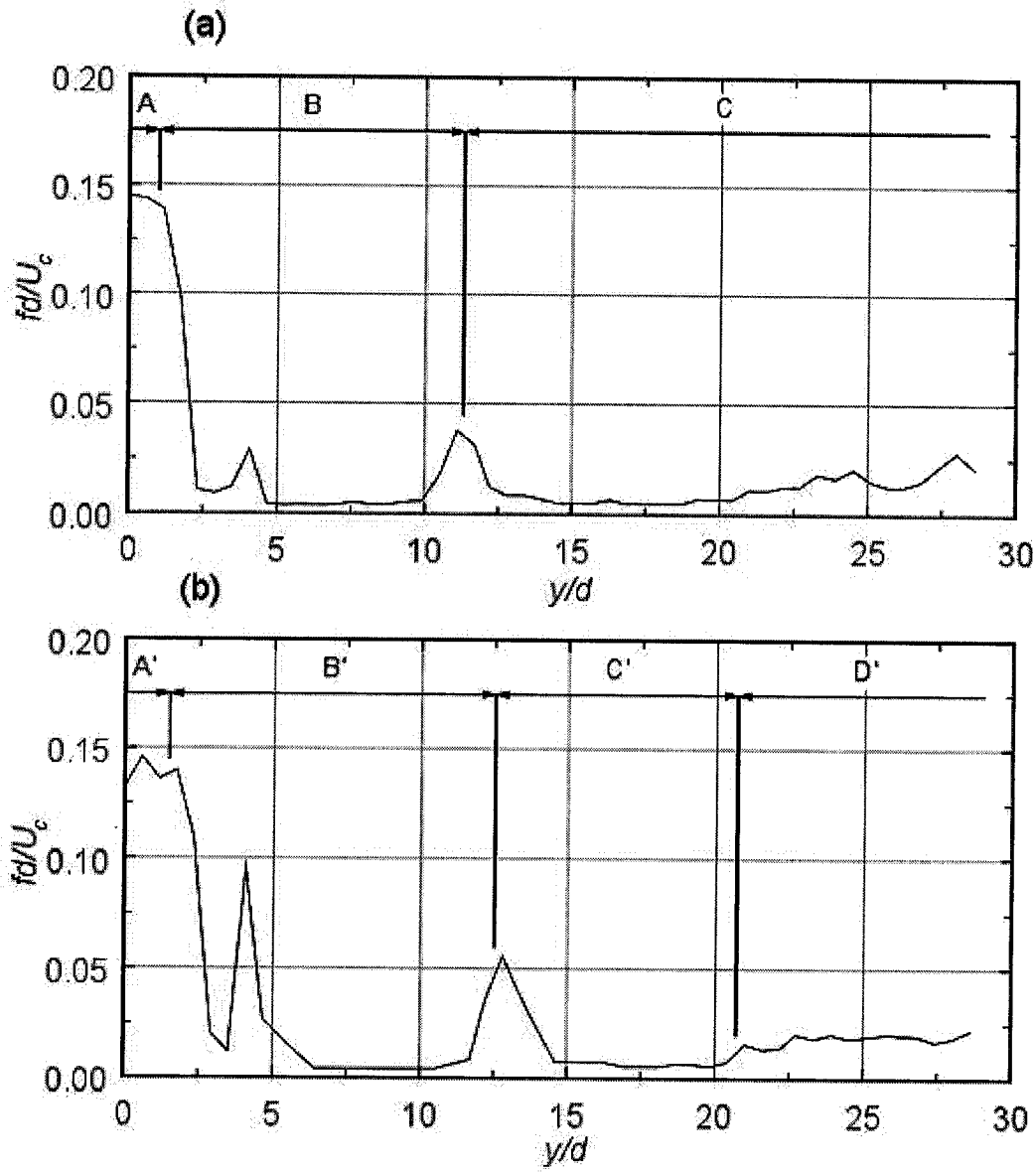

Figure 85: : Maximum local frequency deviation from the mean, for a finite cylinder. (a) Uniform flow at Re = 152, (b) Shear flow at Re = 159, where the velocity increased with increasing *y/d*.

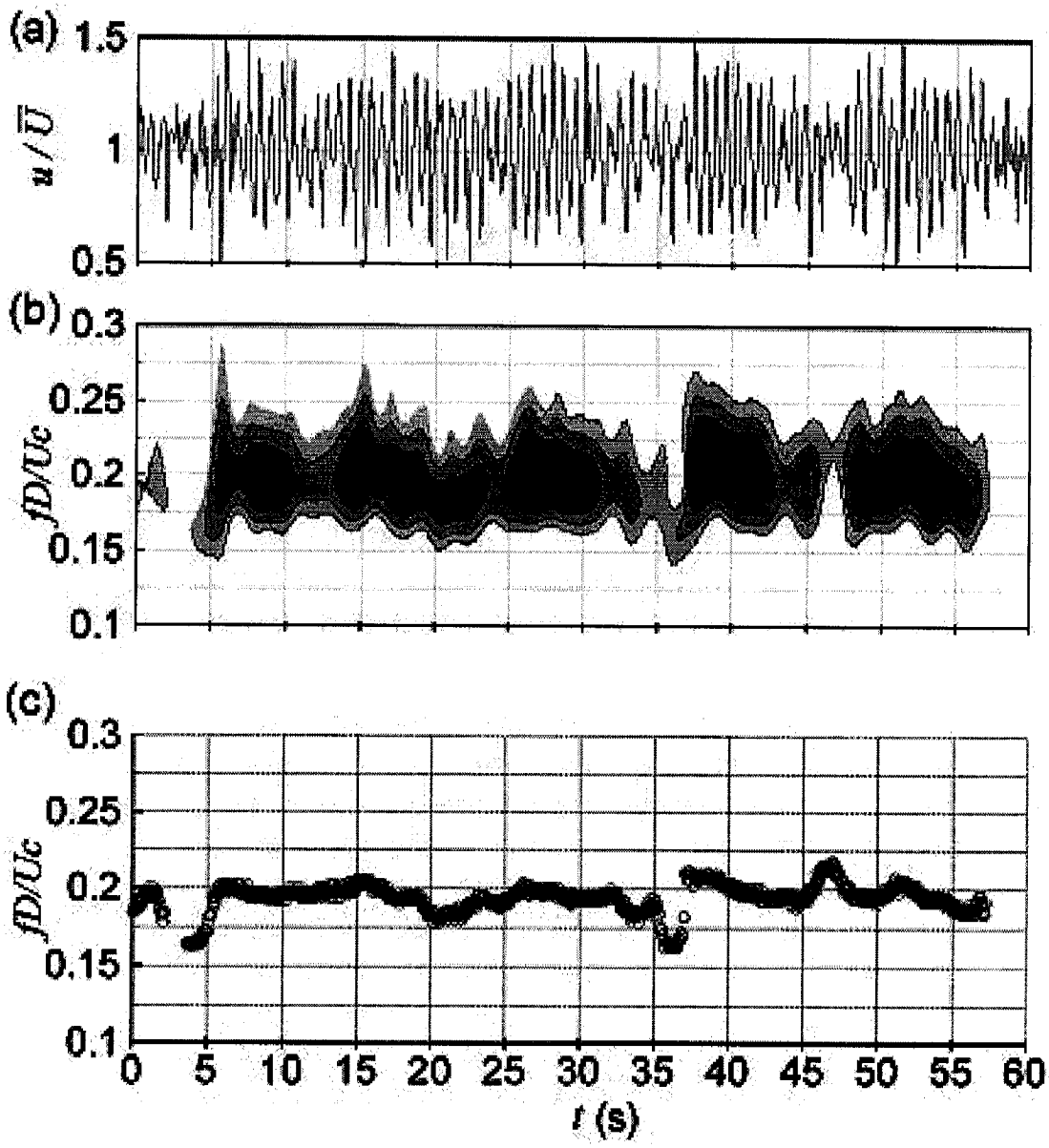

Figure 86: Small double-step cylinder with large *AR* middle section at *y/D* = -5.8 (near the cell boundary behind the lower large cylinder), Re = 295 in uniform flow. (a) Velocity signal, (b) wavelet map, and (c) peak local frequencies.

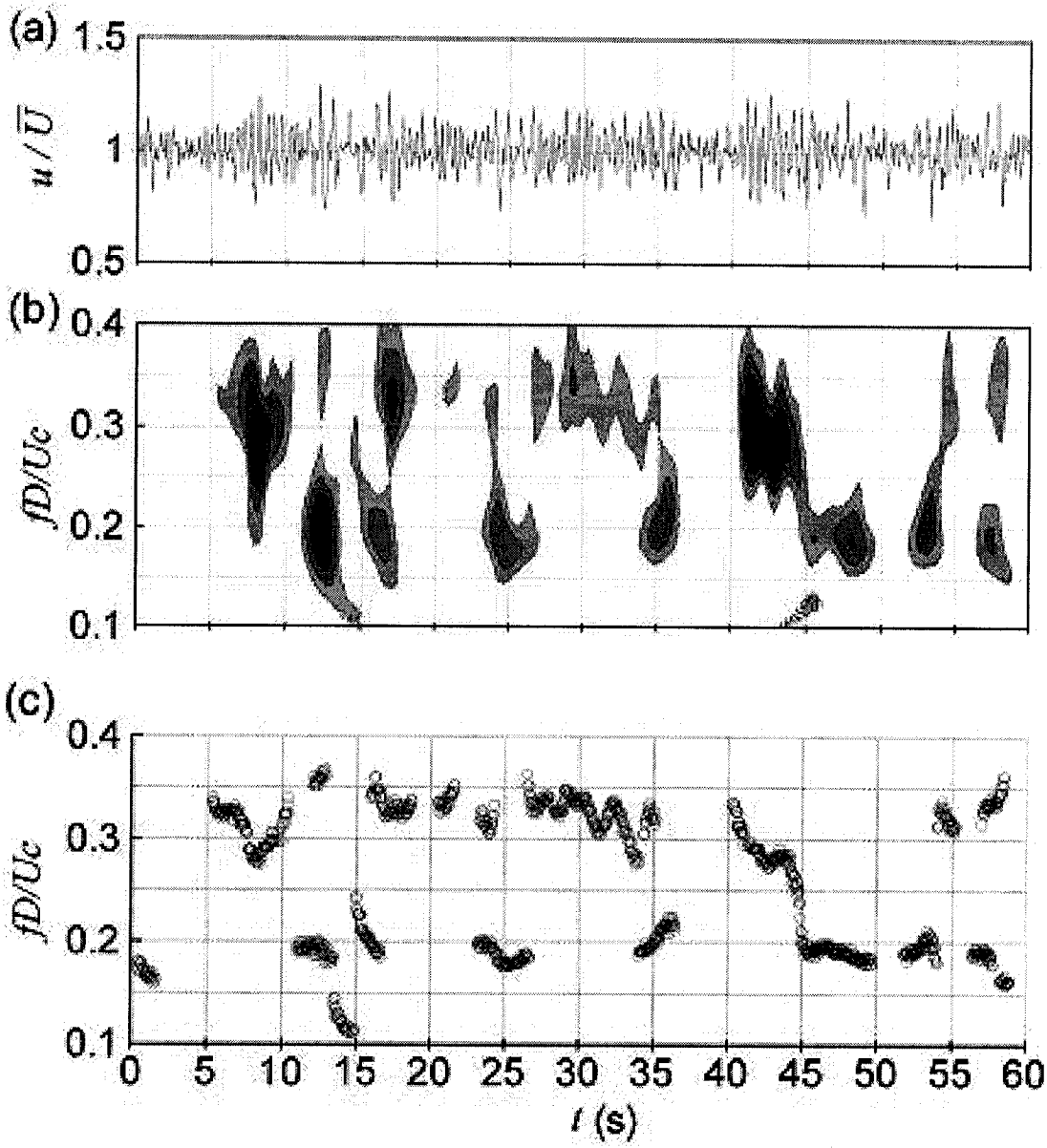

Figure 87: Small double-step cylinder with large *AR* middle section at *y/D* = -0.3 (behind the large cylinder, near the lower step), Re = 295 in uniform flow. (a) Velocity signal, (b) wavelet map, and (c) peak local frequencies.

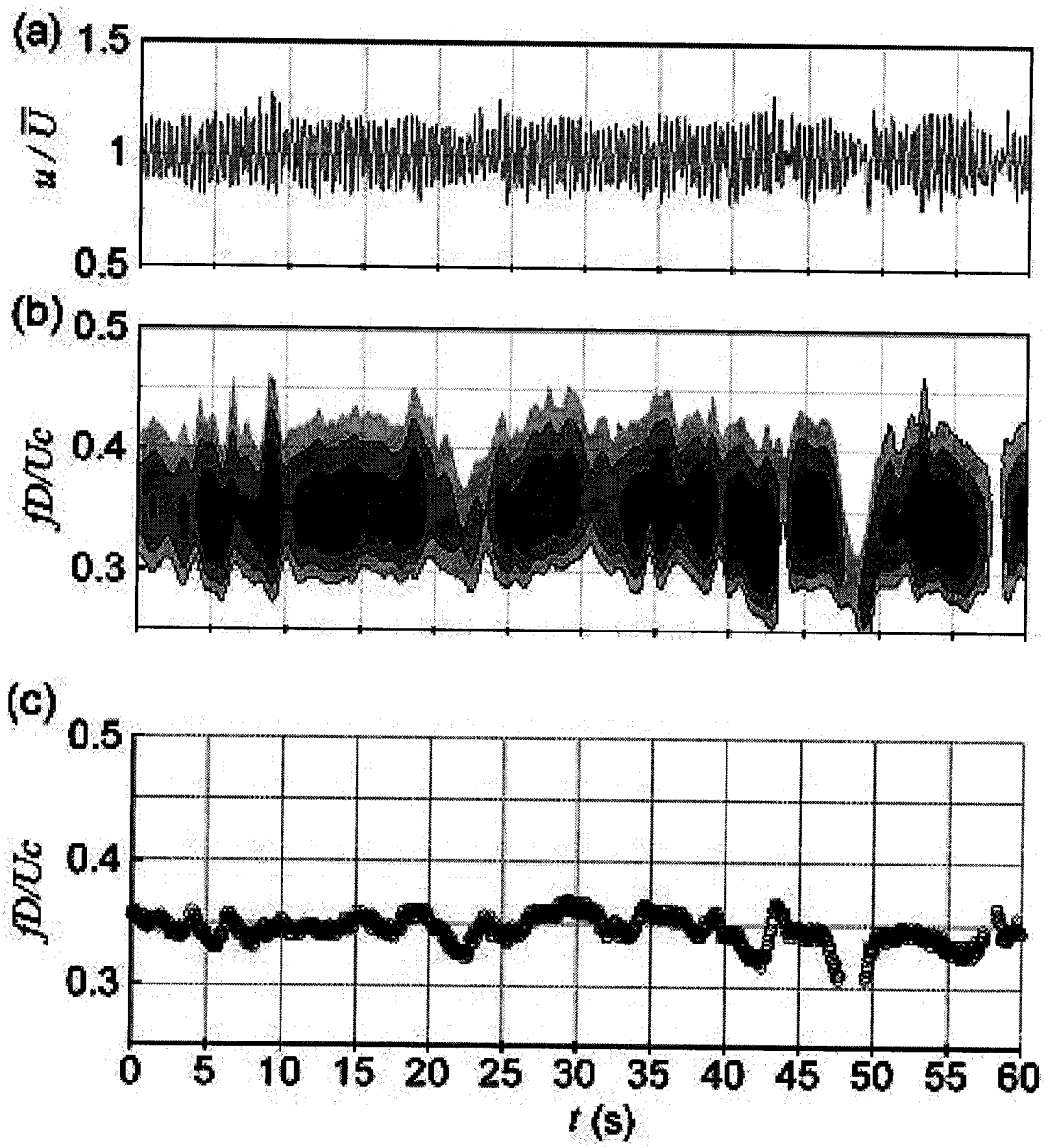

Figure 88: Small double-step cylinder with large *AR* middle section at *y/D* = 5.2 (behind the small cylinder), Re = 295 in uniform flow. (a) Velocity signal, (b) wavelet map, and (c) peak local frequencies.

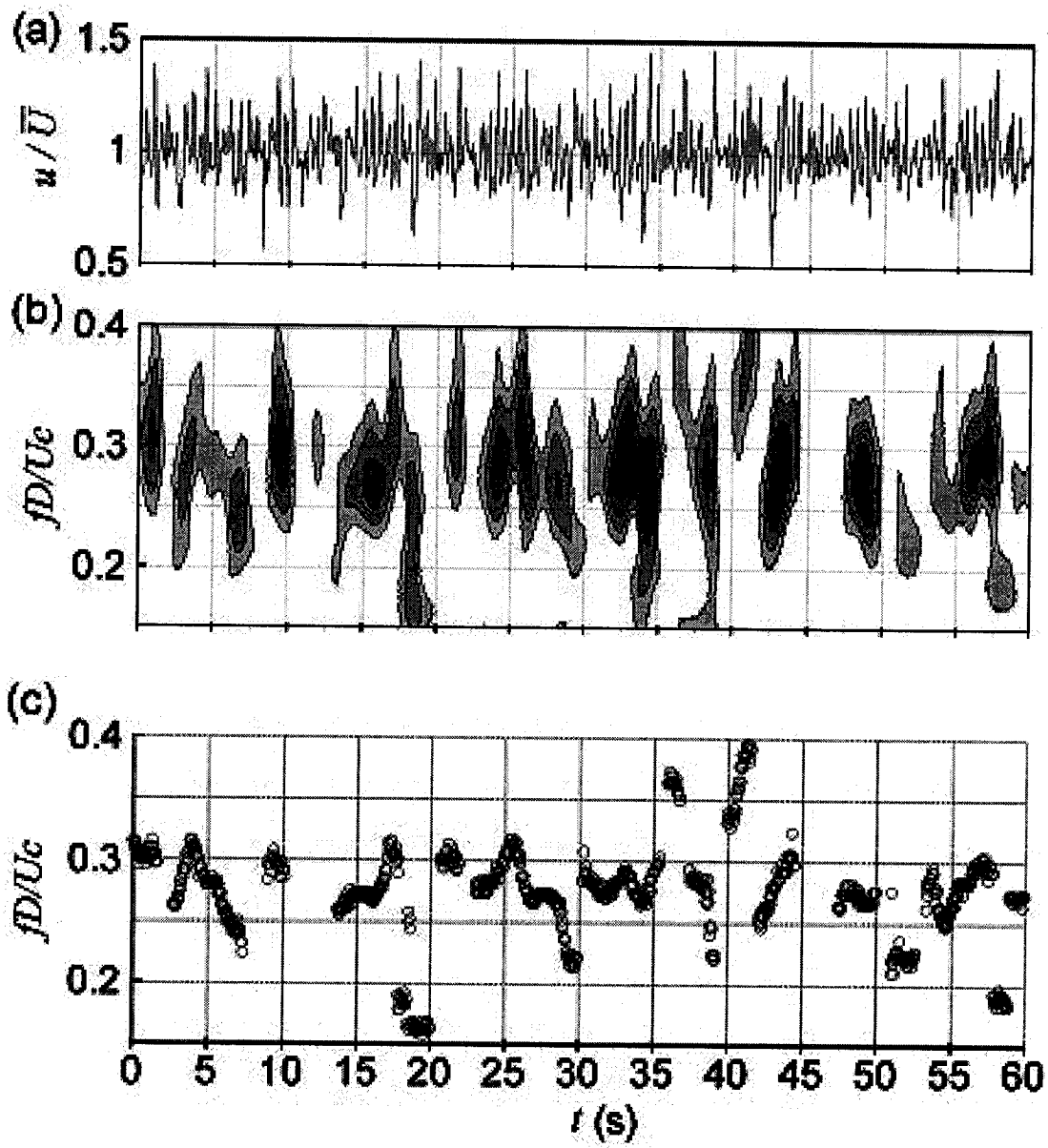

Figure 89: Small double-step cylinder with small *AR* middle section at *y/D* = 1.2 (behind the small cylinder), Re = 279 in uniform flow. (a) Velocity signal, (b) wavelet map, and (c) peak local frequencies.

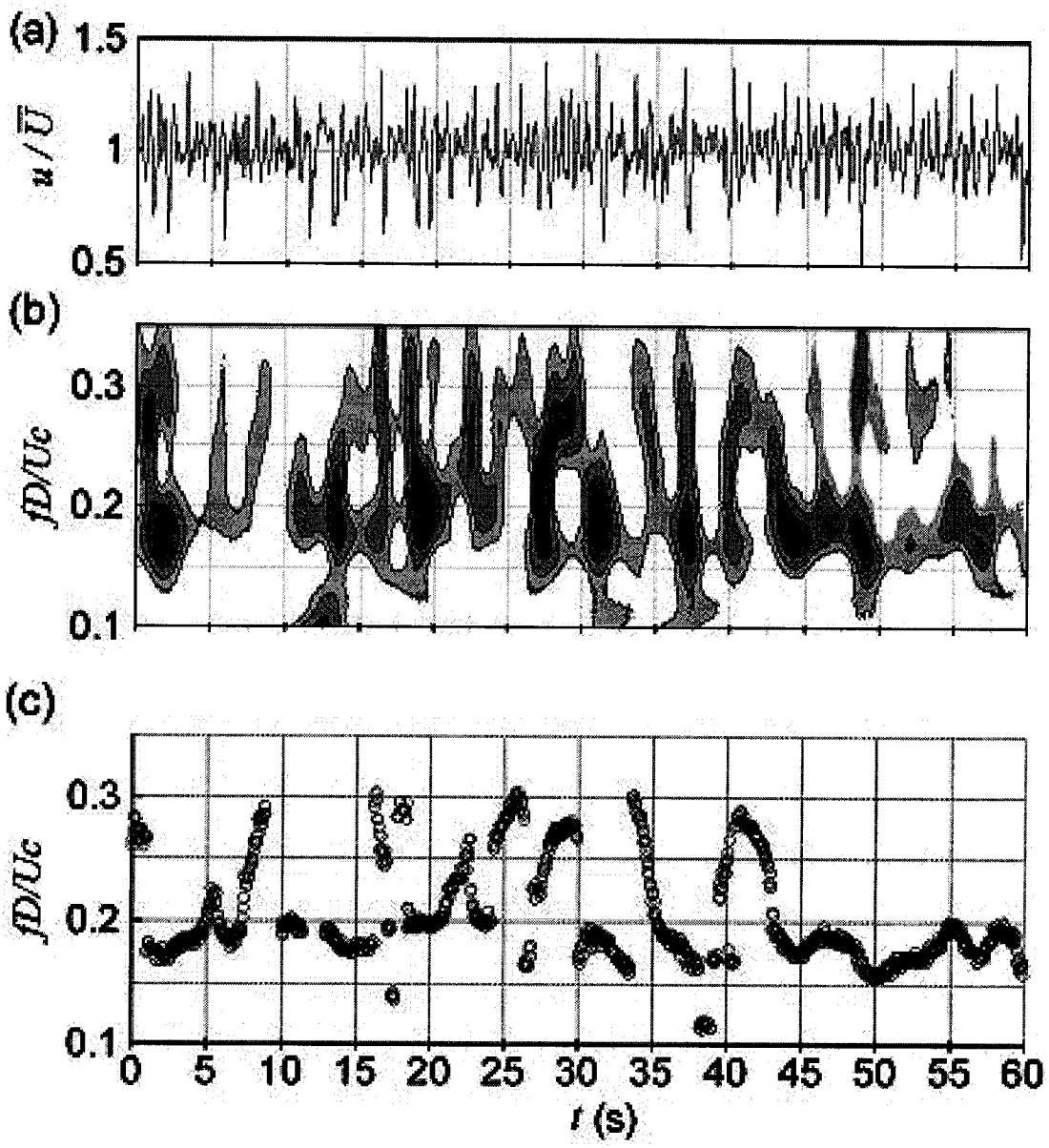

Figure 90: Small double-step cylinder with small *AR* middle section at *y/D* = 2.1 (behind the large cylinder, near the upper step), Re = 279 in uniform flow. (a) Velocity signal, (b) wavelet map, and (c) peak local frequencies.

Figure Credits

Figure 2 Reproduced with permission from Fey, U., Konig, M., and Eckelmann, H. 1998, "A new Strouhal-Reynolds-number relationship for the circular cylinder in the range 47<Re<2x10^5", Phys. Fluids, 10: 1547-1549.

Figure 3 Reproduced with permission from Panton, R.L., 1984, Incompressible Flow, Figure 15-16, pp.388-389, John Wiley & Sons, New York, New York.

Figure 4 Reproduced with permission from Williamson, C.H.K., 1992, "The natural and forced formation of spot-like 'vortex dislocations' in the transition of a wake", J. Fluid Mech., 243: 393-441.

Figure 12 Reproduced with permission from Budwig, R., and Peattie, R., 1989, "Two new circuits for hydrogen bubble flow visualization", J. Phys. E: Sci. Instrum., 22: 250-254

Appendix A

Technical drawings

A.1 Connectors, cylinders, and endplates

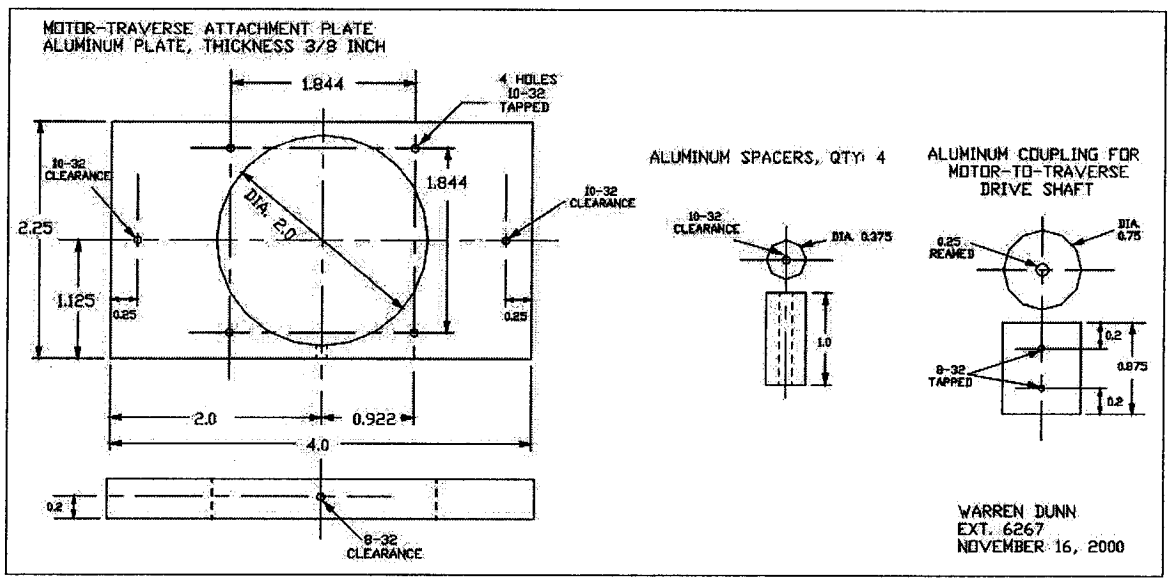

Figure A1: Traverse converter, manual to motor assembly.

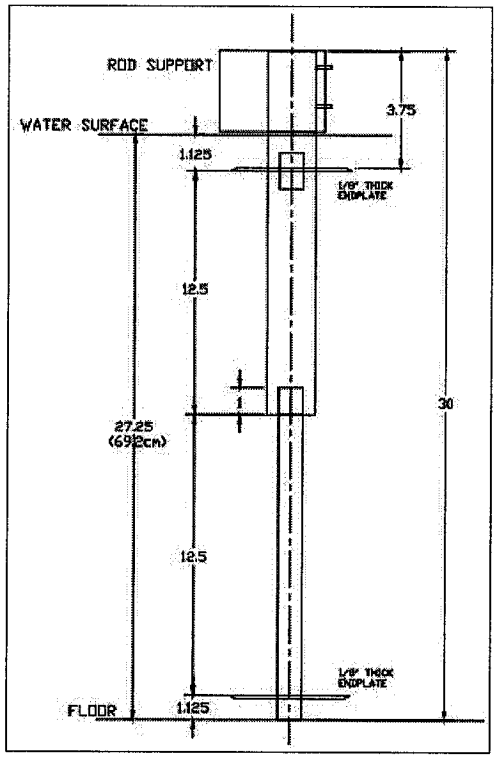

Figure A2: Step-cylinder configuration. All dimensions in inches.

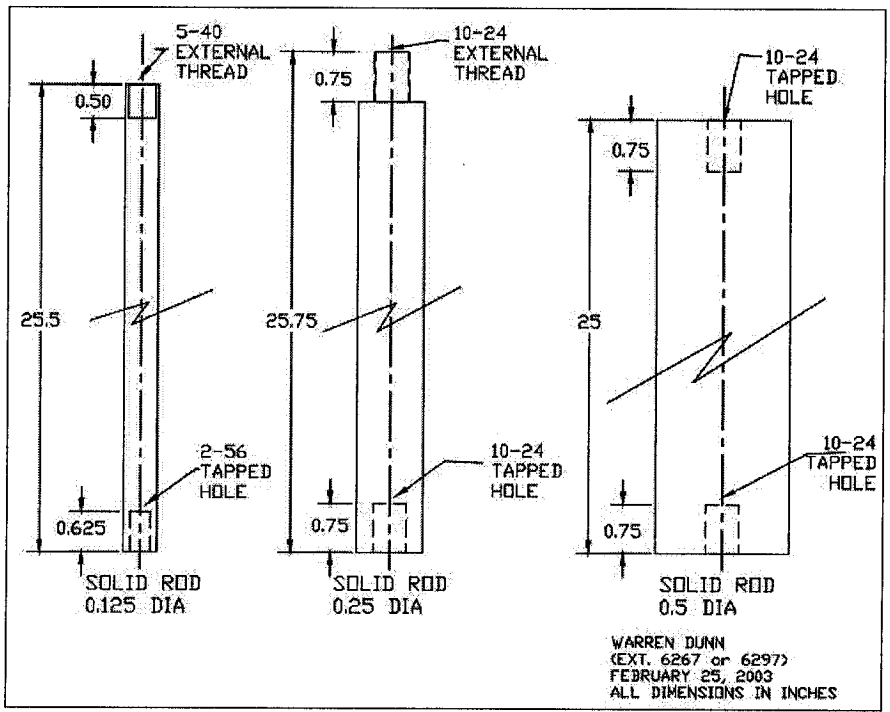

Figure A3: Full-length cylinders.

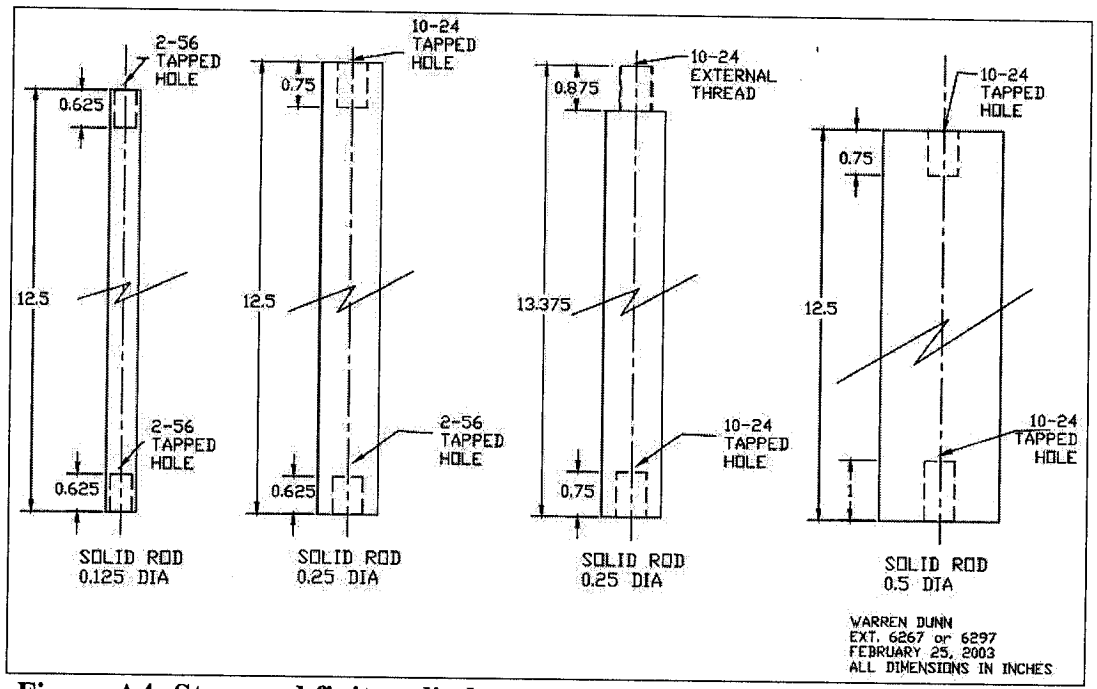

Figure A4: Step- and finite cylinders.

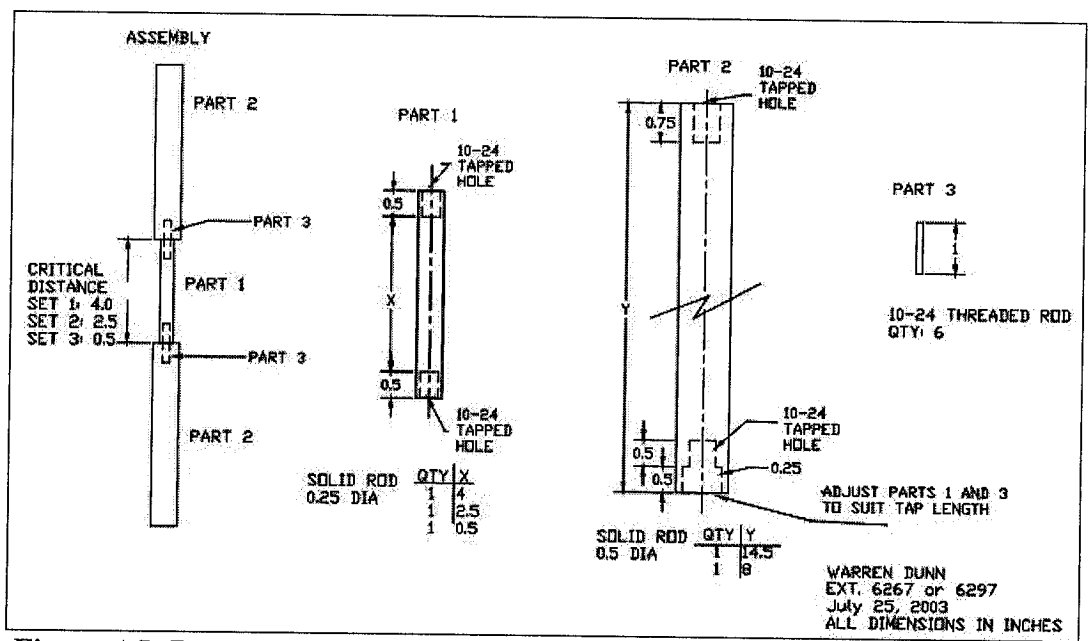

Figure A5: Double-step cylinders.

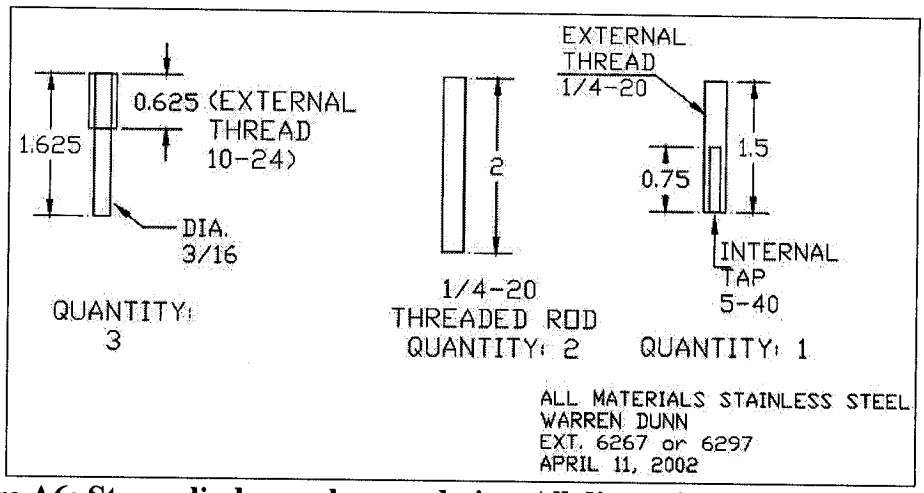

Figure A6: Step-cylinder anchors and pins. All dimensions in inches.

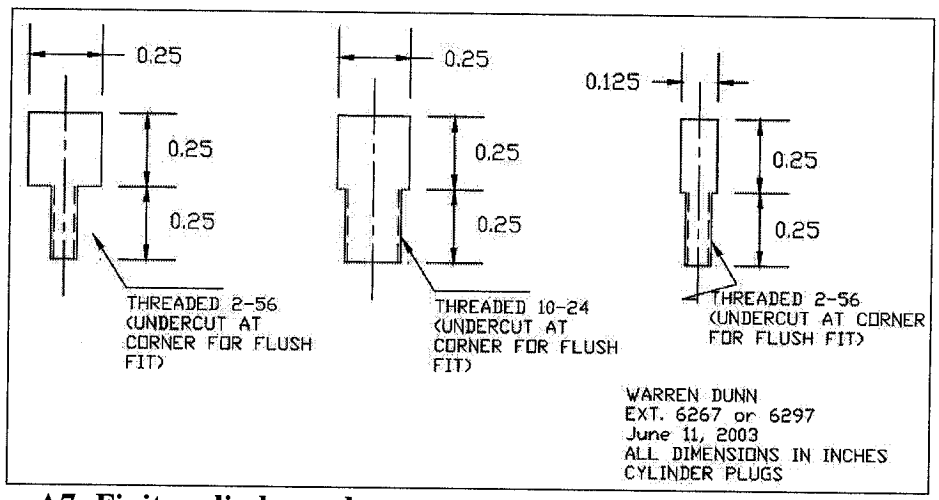

Figure A7: Finite cylinder end caps.

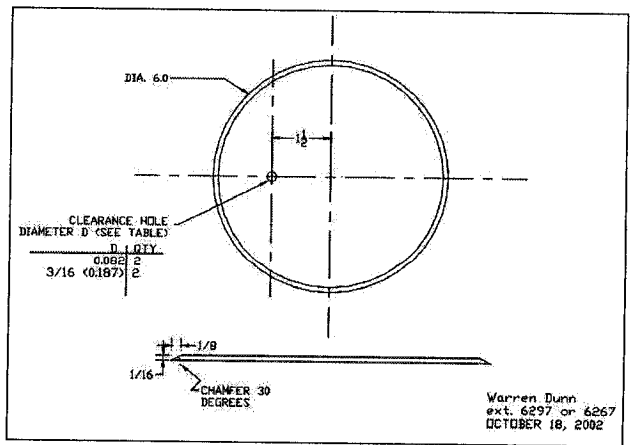

Figure A8: Endplates. All dimensions in inches.

A.2 Shear Generator

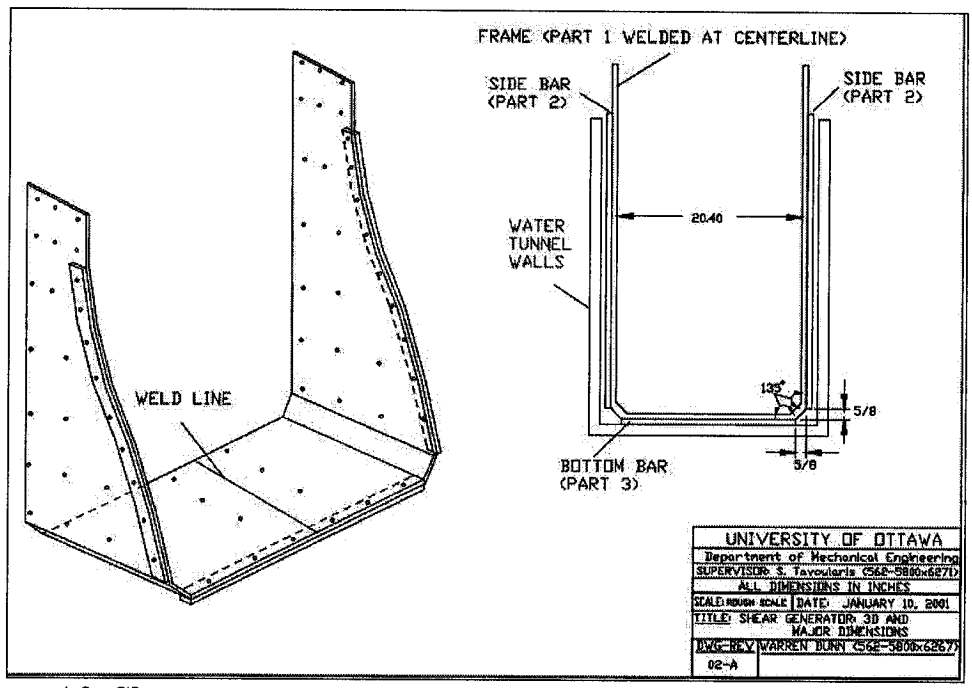

Figure A9: Shear generator frame –assembly.

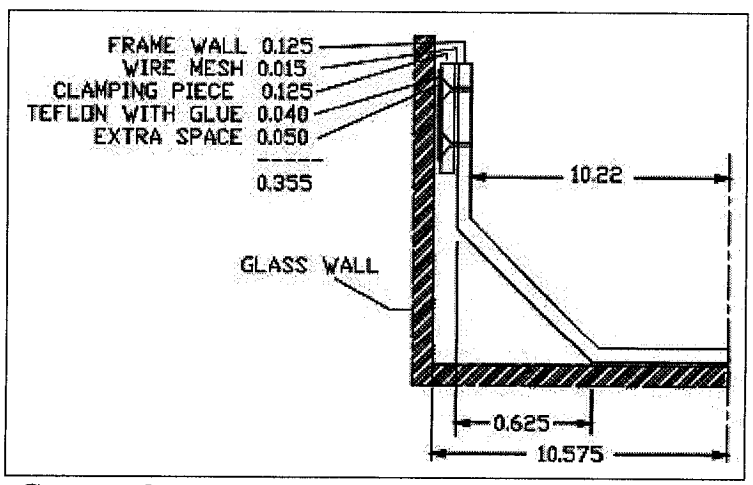

Figure A10: Corner placement inside water channel. All dimensions in inches.

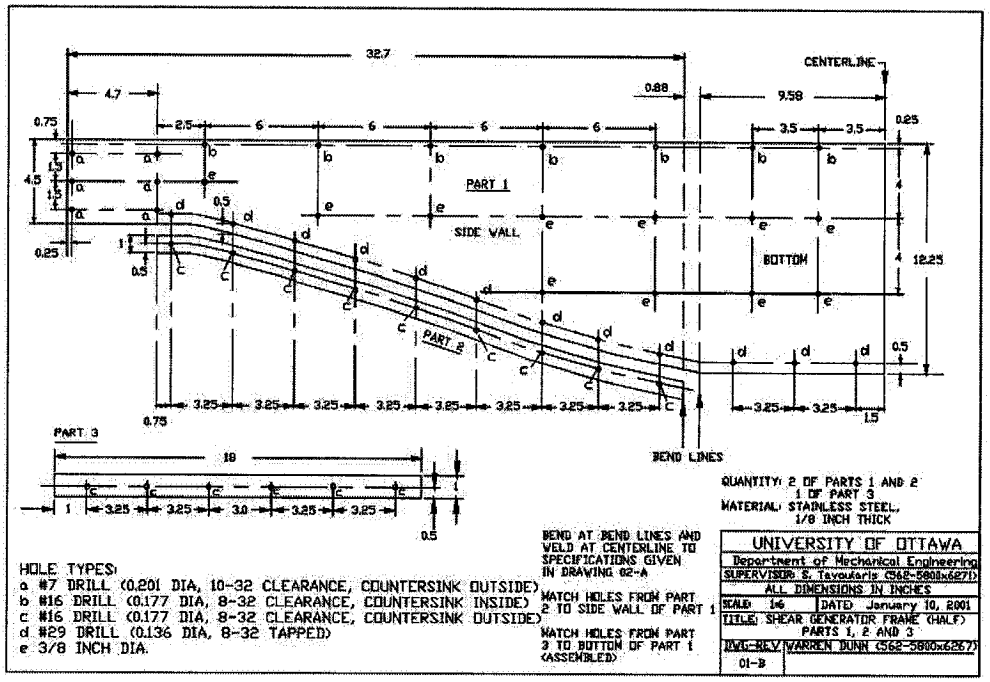

Figure A11: Shear generator hole locations.

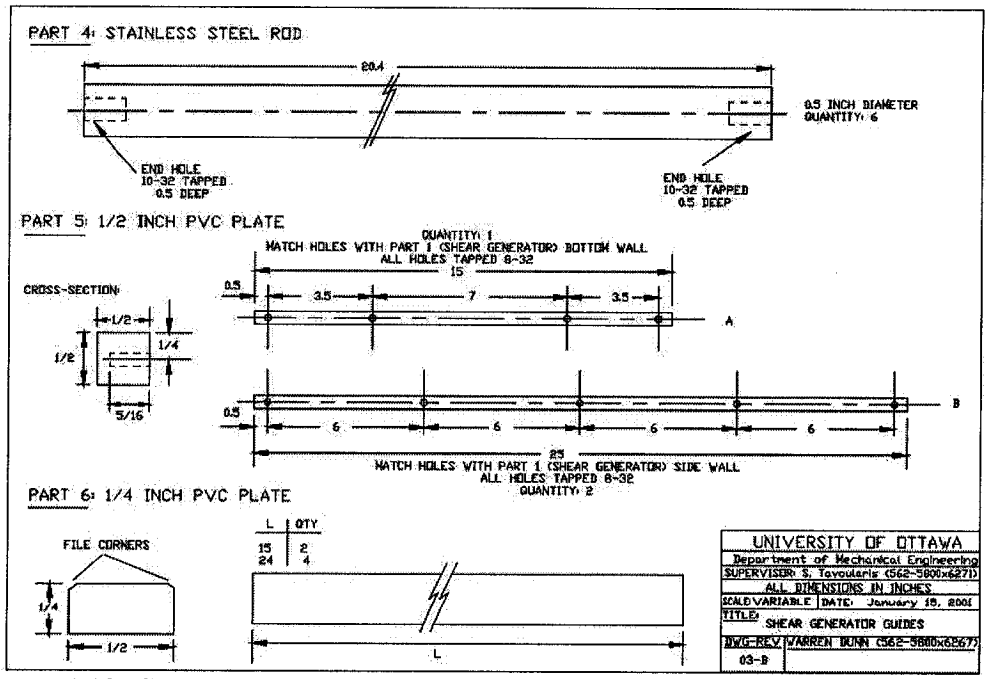

Figure A12: Support and slider rods.

Table A1: Shear generator contour.

y (inches)	*x* (inches)		
	Contour	Holes along contour edge	
0.000	4.500		
4.700	4.500		
5.450	4.500	4.000	
6.415	4.500		
7.000	4.531		
8.000	4.695		
8.700	4.845	4.345	
9.000	4.917		
10.000	5.181		
11.000	5.479		
11.950	5.787	5.287	
12.000	5.804		
13.000	6.150		
14.000	6.511		
15.000	6.885		
15.200	6.961	6.461	
16.000	7.266		
17.000	7.653		
18.000	8.040		
18.450	8.215	7.715	
19.000	8.427		
20.000	8.809		
21.000	9.156		
21.700	9.397	8.897	
22.000	9.499		
23.000	9.838		
24.000	10.169		
24.950	10.473	9.973	
25.000	10.489		
26.000	10.796		
27.000	11.086		
28.000	11.356		
28.200	11.407	10.907	
29.000	11.602		
30.000	11.820		
31.000	12.003		
31.450	12.072	11.572	
32.000	12.144		
33.000	12.233		
33.580	12.250		bend
35.160	12.250	11.750	bottom
38.410	12.250	11.750	bottom
41.660	12.250	11.750	bottom
43.160	12.250		centerline

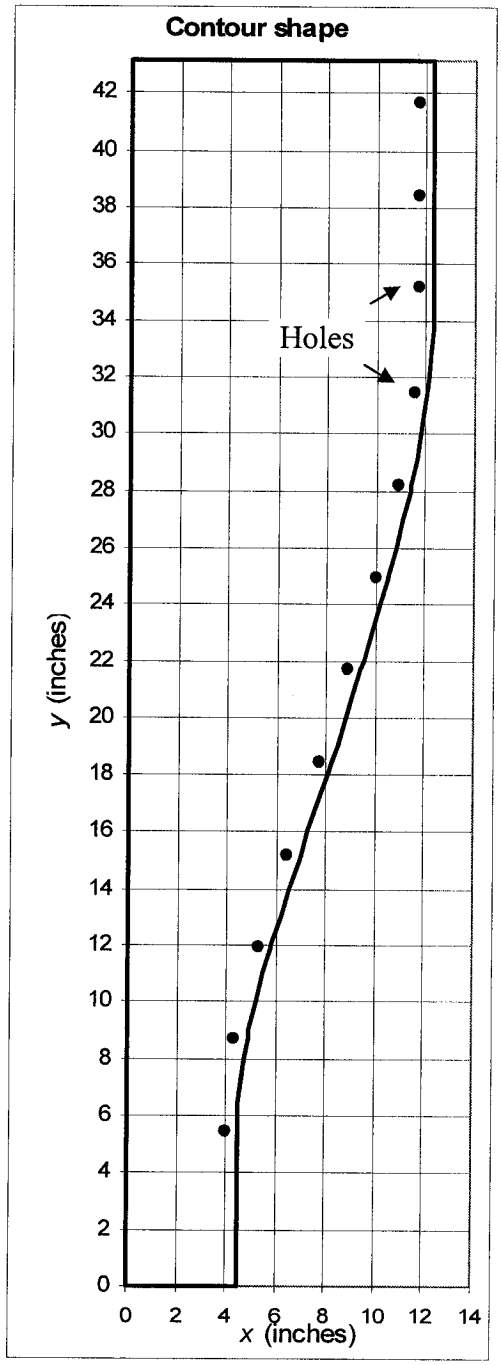

Figure A13: Shear generator frame contour.

Appendix B

Matlab m-files

B.1 Sample-and-hold resampling

The file samplehold.m applies the sample-and-hold type constant data rate resampling to a signal.

```
% Data input file is randomly sampled
% This resamples the vectors at an evenly spaced data rate
% dirpath is the directory path, for example 'c:\matlab6p1\work'
% filename is formatted MonthDD -file is called for example June171#001.txt
% start and finish are first and last data sets to resample

filename=input('Filename: ','s');  %format MonthDD
  if isempty(filename)==1; filename=['April25']; disp(filename);

  start=input('Data point -start: ');
    if isempty(start); start=1; disp(start); end
  finish=input('Data point -end: ');
    if isempty(finish); finish= start; disp(finish);

  checkdir=exist([dirpath '\' filename]); %verify that an output directory exists
    if checkdir==0
     mkdir(dirpath,filename) %if not, then create one
```

```
    end

blank=char(' '); disp(blank);
fr=input('Resample frequency [25Hz]: ');
  if isempty(fr); fr=25; end        %default sampling frequency

  note=char('please wait...',' '); disp(note);
%load appropriate files
for i=start:finish
  if i<10
    LDA=load([filename '1#00' num2str(i) '.txt']);
    filenameRES=[dirpath '\' filename '\' filename '_00' num2str(i) 'r.txt'];
  elseif i<100
    LDA=load([filename '1#0' num2str(i) '.txt']);
    filenameRES=[dirpath '\' filename '\' filename '_0' num2str(i) 'r.txt'];
  else
    LDA=load([filename '1#' num2str(i) '.txt']);
    filenameRES=[dirpath '\' filename '\' filename '_' num2str(i) 'r.txt'];
  end

  clear t u tr ur;

  %Apply sample and hold resampling
  t=LDA(:,1); %time vector
  u=LDA(:,2); %velocity vector

  n=length(t); dt=1/fr;  %original vector length, step size
  nr=fix((t(n)-t(1))/dt); %length of resampled vector

  tr=[0];
  for j=0:nr
    tr(j+1)=(t(1)+j*dt);       %resampled time vector
    a=max(find(t<=tr(j+1)));  %find the max t that is less than the tr value
    ur(j+1)=u(a);              %resampled velocity vector
  end

  ures=[tr' ur'];        %resampled vectors

  save(filenameRES,'ures','-ascii'); %resampled data file
  note=['Resampled signal saved in ' filenameRES]; disp(note);
end
beep
```

B.2 Signal filtering

The file hpfilt.m applies a high-pass filter to a signal with a constant sampling rate.

```
% Data input file is evenly-sampled
% This applies a high-pass filter to the resampled data
%      to remove the 0.1Hz wave from the water tunnel
% dirpath is the directory path, for example 'c:\matlab6p1\work'
% filename is formatted MonthDD -file is called for example June171#001.txt
% start and finish are first and last data sets to filter

filename=input('Filename: ','s');  %format MonthDD
   if isempty(filename)==1; filename=['April25']; disp(filename);

   start=input('Data point -start: ');
      if isempty(start); start=1; disp(start); end
   finish=input('Data point -end: ');
      if isempty(finish); finish= start; disp(finish);

   checkdir=exist([dirpath '\' filename]); %verify that an output directory exists
      if checkdir==0
       mkdir(dirpath,filename) %if not, then create one
      end

blank=char(' '); disp(blank);
cutoff=input('HP filter cutoff frequency [0.25Hz]: ');
   if isempty(cutoff); cutoff=0.25; end %default cutoff frequency

%load appropriate files
for i=start:finish
   if i<10
      LDA=load([filename '_00' num2str(i) 'r.txt']);
      filenameFILT=[dirpath '\' filename '\' filename '_00' num2str(i) 'rf.txt'];
   elseif i<100
      LDA=load([filename '_0' num2str(i) 'r.txt']);
      filenameFILT=[dirpath '\' filename '\' filename '_0' num2str(i) 'rf.txt'];
   else
      LDA=load([filename '_' num2str(i) 'r.txt']);
      filenameFILT=[dirpath '\' filename '\' filename '_' num2str(i) 'rf.txt'];
   end

   clear tr ur trf urf urf1 fr;
```

```
   order=2; %half the Butterworth filter order, since filtfilt doubles the order
   fr=1/(LDA(2,1)-LDA(1,1)); %find series data rate -constant
   tr=LDA(:,1); %time vector
   ur=LDA(:,2); %velocity vector

   %run the high-pass filter on the resampled vector
   [b,a]=butter(order,(2*cutoff)/fr,'high');   %filter coefficients
   urf1=filtfilt(b,a,ur);   %uses the filter forward and backward, doubles filter order
   urf=urf1+mean(ur);
   trf=tr;

   plot(tr,ur,'-x',tr,urf,'--p')
   grid on
   axis([0.5 1.5 min(urf) max(urf)])

   urfilt=[trf urf];     %filtered vectors

   save(filenameFILT,'urfilt','-ascii'); %resampled and filtered data file
   note=['Filtered signal saved in ' filenameFILT]; disp(note);
end
beep
```

B.3 Spectra

The file spect.m calculates and plots the spectrum of an input signal.

```
%loads resampled data sets to calculate power spectrum
% dirpath is the directory path, for example 'c:\matlab6p1\work'
% filename is formatted MonthDD -file is called for example June171#001.txt
% start and finish are first and last data sets to resample

filename=input('Filename: ','s');  %format MonthDD
   if isempty(filename)==1; filename=['April25']; disp(filename);

   start=input('Data point -start: ');
      if isempty(start); start=1; disp(start); end
   finish=input('Data point -end: ');
      if isempty(finish); finish= start; disp(finish);

   checkdir=exist([dirpath '\' filename]); %verify that an output directory exists
      if checkdir==0
```

```
      mkdir(dirpath,filename) %if not, then create one
     end

blank=char(' '); disp(blank);

D=6.604; Uc=95 %must be edited to fit the actual speed

window=input('Window size [2048 points]: ');
  if isempty(window); window=256; end %default window size
overlap=input('Overlap size [512 points]: ');
  if isempty(overlap); overlap=128; end %default overlap
nfft=input('fft size [2048 points]: ');
  if isempty(nfft); nfft=256; end %default overlap
fs=input('Sample data rate [25Hz]: ');
  if isempty(fs); fs=25; end     %default sampling frequency

%load appropriate files
for i=start:finish
  if i<10
    LDA=load([filename '_00' num2str(i) 'rf.txt']);
    filenameSP=[dirpath '\' filename '\' filename '_00' num2str(i) 'sp.txt'];
  elseif i<100
    LDA=load([filename '_0' num2str(i) 'rf.txt']);
    filenameSP=[dirpath '\' filename '\' filename '_0' num2str(i) 'sp.txt'];
  else
    LDA=load([filename '_' num2str(i) 'rf.txt']);
    filenameSP=[dirpath '\' filename '\' filename '_' num2str(i) 'sp.txt'];
  end

  u=LDA(:,2);
  u=u-mean(u);
  [psd,f]=pwelch(u,window,overlap,nfft,fs);
  fr=f.*D/Uc;
  ps=[f psd];

  plot(fr,psd)
  axis([0 .5 min(psd) max(psd)])
  grid on

  save(filenameSP,'ps','-ascii') %save spectral data
  note=['Spectrum data saved in ' filenameSP];  disp(note);
end
beep
```

B.4 Spectral peaks

The file spmax.m finds the highest spectral peak from a spectrum signal.

```
%FINDS THE MAXIMUM FREQUENCY IN A SPECTRUM FILE
% dirpath is the directory path, for example 'c:\matlab6p1\work'
% filename is formatted MonthDD -file is called for example June171#001.txt
% start and finish are first and last data sets to resample

filename=input('Filename: ','s');  %format MonthDD
  if isempty(filename)==1; filename=['April25']; disp(filename);

  start=input('Data point -start: ');
    if isempty(start); start=1; disp(start); end
  finish=input('Data point -end: ');
    if isempty(finish); finish= start; disp(finish);

  checkdir=exist([dirpath '\' filename]); %verify that an output directory exists
    if checkdir==0
     mkdir(dirpath,filename) %if not, then create one
    end

% load moments file containing data summary
% formatted as [point x y z ...]
moments=load([filename '2#001.txt']);

%options=char('Select filename style:','1 June173#001.txt','2 June17_001sp.txt');
%    disp(options);
%    style=input('==> [1] ');
%    if isempty(style);
style=2; %end

%load appropriate data files
for i=start:finish
  if i<10
    if style==1; LDA=load([filename '3#00' num2str(i) '.txt']);
    else LDA=load([filename '_00' num2str(i) 'sp.txt']); end
  elseif i<100
    if style==1; LDA=load([filename '3#0' num2str(i) '.txt']);
    else LDA=load([filename '_0' num2str(i) 'sp.txt']); end
  else
    if style==1; LDA=load([filename '3#' num2str(i) '.txt']);
```

```
    else LDA=load([filename '_' num2str(i) 'sp.txt']); end
  end

  [j,k]=max(LDA(:,2));
  frequency(i-start+1,1:4)=moments(i,1:4);
  frequency(i-start+1,5)=LDA(k);
  frequency(i-start+1,6)=LDA(k,2);

end
figure(2);
plot(frequency(:,3),frequency(:,5))

filenameSP=[dirpath '\' filename '\' filename 'SP.txt'];
save(filenameSP,'frequency','-ascii')
note=['Spectral peaks saved in ' filenameSP];
disp(note);
beep
```

B.5 Wavelet transform

The file wlet.m applies the wavelet transform to a signal.

```
%calculates the complex Morlet wavelet transform of the selected vector
filename=input('Filename: ','s');  %format MonthDD
  if isempty(filename)==1; filename=['April25']; disp(filename);

  start=input('Data point -start: ');
    if isempty(start); start=1; disp(start); end
  finish=input('Data point -end: ');
    if isempty(finish); finish= start; disp(finish);

  checkdir=exist([dirpath '\' filename]); %verify that an output directory exists
    if checkdir==0
     mkdir(dirpath,filename) %if not, then create one
    end

clear fm1 fm2 fmdev k m t1
note=char(' '); disp(note);
p1=input('Start time (s) [0]: ');
  if isempty(p1); p1=0; end
p2=input('Sample duration (s) [205]: ');
```

```
    if isempty(p2); p2=205; end

D=6.604; %diameter in mm
Uc=44.3; %centerline speed in mm/s
clear LDA u t u1 u2

%load appropriate files
for i=start:finish
    if i<10
        LDA=load([filename '_00' num2str(i) 'rf.txt']);
        filenameW=[dirpath '\' filename '\wav\' filename '_00' num2str(i) 'w.txt'];
        filenameWm=[dirpath '\' filename '\wav\' filename '_00' num2str(i) 'wm.txt'];
    elseif i<100
        LDA=load([filename '_0' num2str(i) 'rf.txt']);
        filenameW=[dirpath '\' filename '\wav\' filename '_0' num2str(i) 'w.txt'];
        filenameWm=[dirpath '\' filename '\wav\' filename '_0' num2str(i) 'wm.txt'];
    else
        LDA=load([filename '_' num2str(i) 'rf.txt']);
        filenameW=[dirpath '\' filename '\wav\' filename '_' num2str(i) 'w.txt'];
        filenameWm=[dirpath '\' filename '\wav\' filename '_' num2str(i) 'wm.txt'];
    end

    %find sample data rate
    dt=LDA(2,1)-LDA(1,1);

%define vector
    point2=fix((p1+p2)/dt);
    point1=round(p1/dt);

    u=LDA((point1+1):(point2-1),2);
    t=LDA((point1+1):(point2-1),1);
    t=t-point1*dt; tm=t;
    u1=(u-mean(u));
    u2=u/mean(u);

%calculate complex Morlet wavelet

% Note the use of the center frequency fc and the bandwidth parameter fb are reversed
%   from the documentation. According to waveinfo(cmor), the use should be
%   cmor'fb'-'fc', but a detailed look through cmorwavf.m, which calculates the
%   wavelet coefficients, shows that this is reversed, and should read cmor'fc'-'fb'. In
%   this case, fc=1Hz and fb=2 have been used. This can be confirmed by
%   running centfrq('cmor1-2'), which gives a center frequency of 1Hz.
```

```
   S=(0.1:.002:0.6); %define Strouhal number range
   f=S*Uc/D; %calculate frequencies from there
   scales=(1./f/dt); %use linear scales, calculated from scal2frq of known range
   coef=cwt(u1,scales,'cmor1-2');      %wavelet coefficients
   wfreq=scal2frq(scales,'cmor1-2',dt); %convert scales to equivalent frequency; should=f
   coefs=(abs(coef)).*sqrt(2*pi)./pi^.25;  %obtain coefficients in real space, normalize
properly
   coefs=coefs./max(max(coefs)); %renormalize by maximum value
   flog=wfreq.*D/Uc;  %convert to equivalent Strouhal number; should be =S

   for j=1:length(t)
      a=find(coefs(:,j)<0.4); %apply cutoff of 40% to wavelet coefficients
      coefs(a,j)=0;  %then discard coefs less than 40% max.
      [x,y]=max(coefs(:,j)); %find the scale for max. coefs at a given time
      fm(j)=flog(y);     % then find the appropriate frequency
   end
   c=find(fm<0.11); %coefs of 0 value were by default given a frequency of 0.1 above
   fm(c)=[]; tm(c)=[];  %  ...so discard those

   D=6.604; Uc=44.3; diameter and freestream speed in mm

fmd=std(fm); %standard deviation of peak frequency series
k=find(abs(fm-mean(fm))>3*fmd); %find peaks greater than 3 stds from the mean
fm(k)=[]; %  ... and discard them
t1=t; t1(k)=[];  % form a new time series of the same size
fmdev=max(abs(fm-mean(fm))); %find the maximum deviation from the mean
b(i,:)=[i fmdev fmd]; disp(b(i,:)); %display the maximum and standard deviations

%plot the last wavelet for confirmation
   figure(1)
   subplot(3,1,1)
   plot(t,u2)                    %plot the time series
   axis([min(t) max(t) min(u2) max(u2)])
   title([filename ' point ' num2str(start)])
   grid on

   subplot(3,1,2)
   contour(t,flog,coefs,5)       %plot the wavelet map
   axis([min(t) max(t) 0.1 0.5])
   grid on

   subplot(3,1,3)
```

```
   plot(tm,fm,'.','MarkerSize',3)        %plot the peak frequency
   grid
   axis([min(t1) max(t1) 0.1 0.5])

%reorder matrix for Axum/excel/tecplot plotting
lt=length(t);
ls=length(scales);

p=1;
for n=1:lt
   wmap(p:p+ls-1,1)=t(n);
   wmap(p:p+ls-1,2)=flog';
   wmap(p:p+ls-1,3)=coefs(:,n);
   p=p+ls;
end

checkdir=exist([dirpath '\' filename '\wav']); %verify that an output directory exists
   if checkdir==0
      mkdir(dirpath,[filename '\wav']) %if not, then create one
   end

data1=[t u];
data2=[tm fm];

save(filenameW,'wmap','-ascii')
save(filenameWs,'data1','-ascii')
save(filenameWm,'data2','-ascii')
  note=['Wavelet coefs saved in ' filenameW]; disp(note);
end
beep
```